

# University of Wollongong - Research Online

## Thesis Collection

Title: Mathematical modelling of nanostructures

Author: Duangkamon Baowan

Year: 2008

Repository DOI:

### Copyright Warning

You may print or download ONE copy of this document for the purpose of your own research or study. The University does not authorise you to copy, communicate or otherwise make available electronically to any other person any copyright material contained on this site.

You are reminded of the following: This work is copyright. Apart from any use permitted under the Copyright Act 1968, no part of this work may be reproduced by any process, nor may any other exclusive right be exercised, without the permission of the author. Copyright owners are entitled to take legal action against persons who infringe their copyright. A reproduction of material that is protected by copyright may be a copyright infringement. A court may impose penalties and award damages in relation to offences and infringements relating to copyright material.

Higher penalties may apply, and higher damages may be awarded, for offences and infringements involving the conversion of material into digital or electronic form.

**Unless otherwise indicated, the views expressed in this thesis are those of the author and do not necessarily represent the views of the University of Wollongong.**

Research Online is the open access repository for the University of Wollongong. For further information contact the UOW Library: [research-pubs@uow.edu.au](mailto:research-pubs@uow.edu.au)

*University of Wollongong Theses Collection*

*University of Wollongong Theses Collection*

---

*University of Wollongong*

*Year 2008*

---

# Mathematical modelling of nanostructures

Duangkamon Baowan  
University of Wollongong

Baowan, Duangkamon, Mathematical modelling of nanostructures, PhD thesis, School of Mathematics and Applied Statistics, University of Wollongong, 2008.  
<http://ro.uow.edu.au/theses/51>

This paper is posted at Research Online.  
<http://ro.uow.edu.au/theses/51>

## **NOTE**

This online version of the thesis may have different page formatting and pagination from the paper copy held in the University of Wollongong Library.

## **UNIVERSITY OF WOLLONGONG**

### **COPYRIGHT WARNING**

You may print or download ONE copy of this document for the purpose of your own research or study. The University does not authorise you to copy, communicate or otherwise make available electronically to any other person any copyright material contained on this site. You are reminded of the following:

Copyright owners are entitled to take legal action against persons who infringe their copyright. A reproduction of material that is protected by copyright may be a copyright infringement. A court may impose penalties and award damages in relation to offences and infringements relating to copyright material. Higher penalties may apply, and higher damages may be awarded, for offences and infringements involving the conversion of material into digital or electronic form.

# Mathematical modelling of nanostructures

*A thesis submitted in fulfillment of the  
requirements for the award of the degree of*

**Doctor of Philosophy**

*from*

**University of Wollongong**

*by*

**Duangkamon Baowan**

**B.Math (Hons), Mahidol University**

**School of Mathematics and Applied Statistics**

**2008**

## **CERTIFICATION**

I, Duangkamon Baowan, declare that this thesis, submitted in fulfilment of the requirements for the award of Doctor of Philosophy, in the School of Mathematics and Applied Statistics, University of Wollongong, is wholly my own work unless otherwise referenced or acknowledged. The document has not been submitted for qualifications at any other academic institution.

Duangkamon Baowan

May, 2008

# Acknowledgements

A journey is easier when you travel together. Interdependence is certainly more valuable than independence. This thesis is the result of three years of work whereby I have been accompanied and supported by many people. It is a pleasant aspect that I have now the opportunity to express my gratitude to all of them.

The first person I would like to thank is my supervisor, Professor Jim Hill. During these years I have known him as a sympathetic and principled person. His enthusiasm and his wide ranging view of research has made a deep impression on me. I owe him lots of gratitude for having shown me this approach to research and I am grateful that I have come to know Professor Jim Hill in my life.

I would like to acknowledge my co-supervisor Dr. Ngamta Thamwattana who has constantly kept an eye on the progress of my work and was always available when I needed her advice. Dr. Ngamta is not only my supervisor, but she is also my sister and my friend, who has taken care of me since the first day I arrived here in Australia.

The Nanomechanics Group also substantially contributed to the development of this work. Especially the extensive comments and the interactions with Dr. Barry Cox which have had a direct impact on the quality of this thesis. I would also like to thank my fellow PhD student Tamsyn Hilder for our many discussions and for providing me much sisterly advice.

This research has been supported by a Royal Thai Government Scholarship. I am grateful for their confidence in me. I am also grateful to the School of Mathematics and Applied Statistics at the University of Wollongong for providing me with an excellent working environment during the years of my study.

Last but not least, I wish to express my gratitude to the people who never failed to support me throughout my journey, my father, my mother and my brother.

# Abstract

Worldwide nanotechnology is a major focus in science and technology, and most research in this area deals with chemical, physical and biological issues or a combination of these areas, but to date very little work has been undertaken on mathematical modelling. Rather than employing large-scale computations using molecular dynamics simulation, in this thesis elementary mechanical principles and classical applied mathematical modelling procedures are utilised to examine three specific areas in nanotechnology.

Firstly, the Lennard-Jones potential function for the non-bonded interaction potential energy between two molecules and the continuum approximation, which assumes that the interatomic interactions can be modelled by smearing the atoms uniformly across surfaces, are undertaken to investigate the mechanical properties of certain nanostructures, namely double-walled carbon nanotubes, nanopeapods, nanocones and carbon onions. Owing to their special mechanical, electrical and thermal properties, these nanostructures promise many applications for future nanoscale devices, such as nano-bearings and nano-oscillators. This thesis examines issues regarding nano-oscillators constructed from these nanostructures. In particular, the van der Waals interaction energy, the suction energy, the offset location and the oscillatory behaviour are determined. Analytical expressions are obtained as a function of the radii and the lengths of the structures. In addition, all the predicted mechanical properties derived here are in excellent agreement with results from molecular dynamics simulations.

The second area is the joining of nanostructures by invoking the principle that the atoms arrange themselves in such a way that the total squared deviation of the distance between atoms at the junction and some ideal bond length is a minimum. Initially, toroidal molecules are described, which are formed from three distinct carbon nanotube sections, through minimisation of the total squared deviation of the distance between two carbon atoms at the junction from the ideal physical bond length. Representative formulae for the mean generating toroidal radius and tube radius of the tori are determined. Following this is to determine the perpendicular joining structures for carbon nanotubes and flat graphene by two least squares approaches, which are the variation in bond length and the variation in bond angle.

Such a combined structure might constitute a transmission platform for ultra small computer chips. Given that the corresponding boron nitride nanostructures are also good semiconductors, the corresponding combined structures are also determined. However, the essential mathematical ideas for combining boron nitride structures are quite different to those required for connecting the corresponding carbon structures, since only rings with an even number of sides are energetically favourable.

The third area in this thesis involves the elastic model of carbon nanotubes. Here, carbon nanotubes are assumed to be modelled as transversely isotropic linearly elastic materials which have the same properties in one plane, but vary in the normal direction to this plane. The equilibrium equations are derived and they can be shown to generalise those for isotropic materials. Further, wave-like deformations on the outer-most surface of the oscillating carbon nanotubes are investigated. On neglecting any frictional effects and assuming that the inner surface atoms of the outer tube and those located on the outer surface of the inner tube dominate the van der Waals force, expressions for displacements in the  $r$ - and  $z$ -directions are obtained.

The major contribution of this thesis is the use of conventional applied mathematical modelling techniques to formulate analytical expressions for nanostructures. Broadly three mechanical issues are studied, including (i) van der Waals interaction energy and oscillatory behaviour for nanostructures, (ii) geometry of combining two nanostructures and (iii) deformation of carbon nanotubes as transversely isotropic materials. However, many of the theoretical structures proposed here have yet to be confirmed either experimentally or by molecular dynamics simulations; and as such the work might be considered as a first step to settling some of the important physical principles in nanotechnology. In summary, the new elements of the thesis comprise:

- Analytical expressions to determine the equilibrium locations, force distributions and oscillatory behaviours for nested nanostructures,
- Simple least squares methods to connect two nanostructures,
- Elastic model for the deformations of double-walled carbon nanotubes.



# Contents

<b>I</b>	<b>Introduction</b>	<b>1</b>
<b>1</b>	<b>Overview</b>	<b>2</b>
1.1	Background . . . . .	2
1.1.1	Continuum modelling for nanostructures . . . . .	3
1.1.2	Geometry of joining nanostructures . . . . .	4
1.1.3	Carbon nanotubes as transversely isotropic linearly elastic materials . . . . .	5
1.2	Thesis structure . . . . .	6
<b>II</b>	<b>Continuum modelling of nanostructures</b>	<b>8</b>
<b>2</b>	<b>Introduction to continuum modelling of nanostructures</b>	<b>9</b>
2.1	Carbon and boron nitride nanostructures . . . . .	9
2.2	Interaction energy . . . . .	11
2.3	Overview . . . . .	15
<b>3</b>	<b>Double-walled carbon nanotubes</b>	<b>16</b>
3.1	Nomenclature . . . . .	16
3.2	Introduction . . . . .	17
3.3	Force distribution for double-walled carbon nanotubes . . . . .	19
3.4	Suction force for double-walled carbon nanotubes . . . . .	24
3.5	Offset position for double-walled carbon nanotubes . . . . .	28
3.6	Oscillation of double-walled carbon nanotubes . . . . .	31
3.7	Summary . . . . .	34

<b>4</b>	<b>Nanopeapods</b>	<b>38</b>
4.1	Nomenclature . . . . .	39
4.2	Introduction . . . . .	39
4.3	Encapsulations of $C_{60}$ fullerene . . . . .	42
4.3.1	Encapsulation of a $C_{60}$ head-on at an open end . . . . .	42
4.3.2	Encapsulation of $C_{60}$ around the edge of an open end . . . . .	44
4.3.3	Encapsulation of $C_{60}$ at a defect opening on the tube wall . . . . .	47
4.4	Zigzag and spiral configurations for nanopeapods . . . . .	50
4.4.1	Zigzag nanopeapods comprising $(2k + 1)$ $C_{60}$ molecules . . . . .	50
4.4.2	Numerical solutions for zigzag nanopeapods . . . . .	53
4.4.3	Spiral nanopeapod comprising $k$ $C_{60}$ molecules . . . . .	55
4.4.4	Numerical solutions for spiral nanopeapods . . . . .	57
4.5	Summary . . . . .	58
<b>5</b>	<b>Nanocones</b>	<b>62</b>
5.1	Nomenclature . . . . .	63
5.2	Introduction . . . . .	64
5.3	Carbon nanocones . . . . .	65
5.4	Equilibrium locations for carbon nanocones . . . . .	68
5.4.1	Model formulation for two carbon nanocones . . . . .	68
5.4.2	Model formulation for identical carbon nanocones . . . . .	70
5.4.3	Numerical solutions . . . . .	71
5.5	Suction behaviour for a carbon nanocone . . . . .	75
5.5.1	Cone vertex oriented in negative $z$ -direction . . . . .	75
5.5.2	Cone vertex oriented in positive $z$ -direction . . . . .	77
5.6	Oscillatory behaviour for carbon nanocone . . . . .	80
5.6.1	Force distribution for a carbon nanocone oscillating inside a carbon nanotube . . . . .	80
5.6.2	Oscillation of a carbon nanocone inside a carbon nanotube . . . . .	81
5.7	Boron nitride nanocones . . . . .	84
5.7.1	Model formation for boron nitride cones . . . . .	85
5.7.2	Numerical results for boron nitride cones . . . . .	88
5.8	Summary . . . . .	92

<b>6</b>	<b>Carbon onions</b>	<b>94</b>
6.1	Nomenclature . . . . .	94
6.2	Introduction . . . . .	95
6.3	Interaction energies between shells . . . . .	96
6.4	Numerical results . . . . .	99
6.5	Summary . . . . .	104
<b>III</b>	<b>Geometry of joining nanostructures</b>	<b>105</b>
<b>7</b>	<b>Introduction to the geometry of joining nanostructures</b>	<b>106</b>
7.1	Least squares methods . . . . .	107
7.1.1	Variation in bond length . . . . .	107
7.1.2	Variation in bond angle . . . . .	108
7.2	Euler's polyhedra theorem . . . . .	109
7.3	Bonded interaction for small deformations . . . . .	110
7.4	Overview . . . . .	112
<b>8</b>	<b>Toroidal molecules formed from three distinct carbon nanotubes</b>	<b>113</b>
8.1	Nomenclature . . . . .	113
8.2	Introduction . . . . .	114
8.3	Model formation for an elbow . . . . .	115
8.4	Model formation for a toroidal molecule . . . . .	117
8.5	Results and discussion . . . . .	122
8.6	Summary . . . . .	124
<b>9</b>	<b>Joining carbon nanotubes and flat graphene sheets</b>	<b>127</b>
9.1	Nomenclature . . . . .	127
9.2	Introduction . . . . .	128
9.3	Variation in the bond length . . . . .	129
9.4	Variation in the bond angle . . . . .	132
9.5	Results and discussion . . . . .	137
9.6	Summary . . . . .	140

<b>10</b>	<b>Joining boron nitride nanotubes and flat sheets</b>	<b>142</b>
10.1	Nomenclature . . . . .	143
10.2	Introduction . . . . .	143
10.3	Defect classification . . . . .	145
10.4	Combinatorial theory and possible defects . . . . .	148
10.5	Two least squares approaches . . . . .	154
10.6	Results and discussion . . . . .	155
10.7	Summary . . . . .	158
<b>IV</b>	<b>Transversely isotropic linearly elastic materials</b>	<b>164</b>
<b>11</b>	<b>Introduction to transversely isotropic linearly elastic materials</b>	<b>165</b>
11.1	Elasticity of carbon nanotubes . . . . .	165
11.2	Overview . . . . .	166
<b>12</b>	<b>Governing equations for transversely isotropic linearly elastic material</b>	<b>168</b>
12.1	Nomenclature . . . . .	169
12.2	Hooke's law for transversely isotropic linearly elastic materials . . . .	170
12.3	Hooke's law for isotropic linearly elastic materials . . . . .	172
12.4	Equilibrium equations for transversely isotropic linearly elastic materials . . . . .	173
12.4.1	Cartesian coordinates $(x, y, z)$ . . . . .	173
12.4.2	Cylindrical polar coordinates $(r, \theta, z)$ . . . . .	177
12.5	Simple shear problem for transversely isotropic linearly elastic materials	179
12.6	Simple shear problem for isotropic linearly elastic materials . . . . .	182
<b>13</b>	<b>Wave-like deformations for oscillating carbon nanotubes</b>	<b>184</b>
13.1	Nomenclature . . . . .	184
13.2	Model formulation and boundary conditions . . . . .	185
13.3	Displacement and shear force solutions . . . . .	187
13.4	Tables of elastic constants . . . . .	189
13.5	Numerical results . . . . .	191

13.6 Summary . . . . .	191
------------------------	-----

<b>V</b>	<b>Summary</b>	<b>195</b>
<b>14</b>	<b>Summary</b>	<b>196</b>
14.1	Continuum modelling for nanostructures . . . . .	196
14.2	Geometry of joining nanostructures . . . . .	198
14.3	Carbon nanotubes as transversely isotropic linearly elastic materials .	200
<b>VI</b>	<b>Appendices and Bibliography</b>	<b>202</b>
<b>A</b>	<b>Analytical solution for double-walled carbon nanotubes</b>	<b>203</b>
A.1	Evaluation of the integral $J_n$ . . . . .	203
A.2	Evaluation of the integral $K_n$ . . . . .	205
A.3	Evaluation of the integral $L_n$ . . . . .	207
<b>B</b>	<b>Analytical solution for an offset position defined in (3.5)</b>	<b>208</b>
<b>C</b>	<b>Derivation of interaction energy for <math>C_{60}</math> fullerenes</b>	<b>212</b>
<b>D</b>	<b>Analytical solution for nanopeapods</b>	<b>215</b>
D.1	Evaluation of the integral $G_n$ . . . . .	215
D.2	Evaluation of the integral $H_n$ . . . . .	216
D.3	Evaluation of the integral $I_n$ . . . . .	216
<b>E</b>	<b>Degenerate hypergeometric functions</b>	<b>218</b>
<b>F</b>	<b>Mathematical solution for <math>A_{ni}</math> (<math>i = 1, 2, 3, 4</math>) defined in §13.3</b>	<b>220</b>
<b>G</b>	<b>Relationship of moduli for transversely isotropic linearly elastic materials</b>	<b>222</b>
	<b>Bibliography</b>	<b>226</b>
	<b>List of the author's publications</b>	<b>240</b>

# List of Figures

2.1	The graphite plane of nanotube surface . . . . .	11
2.2	Graph of Lennard-Jones potential . . . . .	13
3.1	Double-walled carbon nanotubes of lengths $2L_1$ and $2L_2$ . . . . .	19
3.2	Four critical positions for two concentric nanocylinders. . . . .	21
3.3	Total potential energy of a (10,10) nanotube with various $L_1$ entering into a (16,16) nanotube with length $L_2 = 500 \text{ \AA}$ . . . . .	23
3.4	Force distribution of a (10,10) nanotube with various $L_1$ entering into a (16,16) nanotube with length $L_2 = 500 \text{ \AA}$ . . . . .	24
3.5	Geometry of a single-walled carbon nanotube entering another single-walled carbon nanotube. . . . .	24
3.6	Force experienced by a (6,6) carbon nanotube due to van der Waals interaction with a semi-infinite carbon nanotube (a) (10,10), (b) (16,16) and (20,20). . . . .	28
3.7	Suction energy for an inner tube (6,6) entering an outer tube. . . . .	29
3.8	Offset location for double-walled carbon nanotube. . . . .	29
3.9	Potential energy of an offset (6,6) carbon nanotube inside a (16,16) and a (20,20) carbon nanotube with respect to the radial distance $\varepsilon$ . . . . .	31
3.10	Extrusion distance $d$ for inner tube oscillating inside outer tube. . . . .	31
3.11	Two regions for the idealised potential energy for double-walled carbon nanotubes oscillator. . . . .	33
3.12	The frequency profile $f$ for three lengths $L_1$ versus the initial velocity $v_0$ when the extrusion distance is zero where $L_2 = 500 \text{ \AA}$ . . . . .	34
3.13	The frequency profile $f$ for three lengths $L_1$ versus extrusion distance $d$ when the initial velocity is zero where $L_2 = 500 \text{ \AA}$ . . . . .	35

4.1	$C_{60}$ fullerene encapsulated in carbon nanotube head-on at an open end.	42
4.2	Energy profile for $C_{60}$ encapsulated by head-on at open end. . . . .	44
4.3	$C_{60}$ fullerene encapsulated in carbon nanotube around the edge of an open end. . . . .	45
4.4	Energy profile for $C_{60}$ encapsulated into (10,10) tube. . . . .	47
4.5	$C_{60}$ fullerene encapsulated in carbon nanotube at defect opening on the tube wall. . . . .	48
4.6	Potential energy profile along the (10,10) tube. . . . .	50
4.7	Zigzag configuration for $(2k+1)$ $C_{60}$ fullerenes inside a carbon nanotube.	51
4.8	Spiral configuration for $k$ $C_{60}$ molecules inside a carbon nanotube. . .	55
5.1	Five possible nanocones with vertex angles $19.20^\circ$ , $38.90^\circ$ , $60.00^\circ$ , $83.60^\circ$ and $112.90^\circ$ . . . . .	66
5.2	(a) Graphene sheet (b) forming the carbon nanocone. . . . .	67
5.3	(a) Geometry of an elliptical cone and (b) diagram for surface inte- grations. . . . .	68
5.4	Geometry for two distinct carbon nanocones. . . . .	68
5.5	Geometry for two identical carbon nanocones. . . . .	70
5.6	Variation of potential energy versus distance between vertices for the cone $N_p = 1$ and $N_p = 2, 3, 4$ and 5 for the second cone. . . . .	73
5.7	Variation of potential energy versus distance between vertices for var- ious combinations of two different cones. . . . .	73
5.8	Variation of potential energy versus distance between vertices for five identical carbon nanocones. . . . .	74
5.9	Shortest distance $x$ between two carbon nanocones at the equilibrium location. . . . .	74
5.10	Geometry of carbon nanocone with vertex oriented in negative $z$ - direction. . . . .	75
5.11	Force experienced by a co-axial carbon nanocone with a semi-infinite carbon nanotube for cone vertex in negative $z$ -direction ( $b - a = 3.4$ $\text{\AA}$ ). . . . .	77



5.12	Suction energy for co-axial carbon nanocones $N_p = 1$ and $N_p = 5$ entering a single-walled carbon nanotube versus the difference of the radii $(b - a)$ . . . . .	78
5.13	Geometry of carbon nanocone with vertex oriented in positive $z$ -direction. . . . .	78
5.14	Force experienced by co-axial carbon nanocone with semi-infinite carbon nanotube for cone vertex in positive $z$ -direction ( $b - a = 3.4 \text{ \AA}$ ). . . . .	79
5.15	Geometry for carbon nanocone oscillating inside single-walled carbon nanotube. . . . .	80
5.16	Potential energy for cone oscillating inside tube. . . . .	82
5.17	Force distribution for cone oscillating inside tube. . . . .	82
5.18	Variation of oscillatory frequency for five possible structures of carbon nanocones with respect to half-length of carbon nanotube. . . . .	84
5.19	Geometry for any two nested nanocones. . . . .	86
5.20	Potential energy versus the distance $Z$ between two vertices for five identical possible boron nitride nanocones. . . . .	90
5.21	Potential energy versus the distance $Z$ between two vertices for boron nitride cones when the outer cone angle $\alpha = 112.9^\circ$ and the inner cone angles $\alpha = 19.2^\circ, 38.9^\circ, 60.0^\circ$ and $83.6^\circ$ . . . . .	91
5.22	Potential energy versus the distance $Z$ between two vertices for boron nitride cones when the outer cone angle $\alpha = 19.2^\circ$ and the inner cone angles $\alpha = 38.9^\circ, 60.0^\circ, 83.6^\circ$ and $112.9^\circ$ . . . . .	91
6.1	Double-shell ellipsoidal carbon onion . . . . .	96
6.2	Potential energy profile for a spherical carbon onion showing the possible radii of the $n$ th-shell for which the energy is minimum. . . . .	100
6.3	Potential energy profile for a five-shell $C_{80}$ carbon onion. . . . .	101
6.4	Equilibrium spacing between adjacent shells of spherical carbon onion assuming a $C_{60}$ core. . . . .	103
6.5	Equilibrium spacing between adjacent shells of spheroidal carbon onions assuming a $C_{24}$ and a $C_{80}$ core. . . . .	103
7.1	Position vectors for variation in bond angle approach. . . . .	109

7.2	Definitions of variables $r$ , $\phi$ and $\tau$ for bonded potential energy given by equation (7.6). . . . .	111
8.1	Basic double elbow unit formed from three nanotube sections. . . . .	116
8.2	Cartesian coordinate system for two single nanotube elbows. . . . .	117
8.3	Elbows formed from three distinct nanotube sections. . . . .	118
8.4	Elbow skeleton formed from three distinct nanotube sections. . . . .	119
8.5	Toroidal coordinate system $(a, \phi, \psi)$ . . . . .	121
8.6	Nanotorus formed from $3(5,0)_{17}6(4,4)_{48}3(7,0)_{19}$ where $\phi_1 + \phi_2 = 60^\circ$ . . . . .	125
8.7	Nanotorus formed from $3(3,3)_{12}6(6,0)_{32}3(4,4)_{24}$ where $\phi_1 + \phi_2 = 60^\circ$ . . . . .	125
9.1	Sixteen possible defects which require another eight bonds for the $sp^2$ network. . . . .	131
9.2	Model formation for joining a (6,0) tube with most symmetric defect where (a) and (b) are for a graphene sheet and (c) and (d) are for a (6,0) tube. . . . .	134
9.3	Three dimensional illustration for a (6,0) tube perpendicularly connected to a graphene sheet. . . . .	135
9.4	Model formation for joining an (8,0) tube with defect #6 where (a) is for a graphene sheet and (b) and (c) are for an (8,0) tube. . . . .	135
9.5	Three dimensional illustrations for an (8,0) connection with a graphene sheet by (a) variation in bond angle and (b) variation in bond length. . . . .	137
9.6	Connecting an (8,0) tube with a graphene sheet for the defect configurations (a) #6 and (b) #3. . . . .	139
9.7	Connecting a (4,4) tube with a graphene sheet for (a) #3-b and (b) #9-a configurations. The second configuration has the smallest variation in bond length in a least squares sense. . . . .	139
10.1	Angle values defined by each of the six sides of a hexagonal lattice. . . . .	145
10.2	Atoms at open end of (a) a zigzag tube and (b) an armchair tube. . . . .	146
10.3	Some typical defects showing the number of edges and the number of atoms that can be joined (those marked * are possible boron nitride defects). . . . .	147
10.4	Most likely physical defects for various zigzag and armchair nanotubes. . . . .	151

10.5	Hexagonal lattice formed from two triangular sublattices for boron nitride network, (a) translational vectors and (b) rotational angles. . . . .	153
10.6	Defect configurations for (a) (3,3), (b) (6,0) and (c) (9,0) boron nitride nanotubes. . . . .	156
10.7	(3,3) nanotube connected with a hexagonal boron nitride sheet by (a) variation in bond length and (b) variation in bond angle. . . . .	156
10.8	(6,0) nanotube connected with a hexagonal boron nitride sheet by (a) variation in bond length and (b) variation in bond angle. . . . .	156
10.9	(9,0) nanotube connected with a hexagonal boron nitride sheet by (a) variation in bond length and (b) variation in bond angle. . . . .	157
10.10	Some typical defect configurations considered to be non-physical. . . . .	162
10.11	Some quasi-circular defects considered to more likely candidates to be joined with a nanotube. . . . .	163
12.1	Diagram for transversely isotropic materials. . . . .	168
12.2	Diagram of double-walled carbon nanotubes. . . . .	180
13.1	Diagram of double-walled carbon nanotube. . . . .	185
13.2	Force distribution approximated by rectangular functions. . . . .	186
13.3	The displacement $u(c, z, t)$ on the outer surface of the outer tube (a) at $t = 0$ , (b) at $t = T/4$ , (c) at $t = T/2$ and (d) at $t = 3T/4$ where $T$ is the period of the oscillation. . . . .	192
13.4	The displacement $w(c, z, t)$ on the outer surface of the outer tube (a) at $t = 0$ , (b) at $t = T/4$ , (c) at $t = T/2$ and (d) at $t = 3T/4$ where $T$ is the period of the oscillation. . . . .	193
B.1	Mapping diagram of (a) $\theta_1 - \theta_2$ plane to (b) $x - y$ plane. . . . .	209
B.2	Diagram of $r^2 - \theta$ plane. . . . .	210
C.1	Diagram of atom interacting with $C_{60}$ fullerene . . . . .	212
C.2	Diagram of two interacting $C_{60}$ fullerenes . . . . .	213

# List of Tables

3.1	Constants used in the model for the carbon system(* Reference [36]) .	37
4.1	Numerical values for binding energy (BE) in eV and the equilibrium distance ( $E_0$ ) in Å for a C <sub>60</sub> fullerene encapsulated in a carbon nanotube around the tube edge at the open end for different angles $\phi$ . . .	46
4.2	Equilibrium distance $Z$ (Å), offset location $\varepsilon$ (Å) and total potential energy of the system $E^{tot}$ (eV) for each pair of C <sub>60</sub> fullerenes in a zigzag configuration nanopeapod comprising $(2k + 1)$ C <sub>60</sub> molecules. .	54
4.3	Angular spacing $\alpha$ , longitudinal spacing $\beta$ , offset location $\varepsilon$ in Å and total potential energy of the system $E^{tot}$ (eV) for each pair of C <sub>60</sub> fullerenes in a spiral configuration nanopeapod comprising $k$ C <sub>60</sub> molecules. . . . .	61
5.1	Relation of number of pentagons $N_p$ and open angle $\alpha$ for carbon nanocones. . . . .	67
5.2	Distance between vertices $Z$ at the equilibrium position for any two carbon nanocones. . . . .	72
5.3	Shortest distance $x$ between the two cones at the equilibrium position for any two carbon nanocones. . . . .	72
5.4	Lennard-Jones constants for boron nitride and carbon-boron nitride systems. . . . .	86
5.5	Equilibrium distance $Z$ (Å) between two vertices and the perpendicular distance $x$ (Å) for boron nitride cones. . . . .	89
5.6	Equilibrium distance $Z$ (Å) between two vertices and the perpendicular distance $x$ (Å) for carbon-boron nitride cones. . . . .	89

6.1	Radius of each shell for a spherical carbon onion predicted from minimisation of the energy $E_o/(\eta_1\eta_2)$ (6.3) and assuming a $C_{60}$ core. . . .	99
6.2	Radii of spherical fullerenes $C_N$ . . . . .	100
6.3	Lateral and vertical sizes for five-layer ellipsoidal carbon onion where $C_{80}$ is the assumed inner core. . . . .	101
6.4	Lateral and vertical sizes for five-layer ellipsoidal carbon onion where $C_{24}$ is the assumed inner core. . . . .	102
8.1	Fundamental parameters for nanotube elbows formed from three distinct carbon nanotube sections. . . . .	123
8.2	Bend angles and base unit section for nanotube elbows. . . . .	123
8.3	Physical parameters of two specific toroidal structures. . . . .	124
9.1	Values of least square function $f$ ( $\text{\AA}^2$ ) and distance $\ell$ ( $\text{\AA}$ ) for 16 configurations of an (8,0) tube and corresponding polygons $P_n$ where $n$ is number of sides. . . . .	132
9.2	Values of least square function $f$ ( $\text{\AA}^2$ ) and distance $\ell$ ( $\text{\AA}$ ) for 32 configurations of a (4,4) tube and corresponding polygons $P_n$ where $n$ is the number of sides. By symmetry #1-a and #1-b are equivalent. . .	133
9.3	Eight coordinate positions for joining an (8,0) tube with defect #6 using the variation in bond length method. . . . .	139
9.4	Eight coordinate positions for joining a (4,4) tube with defect #9-a using the variation in bond length method. . . . .	140
10.1	Relation between the number of edges ( $E$ ) and number of joins ( $J$ ) for defects (those marked * are possible boron nitride defects). . . .	148
10.2	Number of possible defects for zigzag ( $n, 0$ ) and armchair ( $n, n$ ) boron nitride tubes. . . . .	150
10.3	Numerical values for the sum of squared derivations (percentage differences) for joining (3,3), (6,0) and (9,0) boron nitride tubes with a boron nitride sheet by the variation in bond length (a) and the variation in bond angle (b). . . . .	158
10.4	Values of least squares function $f$ ( $\text{\AA}^2$ ) defined by (7.2) and distance $\ell$ ( $\text{\AA}$ ) for joining zigzag boron nitride tubes with some defects. . . .	160

10.5	Values of least squares function $f$ ( $\text{\AA}^2$ ) defined by (7.2) and distance $\ell$ ( $\text{\AA}$ ) for joining armchair boron nitride tubes with some defects. . . .	161
G.1	Elastic constants of single-walled carbon nanotubes $(n, n)$ based on Jin and Yuan [15]. . . . .	223
G.2	Values of elastic constants for single-walled carbon nanotubes $(n_1, n_2)$ based on Lu [20]. . . . .	224
G.3	Values of elastic constants for the series of multi-walled carbon nanotubes $(5n, 5n)$ where $n = 1, 2, 3, \dots$ and $N$ is a number of walls based on Lu [20]. . . . .	224
G.4	Values of elastic constants of single-walled carbon nanotubes $(n, n)$ based on Shen and Li [134]. . . . .	224
G.5	Values of elastic constants of double-walled carbon nanotubes which the inner tube $(5, 5)$ and the outer tube $(n, n)$ based on Shen and Li [134]. . . . .	225
G.6	The values of elastic moduli and elastic constants for single-walled carbon nanotube $(10, 10)$ of three studies [15, 20, 134]. . . . .	225

# Part I

## Introduction

# Chapter 1

## Overview

### 1.1 Background

Mathematics is the natural language of science which focuses on such issues as quantity, structure, space, and change. Mathematicians investigate such concepts aiming to formulate new conjectures and establish their results by expressions and definitions that are universally applicable. Nowadays, mathematics is used throughout many fields, including medicine and economics. There are two main branches for the study of mathematics which are applied mathematics and pure mathematics. In terms of applied mathematics, it is the application of mathematics for which a new discovery can be inspired and made practically useful. Without having any application in mind, pure mathematics provides its own interest and its relevance is often made meaningful much later.

Nanotechnology is multidisciplinary, drawing from fields such as physics, chemistry, biology, material science, and mechanical and electrical engineering. The underlying theme of nanotechnology is the control of matter on the atomic and molecular levels where physical properties are size dependent. The word “nano” is the prefix  $10^{-9}$ , so one nanometer is one billionth of a meter. To put this scale in context, the radius of a human hair is around 7000 nanometers and the size of a virus ranges from 15 to 600 nanometers. The word “technology” is the branch of knowledge that deals with creation, such as industrial arts, engineering, applied science, and pure science. Therefore, “nanotechnology” might be referred to as the study of those small-scale objects which can be assembled to create a novel device. Examples of nanotechnology in modern use are the present day manufacture of textiles, the design of computer chips and the carbon fibre in optical wires.



Worldwide nanotechnology is a current major focus in science and technology. Most research in nanotechnology deals with chemical, physical and biological issues or a combination of these areas, but to date very little work has been undertaken on mathematical modelling which can significantly reduce the time taken in the trial-and-error processes leading to applications, and which in turn decreases the research cost. Rather than employing large-scale computations using molecular dynamics simulations, here elementary mechanical principles and classical mathematical modelling procedures are utilised to investigate the mechanics of nanoscale systems. The models developed in this thesis involve the three specific areas as follows:

1. Continuum modelling of nanostructures, particularly for the van der Waals interaction energy and oscillatory behaviour,
2. Geometry of joining nanostructures, to form toroidal molecules from carbon nanotube elbows and to connect nanotubes with a hexagonal sheet,
3. Elasticity of carbon nanotubes, particularly the model of carbon nanotubes as a transversely isotropic linear elastic material.

### 1.1.1 Continuum modelling for nanostructures

Nanostructures such as carbon nanotubes, nanopeapods, nanocones and carbon onions, provide a possible new basis for the creation of many nano-devices due to their outstanding properties such as their high strength, high flexibility and low weight. One application which has attracted much consideration is as nanoo oscillators [1–4], which can generate frequencies in the gigahertz range [4], and which may form the basis of possible devices in the computer industry. Since the discovery of ultra low friction by Cumings and Zettle [1], double-walled carbon nanotube oscillators have been widely studied using both molecular dynamics simulations and experiments [2, 4–7]. In addition, carbon nanotubes have received much attention for medical applications, especially their use as nanocontainers for drug and gene delivery. In particular, a well-known self-assembled hybrid carbon nanostructure, so-called nanopeapods, may be regarded as a model for possible drug carriers, where

the carbon nanotube can be thought of as the nanocontainer and the  $C_{60}$  molecular chain can be considered as the drug molecule [8].

Nanocones have received much less attention in the literature, primarily because only a small amount of cones tend to occur in the production process [9]. However, the narrow vertex of a cone is an ideal candidate for nanoprobe in scanning microscopy [10]. Furthermore, boron nitride structures are good electrical semiconductors and may also be utilised for such nanoprobe. Carbon onions comprising concentric fullerenes are one family of carbon nanostructures. Experimentally, electron beam irradiation methods are used to modify the multi-layers of carbon onions, but at present there is no procedure to predict the precise shape of the resulting structure.

The majority of work in this area is based on either experiments or molecular dynamics simulations, and mathematical modelling is used to a much lesser extent. In this study, the use of elementary mechanical principles and classical applied mathematical modelling techniques are employed to obtain explicit analytical criteria and ideal model behaviour. Specifically, the mechanical behaviour of the van der Waals interaction energy between two nanostructures, such as double-walled carbon nanotubes, carbon and boron nitride nanocones and carbon onions, and many-body system, such as nanopeapods, are examined. Furthermore, once a nanostructure is encapsulated inside the other, the nature of the resulting oscillatory behaviour is predicted. The Lennard-Jones potential function and the continuum approximation, which assumes that the atoms can be modelled by smearing them uniformly across the surface, are employed throughout this study.

### 1.1.2 Geometry of joining nanostructures

In order to create certain transmission devices for future nanoelectromechanical systems, carbon nanotubes might be used to carry current to a platform comprising a graphene sheet. With this in mind, the perpendicular joining between carbon nanotubes and a flat graphene is determined. In addition, given that a hexagonal boron nitride crystal is geometrically similar to that of graphite in a carbon structure, the perpendicular joining for a tube and a sheet of boron nitride is also examined. Note that the essential mathematical ideas for the combining of boron nitride nanostruc-

tures are quite different to those required for connecting the corresponding carbon structures.

From the work of Cox and Hill [11], the authors have exploited the idea that the basis of joining carbon nanostructures is an underlying requirement that each inter-atomic distance be as close as possible to the ideal carbon-carbon bond length. Indeed, in [11] this procedure accurately produces certain toroidal molecules which are known to exist, along with numerous other predicted molecules. In this thesis, two such least squares approaches are adopted, which are the variation in bond length and the variation in bond angle, and these are undertaken to consider the joining of various nanostructures. To begin, the least squares approach in bond length, which is a dominant term in the bonded interaction energy [12], is employed to investigate toroidal-shaped molecules formed from the joining of three distinct carbon nanotube sections.

Both the variation in bond length and the variation in bond angle approaches are carried out for both carbon and boron nitride systems. These two geometrical approaches are directly related to computer simulations adopted by a number of authors [13–16] for the bonded interaction energy in a small deformation system. In addition, Euler’s polyhedra theorem is employed throughout the study to examine the consistency of the geometrical structures for connected configurations.

### 1.1.3 Carbon nanotubes as transversely isotropic linearly elastic materials

Carbon nanotubes are believed to be perfectly elastic materials, in the sense that they return to their original configuration when the applied loads are released. There are many experiments and molecular dynamics simulations studying the elastic properties of carbon nanotubes [17]. Yu *et al.* [18] obtain the values of Young’s modulus as 270-950 GPa when a load is applied to multi-walled carbon nanotubes. A quantum mechanical and molecular mechanical calculations are utilised by Zhao *et al.* [19] to observe the deformation of carbon nanotubes under load. They find a larger value of Young’s modulus than in any pervious study, around 1 TPa, and they propose that carbon nanotubes are the strongest materials known at present. Using a force-constant model, Lu [20] presents values of elastic moduli for both single-walled and multi-walled carbon nanotubes. Moreover, Lu [20] finds that the elastic

properties are insensitive to the helicity, the radius and the number of walls. Shen and Li [21] study the deformations of carbon nanotubes under a number of loading types and propose that carbon nanotubes can be modelled as transversely isotropic linearly elastic materials. In addition, Jin and Yuan [15] undertake molecular dynamics simulations using the Lennard-Jones potential function to study the elastic properties of single-walled carbon nanotubes. They also determine the elastic moduli using energy and force approaches which result in approximately the same values. Following the work of Shen and Li [21], in three of the chapters of this thesis, carbon nanotubes are assumed to be modelled as transversely isotropic linearly elastic materials.

Transversely isotropic materials possess a single axis about which the material is isotropic, but it is not isotropic with respect to any other axis. In other words, transversely isotropic materials have the same properties in one plane, but which differ in the normal direction to this plane. In terms of the basic equations for transversely isotropic materials, Elliott [22] first introduced the general three-dimensional solutions for such materials. These general solutions are adopted and employed in a number of studies [23–26] to solve many problems. Furthermore, for a problem in a cylindrical coordinate system, Selvadurai [25] considers the displacement and stress equations with no body force and shows that there are three potential functions  $\phi_1(r, \theta, z)$ ,  $\phi_2(r, \theta, z)$  and  $\psi(r, \theta, z)$  for the solutions.

First, the equations for transversely isotropic linearly elastic materials in both a rectangular Cartesian and a cylindrical coordinate system are derived. Utilising the expressions for the force distribution from the study of the mechanics of double-walled carbon nanotubes, wave-like deformations on the outer surface are determined, which are a function of the oscillation frequency and the radii of both the inner and outer tubes. An implication of these findings, is that the waves generated might be used to transmit data in future nano-devices.

## 1.2 Thesis structure

There are six parts in this thesis. Part I contains an overview and a plan of the thesis structure. The continuum modelling, involving the van der Waals interaction energies and the oscillatory behaviour for nanostructures, which are double-walled car-

bon nanotubes, nanopeapods, nanocones and carbon onions, is presented in Part II. Using a least squares principle, the combining of nanostructures is investigated in Part III. In Part IV, double-walled carbon nanotubes are assumed to be modelled as transversely isotropic materials and wave-like deformations occurring on the outermost surface are determined. Finally, Part V comprises some concluding remarks for this thesis and Part VI contains seven appendices and the bibliography.

## Part II

# Continuum modelling of nanostructures

# Chapter 2

## Introduction to continuum modelling of nanostructures

The aim of this study is the use of elementary mechanical principles and classical applied mathematical modelling techniques to formulate explicit analytical criteria and ideal model behaviour in nanotechnology for which previously only experimental and molecular dynamics simulation were available. The Lennard-Jones potential function and the continuum approach, which assumes that the discrete atoms may be replaced by a uniform surface density of atoms, are utilised to determine mechanical behaviour such as the interaction energy, suction condition and oscillation for carbon and boron nitride nanostructures. To start, the structures of carbon and boron nitride are examined. Initially, Lennard-Jones potential function and the continuum approximation are introduced in §2.2 and an overview of Part II is present in §2.3.

### 2.1 Carbon and boron nitride nanostructures

Carbon nanostructures including fullerenes, carbon nanotubes, nanopeapods, nanocones, carbon onions and nanotori have received much attention because of their unique properties, such as their high flexibility, high thermal conductivity and are presently the strongest materials known [27]. Comprehensive pictorial catalogues of many diverse structures which may arise can be found in [28, 29]. Their special properties have not only led to proposals for many potential nano-devices such as drug carriers and scanning microscopy [4, 5, 30] but also to the desire to create further new carbon nanostructures, such as sea urchins, bamboos, beads, helical coils and tripod shapes, as shown in Figure 4 of [31]. All the carbon nanostructures originate from the hexagonal graphene sheet, which may be rolled up to form a tube,

or by adding pentagonal rings formed into a  $C_{60}$  fullerene, or by cutting a part of the sheet out and joining the edges together to form a cone, or twisting the tube-like shape to form a torus. Therefore, the hexagonal network of carbon is examined.

The discovery of carbon nanotubes in 1991 by Iijima [32] offers many scientific challenges for their adaption to a wide variety of applications in nanotechnology. Single-walled carbon nanotubes can be thought of as a graphene sheet which is rolled up to form a cylinder. Multi-walled carbon nanotubes can be envisaged as multi-layers of graphite sheets which are rolled up co-axially.  $C_{60}$  fullerenes are similar in structure to graphene, and are composed of linked hexagonal rings, which also contain pentagonal rings that are needed to close the surface into a spherical shape.

The helical structures of carbon nanotubes can be described by the chiral vector,  $\mathbf{C} = n\mathbf{a}_1 + m\mathbf{a}_2$ , usually represented by  $(n, m)$ , where  $n$  and  $m$  are integers such that  $m \leq n$ , and  $\mathbf{a}_1$  and  $\mathbf{a}_2$  are the basis vectors, as shown in Figure 2.1. Moreover, the chiral angle  $\alpha$  is also depicted in Figure 2.1. There are three types of carbon nanotubes: armchair, zigzag and chiral. The armchair is the structure which has  $n = m$  and  $\alpha = 30^\circ$  and the zigzag is the form which has  $m = 0$  and  $\alpha = 0^\circ$ . A carbon nanotube which is neither armchair nor zigzag, is termed chiral. The electronic structure of carbon nanotubes can also be determined by  $(n, m)$ . If  $(n-m)$  is a multiple of 3, then they will be metallic, otherwise, they will be a semiconductor. Thus all armchair tubes are metallic.

Generally, for  $(n, m)$  carbon nanotubes, where  $n$  and  $m$  are integers, the corresponding radius, denoted here by  $b$ , is determined from

$$b = \sigma \sqrt{3(n^2 + nm + m^2)}/2\pi, \quad (2.1)$$

where  $\sigma$  is the carbon-carbon bond length and throughout this study  $\sigma$  is usually taken to be 1.42 Å.

Boron nitride is a binary chemical compound consisting of equal proportions of boron and nitrogen.

It is isoelectronic with carbon since in the periodic table, boron and nitrogen are adjacent to carbon [33], and, like carbon, boron nitride exists as various polymorphic forms, one of which is analogous to diamond and one analogous to graphite. The



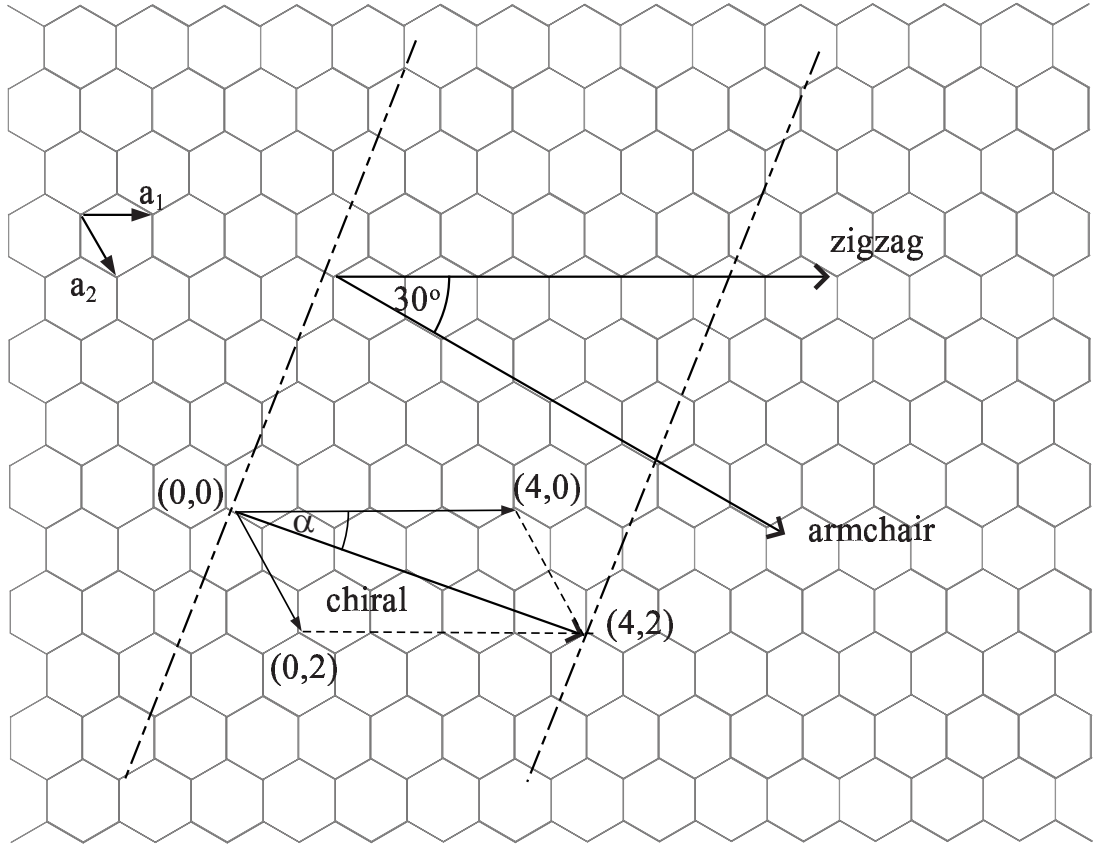


Figure 2.1: The graphite plane of nanotube surface

diamond-like polymorph is one of the hardest materials known and the graphite-like polymorph is a useful lubricant. Moreover, the large band gaps in this material will produce better electronic properties than those of carbon structures [34]. Hexagonal boron nitride is also known to be a good electrical semiconductor with excellent stability and thermal conductivity, which can be used in vacuum technology, nuclear energy, x-rays and lubrication [35]. In this part, only the cone structure of boron nitride is investigated, since it is suggested to be an ideal candidate for nanoprobe in scanning tunneling microscopy.

## 2.2 Interaction energy

The non-bonded interaction energy between two molecules can be obtained by summing the potential interaction for each atom pair

$$E = \sum_i \sum_j \Phi(\rho_{ij}), \quad (2.2)$$

where  $\Phi(\rho_{ij})$  is a potential function for atoms  $i$  and  $j$  on each molecule a distance  $\rho_{ij}$  apart. Following Girifalco *et al.* [36] and Hodak and Girifalco [37], a continuum approach is adopted where atoms are assumed to be uniformly distributed over the surfaces of the molecules. Thus, instead of the double summation in (2.2), the interaction energy can be obtained by performing double surface integrals, averaged over the surface of each entity

$$E = \eta_1 \eta_2 \int \int \Phi(\rho) d\Sigma_1 d\Sigma_2, \quad (2.3)$$

where  $\eta_1$  and  $\eta_2$  are the mean atomic surface density of atoms on each molecule and  $\rho$  denotes the distance between two typical surface elements  $d\Sigma_1$  and  $d\Sigma_2$  on each molecule. In this study, the Lennard-Jones potential is employed, which is given by

$$\Phi(\rho) = -\frac{A}{\rho^6} + \frac{B}{\rho^{12}}, \quad (2.4)$$

where  $A$  and  $B$  are the attractive and repulsive constants, respectively. It should be noted that there are a number of empirically motivated models potentials in the literature, for example, the Morse potential used in Belyschko *et al.* [38], Liew *et al.* [39] and Walther *et al.* [40], and the other models and their applications can be found in Qian *et al.* [17] and Rieth [41]. Alternatively, the Lennard-Jones potential (2.4) can be written in the form

$$\Phi(\rho) = 4\epsilon \left[ -\left(\frac{\sigma}{\rho}\right)^6 + \left(\frac{\sigma}{\rho}\right)^{12} \right], \quad (2.5)$$

where  $\sigma$  is the bond length and  $\epsilon$  denotes the energy well depth,  $\epsilon = A^2/(4B)$ . From (2.5), the equilibrium distance  $\rho_0$  for two atoms is given by  $\rho_0 = 2^{1/6}\sigma = (2B/A)^{1/6}$ , which is depicted in Figure 2.2.

In the case of a many-body problem, the potential energy of the system is the total energy between each pair of molecules, which is called the pair potential approximation [41], is given by

$$U = \frac{1}{2} \sum_{i,j=1, i \neq j}^N E(\rho_{ij}), \quad (2.6)$$

where  $\rho_{ij}$  denotes the distance between a surface element  $i$  and a surface element  $j$ .

The van der Waals interaction force between two typical atoms of two molecules

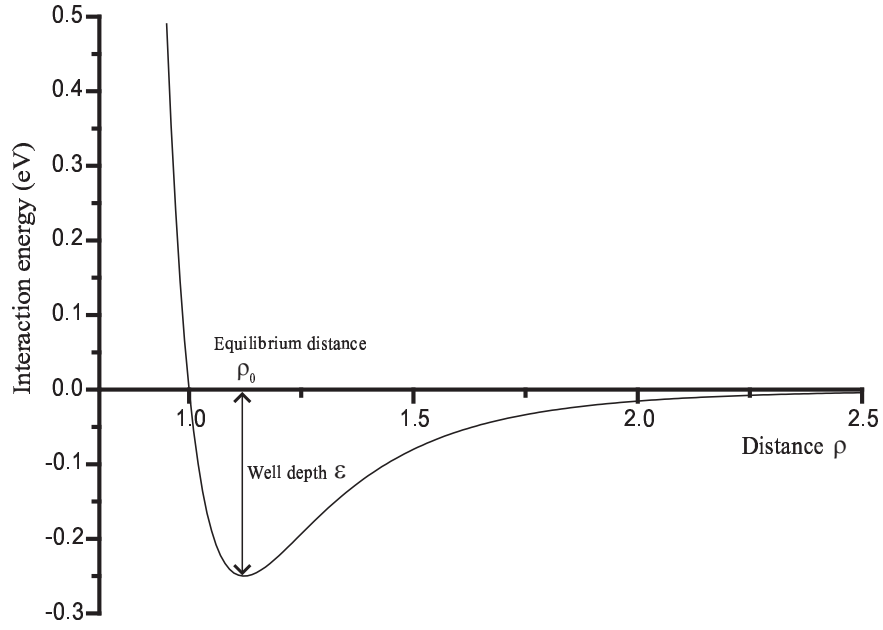


Figure 2.2: Graph of Lennard-Jones potential

is given by

$$F_{vdW} = -\nabla E, \quad (2.7)$$

where the energy  $E$  is given by (2.3). Accordingly, the resultant axial force ( $z$ -direction) is obtained by differentiating the integrated Lennard-Jones potential with respect to  $Z$ , which is defined as the distance between the centres of two molecules, therefore (2.7) simplifies to become

$$F_Z = -\frac{\partial E}{\partial Z}. \quad (2.8)$$

The continuum approach using the Lennard-Jones potential has been successfully employed in a number of studies to determine the van der Waals interaction energy and the force between two carbon nanostructures. Girifalco [42] determines the interaction energy between two  $C_{60}$  fullerenes, and then extends the study in Girifalco *et al.* [36] to find the energy between two identical parallel carbon nanotubes of infinite length and between a carbon nanotube and a  $C_{60}$  fullerene. Girifalco *et al.* [36] also provide the value of the interaction constants in the Lennard-Jones potential for carbon atoms in graphene-graphene,  $C_{60}$ - $C_{60}$  and  $C_{60}$ -graphene. Further, Hodak and Girifalco [37] propose an energy formula for universal graphitic systems includ-

ing the interaction of an ellipsoid inside a single-walled carbon nanotube. Ruoff and Hickamn [43] consider the interaction between a spherical fullerene and a graphite sheet. Henrard *et al.* [44] use a similar technique to Girifalco [42] and obtain the potential for bundles of single-walled carbon nanotubes. Following Girifalco *et al.* [36] and Henrard *et al.* [44], Zheng and Jiang [4] utilise the Lennard-Jones potential to determine the van der Waals restoring force between the inner and outer shells of a multi-walled carbon nanotube and subsequently predict a gigahertz frequency of the oscillatory motion. For spherical carbon onions  $C_{N_1}@C_{N_2}$  ( $N_2 > N_1$ ), Iglesias-Groth *et al.* [45] also adopt the Lennard-Jones potential and the continuum approximation to determine the interlayer interaction. By using the formula of Iglesias-Groth *et al.* [45], Guérin [46] obtains the interaction energy between the interlayer of carbon onions which is in excellent agreement to those obtained from discrete atom-atom summation model given in Lu and Yang [47]. Further, it is also shown in Verberck and Michel [48] that for large carbon nanotubes the continuum approach agrees well with an atomistic model. In general, it is possible to combine both the continuum and discrete approaches to model an interaction between two nanostructures. As shown in both Verberck and Michel [48] and Hilder and Hill [49], the single-walled carbon nanotube is modelled as a continuum, while the fullerene is assumed to retain its discrete atomic structure. Finally, the validity of using the continuum approach over the discrete atom-atom model is discussed by Girifalco *et al.* [36] who point out that

“from a physical point of view the discrete atom-atom model is not necessarily preferable to the continuum model. The discrete model assumes that each atom is the centre of a spherically symmetric electron distribution while the continuum model assumes that the electron distribution is uniform over the surface. Both of these assumptions are incorrect and a case can even be made that the continuum model is closer to reality than a set of discrete Lennard-Jones centres.”

We comment that the continuum approximation represents an averaging procedure and might be expected to be mostly applicable to well defined molecular shapes, such as the cylindrical nanotubes and spherical fullerenes studied here. For non-regular shaped molecules, the continuum approach may not be an accurate approximation

due to the difficulty in the determination of a mean atomic density. However, it is possible to combine both continuum and discrete approaches to model an interaction between regular and non-regular shaped nanostructures [49].

## 2.3 Overview

Part II of this thesis is divided into five chapters. The first is Chapter 2 which contains the background and overview. In Chapter 3, analytical expressions for the interaction energy of double-walled carbon nanotubes are determined. The issues examined include the suction force, offset equilibrium position and oscillatory behaviours for certain configurations of double-walled carbon nanotubes. A well-known self-assembled hybrid carbon nanostructure, known as a nanopeapod, is investigated in Chapter 4. Three encapsulation mechanisms are firstly determined, and once a number of  $C_{60}$  fullerenes are encapsulated inside a single-walled carbon nanotube, zigzag and spiral patterns of  $C_{60}$  chains are examined. Equilibrium position for two carbon, two boron nitride and carbon-boron nitride nanocones are examined in Chapter 5. Furthermore, for the carbon cones the suction and oscillation are also investigated where the oscillation frequency is in the gigahertz range. In Chapter 6, equilibrium spacing between adjacent layers for both spherical and spheroidal carbon onions are determined. In this part, all analytical expressions are obtained either in terms of hypergeometric functions or Legendre functions, and the numerical solutions are graphically shown by the algebraic computer package MAPLE.

# Chapter 3

## Double-walled carbon nanotubes

Advances in nanotechnology have led to the creation of many nanoscale devices and carbon nanotubes are representative materials to construct these devices. Double-walled carbon nanotubes with the inner tube oscillating can be used as gigahertz oscillators and form the basis of possible nano-electronic devices in the micro-computer industry, which are predominantly based on electron transport phenomena. There are many experiments and molecular dynamics simulations which show that a wave is generated on the outer cylinder as a result of the oscillation of the inner carbon nanotube, and that the frequency of this wave is also in the gigahertz range. As a preliminary to analyse and model such devices, it is necessary to estimate accurately the resultant force distribution due to the inter-atomic interactions. Here some new analytical expressions for the van der Waals force using the Lennard-Jones potential for general lengths of the inner and outer tubes are determined. The suction force experienced by a single-walled carbon nanotube located near an open end of a semi-infinite single-walled carbon nanotube, and the equilibrium position of an offset inner tube with reference to the cross-section of the outer tube are investigated. These expressions are utilised together with Newton's second law to determine the motion of an oscillating inner tube, assuming that frictional effects may be neglected. An idealised and simplified representation of the Lennard-Jones force is used to determine a simple formula for the oscillation frequency resulting from an initial extrusion of the inner tube.

### 3.1 Nomenclature

$\varepsilon$  is an offset position of the inner tube from the outer tube axis

$\eta_g$	is the mean atomic number density for graphene
$\rho$	is the distance between two typical surface elements
$\sigma$	is the carbon-carbon covalent bond length
$A, B$	are the Lennard-Jones attractive and repulsive coefficients, respectively
$E^{tot}$	is the total interaction potential
$F_z^{tot}$	is the total force in the $z$ -direction
$L_1, L_2$	are the half-lengths of the inner and the outer tubes, respectively
$M$	is the mass of the inner tube
$Z$	is the distance between the centres of the inner and the outer tubes
$a, b$	are the radii of the inner and the outer tubes, respectively
$d$	is the extrusion distance
$f$	is the oscillation frequency
$v_0$	is the initial velocity of the inner tube

## 3.2 Introduction

The unique properties of carbon nanotubes, such as their high strength, high flexibility, small size and low weight, have been studied by many experiments (see for example, [17, 18, 50, 51]) and molecular dynamics simulations (see for example, [17, 20, 52, 53]), but there are few groups using conventional applied mathematical modelling. Single-walled carbon nanotubes can be thought of as a graphite sheet that is rolled up as a cylinder, and multi-walled carbon nanotubes can be envisaged as multi-layers of graphene sheets that are rolled up. Carbon nanotubes consist of carbon atoms which have a  $(1s)^2(2s)^2(2p)^2$  electronic structure. The  $\pi$  orbitals provide weak van der Waals bonds between adjacent layers of each carbon nanotube, whereas the  $\sigma$  orbitals provide strong in-plane bonds within individual carbon nanotubes. Further details on carbon nanotubes can be found in Dresselhaus *et al.* [27].

A number of nano-oscillators have been examined, including double-walled carbon nanotubes, a  $C_{60}$ - single-walled carbon nanotube and a  $C_{60}$ -carbon nanotorus oscillator [2, 4, 5, 54, 55]. Typically these studies assume that the inner nanostructure oscillates within the outer nanostructure co-axially, although Cox *et al.* [54] examine the possible offset equilibrium configurations for a  $C_{60}$  fullerene in a single-walled carbon nanotube, and Hilder and Hill [55] examine the same circumstance for a  $C_{60}$  orbiting inside a nanotorus. In this study, the suction behaviour is investigated for a single-walled carbon nanotube entering another semi-infinite single-walled carbon nanotube co-axially, and then the possible offset equilibrium position for the inner tube with respect to the outer tube axis is determined. The Lennard-Jones potential and the continuum approach are employed throughout this work, where the continuum model assumes that the atoms at discrete locations can be approximated by an averaged surface density of atoms which is smeared across the entire surface.

Following the work of Cumings and Zettl [1], there are many groups who have studied the oscillations of multi-walled carbon nanotubes. Zheng and Jiang [4] consider multi-walled carbon nanotubes where the outer most shells have open ends and the inner shells have capped ends, and the inner shells are pulled out of the outer tube a certain distance and then released. Using the Lennard-Jones potential energy and Newton's second law, these authors propose that the oscillation of multi-walled carbon nanotubes is in the gigahertz range, and also conclude that the frictional force between the inner and the outer shells can be neglected. A theoretical study of this phenomenon is found in Zheng *et al.* [5]. Moreover, this situation is confirmed by Legoas *et al.* [2] who suggest that the configurations of the inner and outer tubes affect the oscillation frequency. Rivera *et al.* [6, 7] use molecular dynamics simulation to show that the frictional force is very low when compared with the van der Waals force, which is in agreement with Zheng and Jiang [4].

In order to accurately model both the dynamics of the gigahertz oscillator and to analyse the consequent wave formation on the outer carbon nanotube, the resultant force on the inner carbon nanotube needs to be accurately estimated. The analysis of the wave formation on the outer tube will be investigated in Chapter 13, which utilises the transversely isotropic linearly elastic model for carbon nanotubes. Here,



the van der Waals force distribution on the inner carbon nanotube due to the nett interatomic interactions is calculated, using the usual continuum assumption.

Detailed derivations for the force distribution of double-walled carbon nanotubes is presented in the following section. The suction behaviour for an inner carbon nanotube entering an outer carbon nanotube and the offset location for an inner carbon nanotube inside an outer carbon nanotube are determined in §3.4 and §3.5, respectively. On making an idealization of the van der Waals force distribution and employing Newton's second law, a simple expression for the oscillation frequency is obtained and shown in §3.6. Finally, a summary is given in §3.7.

### 3.3 Force distribution for double-walled carbon nanotubes

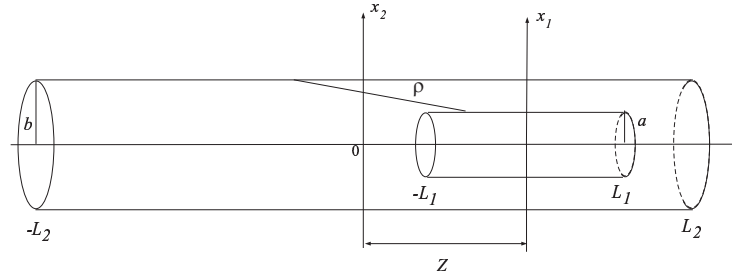


Figure 3.1: Double-walled carbon nanotubes of lengths  $2L_1$  and  $2L_2$ .

The interaction between the inner and outer tubes in the continuum approximation is obtained by averaging the atoms over the surface of each tube. With reference to a rectangular Cartesian coordinate system  $(x_1, y_1, z_1)$  with origin located at the centre of the outer tube, a typical point on the surface of the inner tube has coordinates  $(a \cos \theta_1, a \sin \theta_1, z_1)$  where  $a$  is the assumed radius of the inner tube. Similarly, with reference to a rectangular Cartesian coordinate system  $(x_2, y_2, z_2)$  with origin located at the centre of the outer tube, a typical point on the surface of the outer tube has coordinates  $(b \cos \theta_2, b \sin \theta_2, z_2)$  where  $b$  is the assumed radius of the outer tube, as shown in Figure 3.1. Now assuming the two tubes are concentric, and the distance between their centres is  $Z$ , the distance  $\rho$  between two typical points is given by

$$\rho^2 = (b \cos \theta_2 - a \cos \theta_1)^2 + (b \sin \theta_2 - a \sin \theta_1)^2 + (z_2 - z_1)^2,$$

which may be simplified to yield

$$\rho^2 = a^2 + b^2 - 2ab \cos(\theta_1 - \theta_2) + (z_2 - z_1)^2.$$

From the Lennard-Jones potential (2.4), the total potential energy of all atoms of the inner tube with all atoms of the outer tube is given by

$$E^{tot} = \eta_g^2 ab \int_0^{2\pi} \int_0^{2\pi} (-AI_6 + BI_{12}) d\theta_1 d\theta_2, \quad (3.1)$$

where  $\eta_g$  represents the mean surface density of carbon atoms,  $a$  and  $b$  are the radii of the inner and outer tubes, respectively. Further, the integral  $I_6$  is defined by

$$I_6 = \int_{Z-L_1}^{Z+L_1} \int_{-L_2}^{L_2} \frac{dz_2 dz_1}{\rho^6} = \int_{Z-L_1}^{Z+L_1} \int_{-L_2}^{L_2} \frac{dz_2 dz_1}{[\lambda^2 + (z_2 - z_1)^2]^3},$$

where  $\lambda^2$  denotes  $a^2 + b^2 - 2ab \cos(\theta_1 - \theta_2)$ . On letting  $x = z_2 - z_1$ , the integral becomes

$$I_6 = \int_{Z-L_1}^{Z+L_1} \int_{-L_2-z_1}^{L_2-z_1} \frac{dx dz_1}{(\lambda^2 + x^2)^3} = \frac{1}{\lambda^5} \int_{Z-L_1}^{Z+L_1} \int_{-\tan^{-1}[(L_2+z_1)/\lambda]}^{\tan^{-1}[(L_2-z_1)/\lambda]} \cos^4 \phi \, d\phi dz_1,$$

where the final line follows by making the substitution  $x = \lambda \tan \phi$  to obtain

$$\begin{aligned} I_6 = & \frac{1}{\lambda^5} \int_{Z-L_1}^{Z+L_1} \left\{ \frac{3}{8} \tan^{-1} \left( \frac{L_2 - z_1}{\lambda} \right) + \frac{3}{8} \frac{\lambda(L_2 - z_1)}{[\lambda^2 + (L_2 - z_1)^2]} \right. \\ & + \frac{1}{4} \frac{\lambda^3(L_2 - z_1)}{[\lambda^2 + (L_2 - z_1)^2]^2} + \frac{3}{8} \tan^{-1} \left( \frac{L_2 + z_1}{\lambda} \right) + \frac{3}{8} \frac{\lambda(L_2 + z_1)}{[\lambda^2 + (L_2 + z_1)^2]} \\ & \left. + \frac{1}{4} \frac{\lambda^3(L_2 + z_1)}{[\lambda^2 + (L_2 + z_1)^2]^2} \right\} dz_1. \end{aligned}$$

Finally, using the two substitutions  $x = (L_2 - z_1)/\lambda$  and  $y = (L_2 + z_1)/\lambda$  gives

$$I_6 = \sum_{i=1}^4 (-1)^{i+1} \left\{ \frac{3}{8} \frac{(Z - \ell_i)}{\lambda^5} \tan^{-1} \left( \frac{Z - \ell_i}{\lambda} \right) - \frac{1}{8\lambda^2[\lambda^2 + (Z - \ell_i)^2]} \right\},$$

and by precisely the same method,  $I_{12}$  becomes

$$\begin{aligned} I_{12} = & \sum_{i=1}^4 (-1)^{i+1} \left\{ \frac{63}{256} \frac{(Z - \ell_i)}{\lambda^{11}} \tan^{-1} \left( \frac{Z - \ell_i}{\lambda} \right) - \frac{21}{256\lambda^8[\lambda^2 + (Z - \ell_i)^2]} \right. \\ & \left. - \frac{21}{640\lambda^6[\lambda^2 + (Z - \ell_i)^2]^2} - \frac{3}{160\lambda^4[\lambda^2 + (Z - \ell_i)^2]^3} - \frac{1}{80\lambda^2[\lambda^2 + (Z - \ell_i)^2]^4} \right\}, \end{aligned}$$

where the four lengths  $\ell_i$  ( $i = 1, 2, 3, 4$ ) are defined by  $\ell_1 = -(L_1 + L_2)$ ,  $\ell_2 = -(L_2 - L_1)$ ,  $\ell_3 = L_1 + L_2$  and  $\ell_4 = L_2 - L_1$ , and these are the locations for the four critical positions for the oscillation as shown in Figure 3.2.

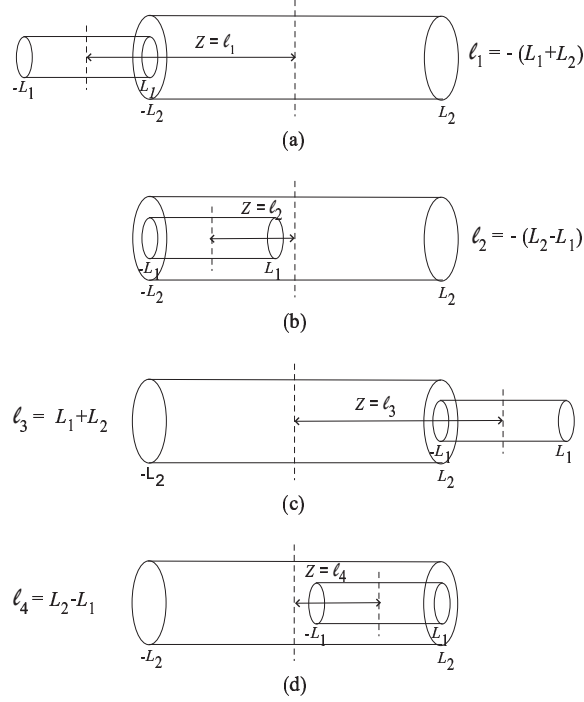


Figure 3.2: Four critical positions for two concentric nanocylinders.

Thus there are two types of integrals needed to evaluate (3.1). Formally, the double integrals  $K_n^*$  and  $L_n^*$  need to be evaluated which are defined by

$$K_n^* = \int_0^{2\pi} \int_0^{2\pi} \frac{d\theta_1 d\theta_2}{\lambda^m (\lambda^2 + P_i^2)^n}, \quad L_n^* = \int_0^{2\pi} \int_0^{2\pi} \frac{1}{\lambda^n} \tan^{-1} \left( \frac{P_i}{\lambda} \right) d\theta_1 d\theta_2,$$

where  $m$  and  $n$  denote certain positive integers,  $P_i = Z - \ell_i$  ( $i = 1, 2, 3, 4$ ) and these details are subsequently presented in Appendix A.2 and A.3, respectively. For completeness the full expression for  $E^{tot}(Z)$  in terms of Appell hypergeometric functions is given below, from which an expression for  $E^{tot}(0)$  may be deduced which is required in §3.6.

$$E^{tot}(Z) = 8\pi ab\eta_g^2 (-AN_6 + BN_{12}), \quad (3.2)$$

where

$$N_6 = \sum_{i=1}^4 (-1)^{i+1} \left[ \frac{3\pi}{16} \sum_{k=0}^{\infty} \frac{(2k)!(Z - \ell_i)^{2k+2}}{2^{2k}(k!)^2(2k+1)(a+b)^5[(a+b)^2 + (Z - \ell_i)^2]^{k+1/2}} \right. \\ \times F_1\left(\frac{1}{2}; \frac{5}{2}, k + \frac{1}{2}; 1; \frac{4ab}{(a+b)^2}, \frac{4ab}{(a+b)^2 + (Z - \ell_i)^2}\right) \\ \left. - \frac{\pi}{16(a+b)^2[(a+b)^2 + (Z - \ell_i)^2]} F_1\left(\frac{1}{2}; 1, 1, 1; \frac{4ab}{(a+b)^2}, \frac{4ab}{(a+b)^2 + (Z - \ell_i)^2}\right) \right],$$

and

$$N_{12} = \sum_{i=1}^4 (-1)^{i+1} \left[ \frac{63\pi}{512} \sum_{k=0}^{\infty} \frac{(2k)!(Z - \ell_i)^{2k+2}}{2^{2k}(k!)^2(2k+1)(a+b)^{11}[(a+b)^2 + (Z - \ell_i)^2]^{k+1/2}} \right. \\ \times F_1\left(\frac{1}{2}; \frac{11}{2}, k + \frac{1}{2}; 1; \frac{4ab}{(a+b)^2}, \frac{4ab}{(a+b)^2 + (Z - \ell_i)^2}\right) \\ - \frac{21\pi}{512(a+b)^8[(a+b)^2 + (Z - \ell_i)^2]} F_1\left(\frac{1}{2}; 4, 1, 1; \frac{4ab}{(a+b)^2}, \frac{4ab}{(a+b)^2 + (Z - \ell_i)^2}\right) \\ - \frac{21\pi}{1280(a+b)^6[(a+b)^2 + (Z - \ell_i)^2]^2} F_1\left(\frac{1}{2}; 3, 2, 1; \frac{4ab}{(a+b)^2}, \frac{4ab}{(a+b)^2 + (Z - \ell_i)^2}\right) \\ - \frac{3\pi}{320(a+b)^4[(a+b)^2 + (Z - \ell_i)^2]^3} F_1\left(\frac{1}{2}; 2, 3, 1; \frac{4ab}{(a+b)^2}, \frac{4ab}{(a+b)^2 + (Z - \ell_i)^2}\right) \\ \left. - \frac{\pi}{160(a+b)^2[(a+b)^2 + (Z - \ell_i)^2]^4} F_1\left(\frac{1}{2}; 1, 4, 1; \frac{4ab}{(a+b)^2}, \frac{4ab}{(a+b)^2 + (Z - \ell_i)^2}\right) \right],$$

where  $F_1(\alpha; \beta, \beta'; \gamma; x, y)$  is the Appell hypergeometric function of the first kind which is defined by the double series (A.3) and given by the integral representation (A.4).

The potential and force distributions for the double-walled carbon nanotubes are determined here. Following the works of Girifalco *et al.* [36, 37] and Ma *et al.* [56], the parameter values for double-walled carbon nanotubes shown in Table 3.1 are employed. Using the algebraic computer package MAPLE, the potential function and van der Waals force versus the difference between the centres of the tubes  $Z$  are shown in Figure 3.3 and Figure 3.4, respectively. In this study, a (10,10) carbon nanotube is assumed to enter into a (16,16) carbon nanotube by varying the

inner tube lengths. It is important to note that the Appell functions are readily summed using MAPLE by means of the series (A.4), and MAPLE is also utilised to differentiate the total energy given by (3.2) with respect to the distance  $Z$  to calculate the axial van der Waals force.

Due to the four critical positions of the distance between the centres of the tubes, there are three regions for the inner tube behaviour,  $(\ell_1, \ell_2)$ ,  $(\ell_2, \ell_4)$  and  $(\ell_4, \ell_3)$ . In terms of the potential function, the inner tube will travel with decreasing potential energy in the first region to reach a constant minimum energy in the second region, after which the energy will increase until it becomes zero at the position that the inner tube leaves the outer tube. For the force distribution, the force is almost zero in the second region and there are two strong attractive forces in the first and the third regions, which tend to keep the inner tube inside. This means that once inside the outer cylinder, the inner tube will tend to oscillate rather than escape from the outer tube, because of the forces at the ends tending to reverse the direction of the motion. However, not every inner tube will necessarily be sucked in by inter-atomic van der Waals force alone, and it may be necessary to either initiate the oscillatory motion by initially extruding the inner cylinder or by giving the inner tube an initial velocity.

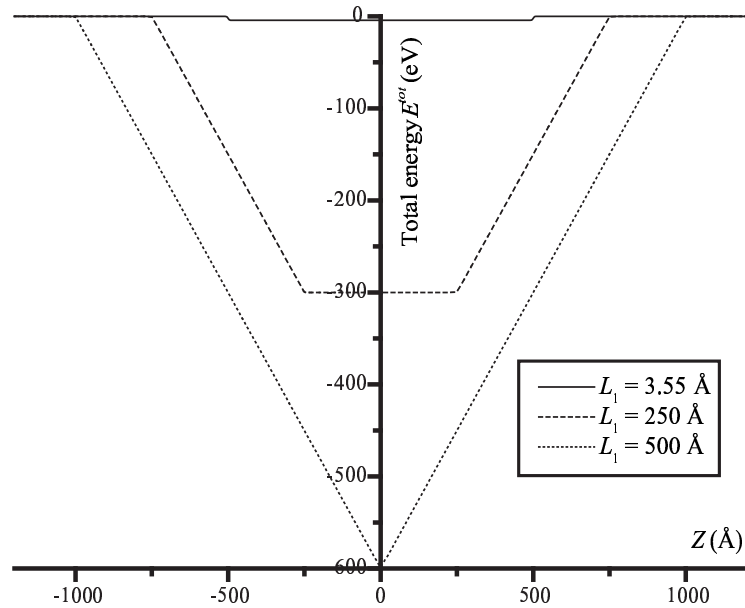


Figure 3.3: Total potential energy of a (10,10) nanotube with various  $L_1$  entering into a (16,16) nanotube with length  $L_2 = 500$  Å.

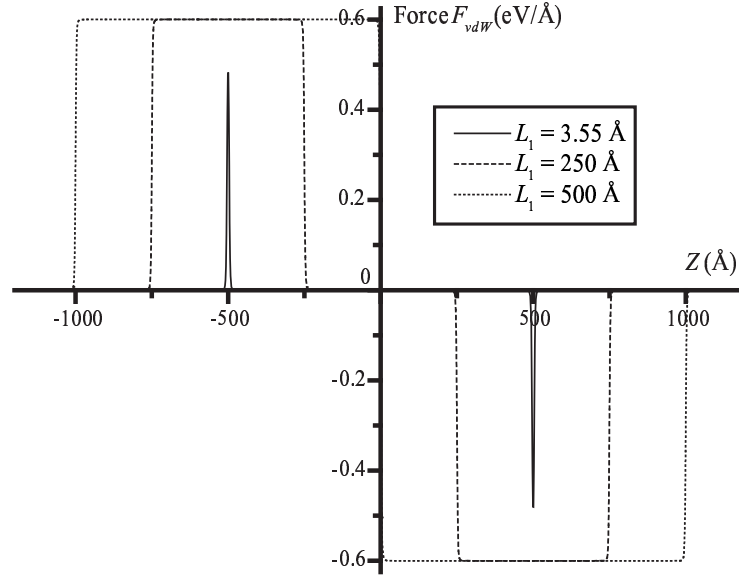


Figure 3.4: Force distribution of a (10,10) nanotube with various  $L_1$  entering into a (16,16) nanotube with length  $L_2 = 500$  Å.

### 3.4 Suction force for double-walled carbon nanotubes

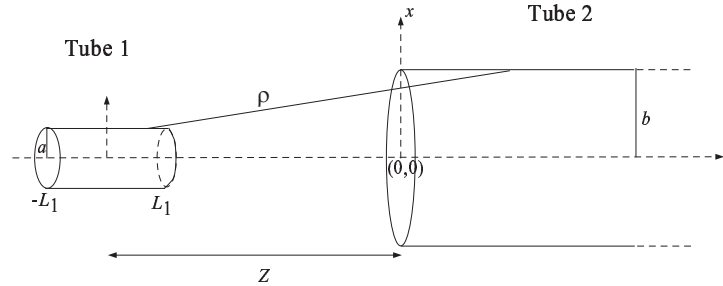


Figure 3.5: Geometry of a single-walled carbon nanotube entering another single-walled carbon nanotube.

The issue of suction of particles into a container is fundamental, particularly for applications of encapsulating drugs or genes in nano-carriers for targeted deliveries to tumour cells. Here the energy of a carbon nanotube being sucked into another carbon nanotube is examined. The suction energy is defined as the total work performed by van der Waals interaction on a molecule entering a carbon nanotube. From a previous study, Cox *et al.* [57] determine the suction behaviour for a carbon atom and a  $C_{60}$  fullerene into a single-walled carbon nanotube. They find that the suction energy depends on the radius of the carbon nanotube. In this thesis, such

behaviour for double-walled carbon nanotubes is examined.

For convenience, Tube 1 is assumed to refer to the carbon nanotube which enters into the open end of the semi-infinite tube, Tube 2, as shown in Figure 3.5, and the origin of the coordinate system is assumed to be located at the left end of Tube 2. It is assuming that Tube 1 is of radius  $a$  and length  $2L_1$  and its centre is located at  $(0, Z)$ , which might be inside or outside Tube 2. Further, Tube 2 of radius  $b$  is assumed to be semi-infinite in length. In an axially symmetric cylindrical polar coordinate system  $(r, \theta, z)$ , the parametric equations for Tube 1 and Tube 2 are given by  $(a \cos \theta_1, a \sin \theta_1, z_1)$  and  $(b \cos \theta_2, b \sin \theta_2, z_2)$ , respectively. In this case, the distance  $\rho$  between two typical surface elements on Tube 1 and Tube 2 is given by

$$\rho^2 = (b \cos \theta_2 - a \cos \theta_1)^2 + (b \sin \theta_2 - a \sin \theta_1)^2 + (z_2 - z_1)^2.$$

Using the Lennard-Jones potential together with the continuum approximation, the total potential energy can be written as

$$E^{tot} = ab\eta_g^2 \int_0^{2\pi} \int_0^{2\pi} (-AI_6 + BI_{12}) d\theta_1 d\theta_2, \quad (3.3)$$

where  $\eta_g$  represents the mean surface density of the carbon nanotube assumed to be the same for both tubes. In this case, the integrals  $I_6$  and  $I_{12}$  are defined as follows

$$I_6 = \int_0^\infty \int_{Z-L_1}^{Z+L_1} \frac{dz_1 dz_2}{\rho^6} = \int_0^\infty \int_{Z-L_1}^{Z+L_1} \frac{dz_1 dz_2}{[\lambda^2 + (z_2 - z_1)^2]^3},$$

$$I_{12} = \int_0^\infty \int_{Z-L_1}^{Z+L_1} \frac{dz_1 dz_2}{\rho^{12}} = \int_0^\infty \int_{Z-L_1}^{Z+L_1} \frac{dz_1 dz_2}{[\lambda^2 + (z_2 - z_1)^2]^6},$$

where  $\lambda^2$  denotes  $a^2 + b^2 - 2ab \cos(\theta_1 - \theta_2)$ . On letting  $x = z_2 - z_1$ , the integral  $I_6$  becomes

$$I_6 = \int_{Z-L_1}^{Z+L_1} \int_{-z_1}^\infty \frac{dx dz_1}{(\lambda^2 + x^2)^3} = \frac{1}{\lambda^5} \int_{Z-L_1}^{Z+L_1} \int_{-\tan^{-1}(z_1/\lambda)}^{\pi/2} \cos^4 \phi d\phi dz_1,$$

where on substituting  $x = \lambda \tan \phi$ , it may be deduced

$$I_6 = \frac{1}{\lambda^5} \int_{Z-L_1}^{Z+L_1} \left( \frac{3\pi}{16} + \frac{3}{8} \tan^{-1}(z_1/\lambda) + \frac{3}{8} \frac{\lambda z_1}{(\lambda^2 + z_1^2)} + \frac{1}{4} \frac{\lambda^3 z_1}{(\lambda^2 + z_1^2)^2} \right) dz_1.$$

Using the substitution  $x = z_1/\lambda$ , an above equation becomes

$$I_6 = \frac{1}{\lambda^4} \left[ \frac{3\pi L_1}{8} \frac{1}{\lambda} + \frac{3(Z + L_1)}{8\lambda} \tan^{-1} \left( \frac{Z + L_1}{\lambda} \right) - \frac{\lambda^2}{8[\lambda^2 + (Z + L_1)^2]} \right. \\ \left. - \frac{3(Z - L_1)}{8\lambda} \tan^{-1} \left( \frac{Z - L_1}{\lambda} \right) + \frac{\lambda^2}{8[\lambda^2 + (Z - L_1)^2]} \right].$$

Similarly,  $I_{12}$  is given by

$$I_{12} = \frac{1}{\lambda^{10}} \left[ \frac{63\pi L_1}{256} \frac{1}{\lambda} + \frac{63(Z + L_1)}{256\lambda} \tan^{-1} \left( \frac{Z + L_1}{\lambda} \right) - \frac{21\lambda^2}{256[\lambda^2 + (Z + L_1)^2]} \right. \\ - \frac{21\lambda^4}{640[\lambda^2 + (Z + L_1)^2]^2} - \frac{3\lambda^6}{160[\lambda^2 + (Z + L_1)^2]^3} - \frac{\lambda^8}{80[\lambda^2 + (Z + L_1)^2]^4} \\ - \frac{63(Z - L_1)}{256\lambda} \tan^{-1} \left( \frac{Z - L_1}{\lambda} \right) + \frac{21\lambda^2}{256[\lambda^2 + (Z - L_1)^2]} + \frac{21\lambda^4}{640[\lambda^2 + (Z - L_1)^2]^2} \\ \left. + \frac{3\lambda^6}{160[\lambda^2 + (Z - L_1)^2]^3} + \frac{\lambda^8}{80[\lambda^2 + (Z - L_1)^2]^4} \right].$$

Thus from (3.3) there are three types of integrals which need to be determined, and they are given by

$$\begin{aligned} J_n^* &= \int_0^{2\pi} \int_0^{2\pi} \frac{d\theta_1 d\theta_2}{\lambda^n}, \\ K_n^* &= \int_0^{2\pi} \int_0^{2\pi} \frac{d\theta_1 d\theta_2}{\lambda^m (\lambda^2 + P_j^2)^n}, \\ L_n^* &= \int_0^{2\pi} \int_0^{2\pi} \frac{1}{\lambda^n} \tan^{-1} \left( \frac{P_j}{\lambda} \right) d\theta_1 d\theta_2, \end{aligned} \tag{3.4}$$

where  $m$  and  $n$  are certain positive integers and  $P_j$  ( $j = 1, 2$ ) is the abbreviation used for  $P_1 = Z + L_1$  and  $P_2 = Z - L_1$ . As shown in Appendix A, (3.4) can be



integrated to yield

$$\begin{aligned}
J_n^* &= \frac{4\pi^2}{(a+b)^2} F\left(\frac{n}{2}, \frac{1}{2}; 1; \frac{4ab}{(a+b)^2}\right), \\
K_n^* &= \frac{4\pi^2}{(a+b)^m [(a+b)^2 + P_j^2]^n} \sum_{i=0}^{\infty} \frac{(1/2)_i (m/2)_i}{(i!)^2} \left(\frac{4ab}{(a+b)^2}\right)^i \times \\
&\quad \times F\left(\frac{1}{2} + i, n; 1 + i; \frac{4ab}{(a+b)^2 + P_j^2}\right), \\
L_n^* &= 4\pi^2 \sum_{k=0}^{\infty} \sum_{i=0}^{\infty} \frac{P_j^{2k+1} (2k)!}{2^{2k} (k!)^2 (2k+1) (a+b)^n [(a+b)^2 + P_j^2]^{k+1/2}} \frac{(1/2)_i (n/2)_i}{(i!)^2} \times \\
&\quad \times \left(\frac{4ab}{(a+b)^2}\right)^i F\left(\frac{1}{2} + i, k + \frac{1}{2}; 1 + i; \frac{4ab}{(a+b)^2 + P_j^2}\right),
\end{aligned}$$

where  $F(a, b; c; z)$  denotes the usual hypergeometric function. Although complicated, numerical values for these integrals may be readily evaluated using the algebraic computer package MAPLE.

From the symmetry of the problem, only the force in the axial direction ( $z$ -direction) is considered, and the resultant axial force is obtained by differentiating the total energy with respect to the axial direction  $Z$ . Noting that due to the complexity of the expression, obtaining an analytical expression for  $F_Z^{tot}$  is not a simple task. Using the algebraic computer package MAPLE, together with the constants given in Table 3.1, the numerical solutions for the suction force for carbon nanotubes are illustrated in Figure 3.6, where Tube 1 is assumed to be (6,6) and its length is 120 Å.

The area under the graph in Figure 3.6 represents the work done by the van der Waals force. For Tube 1 to be sucked into Tube 2, the sum of the work which is obtained by moving the inner tube from  $Z = -\infty$  to  $Z_0$ , where  $Z_0$  is the positive root of  $F_Z^{tot} = 0$ , or in the other words  $W_a = \int_{-\infty}^{Z_0} F_Z^{tot} dZ$ , needs to be greater than zero. In Figure 3.6, the force experienced by a (6,6) nanotube upon entering (10,10), (16,16) and (20,20) nanotubes are plotted. It can be seen from Figure 3.6(a) that a (10,10) tube will not allow a (6,6) tube to enter since  $W_a < 0$ , resulting in a strong repulsive force at the tube extremity. In Figure 3.6(b), it can be seen that  $W_a > 0$ , which gives rise to a (6,6) nanotube (Tube 1) being sucked into Tube 2, which is

either a (16,16) or (20,20) nanotube. In addition,  $W_a$  decreases as the radius of the outer tube increases. This is due to the fact that when the difference in radii of the inner and outer tubes moves further away from 3.44 Å (inter-spacing of two graphene sheets), such a double-walled carbon nanotube is not an ideal configuration.

Further, the suction energy which is the total work performed by van der Waals interactions on the inner tube upon entering the outer tube is considered. In other words, the suction energy can be represented mathematically by  $W = \int_{-\infty}^{\infty} F_Z^{tot} dZ$ . In Figure 3.7, the suction energy for a (6,6) carbon nanotube entering an outer nanotube with radii in the range  $6.5 < b < 9$  Å is depicted. Noting from the figure that  $W$  is positive when  $b > 7$  Å and has its maximum value when  $b = 7.511$  Å, for which the difference in radii of the inner and outer tubes is 3.44 Å, which is the inter-spacing between two graphene sheets [2, 4, 5].

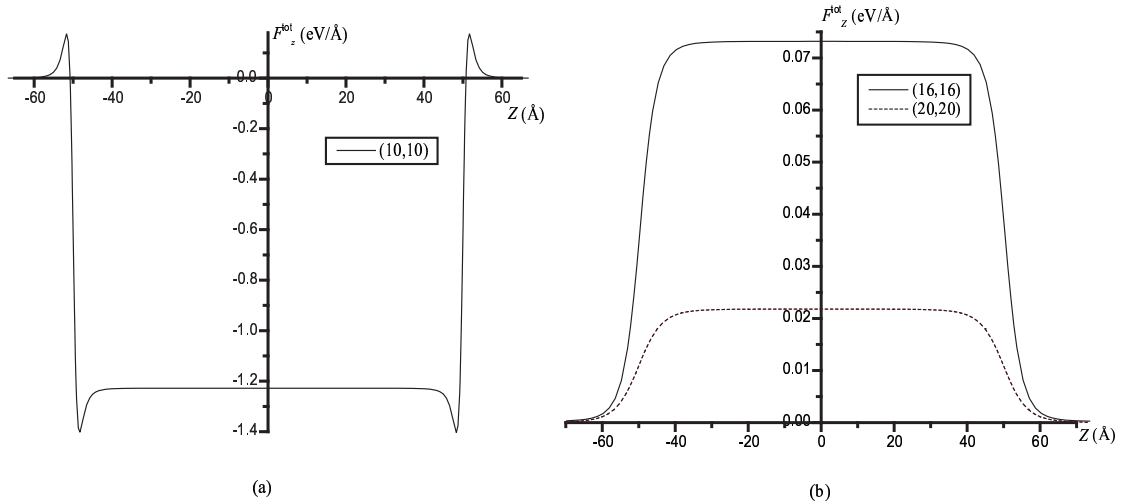


Figure 3.6: Force experienced by a (6,6) carbon nanotube due to van der Waals interaction with a semi-infinite carbon nanotube (a) (10,10), (b) (16,16) and (20,20).

### 3.5 Offset position for double-walled carbon nanotubes

The Lennard-Jones potential together with the continuum approximation is utilised to determine the preferred position of an offset inner nanotube with reference to the cross-section of the outer single-walled carbon nanotube. The preferred position is the location of the minimum potential energy for the inner nanostructure. The work of Cox *et al.* [54] for an offset carbon atom and an offset  $C_{60}$  fullerene inside

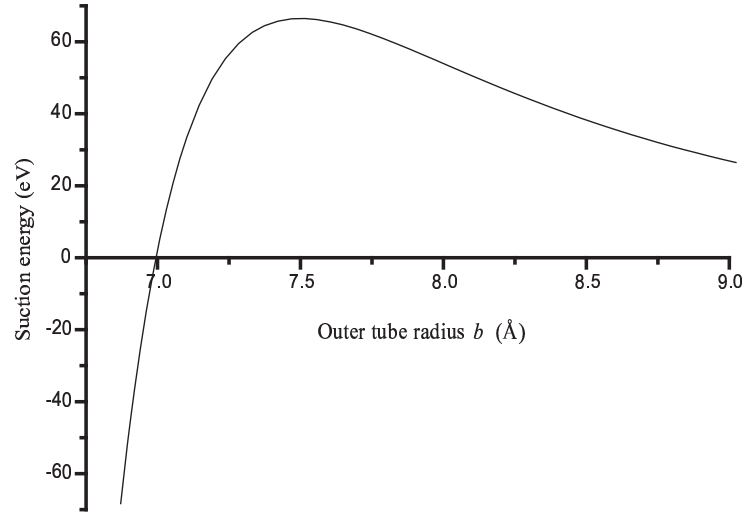


Figure 3.7: Suction energy for an inner tube (6,6) entering an outer tube.

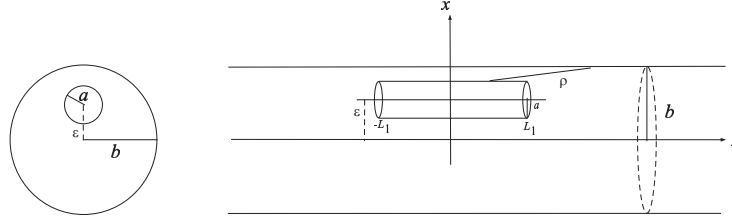


Figure 3.8: Offset location for double-walled carbon nanotube.

a single-walled carbon nanotube leads to study of an offset single-walled carbon nanotube.

In terms of a double-walled carbon nanotube, the parametric equation for an offset inner tube of radius  $a$  is  $(a \cos \theta_1 + \varepsilon, a \sin \theta_1, z_1)$  and the parametric equation for an outer tube of radius  $b$  is  $(b \cos \theta_2, b \sin \theta_2, z_2)$ . The length of the inner tube is assumed to be  $2L_1$  and the length of the outer tube is assumed to be  $2L_2$  where  $L_2$  tends to infinity, and  $\varepsilon$  is the distance between the centres of two tubes in the radial direction as shown in Figure 3.8. Thus, the distance  $\rho$  from any infinitesimal point on the surface of the inner tube to any infinitesimal point on the surface of the outer tube can be written as

$$\rho^2 = [b \cos \theta_2 - (a \cos \theta_1 + \varepsilon)]^2 + (b \sin \theta_2 - a \sin \theta_1)^2 + (z_2 - z_1)^2,$$

and the total potential energy is then given by

$$E^{tot} = ab\eta_g^2 \int_0^{2\pi} \int_0^{2\pi} (-AI_6 + BI_{12}) d\theta_1 d\theta_2,$$

where  $\eta_g$  is a mean surface density of a carbon nanotube. In this case,  $I_6$  is defined by

$$I_6 = \int_{-L_2}^{L_2} \int_{-L_1}^{L_1} \frac{1}{\rho^6} dz_1 dz_2 = \int_{-L_2}^{L_2} \int_{-L_1}^{L_1} \frac{1}{[\lambda^2 + (z_2 - z_1)^2]^3} dz_1 dz_2,$$

where

$$\begin{aligned} \lambda^2 &= [b \cos \theta_2 - (a \cos \theta_1 + \varepsilon)]^2 + (b \sin \theta_2 - a \sin \theta_1)^2 \\ &= a^2 + b^2 - 2ab \cos(\theta_1 - \theta_2) - 2\varepsilon(b \cos \theta_2 - a \cos \theta_1) + \varepsilon^2, \end{aligned}$$

and on letting  $x = (z_2 - z_1)$ , it may be deduced

$$I_6 = \int_{-L_1}^{L_1} \int_{-L_2-z_1}^{L_2-z_1} \frac{1}{(\lambda^2 + x^2)^3} dx dz_1 = \frac{1}{\lambda^5} \int_{-L_1}^{L_1} \int_{-\pi/2}^{\pi/2} \cos^4 \phi d\phi dz_1,$$

which is obtained by substituting  $x = \lambda \tan^2 \phi$  and letting  $L_2$  tends to infinity. Finally,  $I_6$  can be simplified to obtain

$$I_6 = \frac{1}{\lambda^5} \int_{-L_1}^{L_1} \frac{3\pi}{8} dz_1 = \frac{3\pi L_1}{4} \frac{1}{\lambda^5}.$$

By precisely the same method,  $I_{12}$  becomes

$$I_{12} = \int_{-L_2}^{L_2} \int_{-L_1}^{L_1} \frac{1}{\rho^{12}} dz_1 dz_2 = \frac{63\pi L_1}{128} \frac{1}{\lambda^{11}}.$$

Therefore, the total potential energy for the double-walled carbon nanotube with an offset inner tube becomes

$$E^{tot} = ab\eta_g^2 \pi L_1 \int_0^{2\pi} \int_0^{2\pi} \left( -\frac{3A}{4} \frac{1}{\lambda^5} + \frac{63B}{128} \frac{1}{\lambda^{11}} \right) d\theta_1 d\theta_2, \quad (3.5)$$

where  $\lambda^2 = a^2 + b^2 - 2ab \cos(\theta_1 - \theta_2) - 2\varepsilon(b \cos \theta_2 - a \cos \theta_1) + \varepsilon^2$ .

The derivation of the analytical solution for (3.5) is determined in Appendix B. Here, using the algebraic computer package MAPLE, equation (3.5) is numerically solved and graphically shown in Figure 3.9, for the relation of the potential energy and the offset position for a (6,6) carbon nanotube inside a (16,16) and a (20,20) carbon nanotube. The value of  $\varepsilon$  for the (6,6) tube inside the (16,16) tube and the (6,6) tube inside the (20,20) tube is 3.567 Å and 6.300 Å, respectively which correspond to the distance  $(b - \varepsilon)$  along a radius between the centre of the inner tube and the wall of the outer tube of 7.279 Å and 7.257 Å, respectively. Moreover, the

larger the outer tube, the smaller the inter-spacing between the walls of the inner and the outer tubes. This result agrees with the works by Girifalco *et al.* [36] and Cox *et al.* [54].

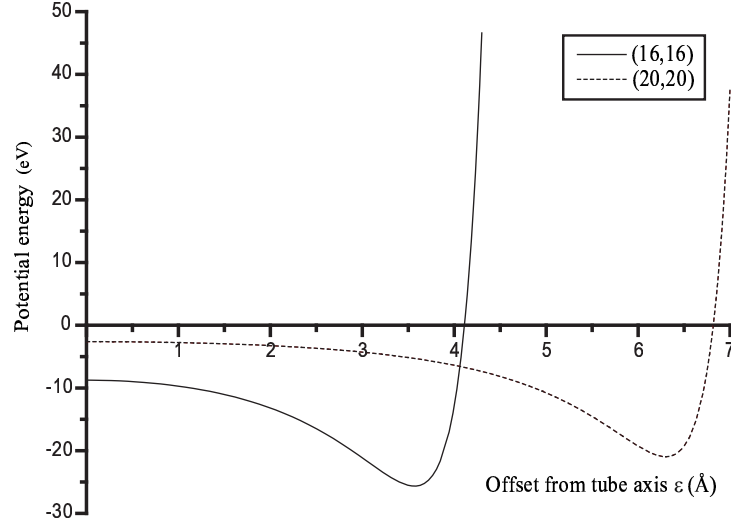


Figure 3.9: Potential energy of an offset (6,6) carbon nanotube inside a (16,16) and a (20,20) carbon nanotube with respect to the radial distance  $\varepsilon$ .

### 3.6 Oscillation of double-walled carbon nanotubes

In this section, Newton's second law is adopted to describe the oscillation behaviour of double-walled carbon nanotubes with the inner tube oscillating. The frequency of the oscillation for the case where the inner tube is pulled out with a distance  $d$  and released is investigated, as shown in Figure 3.10. The frictional force is assumed to be negligible for the movement on the inner tube.

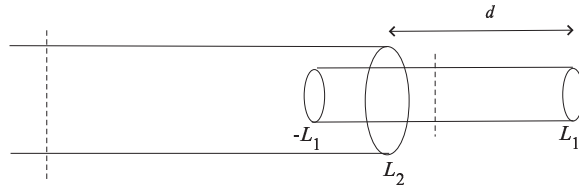


Figure 3.10: Extrusion distance  $d$  for inner tube oscillating inside outer tube.

Newton's second law on neglecting the frictional force can be written as

$$M \frac{d^2 Z}{dt^2} = F_Z^{tot}(Z), \quad (3.6)$$

where  $Z$  is the distance between centres of the tubes and  $M$  is the mass of the inner tube. From the relation for the potential energy and the force in (2.8), equation (3.6) becomes

$$M \frac{d^2 Z}{dt^2} = - \frac{\partial E^{tot}}{\partial Z}. \quad (3.7)$$

By multiplying both sides by  $dZ/dt$  and integrating (3.7), the above equation becomes

$$\frac{M}{2} \left( \frac{dZ}{dt} \right)^2 + E(Z) = \frac{M}{2} v_0^2 + E_0, \quad (3.8)$$

where  $v_0$  is the prescribed initial velocity and  $E_0$  is the initial potential energy, which is a function of the extrusion length  $d$ . Because of the symmetry of the oscillating inner tube, two regions for its motion shown in Figure 3.11 are considered. In the first region, the inner tube is pulled out a distance  $d$  and released, then the distance between centres becomes  $Z_0 = L_2 - L_1 + d = \ell_4 + d$  which leads to the geometric constraint  $d \leq 2L_1$ . On assuming that the prescribed initial velocity at this point is  $v_0$ , it can be deduced

$$\frac{dZ}{dt} = -\sqrt{v_0^2 + \alpha^2(Z_0 - Z)}, \quad \ell_4 \leq Z \leq Z_0,$$

where  $\alpha^2 = 2E(0)/[M(\ell_4 - \ell_3)]$ , and  $E(0)$  is the potential energy at  $Z = 0$ . Thus the displacement equation in this region can be written as

$$Z(t) = Z_0 - \frac{\alpha^2}{4} t^2 - v_0 t, \quad \ell_4 \leq Z \leq Z_0,$$

and the time for the inner tube to travel the length of this region is

$$t_1 = \frac{2}{\alpha^2} \left( \sqrt{v_0^2 + \alpha^2 d} - v_0 \right).$$

In the second region, from equation (3.8) it may be deduced

$$\frac{dZ}{dt} = -\sqrt{v_0^2 + \alpha^2 d}, \quad 0 \leq Z \leq \ell_4.$$

Since at  $t = t_1$ ,  $Z(t_1) = \ell_4$ , the displacement equation becomes

$$Z(t) = \ell_4 + \frac{2}{\alpha^2} \left( v_0^2 + \alpha^2 d \right) - \left( t + \frac{2v_0}{\alpha^2} \right) \sqrt{v_0^2 + \alpha^2 d}, \quad 0 \leq Z \leq \ell_4.$$

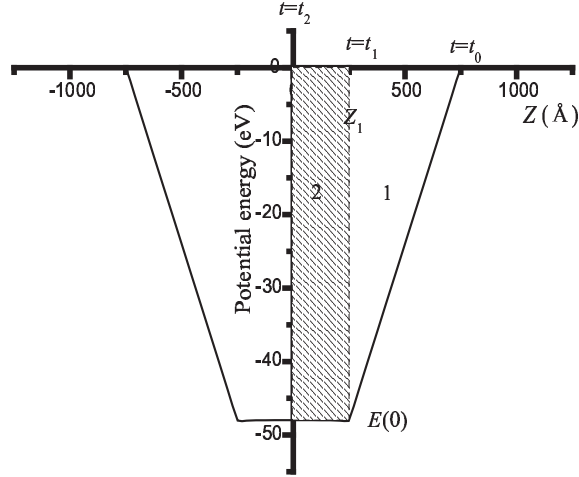


Figure 3.11: Two regions for the idealised potential energy for double-walled carbon nanotubes oscillator.

Thus the overall time for the inner tube to travel in these two regions is given by

$$t_2 = \frac{2v_0^2 - 2v_0\sqrt{v_0^2 + \alpha^2 d} + \alpha^2(\ell_4 + 2d)}{\alpha^2\sqrt{v_0^2 + \alpha^2 d}}.$$

The period for the inner tube to move is  $4t_2$ , and then the oscillation frequency can be written as

$$f = \frac{\alpha^2\sqrt{v_0^2 + \alpha^2 d}}{4[2v_0^2 - 2v_0\sqrt{v_0^2 + \alpha^2 d} + \alpha^2(2d + \ell_4)]}, \quad (3.9)$$

which for prescribed  $v_0$  has a maximum frequency at  $d = (\alpha^2\ell_4 - 2v_0^2)/(2\alpha^2)$ .

Of particular practical interest is the case  $v_0 \equiv 0$  for which (3.9) simplifies to give  $f = \alpha\sqrt{d}/[4(2d + \ell_4)]$ , which has a maximum value at  $d = \ell_4/2$ . In addition, the extrusion distance  $d$  must be less than the length of the inner tube  $2L_1$ . As detailed in Cox *et al.* [58] for a physical sensible result that the frequency only applied when the length lies within the limits  $L_1 + 2d_{min} < L_2 < 5L_1$  where  $d_{min}$  denotes the practical limitation on the minimum extrusion distance.

The frequency always increases when the initial velocity is increased, as shown in Figure 3.12. Further, the shorter the inner tube the higher frequency, which is in agreement with Zheng and Jiang [4]. This is because the force is a constant in each case, so that the lighter weight of the shorter tube increases the velocity to give a higher frequency. Furthermore, the longer extrusion distance tends to increase the oscillatory frequency because it leads to a higher potential energy level. This in turn gives a higher van der Waals force, and a higher velocity, and as a result gives rise to

a higher frequency, which is also in agreement with the observation made by Liu *et al.* [59]. In the case of equal lengths, when the extrusion distance is increased, this increases the distance for the inner tube to move from one end to the other, which leads to a lower oscillation frequency. The longer length also leads to a larger mass which tends to slow down the movement as shown in Figure 3.13. Noting in the case  $L_1 = L_2$ , it gives rise to small oscillations near a stable equilibrium point, moreover, when the extrusion  $d = 0$  and the initial velocity  $v_0 \equiv 0$ , the system becomes static.

For the example of Cumings and Zettl [1] with the same parameter values and  $M$  which is used in equation (18) in Zheng, Liu and Jiang [5], a frequency of 0.153 GHz is obtained for an extrusion of 330 nm which is the half length of the inner tube and 1.433 GHz for a 100 nm inner tube length with an extrusion distance of one quarter of the inner tube length. These results differ from Zheng, Liu and Jiang [5] by only 2.68% and 3.09%, respectively.

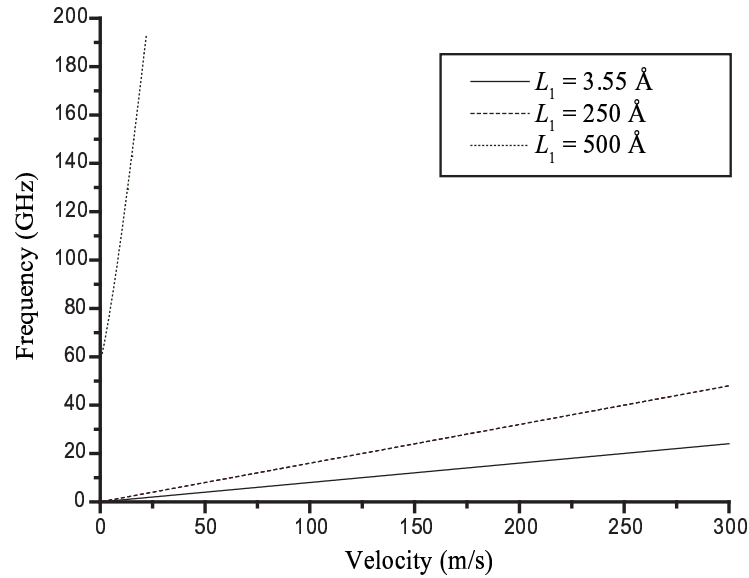


Figure 3.12: The frequency profile  $f$  for three lengths  $L_1$  versus the initial velocity  $v_0$  when the extrusion distance is zero where  $L_2 = 500 \text{ \AA}$ .

### 3.7 Summary

Force distributions arising from the interatomic interactions for two concentric carbon nanotubes of radii  $a$  and  $b$  ( $a < b$ ) and of lengths  $2L_1$  and  $2L_2$  ( $L_1 < L_2$ ) are considered. Making the usual continuum approximation, the integration of the Lennard-Jones potential is performed to determine the van der Waals force in terms



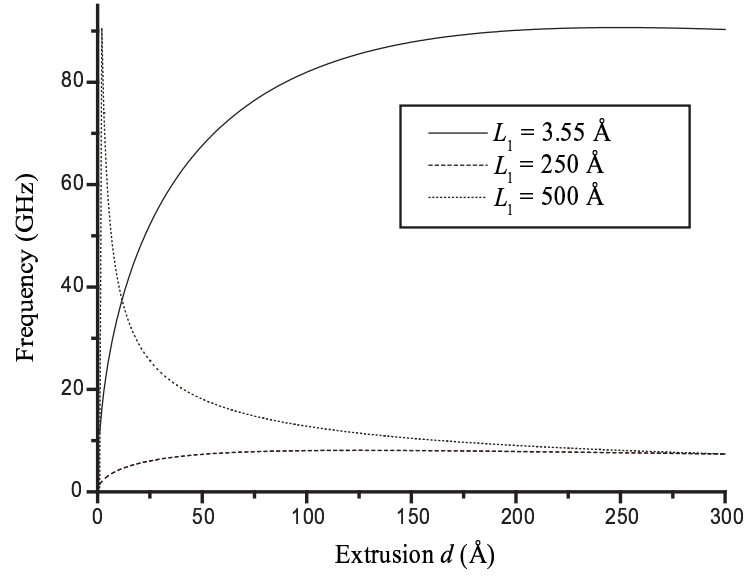


Figure 3.13: The frequency profile  $f$  for three lengths  $L_1$  versus extrusion distance  $d$  when the initial velocity is zero where  $L_2 = 500$  Å.

of the Appell hypergeometric function and the standard hypergeometric function. The complete expression for the Lennard-Jones potential can be used together with the algebraic computer package MAPLE to show the corresponding force distribution for a variety of cylindrical geometries.

The force distribution is approximately to be a rectangular function, where the small variations associated with the four critical positions  $\ell_1 = -(L_1 + L_2)$ ,  $\ell_2 = -(L_2 - L_1)$ ,  $\ell_3 = L_1 + L_2$ ,  $\ell_4 = L_2 - L_1$  are neglected. This has the advantage that Newton's second law may be utilised to follow the oscillatory motion of the inner carbon nanotube when extruded a distance  $d$  ( $\leq 2L_1$ ) and given an initial velocity  $v_0$  in the negative  $z$ -direction, and the frequency of oscillation is determined as given by (3.9). Note in particular that the case  $v_0 \equiv 0$  yields the simple elegant formula for the frequency

$$f = \frac{|E(0)|^{1/2} d^{1/2}}{4(ML_1)^{1/2}(2d + L_2 - L_1)}, \quad (3.10)$$

where  $M$  denotes the mass of the inner tube and  $E(0)$  denotes the value of  $E^{tot}(Z)$  at  $Z = 0$ , which is a complicated function of the geometric parameters and can be determined explicitly from the formula given in (3.2). The above simple formula predicts a maximum frequency occurring at an extrusion length  $d = (L_2 - L_1)/2$ , which is entirely consistent with known behaviour that the frequency will increase with decreasing inner tube length. However, the singularity occurs when  $d = 0$ ,  $v_0$

and  $L_1 = L_2$  for which the system becomes static problem.

Note that the dependence on the extrusion distance  $d$  in (3.10) is in agreement with the formula given by Zheng, Liu and Jiang [5], and in the terminology of this study, their  $\Delta$  and  $\Delta_0$  become  $Z_0$  and  $\ell_4$ , respectively, and therefore their  $\beta/\Delta^{1/2}$  becomes  $\sqrt{d}/(2d + \ell_4)$  which is in complete accord with (3.10). From the integral (3.1), the following approximate expression for  $|E(0)|$  becomes

$$|E(0)| = 6.847 \times 10^{-5} + 0.192L_1,$$

for the particular values given in Table 3.1.

The suction energy for a single-walled carbon nanotube entering co-axially into another semi-infinite tube is obtained analytically. The condition for the suction behaviour depends on the difference of their radii  $(b - a)$ , where the closer this value to zero, the less likely the inner tube is accepted into the outer one. Further, the inner tube is spontaneously sucked into the outer tube and has its maximum suction energy when the difference of their radii is 3.44 Å, which is the optimum inter-spacing value for two graphene sheets. The equilibrium offset position for a double-walled carbon nanotube is also determined, assuming that the inner tube is already accepted inside. This equilibrium position (the global minimum energy position) of the offset inner tube tends to be closer to the outer tube wall as the radius of the outer tube increases. The advantage of this approach is to predict whether or not particles might be sucked into a carbon nanotube, which will become an important issue for applications involving drug delivery research.

Table 3.1: Constants used in the model for the carbon system(\* Reference [36])

Radius of (6, 6)	4.071 Å
Radius of (10, 10)	6.784 Å
Radius of (16, 16)	10.846 Å
Radius of (20, 20)	13.557 Å
Radius of C <sub>60</sub>	$a = 3.55$ Å
Attractive constant - C <sub>60</sub> -C <sub>60</sub>	$A = 20.0 \text{ eV} \times \text{Å}^6 *$
Repulsive constant - C <sub>60</sub> -C <sub>60</sub>	$B = 34.8 \times 10^3 \text{ eV} \times \text{Å}^{12} *$
Attractive constant - C <sub>60</sub> -graphene	$A = 17.4 \text{ eV} \times \text{Å}^6 *$
Repulsive constant - C <sub>60</sub> -graphene	$B = 29.0 \times 10^3 \text{ eV} \times \text{Å}^{12} *$
Attractive constant - graphene-graphene	$A = 15.2 \text{ eV} \times \text{Å}^6 *$
Repulsive constant - graphene-graphene	$B = 24.1 \times 10^3 \text{ eV} \times \text{Å}^{12} *$
Carbon-carbon bond length	$\sigma = 1.42$ Å
Mean surface density - graphene $[4\sqrt{3}/(6\sigma^2)]$	$\eta_g = 0.3812 \text{ Å}^{-2}$
Mean surface density - C <sub>60</sub> $[60/(4\pi a^2)]$	$\eta_f = 0.3787 \text{ Å}^{-2}$

# Chapter 4

## Nanopeapods

While the investigation of the packing of  $C_{60}$  molecules inside a carbon nanotube is usually achieved through either experimentation or large scale computation, here this study adopts elementary mechanical principles and classical applied mathematical modelling techniques to formulate explicit analytical criteria and ideal model behaviour for such an encapsulation. In particular, the Lennard-Jones potential and the continuum approximation are employed to determine three encapsulation mechanisms for a  $C_{60}$  fullerene entering a tube: (i) through the tube open end (head-on), (ii) around the edge of the tube open end and (iii) through a defect opening on the tube wall. These three encapsulation mechanisms are undertaken for each of the three specific carbon nanotubes (10,10), (16,16) and (20,20). All configurations are assumed to be in a vacuum and the  $C_{60}$  fullerene is initially at rest. Double integrals are performed to determine the energy of the system and analytical expressions are obtained in terms of hypergeometric functions. The results suggest that a  $C_{60}$  fullerene is most likely to be encapsulated head-on through the open tube end and that encapsulation around the tube edge is least likely to occur because of the large van der Waals energy barriers which exist at the tube ends.

Moreover, the packing of  $C_{60}$  fullerene chains inside a single-walled carbon nanotube is investigated, again by utilising the Lennard-Jones potential function and the continuum approximation. Both zigzag and spiral chain configurations inside (10,10), (16,16) and (20,20) carbon nanotubes are examined and analytical expressions in terms of hypergeometric functions for the potential energy for such configurations are obtained. For a (10,10) tube, the  $C_{60}$  fullerene chain is formed linearly along the tube axis. In the case of both (16,16) and (20,20) tubes, both zigzag and

spiral configurations are more clearly evident along the tube. In general, all results obtained are in good agreement with experiments and computer simulations.

## 4.1 Nomenclature

$\eta_g, \eta_f$	are the mean atomic number densities for graphene and fullerene, respectively
$\rho$	is the distance between two typical surface elements
$A, B$	are the Lennard-Jones attractive and repulsive coefficients, respectively
$E^*$	is the interaction potential between a $C_{60}$ fullerene and a carbon atom
$E^{tot}$	is the total interaction potential
$L$	is the half-lengths of the defect pad on the nanotube
$Z$	is the distance in the $z$ -direction
$a$	is the radius of the fullerene
$b$	is the radius of the carbon nanotube
$k$	is the number of fullerenes inside the carbon nanotube

## 4.2 Introduction

Carbon nanostructures such as carbon nanotubes and  $C_{60}$  fullerenes have received considerable attention because of their underlying unique mechanical properties arising from the van der Waals interaction force and their electronic properties arising from the large surface to volume ratio [27, 60]. The combination of a single-walled carbon nanotube and a  $C_{60}$  fullerene chain, a so-called nanopeapod, also embodies such properties and is a new hybrid nanostructure. Nanopeapods were originally observed in 1998 by Smith *et al.* [61] and later synthesised by Smith and Luzzi [62], who employed high-resolution transmission electron microscopy to show the self-assembly of the hybrid structures. In particular, nanopeapods capable of being realised as the prototype nanocarrier for drug delivery, where the carbon nanotube can be thought of as the nanocontainer and the  $C_{60}$  molecule chain can be considered

as the drug molecule [8]. We comment that drug molecules may be administered to patients in a solvent medium, and the use of carbon nanotubes may avoid the need for solvents since the drug can cross cell membranes and react within the cell. Therefore, the encapsulation of  $C_{60}$  molecules into a carbon nanotube in vacuum environment constitutes a necessary preliminary calculation which might provide some overall guidelines. We refer the reader to Simon *et al.* [63] for the experimental study of the encapsulation of  $C_{60}$  fullerenes into carbon nanotubes in the solvent medium. Moreover, the present model can easily be modified to account for a solvent medium by choosing the appropriate Lennard-Jones parameters [64].

Several studies have proposed the actual assembly of nanopeapods by utilising either experimentation or computer simulation. Qian *et al.* [3] employ molecular dynamics studies and suggest that the (9,9) and (10,10) single-walled carbon nanotubes will accept a  $C_{60}$  molecule from rest, but this behaviour will not occur for the (8,8) carbon nanotube. From the study of the energetics and electronic structures of nanopeapods, Okada *et al.* [65] propose that the smallest radius of a nanotube which can encapsulate a  $C_{60}$  molecule is approximately 6.4 Å, which is approximately the radius of a (10,10) carbon nanotube. This result compares well with Cox *et al.* [57] and Hodak and Girifalco [66], but conflicts with Qian *et al.* [3] who show that the fullerene can be accepted into a (9,9) nanotube which has a radius of 6.102 Å. Moreover, from Okada *et al.* [65], Hodak and Girifalco [66], and others [8, 67–70], have confirmed that the encapsulation energy of nanopeapods depends only on the tube radius, and that it is independent of the tube chirality [69].

There are three possible scenarios for  $C_{60}$  molecules to become encapsulated into a carbon nanotube and form a nanopeapod. The first such scenario is that the  $C_{60}$  molecule is sucked in through the tube open end when the  $C_{60}$  fullerene is initially located outside the tube but situated on the tube axis, and in a head-on configuration [71]. The encapsulation of the  $C_{60}$  fullerene around the edge of the tube is a second possible scenario, and the final possible scenario is the absorption of the  $C_{60}$  fullerene through a large defect opening on the tube wall. These three encapsulation scenarios are investigated by Berber *et al.* [72] who use the electronic Hamiltonian method, and Ulbricht and Hertel [71] and Ulbricht *et al.* [73] who utilise molecular dynamics calculations based on the Lennard-Jones potential function. Berber *et al.* [72]

suggest that the encapsulation of the  $C_{60}$  molecule is most likely to occur at a defect opening of the tube wall. In contrast, Ulbricht and Hertel [71] and Ulbricht *et al.* [73] propose that the  $C_{60}$  fullerene is most likely to be encapsulated by head-on at the tube ends. Moreover, they find that although encapsulation around a tube edge and absorption at a defect opening can occur, these outcomes are less likely.

Once a number of  $C_{60}$  molecules are encapsulated into a single-walled carbon nanotube, a nanopeapod is formed. As shown in Okada *et al.* [65], Hodak and Girifalco [66, 74], Khlobystov *et al.* [75] and Dubay and Kresse [76], in (10,10) and (11,11) nanotubes, the  $C_{60}$  molecules form a quasi one-dimensional system, and the energy is close to a one-dimensional system of  $C_{60}$  molecules to which the interaction energy with the tube is added. However, a phase transition occurs when the tube radius becomes larger, resulting in an increase in the dimensionality of the  $C_{60}$  fullerenes inside the tube. From a Monte Carlo study, Hodak and Girifalco [66] report a zigzag structure of  $C_{60}$  molecules inside a (15,15) nanotube. To obtain the interaction energy in a quasi one-dimensional system (e.g.  $C_{60}$  fullerenes in a (10,10) tube), only three nearest neighbour interactions are taken into account, while for three-dimensional  $N$  molecules, Hodak and Girifalco [66] assume that the potential energy consists of two parts. These comprise, firstly, the nearest neighbour interactions between molecules which depend on the inter-molecular distance measured along the axial direction, and secondly, the contribution from the energy that depends on the offset distance of each molecule from the tube central axis.

From the literature, very little work has been undertaken on the mathematical modelling to describe the encapsulation behaviour of nanopeapods. The aim of this study is to utilise fundamental mechanical principles and conventional applied mathematical modelling to determine the energy behaviour for the three encapsulation scenarios of the  $C_{60}$  fullerene, which are presented in §4.3. In addition, the Lennard-Jones potential function and the continuum approximation are employed to determine the van der Waals energy for the  $C_{60}$  fullerene encapsulated into a carbon nanotube. In particular, the (10,10), (16,16) and (20,20) carbon nanotubes are investigated where their radii are in the range 6.27 - 13.57 Å following Hodak and Girifalco [74], who determine fullerene peapod patterns. Carbon nanotubes with radii smaller than that of a (10,10) nanotube are not studied here, since it has

already been shown that a  $C_{60}$  fullerene will not be sucked into such tubes (see for example Cox *et al.* [57]). Once  $C_{60}$  fullerenes are encapsulated into a single-walled carbon nanotube, the total potential energy and configuration, which is assumed to form either a zigzag or a spiral pattern, of the nanopeapod are determined and are shown in §4.4.

Note that by adopting the continuum approximation, the chirality effect of a carbon nanotube is not taken into account, and the use of  $(n, m)$  therefore refers only to a representative of the tube size given by (2.1). In all cases, a vacuum environment and an isothermal mechanical system are assumed, and the  $C_{60}$  fullerene is assumed to be at rest.

### 4.3 Encapsulations of $C_{60}$ fullerene

To determine the interaction energy between a spherical fullerene and a carbon nanotube for a typical point on the carbon nanotube, the surface integral of the Lennard-Jones potential over the sphere is firstly performed, which is detailed in Appendix C. The interaction energy between a  $C_{60}$  molecule and a nanotube is subsequently obtained by performing another surface integral over the cylindrical tube. In this section, three encapsulation mechanisms for a  $C_{60}$  fullerene entering a tube, which are (i) through the tube open end (head-on), (ii) around the edge of the tube open end and (iii) through a defect opening on the tube wall, are investigated, and the details are presented.

#### 4.3.1 Encapsulation of a $C_{60}$ head-on at an open end

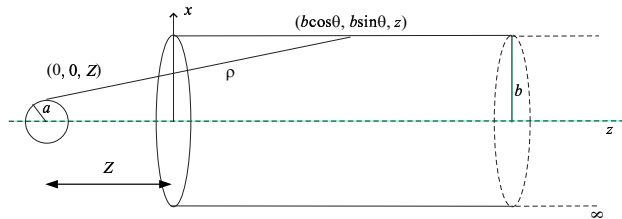


Figure 4.1:  $C_{60}$  fullerene encapsulated in carbon nanotube head-on at an open end.

The encapsulation of a  $C_{60}$  molecule into a single-walled carbon nanotube by head-on at the tube open end, as shown in Figure 4.1, is determined here. The  $C_{60}$



fullerene is assumed to be located on the tube axis and initially at rest. In fact, this is the model in Cox *et al.* [57] for the acceptance condition and suction energy of the C<sub>60</sub> fullerene and the single-walled carbon nanotube.

With reference to a rectangular Cartesian coordinate system  $(x, y, z)$  with origin located at the tube end, a typical point on the surface of the tube has the coordinates  $(b \cos \theta, b \sin \theta, z)$  where  $b$  is the radius of the semi-infinite tube. Similarly, with reference to the same rectangular Cartesian coordinate system  $(x, y, z)$ , the centre of the C<sub>60</sub> molecule has coordinates  $(0, 0, Z)$  where  $Z$  is the distance in the  $z$ -direction which can be either positive or negative. Thus the distance  $\rho$  between the centre of the C<sub>60</sub> fullerene and a typical point on the tube is given by

$$\rho^2 = b^2 + (z - Z)^2. \quad (4.1)$$

Using the Lennard-Jones potential function together with the continuum approximation, the total potential can be written as

$$E = b\eta_g \int_{-\pi}^{\pi} \int_0^{\infty} E^*(\rho) dz d\theta,$$

where  $\eta_g$  represents the mean atomic surface density of the carbon nanotube,  $\rho$  is given in (4.1) and  $E^*(\rho)$  is defined by

$$E^*(\rho) = \frac{\pi a \eta_f}{\rho} \left[ \frac{A}{2} \left( \frac{1}{(\rho + a)^4} - \frac{1}{(\rho - a)^4} \right) - \frac{B}{5} \left( \frac{1}{(\rho + a)^{10}} - \frac{1}{(\rho - a)^{10}} \right) \right]. \quad (4.2)$$

By expanding the denominators, the integrals which need to be evaluated are of the form

$$\begin{aligned} G_n &= \int_{-\pi}^{\pi} \int_0^{\infty} \frac{1}{(\rho^2 - a^2)^n} dz d\theta \\ &= \int_{-\pi}^{\pi} \int_0^{\infty} \frac{1}{[b^2 - a^2 + (z - Z)^2]^n} dz d\theta, \end{aligned} \quad (4.3)$$

where  $n$  is a certain positive integer. It is clear that (4.3) is independent of  $\theta$  so that

$$G_n = 2\pi \int_0^{\infty} \frac{1}{[b^2 - a^2 + (z - Z)^2]^n} dz. \quad (4.4)$$

The details of the analytical expression (4.4) are presented in Appendix D.1 and the numerical solution is evaluated as follows.

Using the parameter values from Table 3.1, the relation between the potential

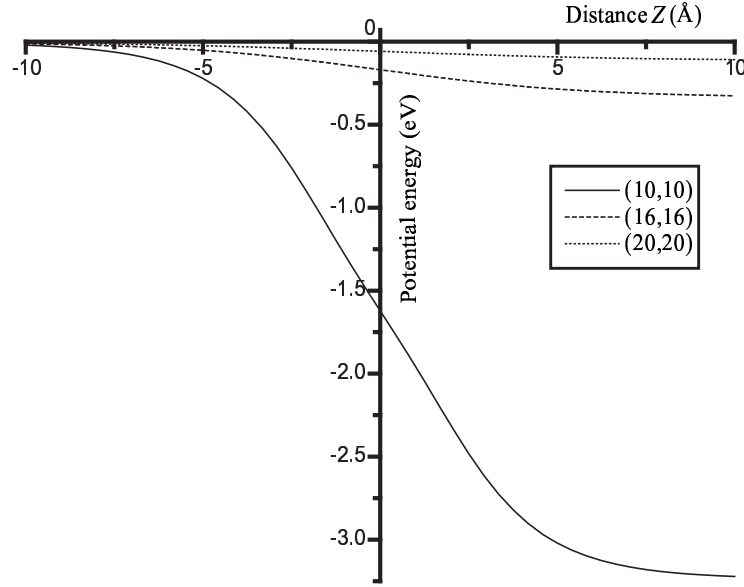


Figure 4.2: Energy profile for  $C_{60}$  encapsulated by head-on at open end.

energy and the distance  $Z$  for the  $C_{60}$  molecule encapsulated into the (10,10), (16,16) and (20,20) carbon nanotubes by head-on are shown in Figure 4.2. We comment that this energy profile of Figure 4.2 was first given in Hodak's thesis [77]. The energetically favourable location for the  $C_{60}$  fullerene is inside the tube, in the positive direction of  $Z$ , for all three cases. Furthermore, the binding energies which is the energy required to separate the two bodies are 3.222, 0.326 and 0.109 eV for the (10,10), (16,16) and (20,20) carbon nanotubes, respectively. The lowest potential energy is observed to occur for the case of the (10,10) tube, since the preferred location of the  $C_{60}$  molecule is on the tube axis [36]. As a result, offset locations from the tube axis for the (16,16) and (20,20) tubes are required to give rise to the most stable configurations and these details can be found in Girifalco *et al.* [36] and Cox *et al.* [54]. We comment that the energy profile of Figure 4.2 was first given in Hodak's thesis [77].

### 4.3.2 Encapsulation of $C_{60}$ around the edge of an open end

In this subsection, the energy for a  $C_{60}$  molecule encapsulated into a carbon nanotube by entering the tube around the tube edge at the open end is investigated. With reference to the same rectangular Cartesian coordinate system  $(x, y, z)$ , a typical point on the surface of the tube has the coordinates  $(b \cos \theta, b \sin \theta, z)$  where  $b$  is the radius of the semi-infinite tube. Similarly, with reference to the rectangular

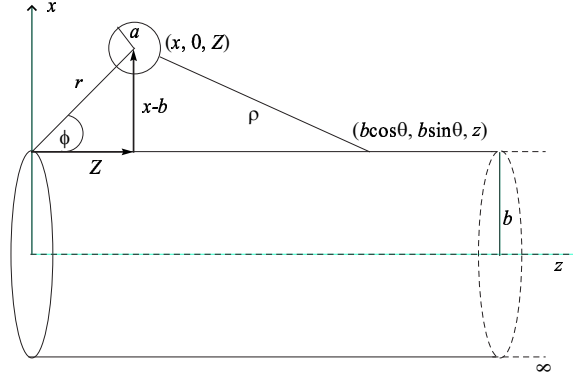


Figure 4.3:  $C_{60}$  fullerene encapsulated in carbon nanotube around the edge of an open end.

Cartesian coordinate system  $(x, y, z)$ , the centre of the  $C_{60}$  molecule has coordinates  $(x, 0, Z)$  where  $Z$  is the distance in the  $z$ -direction which can be either positive or negative. The distance  $Z$  and the coordinate  $x$  can also be described in terms of an angle  $\phi$  and the distance  $r$  in the radial direction,  $Z = r \cos \phi$  and  $x = r \sin \phi + b$ , as illustrated in Figure 4.3. Thus the distance  $\rho$  between the centre of the  $C_{60}$  fullerene and a typical point on the tube is given by

$$\begin{aligned} \rho^2 &= (b \cos \theta - x)^2 + b^2 \sin^2 \theta + (z - Z)^2 \\ &= (b - x)^2 + 4bx \sin^2(\theta/2) + (z - Z)^2. \end{aligned} \quad (4.5)$$

The total potential energy is obtained by integrating  $E^*(\rho)$ , which is defined by (4.2), over the tube length and the angle  $\theta$ . Thus there is one form of the integral which needs to be evaluated, given by

$$H_n = \int_{-\pi}^{\pi} \int_0^{\infty} \frac{1}{(\rho^2 - a^2)^n} dz d\theta, \quad (4.6)$$

where  $\rho$  is given by (4.5). Further, there are three possible expressions for (4.6) and these details are presented in the Appendix D.2. Although the analytical expressions for (4.6) are clearly complicated, numerical values may be readily evaluated using the algebraic computer package MAPLE. Note that the total potential energy in terms of the distance  $r$  and the angle  $\phi$  can be obtained by replacing  $Z = r \cos \phi$  and  $x = r \sin \phi + b$ .

To confirm the results the numerical evaluation for the encapsulation of the  $C_{60}$  molecule around the edge at the tube end are determined using both polar and

Cartesian coordinate systems. In terms of the polar coordinate system, the relation between the binding energy and the equilibrium distance for different angles  $\phi$  is presented in Table 4.1. The lowest binding energy is observed to occur at  $\phi \approx 165^\circ$  for all three cases due to the edge effect. Consequently, this value of  $\phi$  is the critical value which determines whether or not the  $C_{60}$  molecule is encapsulated into the tube. The “equilibrium distance” refers to the cross-sectional location adopted by the  $C_{60}$  fullerene in the carbon nanotube, and it is defined as the distance between the tube edge and the centre of the fullerene at equilibrium. The equilibrium distance are obtained as 6.775, 6.540, and 6.550 Å for  $\phi = 270^\circ$  and for each of the (10,10), (16,16) and (20,20) tubes, respectively. These values are equivalent to 0.009, 4.306 and 7.007 Å, respectively, away from the tube axis to the centre of the  $C_{60}$  fullerene in the  $x$ -direction, which is in agreement with the work of Cox *et al.* [54].

Table 4.1: Numerical values for binding energy (BE) in eV and the equilibrium distance ( $E_0$ ) in Å for a  $C_{60}$  fullerene encapsulated in a carbon nanotube around the tube edge at the open end for different angles  $\phi$ .

$\phi$	(10,10)		(16,16)		(20,20)	
	BE	$E_0$	BE	$E_0$	BE	$E_0$
15°	0.53424	25.16055	0.58315	25.14903	0.60398	25.14903
30°	0.53026	13.01349	0.57883	13.00486	0.59953	13.00486
45°	0.51050	9.18529	0.55756	9.20351	0.57737	9.18603
60°	0.45467	7.53991	0.49675	7.56151	0.51479	7.54922
75°	0.35970	6.77549	0.39343	6.79463	0.40775	6.81484
90°	0.26722	6.47536	0.29169	6.51166	0.30211	6.51166
105°	0.20322	6.32529	0.22146	6.36167	0.22892	6.35916
120°	0.16640	6.30654	0.17929	6.32301	0.18476	6.32103
135°	0.14647	6.26761	0.15413	6.21275	0.15967	6.28291
150°	0.13894	6.26761	0.14378	6.21275	0.14722	6.28291
165°	0.14169	6.26761	0.14250	6.21275	0.14412	6.28291
180°	0.15563	6.26761	0.14998	6.21275	0.14929	6.28291
195°	0.18511	6.26761	0.16666	6.21275	0.16318	6.28291
210°	0.24079	6.30654	0.19779	6.30216	0.18779	6.28291
225°	0.34809	6.34427	0.24633	6.30216	0.22694	6.32103
240°	0.56623	6.44215	0.32206	6.34055	0.28746	6.32103
255°	1.01175	6.66655	0.43751	6.42551	0.38012	6.40225
270°	1.62119	6.77519	0.60665	6.53999	0.51827	6.55048

In terms of the Cartesian coordinate system, the potential energy of the system depends on both distances in the  $x$ - and  $z$ -directions. An example of the potential energy versus the distance  $Z$  for the encapsulation of the  $C_{60}$  fullerene into the

(10,10) tube is presented. Primarily, our interest is in the positive  $z$ -direction where the  $C_{60}$  molecule is located above the tube. As shown in Figure 4.4, the  $C_{60}$  fullerene will not be encapsulated into the tube if its location is far from the edge of the tube. This is because of the lower energy level at that position and the high energy peak near the tube end. However, a nanopeapod might be formed if an initial energy is given to the  $C_{60}$  molecule to overcome the energy barrier. The  $C_{60}$  fullerene has a greater probability of encapsulation around the tube edge if it is initiated from rest closer to the tube edge. If the value of  $x$  is greater than  $13.034 \text{ \AA}$ , the  $C_{60}$  fullerene has no chance of being sucked into the carbon nanotube since the global minimum energy position is located further along the tube in the positive  $z$ -direction. Note that for the  $C_{60}$  molecule to overcome the energy barrier and located in the negative  $z$ -direction, the analysis for the suction by head-on applies for the encapsulation.

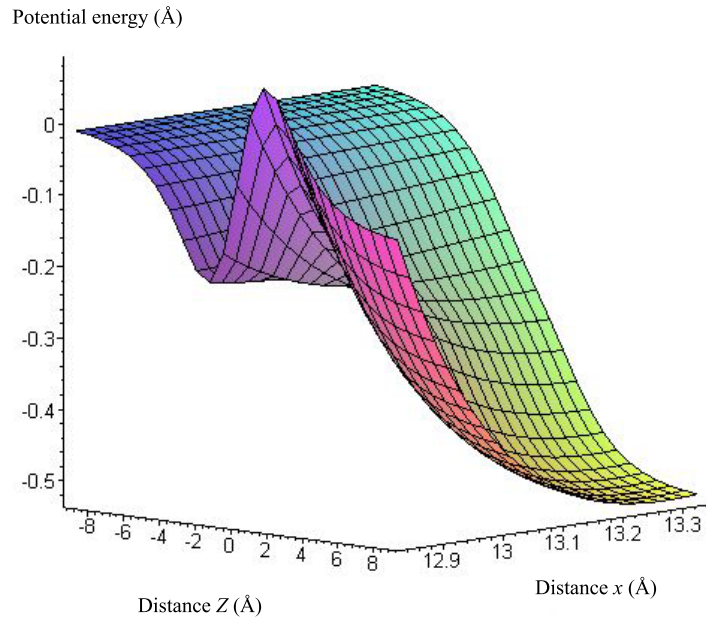


Figure 4.4: Energy profile for  $C_{60}$  encapsulated into (10,10) tube.

### 4.3.3 Encapsulation of $C_{60}$ at a defect opening on the tube wall

The potential energy for a  $C_{60}$  fullerene encapsulated into a carbon nanotube at a defect opening on the tube wall, which is centrally located mid-way along the tube length, is determined here. Since the Lennard-Jones potential is only effective at short range, the carbon nanotube is assumed to be infinite in length. From (2.3)

the total potential energy of the system is obtained by subtracting the total energy of the  $C_{60}$  fullerene interacting with the defect pad from the total potential energy of the  $C_{60}$  fullerene interacting with the infinite carbon nanotube, as illustrated in Figure 4.5.

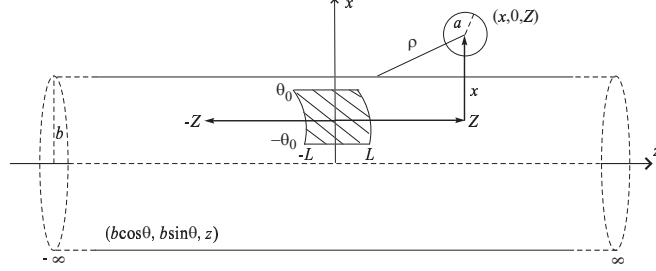


Figure 4.5:  $C_{60}$  fullerene encapsulated in carbon nanotube at defect opening on the tube wall.

Again with reference to the rectangular Cartesian coordinate system  $(x, y, z)$ , a typical point on the surface of the tube has the coordinates  $(b \cos \theta, b \sin \theta, z)$  where  $b$  is the radius of the infinite tube. Similarly, with reference to the rectangular Cartesian coordinate system  $(x, y, z)$  with origin located at the centre of the tube, the centre of the  $C_{60}$  molecule is assumed to have coordinates  $(x, 0, Z)$  where  $Z$  is the distance in the  $z$ -direction which can be either positive or negative. Thus the distance  $\rho$  between the centre of the  $C_{60}$  fullerene and a typical point on the tube is given by

$$\begin{aligned} \rho^2 &= (b \cos \theta - x)^2 + b^2 \sin^2 \theta + (z - Z)^2 \\ &= (b - x)^2 + 4bx \sin^2(\theta/2) + (z - Z)^2. \end{aligned} \quad (4.7)$$

The total potential energy for the entire tube interacting with the  $C_{60}$  fullerene is given by

$$E_{tube} = b\eta_g \int_{-\pi}^{\pi} \int_{-\infty}^{\infty} E^*(\rho) dz d\theta, \quad (4.8)$$

where  $\eta_g$  denotes the mean atomic surface density of the carbon nanotube,  $E^*(\rho)$  is defined by (4.2) and  $\rho$  is given in (4.7). The defect pad is assumed to occupy the region  $Z \in (-L, L)$  and  $\theta \in (-\theta_0, \theta_0)$  so that the interacting energy between the  $C_{60}$  molecule and the defect pad is given by

$$E_{pad} = b\eta_g \int_{-\theta_0}^{\theta_0} \int_{-L}^L E^*(\rho) dz d\theta, \quad (4.9)$$

where  $\rho$  is also given by (4.7). Thus the total potential energy for the  $C_{60}$  fullerene encapsulated in the carbon nanotube at the defect opening on the tube wall is obtained from

$$E = b\eta_g \left( \int_{-\pi}^{\pi} \int_{-\infty}^{\infty} E^*(\rho) dz d\theta - \int_{-\theta_0}^{\theta_0} \int_{-L}^L E^*(\rho) dz d\theta \right). \quad (4.10)$$

By precisely the same analytical method as shown in the pervious section, (4.8) and (4.9) are separately determined and the total potential energy (4.10) is numerically calculated for the system.

The defect pad is arbitrarily chosen to be a square such that the length  $L$  is the radius  $a$  of the  $C_{60}$  fullerene plus the equilibrium interspacing between the  $C_{60}$  fullerene and the graphene which is 3.25 Å [36]. Using the arc length formula  $s = b\theta$ , the limit of the integration  $\theta_0$  is adopted to be determined from  $L = b\theta_0$ . Note that varying  $\theta_0$  has only a minor effect on the energy profile and that the overall properties of the system remain the same when  $L$  is greater than the critical value 6.8 Å.

The relation between the potential energy and the distance  $Z$  for different values of  $x$ , which is the interspacing between the  $C_{60}$  molecule and the tube wall, is examined, and all cases have similar behaviour. An example for the energy profile for the interacting of the  $C_{60}$  molecule and the (10,10) tube is shown in Figure 4.6. In terms of the binding energy, such energy is concentrated at both edges of the defect pad because of the point-force singularity effected from the edges. In this case, an approximate value at 0.225 eV is obtained from both edges of the defect pad. Using the Boltzmann formula  $3kT/2$  for kinetic energy where  $k = 1.38065 \times 10^{-23} \text{ m}^2\text{kgs}^{-1}\text{K}$ , this corresponds to a temperature of approximately 1972 K, and therefore an energy of 0.039 eV is required for the  $C_{60}$  molecule to be encapsulated into the (10,10) at room temperature  $T = 300\text{K}$ . Moreover, two potential energy peaks near the edges of the defect pad for  $x \leq 13.034 \text{ Å}$  are observed, so that if the  $C_{60}$  molecule is located outside the region of the pad, an initial energy is required for the  $C_{60}$  fullerene to be absorbed into the nanotube. However, the  $C_{60}$  molecule is spontaneously sucked in through the defect opening when its position is directly above the defect. Furthermore, if the value of  $x$  is greater than 13.034 Å, the global minimum energy position is always located outside the region of the pad along the tube in the  $z$ -position. Subsequently, the  $C_{60}$  fullerene will not be adsorbed through

the pad and a nanopeapod cannot be formed.

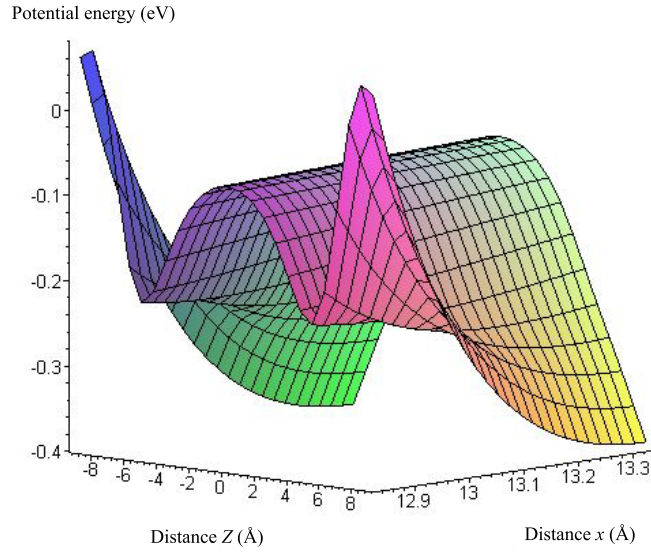


Figure 4.6: Potential energy profile along the (10,10) tube.

## 4.4 Zigzag and spiral configurations for nanopeapods

The continuum approximation and the Lennard-Jones potential function are used to determine the potential energy of a nanopeapod, which is assumed to form either a zigzag or a spiral configuration. The analysis for zigzag nanopeapods comprising  $(2k + 1)$   $C_{60}$  molecules is then presented in the following subsection. Furthermore, the investigation for nanopeapods with a spiral configuration and comprising  $k$   $C_{60}$  molecules is presented in subsection §4.4.3. For both cases analytical expressions are obtained and the minimum energy configurations are determined.

### 4.4.1 Zigzag nanopeapods comprising $(2k + 1)$ $C_{60}$ molecules

The preferred pattern for a zigzag chain of  $C_{60}$  fullerenes inside a single-walled carbon nanotube, the so-called nanopeapod, is investigated, and an interaction energy is determined in the following manner. A configuration, as shown in Figure 4.7, is assumed to comprise  $(2k + 1)$   $C_{60}$  molecules located as indicated and the total energy of the system is assumed to comprise:

1.  $(2k + 1)$   $C_{60}$  fullerenes each interacting with all the carbon atoms of the carbon nanotube,



2.  $2(2k - 1)$  type I interactions, comprising two for each  $j = 2, 3, \dots, k$  and  $i = 2, 3, \dots, k - 1$  and one for each of  $j = 1, k + 1$  and  $i = 1, k$ ; thus  $2(k - 1 + k - 2) + 4 = 2(2k - 1)$ ,
3.  $4k$  type II interactions, comprising two for each  $j = 2, 3, \dots, k$  and  $i = 1, 2, \dots, k$  and one for each of  $j = 1, k + 1$ ; thus  $2(k - 1 + k) + 2 = 4k$ ,

where the nearest neighbour interactions of types I and II are shown in Figure 4.7. Furthermore, all other non-nearest neighbour interactions are assumed to be sufficiently small such that their contributions to the total energy can be neglected. Note that the van der Waals force is a short-range force, so that for example for two interacting  $C_{60}$  fullerenes, it operates at the van der Waals diameter of  $8.9424 \text{ \AA}$ , and since the nearest neighbour approximation involves a distance between fullerene centres of at least  $10.0375 \text{ \AA}$ , only a single nearest neighbour interaction needs to be considered. The distance in the  $z$  direction between centres of adjacent molecules is assumed to be  $Z$ . Then the centre of the upper  $j^{\text{th}}$   $C_{60}$  molecule ( $j = 1, 2, \dots, k + 1$ ) is located at position  $2(j - 1)Z$ , while the centre of the lower  $i^{\text{th}}$   $C_{60}$  molecule ( $i = 1, 2, \dots, k$ ) is located at position  $Z + 2(i - 1)Z = (2i - 1)Z$ .

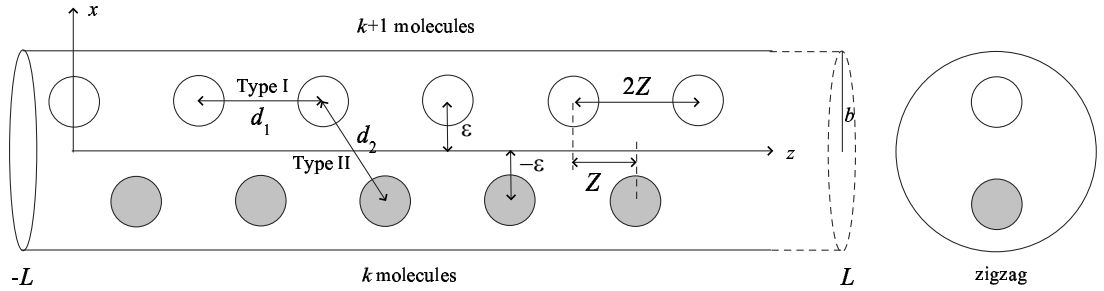


Figure 4.7: Zigzag configuration for  $(2k+1)$   $C_{60}$  fullerenes inside a carbon nanotube.

With reference to a rectangular Cartesian coordinate system  $(x, y, z)$ , a typical point on the surface of the tube has coordinates  $(b \cos \theta, b \sin \theta, z)$  where  $b$  is the radius of the tube. The length of the tube is assumed to be  $2L$  where  $L$  may tend to infinity. Similarly, with reference to a rectangular Cartesian coordinate system  $(x, y, z)$  with the origin located at the centre of the most left  $C_{60}$  molecule, the centres of the upper  $j^{\text{th}}$   $C_{60}$  molecules have coordinates  $(\epsilon, 0, 2Z(j - 1))$  ( $j = 1, 2, \dots, (k + 1)$ ) and the centres of the lower  $i^{\text{th}}$   $C_{60}$  molecules have coordinates  $(-\epsilon, 0, Z(2i - 1))$

( $i = 1, 2, \dots, k$ ), where  $Z$  is the distance between centres of adjacent  $C_{60}$  fullerenes and  $\varepsilon$  is the offset position from the centre of the tube to the centre of the  $C_{60}$  fullerene in the  $x$  direction, as illustrated in Figure 4.7. Then from equation (2.6) for a many-body system, the total potential energy is obtained by

$$E^{tot} = \sum_{i=1}^k E_i(\rho_i) + \sum_{j=1}^{k+1} E_j(\rho_j) + (2k-1)E^{**}(d_1) + 2kE^{**}(d_2),$$

where  $d_1$  and  $d_2$  are the distances between the centres of  $C_{60}$  fullerenes as shown in Figure 4.7, and  $d_1^2 = 4Z^2$  and  $d_2^2 = 4\varepsilon^2 + Z^2$ . The potential functions  $E^{**}(d_1)$  and  $E^{**}(d_2)$  arise from the type I and type II interactions between a pair of  $C_{60}$  molecules, respectively, and are defined by

$$E^{**}(d) = \eta_f^2(AP_6 + BP_{12}), \quad (4.11)$$

where

$$P_n = \frac{4\pi^2 a^2}{d(2-n)(3-n)} \left( \frac{1}{(2a+d)^{n-3}} - \frac{1}{d^{n-3}} - \frac{1}{(2a-d)^{n-3}} + \frac{1}{(-d)^{n-3}} \right),$$

as derived in Appendix C. The potential functions  $E_i$  and  $E_j$  represent the energy of a  $C_{60}$  fullerene interacting with the carbon nanotube, which is obtained from

$$E_m = b\eta_g \int_{-\pi}^{\pi} \int_{-L}^L E^*(\rho_m) dz d\theta, \quad (m = i, j) \quad (4.12)$$

where  $\eta_g$  is the mean atomic surface density for a carbon nanotube and the length  $L$  is subsequently taken to be infinite. The potential function  $E^*$  is defined by (4.2) and  $\rho_m$  ( $m = i$  and  $j$ ) are given by

$$\begin{aligned} \rho_i^2 &= (b + \varepsilon)^2 - 4b\varepsilon \sin^2(\theta/2) + [z - Z(2i - 1)]^2, \\ \rho_j^2 &= (b - \varepsilon)^2 + 4b\varepsilon \sin^2(\theta/2) + [z - 2Z(j - 1)]^2. \end{aligned}$$

According to equations (C.2), (C.3) and (4.12), the following equation needs to be evaluated

$$I_n = \int_{-\pi}^{\pi} \int_{-\infty}^{\infty} \frac{1}{(\rho_m^2 - a^2)^n} dz d\theta, \quad (4.13)$$

where  $n$  is an integer. The details for evaluating (4.13) are presented in Appendix D.3, which can be written as

$$I_n = \frac{\pi^2}{2^{2n-3}(\alpha_m + \beta_m)^{n-1/2}} \binom{2(n-1)}{n-1} F\left(n - \frac{1}{2}, \frac{1}{2}; 1; 1 - \gamma_m\right),$$

where  $F(a, b; c; z)$  denotes the usual hypergeometric function,  $\binom{x}{y}$  represents the usual binomial coefficient,  $\gamma_m = \alpha_m/(\alpha_m + \beta_m)$  ( $m = i$  and  $j$ ),  $\alpha_i = (b + \varepsilon)^2 - a^2$ ,  $\beta_i = -4b\varepsilon$ ,  $\alpha_j = (b - \varepsilon)^2 - a^2$  and  $\beta_j = 4b\varepsilon$ .

#### 4.4.2 Numerical solutions for zigzag nanopeapods

By minimising the total energy of the system, the offset location  $\varepsilon$  from the centre of the tube to the centre of the  $C_{60}$  fullerene and an equilibrium distance  $Z$  between centres of a pair of  $C_{60}$  molecules for zigzag nanopeapods are determined. The total potential energy consists of two nearest neighbour interactions of two  $C_{60}$  fullerenes and one interaction between the  $C_{60}$  fullerene and the carbon nanotube. An infinite length nanopeapod comprising  $(2k + 1)$   $C_{60}$  molecules inside (10,10), (16,16) and (20,20) carbon nanotubes are examined. Using the algebraic computer package MAPLE together with the parameter values in Table 3.1, the numerical values for the offset location  $\varepsilon$ , the equilibrium distance  $Z$  and the total potential energy  $E^{tot}$  are presented in Table 4.2. Note that the global minimum energy location of the system is first plotted to ensure a genuine global minimum and the optimisation package in MAPLE is then utilised to find the optimum values for each parameter at this location.

In the case of the (10,10) carbon nanotube, an offset position is obtained as  $\varepsilon = 0$  which is equivalent to a distance of 3.234 Å from the tube wall to the nearest atom on the  $C_{60}$  molecule, which compares well with Okada *et al.* [65]. The equilibrium distance is shown to be  $Z = 10.0375$  Å for three  $C_{60}$  molecules inside the tube, which is in excellent agreement with Rochefort [67]. As a result, all  $C_{60}$  fullerenes inside the (10,10) tube are likely to align and form a linear chain along the tube axis. The equilibrium distance decreases slightly as the number of the  $C_{60}$  molecules is increased due to the packing of the molecules. Moreover, the  $C_{60}$  fullerenes move closer to the wall as the radius of the tube increase. The offset positions of  $\varepsilon = 4.30$  Å and  $\varepsilon = 7.02$  Å are obtained and these are equivalent to the equilibrium distances

Table 4.2: Equilibrium distance  $Z$  (Å), offset location  $\varepsilon$  (Å) and total potential energy of the system  $E^{tot}$  (eV) for each pair of  $C_{60}$  fullerenes in a zigzag configuration nanopeapod comprising  $(2k + 1)$   $C_{60}$  molecules.

$k$	(10,10)			(16,16)			(20,20)		
	$Z$	$\varepsilon$	$E^{tot}$	$Z$	$\varepsilon$	$E^{tot}$	$Z$	$\varepsilon$	$E^{tot}$
1	10.0550	0	-6.7632	5.2176	4.2977	-2.7048	0	7.0213	-2.0941
2	10.0543	0	-13.8074	5.0390	4.3216	-6.2354	5.0267	7.0220	-4.7420
3	10.0542	0	-20.8516	5.0366	4.3232	-9.7692	5.0269	7.0217	-7.3973
4	10.0542	0	-27.8958	5.0358	4.3239	-13.3031	5.0269	7.0215	-10.0526
5	10.0541	0	-34.9400	5.0354	4.3244	-16.8370	5.0269	7.0214	-12.7079
10	10.0541	0	-70.1612	5.0347	4.3251	-34.5067	5.0270	7.0212	-25.9845
15	10.0540	0	-105.3823	5.0345	4.3255	-52.1764	5.0270	7.0211	-39.2611
20	10.0540	0	-140.6034	5.0344	4.3255	-69.8460	5.0270	7.0211	-52.5377
25	10.0540	0	-175.8245	5.0344	4.3256	-87.5157	5.0270	7.0210	-65.8143
50	10.0540	0	-351.9301	5.0343	4.3257	-175.8641	5.0270	7.0210	-132.1973
100	10.0540	0	-704.1413	5.0342	4.3258	-352.5610	5.0270	7.0210	-274.9634

of  $Z = 5.024$  Å and  $Z = 5.018$  Å for the (16,16) and (20,20) carbon nanotubes, respectively. For these two cases, the zigzag pattern is more clearly evident along the tube. However, for the three  $C_{60}$  fullerenes inside the (20,20) carbon nanotube, the equilibrium distance is obtained as  $Z = 0$  which means that although a zigzag pattern exists, all three of the  $C_{60}$  molecules are in the same plane. This is because there is a sufficient amount of space for the three  $C_{60}$  molecules to align themselves due to the large circumference of tube. This result is related to the investigation made by Hodak and Girifalco [74]. Furthermore, upon considering  $C_{60}$  fullerenes inside a (15,15) nanotube, the results suggest  $\varepsilon \simeq 3.6$  Å and  $Z \simeq 6.9$  Å which agree well with Hodak and Girifalco [66].

The offset locations for all three nanopeapod configurations found in this investigation are in a very good agreement with Cox *et al.* [57] for a single  $C_{60}$  fullerene inside a single-walled carbon nanotube. Moreover, the interaction energy between the  $C_{60}$  fullerenes is observed to have more effect in forming the chain conformation than the interaction energy between the tube and the  $C_{60}$  fullerene. For example, an equilibrium distance of 10.036 Å is obtained for (10,10) nanopeapod, which is comparable to the equilibrium distance between two  $C_{60}$  molecules as determined in Appendix C. Furthermore, the number of  $C_{60}$  molecules in the system makes only

a minor contribution to the alignment of the molecules as shown in Table 4.2.

#### 4.4.3 Spiral nanopeapod comprising $k$ $C_{60}$ molecules

In this subsection, a spiral configuration is assumed for  $k$   $C_{60}$  fullerenes, which are located inside a single-walled carbon nanotube, as shown in Figure 4.8. The energy of the system is minimised and the angular spacing  $\alpha$ , the longitudinal spacing  $\beta$  and the offset location  $\varepsilon$  for a spiral pattern are determined. The total potential energy of the system is assumed to comprise:

1.  $k$   $C_{60}$  fullerenes each interacting with all the carbon atoms of the carbon nanotube,
2.  $2(k-1)$  type I interactions, comprising two for each  $i = 2, 3, \dots, k-1$  and one for each of  $i = 1$  and  $i = k$ ; thus  $2(k-2) + 2 = 2(k-1)$ ,
3.  $2(k-2)$  type II interactions, comprising two for each  $i = 3, 4, \dots, k-2$  and one for each of  $i = 1, 2$  and  $i = k-1, k$ ; thus  $2(k-4) + 4 = 2(k-2)$ ,
4.  $2(k-3)$  type III interactions, comprising two for each  $i = 4, 5, \dots, k-3$  and one for each of  $i = 1, 2, 3$  and  $i = k-2, k-1, k$ ; thus  $2(k-6) + 6 = 2(k-3)$ ,
5.  $2(k-4)$  type IV interactions, comprising two for each  $i = 5, 6, \dots, k-4$  and one for each of  $i = 1, 2, 3, 4$  and  $i = k-3, k-2, k-1, k$ ; thus  $2(k-8) + 8 = 2(k-4)$ ,

where the four nearest neighbour interactions of types I, II, III and IV are as shown in Figure 4.8.

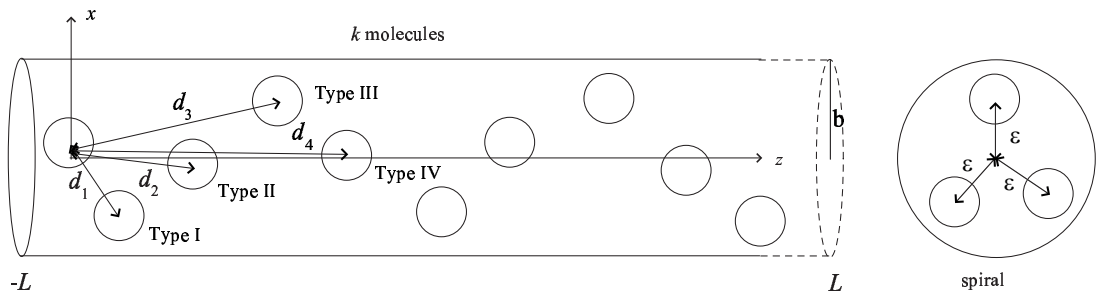


Figure 4.8: Spiral configuration for  $k$   $C_{60}$  molecules inside a carbon nanotube.

With reference to a rectangular Cartesian coordinate system  $(x, y, z)$ , a typical point on the surface of the tube has the coordinates  $(b \cos \theta, b \sin \theta, z)$  where  $b$  is

the radius of the tube. The length of the tube is assumed to be  $2L$ , where  $L$  can tend to infinity. Similarly, with reference to a rectangular Cartesian coordinate system  $(x, y, z)$  with the origin located at the centre of the left most  $C_{60}$  molecule, the centres of  $C_{60}$  molecules have coordinates  $(\varepsilon \cos \alpha i, \varepsilon \sin \alpha i, \beta i)$  ( $i = 1, 2, \dots, k$ ), where  $\varepsilon$  represents the offset location, and  $\alpha$  and  $\beta$  denote the angular and the longitudinal spacings for the spiral shape, respectively. Noting that  $\alpha = \pi$ , gives rise to the special case of the zigzag pattern. From a potential energy for many-body system (2.6), the total potential energy is given by

$$E^{tot} = \sum_{i=1}^k E_i(\rho_i) + (k-1)E^{**}(d_1) + (k-2)E^{**}(d_2) + (k-3)E^{**}(d_3) + (k-4)E^{**}(d_4),$$

where  $d_\ell$  ( $\ell = 1, 2, 3, 4$ ) are the distances between centres of  $C_{60}$  fullerenes as shown in Figure 4.8, and

$$d_\ell^2 = 4\varepsilon^2 \sin^2(\ell\alpha/2) + (\ell\beta)^2. \quad (4.14)$$

The potential function  $E^{**}(d_\ell)$  represents types I, II, III and IV interactions which are the potential energies between a pair of  $C_{60}$  fullerenes defined by (4.11). The potential function  $E_i$  ( $i = 1, 2, \dots, k$ ) represents the energy of a  $C_{60}$  fullerene interacting with the carbon nanotube, which is obtained from (4.12) where in this case  $m = i$  and  $i = 1, 2, \dots, k$ . The function  $E^*$  is defined by (4.2) and  $\rho_i$  ( $i = 1, 2, \dots, k$ ) is given by

$$\rho_i^2 = (b - \varepsilon)^2 + 4b\varepsilon \sin^2[(\theta - \alpha i)/2] + (z - \beta i)^2.$$

Because of the assumed symmetry of the tube, the term  $\alpha i$  has no effect for the integral in (4.12) so on assuming  $\alpha i = 0$ ,  $\rho_i^2$  simplifies to obtain

$$\rho_i^2 = (b - \varepsilon)^2 + 4b\varepsilon \sin^2(\theta/2) + (z - \beta i)^2.$$

According to equations (C.2), (C.3) and (4.12), in the limit as  $L$  tends to infinity the following integral needs to be evaluated

$$I_n = \int_{-\pi}^{\pi} \int_{-\infty}^{\infty} \frac{1}{(\rho_i^2 - a^2)^n} dz d\theta, \quad (4.15)$$

where  $n$  is an integer. Using precisely the same method as the derivation of (4.13), it can be shown that the solution for (4.15) is again in the form of the hypergeometric

function and can be written as

$$I_n = \frac{\pi^2}{2^{2n-3}(\alpha_i + \beta_i)^{n-1/2}} \binom{2(n-1)}{n-1} F\left(n - \frac{1}{2}, \frac{1}{2}; 1; 1 - \gamma_i\right),$$

where as before  $F(a, b; c; z)$  denotes the usual hypergeometric function,  $\binom{x}{y}$  represents the usual binomial coefficient,  $\alpha_i = (b - \varepsilon)^2 - a^2$ ,  $\beta_i = 4b\varepsilon$  and  $\gamma_i = [(b - \varepsilon)^2 - a^2]/[(b + \varepsilon)^2 - a^2]$ .

#### 4.4.4 Numerical solutions for spiral nanopeapods

The energy minimisation technique is employed here to determine the stable configurations of a spiral chain of  $C_{60}$  fullerenes inside a single-walled carbon nanotube. Nanopeapods comprising  $k$   $C_{60}$  molecules inside infinite (10,10), (16,16) and (20,20) carbon nanotubes with four possible nearest neighbour interactions for two  $C_{60}$  molecules and one interaction between the  $C_{60}$  molecule and all the atoms of the carbon nanotube are considered. Again, using the algebraic computer package MAPLE and the parameter values in Table 3.1, numerical values for the angular spacing  $\alpha$ , the longitudinal spacing  $\beta$ , the offset location  $\varepsilon$  and the total potential energy  $E^{tot}$  for such a chain are obtained, which are shown in Table 4.3. Note that  $\beta$  is analogous to the equilibrium distance  $Z$  for the zigzag configuration.

For the (10,10) carbon nanotube, the offset location is also obtained as  $\varepsilon = 0$ . Moreover, from (4.14), the angular spacing  $\alpha$  has no effect on this configuration, and the longitudinal spacing  $\beta$  is found to be 10.03 Å. Subsequently, the  $C_{60}$  fullerenes form a linear chain along the tube axis. These three parameters,  $\alpha$ ,  $\beta$  and  $\varepsilon$ , change slightly as the number of  $C_{60}$  fullerenes in the tube increases. The angular spacing is  $\alpha \simeq \pi$  for the (16,16) tube, which corresponds to the zigzag configuration, and is close to  $\pi/2$  for the (20,20) tube. For  $k = 100$ ,  $\beta = 5.0217$  Å,  $\varepsilon = 4.3228$  Å and  $\beta = 2.2918$  Å,  $\varepsilon = 6.8902$  Å for the (16,16) and the (20,20) tubes, respectively. Consequently, spiral patterns for  $C_{60}$  fullerenes in both the (16,16) and the (20,20) nanotubes are clearly observed.

In particular, the zigzag configuration can be thought of as a special case of the spiral configuration with angular spacing  $\alpha = \pi$ . The comparable numerical values for the offset location  $\varepsilon$  and the longitudinal spacing  $\beta$  for all sizes of the tubes are obtained, and an example is shown for the case of a (16,16) carbon nanotube in

Table 4.3. Moreover, in the case of a (20,20) tube, at least four  $C_{60}$  molecules are required to form a stable spiral configuration. This observation is related to the findings of Hodak and Girifalco [74] in the sense that four molecules are required on each layer within the carbon nanotube with radius 13.5 Å to 14.05 Å.

## 4.5 Summary

In this chapter, a well-known self-assembled hybrid carbon nanostructure of  $C_{60}$  fullerenes and a carbon nanotube, so-called nanopeapod, is investigated. Throughout this study, Lennard-Jones potential function together with the continuum approximation and double surface integrals are evaluated to determine the potential energy which may be expressed analytically in terms of the hypergeometric function. Due to the complicated analytical expressions, numerical evaluations are performed by using the algebraic computer package MAPLE.

Firstly, three suction site scenarios are considered for a  $C_{60}$  molecule entering a carbon nanotube, which are (i) by head-on at the tube open end, (ii) around a tube edge at the tube open end and (iii) at a defect opening on the tube wall. The  $C_{60}$  fullerene is assumed to be initially at rest prior to entering into the three specific carbon nanotubes (10,10), (16,16) and (20,20) in a vacuum environment. The binding energies for the three encapsulation mechanisms are compared and it is found that the  $C_{60}$  molecule is most likely to enter through the carbon nanotube by the head-on configuration. This is because of the overall attractive force arising from the entire tube, and this mechanism avoids the point force singularity acting at the tube edge. Absorption at a defect is the second most likely mechanism to form the nanopeapod. There is an effect from the edges of the defect, but when the  $C_{60}$  fullerene is directly above the defect it is a straightforward matter for the  $C_{60}$  fullerene to be sucked into the tube. The least feasible mechanism to encapsulate the  $C_{60}$  fullerene is entering around the edge of the tube open end, since the  $C_{60}$  molecule must overcome strong repulsive forces at the tube end and change the moving direction to enter into the tube. However, the encapsulation around the edge of the tube open end may provide a way for molecules which do not approach the tube along its axis to enter into the tube, and it is an important mechanism to collect molecules along the outside of the tube. As a result, the quantitative



investigations in this study are in agreement with previous studies such as Ulbricht and Hertel [71] and Ulbricht *et al.* [73], but our predictions contradict those of Berber *et al.* [72]. This disagreement may occur due to the probability of achieving encapsulation. While the head on configuration is the most favourable energetically, the probability of a molecule hitting an open end is much less than a molecule going through an edge or defect configuration. A molecule is readily adsorbed on the tube, and its translation across the tube surface is rapid and nearly energy free.

Once  $C_{60}$  molecules are encapsulated into a single-walled carbon nanotube, two nonlinear patterns for a  $C_{60}$  fullerene chain, which are assumed to be zigzag and spiral, are examined. For the zigzag configuration, there is assumed to be  $(2k+1)$   $C_{60}$  molecules inside (10,10), (16,16) and (20,20) single-walled carbon nanotubes, and the offset location  $\varepsilon$  and the equilibrium distance  $Z$  are determined. The total potential energy of the system comprises the interaction energy between the  $C_{60}$  fullerenes and the tube and the two nearest neighbour interactions of the  $C_{60}$  molecules. The chain of  $C_{60}$  molecules is found to be formed linearly along the (10,10) tube axis and discernible zigzag patterns exist for both the (16,16) and (20,20) tubes. The spiral configuration comprising  $k$   $C_{60}$  molecules is also investigated. The interaction energy between the  $C_{60}$  fullerenes and the tube and the four nearest neighbour interactions between the  $C_{60}$  molecules is considered. The angular spacing  $\alpha$ , the longitudinal spacing  $\beta$  and the offset location  $\varepsilon$  are determined from minimisation of the interaction energies. A linear  $C_{60}$  fullerene chain along the (10,10) tube axis and spiral patterns for the (16,16) and (20,20) tubes are obtained. In particular,  $\alpha = \pi$  gives rise to the special case of the zigzag pattern, and comparable numerical values for the zigzag configuration from the spiral configuration by setting  $\alpha = \pi$  are observed.

In general, the interaction energy between the  $C_{60}$  molecules themselves dominates the energy of the system. The interaction between the  $C_{60}$  molecules determines the equilibrium position and the angular spacing of the system, whereas the interaction between the  $C_{60}$  fullerene and the carbon nanotube determines the offset position of the chain. Further, in the zigzag configuration, the number of  $C_{60}$  molecules makes a minor contribution to both the offset location and the equilibrium distance so that the assumption of periodicity made for the molecular dynamics

simulations is quite reasonable. However, the periodicity assumption may not apply for the spiral configuration since as the radius of the tube increases the system requires more  $C_{60}$  molecules to maintain the stability of the system. Finally, for a tube which is finite in length, the results given here also apply providing that the two fullerenes located closest to the tube ends are at a distance from the end which is at least the van der Waals radius 4.4712 Å. If this is not the case, some small variation of the numerical values given here might be expected, since at the tube ends peak-like forces exist (see for example Cox *et al.* [54]) which would tend to diminish the distance between centres.

Table 4.3: Angular spacing  $\alpha$ , longitudinal spacing  $\beta$ , offset location  $\varepsilon$  in Å and total potential energy of the system  $E^{tot}$  (eV) for each pair of  $C_{60}$  fullerenes in a spiral configuration nanopeapod comprising  $k$   $C_{60}$  molecules.

$k$	(10,10)				(16,16)				(20,20)			
	$\alpha$	$\beta$	$\varepsilon$	$E^{tot}$	$\alpha$	$\beta$	$\varepsilon$	$E^{tot}$	$\alpha$	$\beta$	$\varepsilon$	$E^{tot}$
3	0	10.0545	0	-10.2852	3.1416	5.0442	4.3195	-4.4671	1.3490	4.9083	7.0251	-3.6709
4	0	10.0543	0	-13.8075	3.1416	5.0385	4.3216	-6.2395	1.5566	0.8831	7.0239	-5.2978
5	0	10.0543	0	-17.3297	3.1416	5.0366	4.3226	-8.0120	1.5436	2.4984	7.0057	-6.6966
10	0	10.0541	0	-34.9409	3.1416	5.0341	4.3244	-16.8749	1.5565	2.5063	6.9840	-14.9446
15	0	10.0540	0	-52.5521	3.1416	5.0335	4.3249	-25.7379	1.5649	2.5078	6.9709	-23.1989
20	0	10.0540	0	-70.1633	3.1416	5.0333	4.3251	-34.6029	1.7194	2.2931	6.9181	-33.5703
25	0	10.0540	0	-87.7745	3.1416	5.0331	4.3253	-43.4640	1.7194	2.2934	6.9163	-42.5048
50	0	10.0540	0	-175.8306	3.1416	5.0329	4.3256	-87.7791	1.7194	2.2941	6.9126	-87.1785
100	0	10.0539	0	-351.9426	3.1416	5.0327	4.3259	-176.4093	1.7194	2.2944	6.9108	-176.5269

# Chapter 5

## Nanocoones

In the synthesis and production of carbon nanostructures, carbon nanocoones tend to occur less frequently relative to other structures, and it is known that five different pitched cones may occur, depending on the number of pentagons in the atomic network. Most of the research on carbon nanocoones deal with their electronic structure, since they are the ideal candidate for the probes of scanning tunneling microscopes. The simple geometric structure of carbon nanocoones certainly facilitates calculations for their potential energy. Here, the Lennard-Jones potential energy function and the continuum approximation are employed to determine the energy for two such nested carbon nanocoones which are located co-axially. The energy profiles for any two carbon nanocoones arising from the five possible structures are presented. For two distinct cones and two identical cones, the equilibrium location moves further away from the vertex as the number of pentagons is increased. However, this equilibrium position occurs such that one cone is always inside the other, and therefore nested double-cones are formed according to these results.

Moreover, their oscillatory properties inside carbon nanotubes are examined. The carbon nanocoone located co-axially is shown to be sucked into a carbon nanotube when the difference between the cone base radius and the tube radius exceeds  $2.5 \text{ \AA}$ , irrespective of the direction of the vertex, and the maximum suction energy occurs when these radii differ by  $3.0 \text{ \AA}$ . The oscillatory behaviour of a nanocoone once inside a nanotube is then determined, and pulse-like forces at both ends of the tube which maintain the oscillatory motion along the tube length are obtained. On neglecting frictional effects and approximating the pulse-like forces by Dirac delta functions, Newton's second law is employed to determine the oscillation frequency.

This is shown to be in the order of 15 to 90 gigahertz, which is the same order of magnitude as that obtained for oscillating co-axial carbon atom.

The hexagonal structure of boron nitride is geometrically similar to that of graphene in a carbon structure, since both boron and nitrogen atoms are adjacent to carbon in the periodic table [33]. Given that boron nitride is a good electrical semiconductor, boron nitride cones can also be a good candidate for electronic devices. In this chapter, the interaction energies between two cones of boron nitride and carbon-boron nitride cones are also studied. The results are obtained in such a way that the equilibrium positions always occur inside the other, and therefore the formation of nested double-cones is suggested.

## 5.1 Nomenclature

$\alpha$	is the cone angle
$\epsilon$	is the well depth
$\eta_1, \eta_2$	are the mean atomic number densities for the two surfaces
$\eta_\sigma, \eta_g$	are the mean atomic number densities for carbon atom and graphene, respectively
$\theta$	is the disclination angle
$\rho$	is the distance between two typical surface elements
$\sigma$	is the carbon-carbon covalent bond length
$A, B$	are the Lennard-Jones attractive and repulsive coefficients, respectively
$E^{tot}$	is the total interaction potential
$F_z^{tot}$	is the total force in the $z$ -direction
$L$	is the half-lengths of carbon nanotube
$N_p$	is the number of pentagons
$Z$	is the distance between cone vertices

- $Z_1$  is the distance between the cone vertex and the nanotube end
- $Z_2$  is the distance between the cone vertex and the nanotube centre
- $a, a_1, a_2$  are the cone base radii
- $b$  is the radius of the carbon nanotube
- $h, h_1, h_2$  are the cone heights

## 5.2 Introduction

Many studies utilise molecular dynamics simulation to calculate the energy of carbon nano systems and these investigations emphasise systems involving  $C_{60}$  fullerenes, carbon nanotubes and carbon nanotori, but very little of the existing literature deals with carbon nanocones [2–5, 36, 37, 42, 54, 57, 78]. Carbon nanocones have received less attention primarily because only a small amount tend to occur in the production process [9]. There are five possible ways to construct carbon nanocones depending on the number of pentagons which are needed to close the vertex, and most research on nanocones deals with their electronic structure [10, 79]. It is believed that the different number of pentagons in carbon nanocones is the key to the puzzle of nucleation in atomic construction [10, 80]. Kim *et al.* [81] utilise the catalytic chemical vapor deposition method to synthesise carbon nanocones inside carbon nanotubes, and they find that the resulting structures have different physical and electronic properties than that of the original carbon structure. Charlier and Rignanese [10] use tight-binding and *ab initio* calculations to examine the local density near the apex of the five possible carbon nanocones, and propose that carbon nanocones are ideal candidates for nanoprobe in scanning tunneling microscopy. The electronic structure of carbon nanocones is examined by Pincak and Osipov [79]. They employ the effective-mass theory for a graphite monolayer and gauge theory of disclinations on fluctuating elastic surfaces to obtain a mathematical equation, and finally they find that the electron states are dependent on the position of the pentagons. The mechanical properties of carbon nanocones are investigated by Jordan and Crespi [82]. They obtain the nonlinear mechanical behaviour for both the original shape and the inverse carbon nanocone which is obtained from the original cone by inversion.

To start, the general information including the geometric structure of nanocones is discussed in §5.3. However, from the literature there is little work examining the potential energy behaviour of carbon nanocones. In this study the potential energy for two carbon nanocones, which are assumed to be co-axial, is determined and shown in §5.4. The Lennard-Jones potential energy together with the continuum approximation, which assumes that carbon atoms are uniformly distributed over the surface of each molecule, is utilised throughout this study to calculate the potential energy of the system. Furthermore, the oscillatory behaviour of a carbon nanocone inside a single-walled carbon nanotube is investigated. In particular, the van der Waals interaction energy and the resulting oscillatory motion are determined. The suction energy for a carbon nanocone entering a carbon nanotube is firstly considered and presented in §5.5. Once the cone is sucked into the tube, in §5.6 the oscillatory behaviour of the system is examined. On assuming that the frictional force can be neglected [1], Newton's second law is employed to determine the frequency of the oscillating cone inside the tube. In addition, nanocones of hexagonal boron nitride are examined. In particular, the potential energies between carbon and boron nitride and two boron nitride cones are investigated as shown in §5.7. A summary is then given in §5.8.

### 5.3 Carbon nanocones

Carbon nanocones were discovered by Ge and Sattler [83] and subsequently synthesised by Krishnan *et al.* [80]. Typically, carbon nanocones are observed together with carbon nanotubes and nanotube bundles during the synthesis process [9], and carbon nanocones tend to be found at the cap of carbon nanotubes. There are five possible structures for nanocones, as shown in Figure 5.1, because the cone angle depends on the number of pentagons needed to close the structure. Cones are formed from hexagons on a honeycombed lattice by adding fewer pentagons than the six which are needed by Euler's polyhedra theorem [27] for a closed structure. In  $C_{60}$  fullerenes, a hexagonal lattice of any size or shape can only form a closed structure with precisely twelve pentagons. The carbon nanotube cap, which is a half  $C_{60}$  fullerene, contains six pentagons, and therefore carbon nanocones must have a number of pentagons which is less than six.

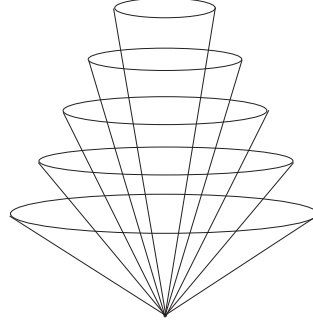


Figure 5.1: Five possible nanocones with vertex angles  $19.20^\circ$ ,  $38.90^\circ$ ,  $60.00^\circ$ ,  $83.60^\circ$  and  $112.90^\circ$ .

The disclination number of pentagons on the graphene gives the change with  $\theta$  in the form

$$\theta = \frac{\pi N_p}{3},$$

where  $N_p$  is the number of the pentagons which ranges from 0 to 6. From the diagram of the cone shown in Figure 5.2, it is clear that  $\sin(\alpha/2) = r/R$  and  $c = 2\pi r = 2\pi(1 - N_p/6)R$ . Therefore, the relation of the cone angle and the number of pentagons is obtained as

$$\sin(\alpha/2) = 1 - \frac{N_p}{6}.$$

There are seven possible values of the angle  $\alpha$  depending on the number of pentagons which are shown in Table 5.1. Note that for  $N_p = 0$  a graphene sheet is formed and for  $N_p = 6$  a capped carbon nanotube is obtained. Hence there are only five possible values giving rise to carbon nanocones. The mean atomic surface density of the carbon nanocones is assumed to be the mean atomic surface density of a graphene sheet,  $0.3812 \text{ \AA}^{-2}$ , due to the fact that the carbon nanocones are formed from the graphene sheet and the number of pentagons has very small effect on the mean atomic surface density of a cone.

The surface shown in Figure 5.3(a) is a double right cone. A right cone is one for which the vertex is directly above the centre of the base. However, when used without qualification, the term cone often means right cone. A right cone is the surface in three-dimensional space generated by a line that revolves about a fixed axis in such a way that the line passes through a fixed point on the axis and always makes the same angle with the axis, and the fixed point is called the vertex of the cone. A cone consists of two parts, called nappes, that intersect at the vertex [84].



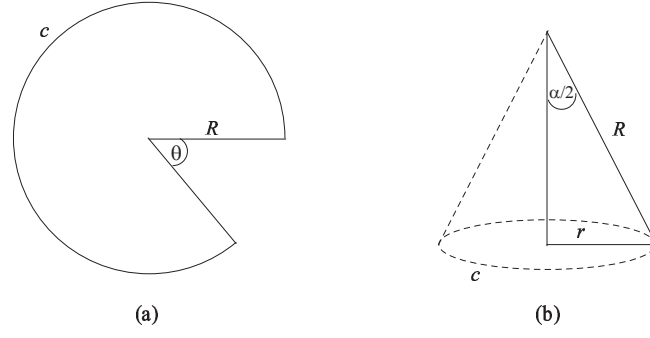


Figure 5.2: (a) Graphene sheet (b) forming the carbon nanocone.

Table 5.1: Relation of number of pentagons  $N_p$  and open angle  $\alpha$  for carbon nanocones.

Number of pentagons ( $N_p$ )	Angle of cone ( $\alpha$ )
0	$180^\circ$
1	$112.90^\circ$
2	$83.60^\circ$
3	$60.00^\circ$
4	$38.90^\circ$
5	$19.20^\circ$
6	$0^\circ$

The quadratic equation in Cartesian coordinates  $(x, y, z)$  for double cones is given by

$$\frac{x^2}{a^2} + \frac{y^2}{b^2} = \frac{z^2}{c^2}, \quad (5.1)$$

where  $a, b$  and  $c$  are constants. Alternatively, in cylindrical coordinates  $(r, \theta, z)$  the equation for the cone can be defined as  $r = z \tan(\alpha/2)$  where  $\alpha$  is the cone angle. The surface integral of the cone is needed to calculate the Lennard-Jones potential energy using in the continuum approach. The surface integral of a single cone is given by

$$\text{Area} = \int_0^h \int_0^{2\pi} r d\theta ds.$$

From Figure 5.3(b), it can be seen that  $ds = dz / \cos(\alpha/2)$  and  $r = z \tan(\alpha/2)$ , therefore, the surface integral is of the form

$$\text{Area} = \frac{\tan(\alpha/2)}{\cos(\alpha/2)} \int_0^h \int_0^{2\pi} z d\theta dz = \frac{a\ell}{h^2} \int_0^h \int_0^{2\pi} z d\theta dz = \pi a\ell,$$

where  $\ell = \sqrt{a^2 + h^2}$ .

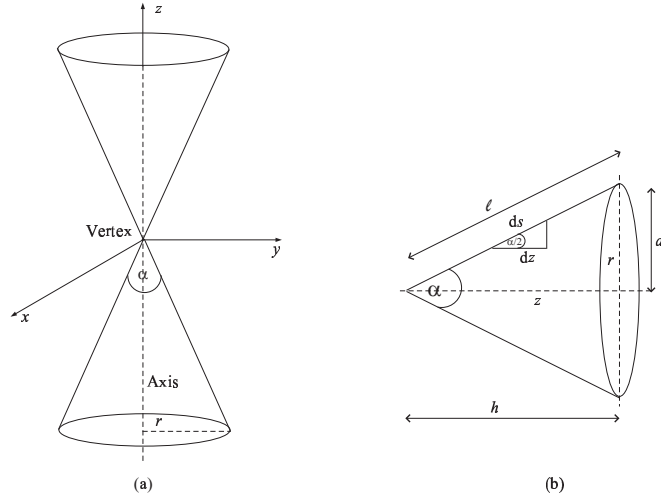


Figure 5.3: (a) Geometry of an elliptical cone and (b) diagram for surface integrations.

## 5.4 Equilibrium locations for carbon nanocones

This section considers the equilibrium locations for any two nested carbon nanocones, utilising the Lennard-Jones potential function and the continuum approach. The case of two identical nanocones is also investigated, and the details of that configuration are presented in the following section.

### 5.4.1 Model formulation for two carbon nanocones

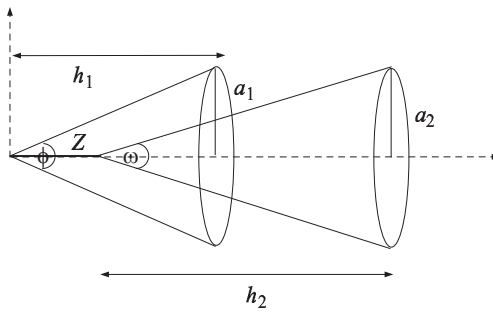


Figure 5.4: Geometry for two distinct carbon nanocones.

With reference to a rectangular Cartesian coordinate system  $(x_1, y_1, z_1)$  with the origin located at the vertex of the left most cone, shown in Figure 5.4, a typical point on its surface has coordinates  $(r_1 \cos \theta_1, r_1 \sin \theta_1, z_1)$ . Similarly, with reference to a rectangular Cartesian coordinate system  $(x_2, y_2, z_2)$  with origin located at the vertex of the second cone, a typical point on its surface has coordinates

$(r_2 \cos \theta_2, r_2 \sin \theta_2, Z + z_2)$  with respect to the coordinate system with origin located at the vertex of first cone, where  $Z$  is the distance between their vertices. The first cone has the open angle  $\phi$  with base radius  $a_1$  and height  $h_1$ , and  $r_1 = \beta z_1$  where  $\beta = \tan(\phi/2)$ . The second cone has the open angle  $\omega$  with base radius  $a_2$  and height  $h_2$ , and  $r_2 = \gamma z_2$  where  $\gamma = \tan(\omega/2)$ . The distance between two typical points on the first and the second cone is then given by

$$\begin{aligned} \rho^2 &= (r_1 \cos \theta_1 - r_2 \cos \theta_2)^2 + (r_1 \sin \theta_1 - r_2 \sin \theta_2)^2 + [z_1 - (Z + z_2)]^2, \\ &= (\beta z_1 \cos \theta_1 - \gamma z_2 \cos \theta_2)^2 + (\beta z_1 \sin \theta_1 - \gamma z_2 \sin \theta_2)^2 + [z_1 - (Z + z_2)]^2, \\ &= (\beta^2 + 1)z_1^2 + (\gamma^2 + 1)z_2^2 - 2z_1 z_2(\beta\gamma + 1) - 2Z(z_1 - z_2) + Z^2 \\ &\quad + 4\beta\gamma z_1 z_2 \sin^2\left(\frac{\theta_1 - \theta_2}{2}\right). \end{aligned}$$

By using the Lennard-Jones potential together with the continuum approximation, the total potential energy is given by

$$\begin{aligned} E^{tot} &= \eta_1 \eta_2 \left( \frac{a_1 a_2 \sqrt{(a_1^2 + h_1^2)(a_2^2 + h_2^2)}}{h_1^2 h_2^2} \right) \times \\ &\quad \times \int_0^{h_2} \int_0^{h_1} \int_0^{2\pi} \int_0^{2\pi} z_1 z_2 \left( -\frac{A}{\rho^6} + \frac{B}{\rho^{12}} \right) d\theta_1 d\theta_2 dz_1 dz_2, \end{aligned}$$

where  $\eta_1$  and  $\eta_2$  are the mean surface densities of the first and the second carbon nanocones, respectively. Further, the integral  $J_n^*$  is defined as

$$J_n^* = \int_0^{2\pi} \int_0^{2\pi} \frac{d\theta_1 d\theta_2}{\rho^n} = \int_0^{2\pi} \int_0^{2\pi} \frac{d\theta_1 d\theta_2}{\{\lambda + \xi \sin^2[(\theta_1 - \theta_2)/2]\}^{n/2}}, \quad (5.2)$$

where  $n = 6$  and  $12$ ,  $\lambda = (\beta^2 + 1)z_1^2 + (\gamma^2 + 1)z_2^2 - 2z_1 z_2(\beta\gamma + 1) - 2Z(z_1 - z_2) + Z^2$  and  $\xi = 4\beta\gamma z_1 z_2$ . In Appendix A.1, it is shown that the integrals  $J_n^*$  can be evaluated either in terms of hypergeometric functions or Legendre functions. In terms of the hypergeometric function, they may be written as

$$\begin{aligned} J_6^* &= \frac{4\pi^2}{(\lambda + \xi)^3} F\left(3, \frac{1}{2}; 1; \frac{\xi}{\lambda + \xi}\right), \\ J_{12}^* &= \frac{4\pi^2}{(\lambda + \xi)^6} F\left(6, \frac{1}{2}; 1; \frac{\xi}{\lambda + \xi}\right). \end{aligned} \quad (5.3)$$

These are both degenerate hypergeometric functions, for which the details are pre-

sented in Appendix E, as such

$$\begin{aligned}
 J_6^* &= \frac{4\pi^2}{\lambda^2 \sqrt{\lambda(\lambda + \xi)}} \left[ 1 - \frac{\xi}{\lambda + \xi} + \frac{3}{8} \left( \frac{\xi}{\lambda + \xi} \right)^2 \right], \\
 J_{12}^* &= \frac{4\pi^2}{\lambda^5 \sqrt{\lambda(\lambda + \xi)}} \left[ 1 - \frac{5}{2} \left( \frac{\xi}{\lambda + \xi} \right) + \frac{15}{4} \left( \frac{\xi}{\lambda + \xi} \right)^2 - \frac{25}{8} \left( \frac{\xi}{\lambda + \xi} \right)^3 \right. \\
 &\quad \left. + \frac{175}{128} \left( \frac{\xi}{\lambda + \xi} \right)^4 - \frac{63}{256} \left( \frac{\xi}{\lambda + \xi} \right)^5 \right].
 \end{aligned} \tag{5.4}$$

Then the total potential energy becomes

$$E^{tot} = \eta_1 \eta_2 \left( \frac{a_1 a_2 \sqrt{(a_1^2 + h_1^2)(a_2^2 + h_2^2)}}{h_1^2 h_2^2} \right) \int_0^{h_2} \int_0^{h_1} z_1 z_2 (-A J_6^* + B J_{12}^*) dz_1 dz_2. \tag{5.5}$$

However, for the final solution for  $E^{tot}$ , equation (5.5) must be integrated with respect to  $z_1$  and  $z_2$ , which may be readily evaluated using the algebraic computer package MAPLE.

#### 5.4.2 Model formulation for identical carbon nanocones

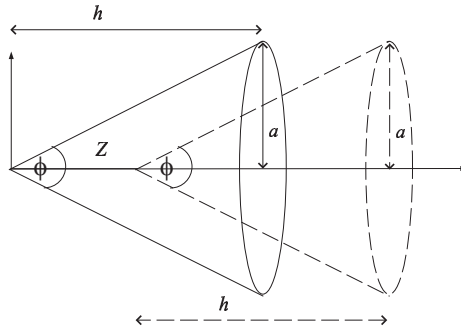


Figure 5.5: Geometry for two identical carbon nanocones.

For this particular case, the two identical carbon nanocones, as shown in Figure 5.5, which the distance between their vertices denoted by  $Z$ , are considered. They both have the cone angle  $\phi$  which corresponds to base radius  $a$  and height  $h$ . The relations between  $r$  and  $z$  for both cones are given by  $r_1 = \beta z_1$  and  $r_2 = \beta z_2$ , respectively, where  $\beta = \tan(\phi/2) = a/h$ . In cylindrical polar coordinates  $(r, \theta, z)$ , the parametric equations for the first and the second cone can be written as  $(r_1 \cos \theta_1, r_1 \sin \theta_1, z_1)$  and  $(r_2 \cos \theta_2, r_2 \sin \theta_2, Z + z_2)$ , respectively. Then

the distance between two typical points on each cone is given by

$$\begin{aligned}
 \rho^2 &= (r_1 \cos \theta_1 - r_2 \cos \theta_2)^2 + (r_1 \sin \theta_1 - r_2 \sin \theta_2)^2 + [z_1 - (Z + z_2)]^2, \\
 &= (\beta z_1 \cos \theta_1 - \beta z_2 \cos \theta_2)^2 + (\beta z_1 \sin \theta_1 - \beta z_2 \sin \theta_2)^2 + [z_1 - (Z + z_2)]^2, \\
 &= (\beta^2 + 1)(z_1 - z_2)^2 - 2Z(z_1 - z_2) + Z^2 + 4\beta^2 z_1 z_2 \sin^2[(\theta_1 - \theta_2)/2].
 \end{aligned}$$

Therefore, the total potential energy can be written as

$$E^{tot} = \eta_\sigma^2 \left( \frac{a^4}{h^4} + \frac{a^2}{h^2} \right) \int_0^h \int_0^h \int_0^{2\pi} \int_0^{2\pi} z_1 z_2 \left( -\frac{A}{\rho^6} + \frac{B}{\rho^{12}} \right) d\theta_1 d\theta_2 dz_1 dz_2,$$

where  $\eta_\sigma$  is the mean surface density of a carbon nanocone. The integral  $J_n^*$  defined by (5.2) must be evaluated, where in this case  $\lambda = (\beta^2 + 1)(z_1 - z_2)^2 - 2Z(z_1 - z_2) + Z^2$  and  $\xi = 4\beta^2 z_1 z_2$ . By precisely the same method as used previously, it may be deduced that

$$E^{tot} = \eta_\sigma^2 \left( \frac{a^4}{h^4} + \frac{a^2}{h^2} \right) \int_0^h \int_0^h z_1 z_2 (-AJ_6^* + BJ_{12}^*) dz_1 dz_2,$$

which is also evaluated numerically to obtain the final solution for  $E^{tot}$ .

### 5.4.3 Numerical solutions

The potential energies for two carbon nanocones of the five possible structures are examined. Using the algebraic computer package MAPLE, the relation between the potential energy and the distance between vertices  $Z$  is depicted. Due to the lack of the Lennard-Jones constants, namely the attractive constant  $A$  and repulsive constant  $B$  specifically for carbon nanocones, the Lennard-Jones constants for graphene sheet are employed. Following the work of Girifalco [42],  $A = 15.2 \text{ eV}\text{\AA}^6$  and  $B = 24.1 \times 10^3 \text{ eV}\text{\AA}^{12}$  are obtained. We comment that the two parameters  $A$  and  $B$  have only minor effect on the numerical results. The values of  $a$  and  $h$  are given by  $a = \ell \sin(\alpha/2) = 3m\sigma \sin(\alpha/2)/2$  and  $h = \ell \cos(\alpha/2) = 3m\sigma \cos(\alpha/2)/2$ , where  $\sigma$  is a carbon-carbon bond length which is taken to be  $\sigma = 1.42 \text{ \AA}$  and  $m$  is a positive integer indicating the size of the carbon nanocone. For the analysis presented here,  $m$  is chosen to be 50.

The potential energies for system of the two carbon nanocones are shown in Figure 5.6 - 5.8. For the combination of the cone containing one pentagon, the equilibrium distance for the other four cones is approximately  $3 \text{ \AA}$  between their

vertices, illustrated in Figure 5.6, and the most stable equilibrium occurs for the cone  $N_p = 2$ . The equilibrium distance increases and the system has less stability as the number of pentagons increases, as shown in Figure 5.7. Of particular interest, for two identical carbon nanocones the increased number of carbon atoms at the vertex causes the equilibrium distance between their vertices to increase, as demonstrated in Figure 5.8. Values for the distances between their vertices  $Z$  at the equilibrium configuration for any two carbon nanocones is given in Table 5.2.

The shortest equilibrium distance between the two cones is denoted by  $x$  as illustrated in Figure 5.9, and values of  $x$  are shown in Table 5.3. For the two identical carbon nanocones, a value of 3.4 Å is obtained which is also the inter-spacing distance for two graphene sheets. Otherwise, values of approximately 2.6 Å are found, which less than the equilibrium spacing for two graphene sheets. This discrepancy is due to the fact that the two surfaces are not parallel. By observation,  $x$  increases as the number of pentagons increases.

Table 5.2: Distance between vertices  $Z$  at the equilibrium position for any two carbon nanocones.

$N_p$ of inner cone $N_p$ of outer cone	1	2	3	4	5
1	4.0955	3.0787	3.1238	3.1440	3.1591
2	-	5.1136	3.8643	3.9320	3.9597
3	-	-	6.8717	5.1959	5.2788
4	-	-	-	10.3052	7.8713
5	-	-	-	-	20.5229

Table 5.3: Shortest distance  $x$  between the two cones at the equilibrium position for any two carbon nanocones.

$N_p$ of inner cone $N_p$ of outer cone	1	2	3	4	5
1	3.4132	2.5658	2.6034	2.6202	2.6328
2	-	3.4084	2.5757	2.6208	2.6393
3	-	-	3.4358	2.5980	2.6394
4	-	-	-	3.4315	2.6210
5	-	-	-	-	3.4226

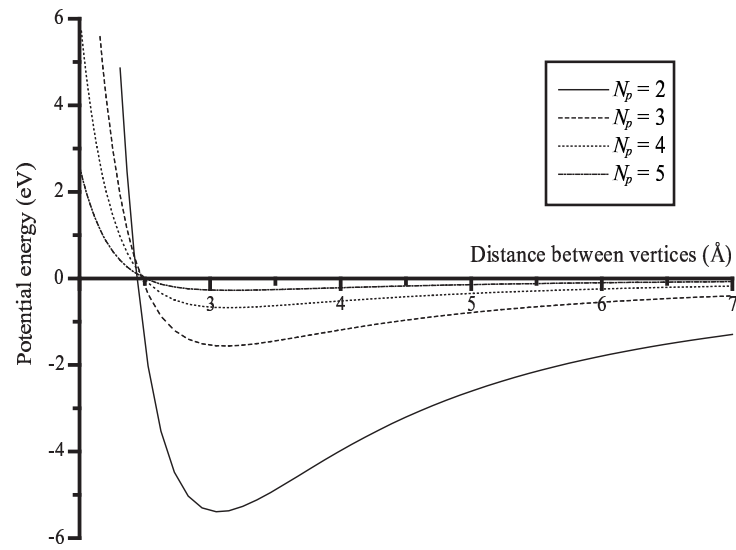


Figure 5.6: Variation of potential energy versus distance between vertices for the cone  $N_p = 1$  and  $N_p = 2, 3, 4$  and 5 for the second cone.

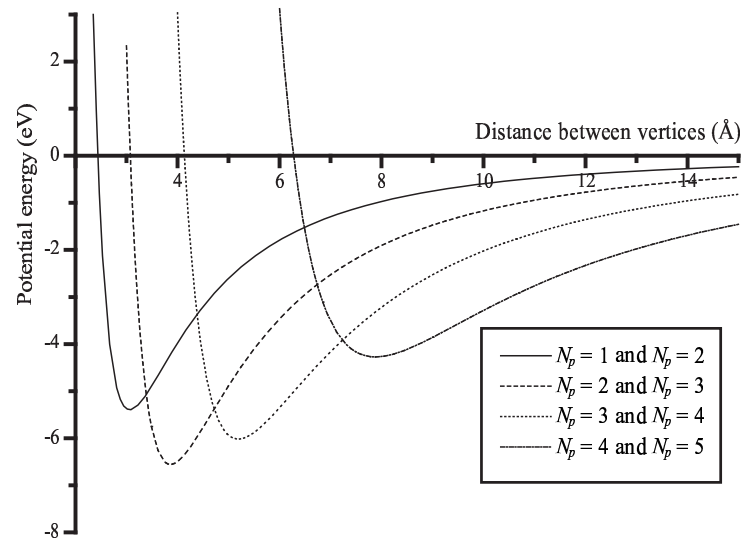


Figure 5.7: Variation of potential energy versus distance between vertices for various combinations of two different cones.

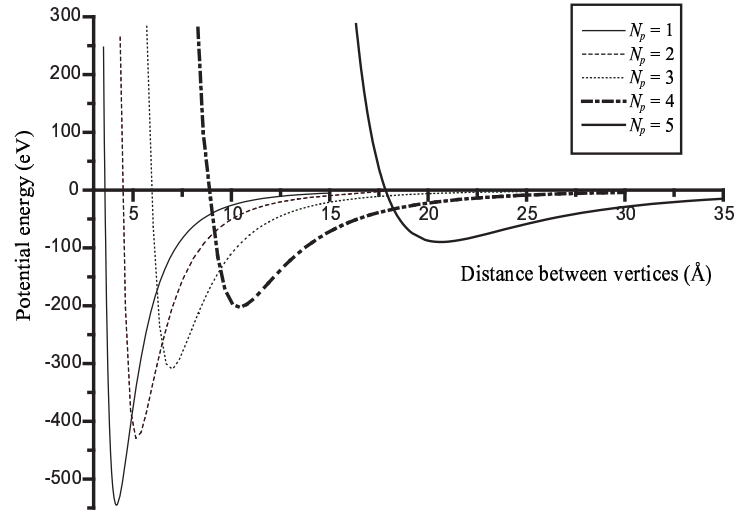


Figure 5.8: Variation of potential energy versus distance between vertices for five identical carbon nanocones.

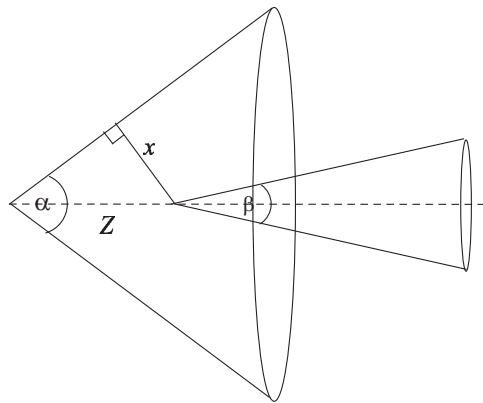


Figure 5.9: Shortest distance  $x$  between two carbon nanocones at the equilibrium location.



## 5.5 Suction behaviour for a carbon nanocone

The corresponding suction properties for a carbon nanocone entering a single-walled carbon nanotube are investigated. For the cone to be sucked into the tube, the total work which is obtained by moving from  $-\infty$  to  $\infty$  needs to be greater than zero. For convenience, two specific models are determined according to whether the direction of the cone vertex is in the positive or negative direction of the  $z$ -axis.

### 5.5.1 Cone vertex oriented in negative $z$ -direction

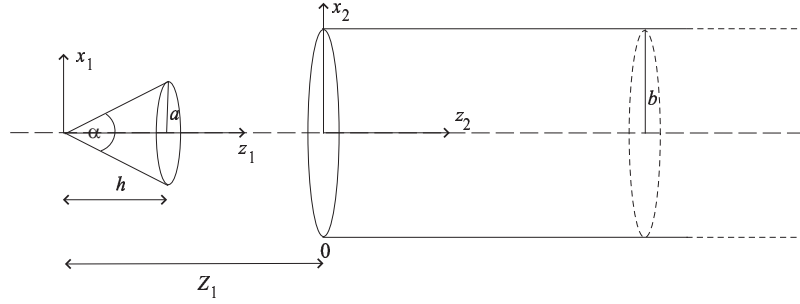


Figure 5.10: Geometry of carbon nanocone with vertex oriented in negative  $z$ -direction.

In this section, the vertex of the carbon nanocone is assumed to point in the negative  $z$ -direction and the cone and the tube are assumed to be co-axial, as shown in Figure 5.10. With reference to a rectangular Cartesian coordinate system  $(x_1, y_1, z_1)$  with the origin located at the tube edge, a typical point on the nanocone surface has coordinates  $(r_1 \cos \theta_1, r_1 \sin \theta_1, z_1 - Z_1)$ , where  $Z_1$  is the distance between the vertex and the tube end. The cone has vertex angle  $\alpha$  with base radius  $a$  and height  $h$ , and  $r_1 = \beta z_1$  where  $\beta = \tan(\alpha/2) = a/h$ . Similarly, with reference to a rectangular Cartesian coordinate system  $(x_2, y_2, z_2)$  with origin located at the tube end, a typical point on the tube surface has coordinates  $(b \cos \theta_2, b \sin \theta_2, z_2)$ . The tube is assumed to be semi-infinite in length and of radius  $b$ . The distance between two typical points on the cone and the tube is given by

$$\begin{aligned} \rho^2 &= (r_1 \cos \theta_1 - b \cos \theta_2)^2 + (r_1 \sin \theta_1 - b \sin \theta_2)^2 + [(z_1 - Z_1) - z_2]^2, \\ &= (\beta z_1 - b)^2 + (z_1 - Z_1 - z_2)^2 + 4\beta b z_1 \sin^2[(\theta_1 - \theta_2)/2]. \end{aligned}$$

By using the Lennard-Jones potential together with the continuum approximation, the total potential energy is given by

$$E^{tot} = \eta_\sigma \eta_g ab \frac{\sqrt{a^2 + h^2}}{h^2} \int_0^\infty \int_0^h \int_0^{2\pi} \int_0^{2\pi} z_1 \left( -\frac{A}{\rho^6} + \frac{B}{\rho^{12}} \right) d\theta_1 d\theta_2 dz_1 dz_2, \quad (5.6)$$

where  $\eta_\sigma$  and  $\eta_g$  are mean surface densities of the carbon nanocone and the carbon nanotube, respectively. The constants  $A$  and  $B$  are the attractive and repulsive Lennard-Jones constants, respectively. The known numerical values for the attractive constant  $A$  and the repulsive constant  $B$  for graphene sheet are employed to the present system, following the work of Girifalco [42], thus  $A = 15.2 \text{ eV}\text{\AA}^6$  and  $B = 24.1 \times 10^3 \text{ eV}\text{\AA}^{12}$ . Further, the integral  $J_n^*$  defined by (5.2) needs to be determined, and in this case  $\lambda = (\beta z_1 - b)^2 + (z_1 - Z_1 - z_2)^2$  and  $\xi = 4\beta b z_1$ . In Appendix A.1, the evaluation of  $J_n^*$  is presented which can be obtained either in terms of hypergeometric functions or Legendre functions. In terms of the hypergeometric function, it can be deduced to give rise to equation (5.3) which can be further deduced to obtain the degenerate hypergeometric functions shown in (5.4). Then the total potential energy becomes

$$E^{tot} = \eta_\sigma \eta_g ab \frac{\sqrt{a^2 + h^2}}{h^2} \int_0^\infty \int_0^h z_1 (-AJ_6^* + BJ_{12}^*) dz_1 dz_2. \quad (5.7)$$

However, to evaluate  $E^{tot}$  equation (5.7) must be integrated with respect to  $z_1$  and  $z_2$  which is performed numerically. Although clearly complicated, numerical values for these integrals may be readily evaluated using the algebraic computer package MAPLE. The solution for  $F_Z^{tot}$  is also calculated numerically by the relation presented in (2.8).

The suction energy and the interatomic van der Waals force for the suction behaviour of a carbon nanocone entering a single-walled carbon nanotube are examined. A larger van der Waals force experienced by a cone when it is outside the tube (negative  $z$ ) than when it is inside the tube (positive  $z$ ) is observed and shown in Figure 5.11. This is because the first interacting part is between the tube and the cone base which has the inter-spacing distance around  $3.4 \text{ \AA}$  and it gives rise to the maximum force. At this point, the entire cone is outside the tube, therefore the greater force occurs outside the tube. The area under the graph in Figure 5.11 represents the work done by the van der Waals force or suction energy and this area

must be positive for the cone to enter the tube.

The suction energy for various radii of the carbon nanotube  $b$  is shown in Figure 5.12. The suction energy is positive when  $(b-a) > 2.49 \text{ \AA}$  for a cone with  $N_p = 1$  and  $(b-a) > 2.54 \text{ \AA}$  for a cone with  $N_p = 5$ . The maximum suction energy values occur at  $(b-a) = 3.00 \text{ \AA}$  and  $(b-a) = 3.05 \text{ \AA}$  for  $N_p = 1$  and  $N_p = 5$ , respectively. Noting that for the other three possible structures of carbon nanocones, the tube begins to suck the cone inside for  $2.49 \text{ \AA} < (b-a) < 2.54 \text{ \AA}$  and the maximum suction energies occur for  $3.00 \text{ \AA} < (b-a) < 3.05 \text{ \AA}$ . The differences in the radii are noted to be less than  $3.4 \text{ \AA}$ , which is the inter-spacing distance between two graphene sheets [36], due to the fact that the two surfaces are not parallel.

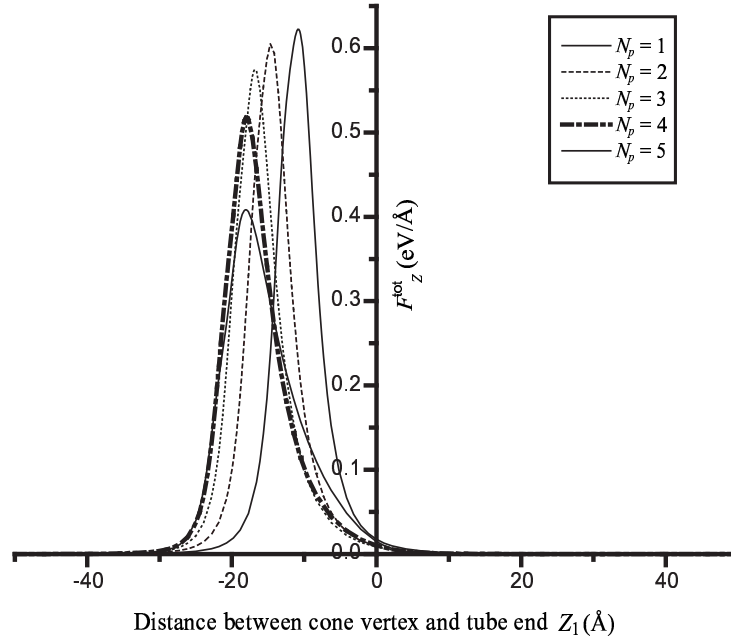


Figure 5.11: Force experienced by a co-axial carbon nanocone with a semi-infinite carbon nanotube for cone vertex in negative  $z$ -direction ( $b-a = 3.4 \text{ \AA}$ ).

### 5.5.2 Cone vertex oriented in positive $z$ -direction

Here the cone vertex is assumed to be oriented in the positive  $z$ -direction and the axis of the cone and that of the tube are co-axial, as shown in Figure 5.13. Similarly, a typical point on the surface of the cone has coordinates  $(r_1 \cos \theta_1, r_1 \sin \theta_1, -z_1 - Z_1)$ , where  $Z_1$  is the distance between the vertex and the tube end. As mentioned in the previous subsection, the cone has vertex angle  $\alpha$  with base radius  $a$  and height  $h$ , but here  $r_1 = -\beta z_1$  where  $\beta = \tan(\alpha/2) = a/h$ . A typical point on the tube surface has

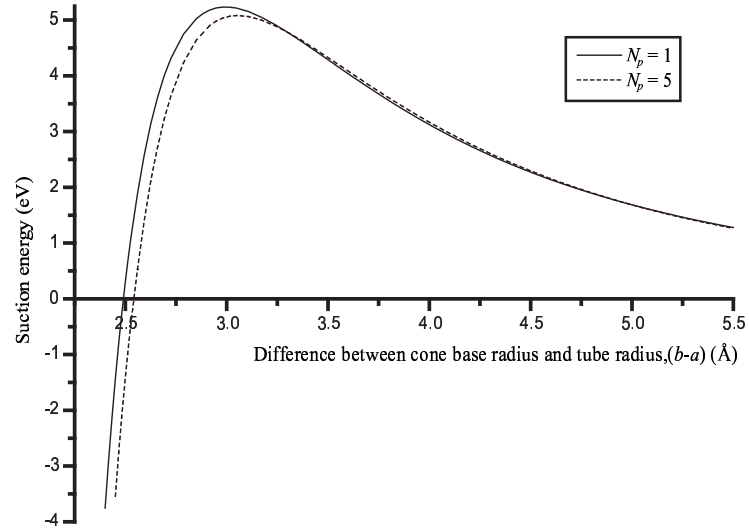


Figure 5.12: Suction energy for co-axial carbon nanocones  $N_p = 1$  and  $N_p = 5$  entering a single-walled carbon nanotube versus the difference of the radii  $(b - a)$ .

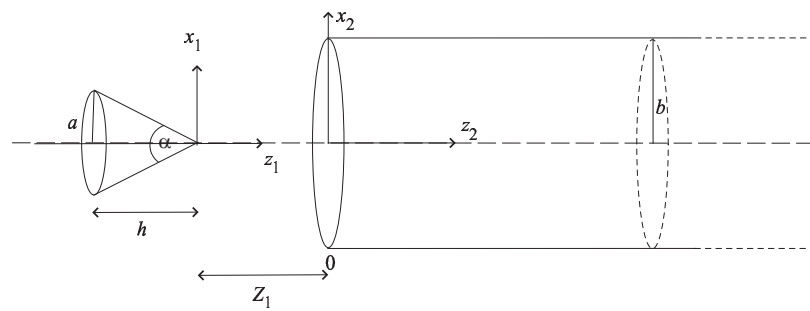


Figure 5.13: Geometry of carbon nanocone with vertex oriented in positive  $z$ -direction.

coordinates  $(b \cos \theta_2, b \sin \theta_2, z_2)$  and again the tube is assumed to be semi-infinite in length and of radius  $b$ . The distance between two typical points on the cone and the tube is given by

$$\begin{aligned}\rho^2 &= (r_1 \cos \theta_1 - b \cos \theta_2)^2 + (r_1 \sin \theta_1 - b \sin \theta_2)^2 + [(-z_1 - Z_1) - z_2]^2, \\ &= (\beta z_1 + b)^2 + (z_1 + Z_1 + z_2)^2 - 4\beta b z_1 \sin^2[(\theta_1 - \theta_2)/2].\end{aligned}$$

Therefore, the total potential energy can be written as (5.6). The integral  $J_n^*$  in (5.2) needs to be evaluated, but in this case  $\lambda = (\beta z_1 + b)^2 + (z_1 + Z_1 + z_2)^2$  and  $\xi = -4\beta b z_1$ . By precisely the same method as used previously, (5.7) is also evaluated numerically to obtain the final solution of  $E^{tot}$  and  $F_Z^{tot}$ .

The same behaviour and the same values for the suction energy in terms of the difference between the cone base radius and the tube radius are observed as in §5.5.1. However, they differ in terms of the force experienced by the carbon nanocone. In this case, the force experienced by the carbon nanocone when the cone is inside the tube (positive  $z$ ) is greater than that when the cone is outside the tube (negative  $z$ ) as shown in Figure 5.14. This is because the entire cone has to enter into the tube to reach the maximum van der Waals force when the tube interacting with the cone base.

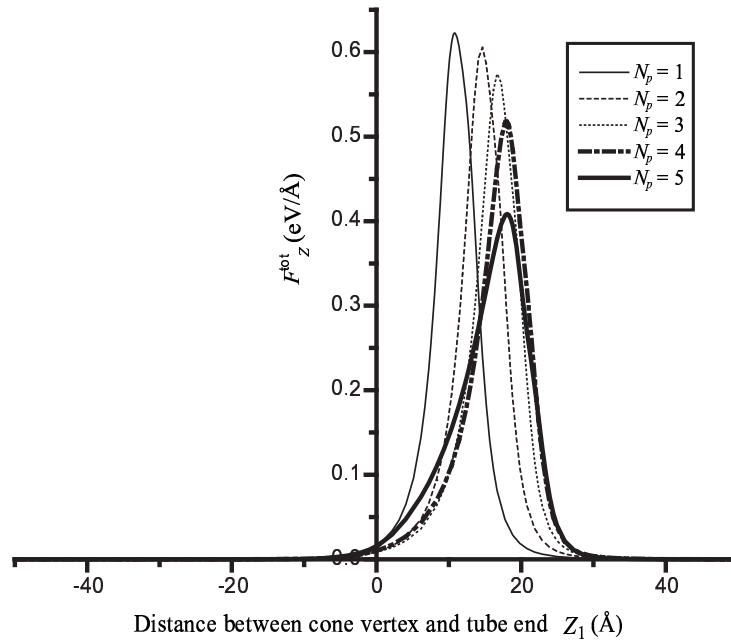


Figure 5.14: Force experienced by co-axial carbon nanocone with semi-infinite carbon nanotube for cone vertex in positive  $z$ -direction ( $b - a = 3.4 \text{ \AA}$ ).

## 5.6 Oscillatory behaviour for carbon nanocone

In order to accurately model the dynamics of the gigahertz oscillator, the force experienced by the carbon nanocone oscillating inside the single-walled carbon nanotube needs to be accurately estimated. The Lennard-Jones potential function together with the usual continuum approximation is utilised to calculate the van der Waals force. In this study, the frictional force is assumed to be negligible, and Newton's second law is employed to determine the oscillatory behaviour.

### 5.6.1 Force distribution for a carbon nanocone oscillating inside a carbon nanotube

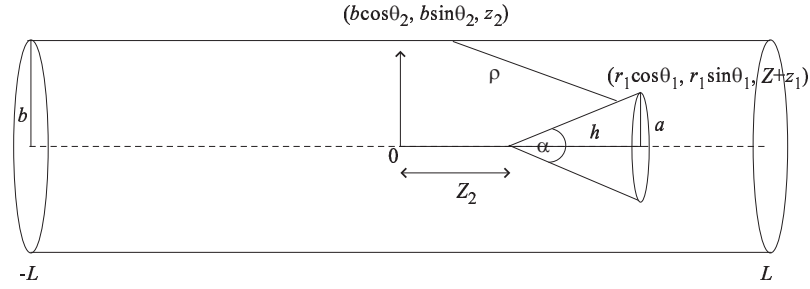


Figure 5.15: Geometry for carbon nanocone oscillating inside single-walled carbon nanotube.

From the result in §5.5, only the case when the cone vertex is in the negative  $z$ -direction is considered. With reference to a rectangular Cartesian coordinate system  $(x_1, y_1, z_1)$  with the origin located at the vertex of the carbon nanocone, a typical point on the surface of the carbon nanocone has coordinates  $(r_1 \cos \theta_1, r_1 \sin \theta_1, Z_2 + z_1)$ , where  $Z_2$  is the distance between the vertex of the cone and the centre of the tube. Similarly, with reference to a rectangular Cartesian coordinate system  $(x_2, y_2, z_2)$  with origin located at the centre of the tube, a typical point on the tube surface has coordinates  $(b \cos \theta_2, b \sin \theta_2, z_2)$ , where  $b$  is the assumed radius of the  $2L$  length tube, as shown in Figure 5.15. The distance  $\rho$  between two typical points is given by

$$\begin{aligned} \rho^2 &= (r_1 \cos \theta_1 - b \cos \theta_2)^2 + (r_1 \sin \theta_1 - b \sin \theta_2)^2 + [(Z_2 + z_1) - z_2]^2, \\ &= (\beta z_1 - b)^2 + (Z_2 + z_1 - z_2)^2 + 4\beta b z_1 \sin^2[(\theta_1 - \theta_2)/2]. \end{aligned}$$

Using the Lennard-Jones potential function with the usual continuum approach, the total potential energy for the system is given by

$$E^{tot} = \eta_\sigma \eta_g ab \frac{\sqrt{a^2 + h^2}}{h^2} \int_{-L}^L \int_0^h \int_0^{2\pi} \int_0^{2\pi} z_1 \left( -\frac{A}{\rho^6} + \frac{B}{\rho^{12}} \right) d\theta_1 d\theta_2 dz_1 dz_2,$$

where  $\eta_\sigma$  and  $\eta_g$  are the mean surface densities of the carbon nanocone and the carbon nanotube, respectively. The integral  $J_n^*$ , which is given by (5.2) needs to be determined, but in this case  $\lambda = (\beta z_1 - b)^2 + (Z_2 + z_1 - z_2)^2$  and  $\xi = 4\beta b z_1$ . By precisely the same method as used previously, it can be deduced

$$E^{tot} = \eta_\sigma \eta_g ab \frac{\sqrt{a^2 + h^2}}{h^2} \int_{-L}^L \int_0^h z_1 (-AJ_6^* + BJ_{12}^*) dz_1 dz_2,$$

and the force distribution may be obtained numerically by the relation (2.8).

By using the algebraic computer package MAPLE, the potential energy and the force distribution for the carbon nanocone oscillating inside the single-walled carbon nanotube are shown in Figure 5.16 and Figure 5.17, respectively. The potential energy can be modelled by use of the rectangular function  $E_{max}[H(Z_2 + L + h) - H(Z_2 - L - h)]$  where  $H(x)$  is a Heaviside step function. In terms of the force distribution, the force is very close to zero everywhere except at both ends of the tube where there are pulse-like forces which tend to attract the cone back towards the centre of the tube. As both  $a$  and  $b$  tend to zero in such a way that  $a < b \ll L$ ,  $F_{Z_2}^{tot}$  can be estimated using the Dirac delta functions, and can be written as

$$F_{Z_2}^{tot} = E_{max}[\delta(Z_2 + L + h) - \delta(Z_2 - L - h)], \quad (5.8)$$

where  $E_{max}$  is the energy of the cone which is defined by

$$E_{max} = \int_{-\infty}^0 F_{Z_2}^{tot} dZ_2 = - \int_0^{\infty} F_{Z_2}^{tot} dZ_2.$$

### 5.6.2 Oscillation of a carbon nanocone inside a carbon nanotube

In this subsection, Newton's second law is applied to describe the oscillatory behaviour of a carbon nanocone oscillating inside a single-walled carbon nanotube. The frictional forces is assumed negligible, which may be justified for certain chiralities and diameters of the tube [2]. From Newton's second law on neglecting friction,

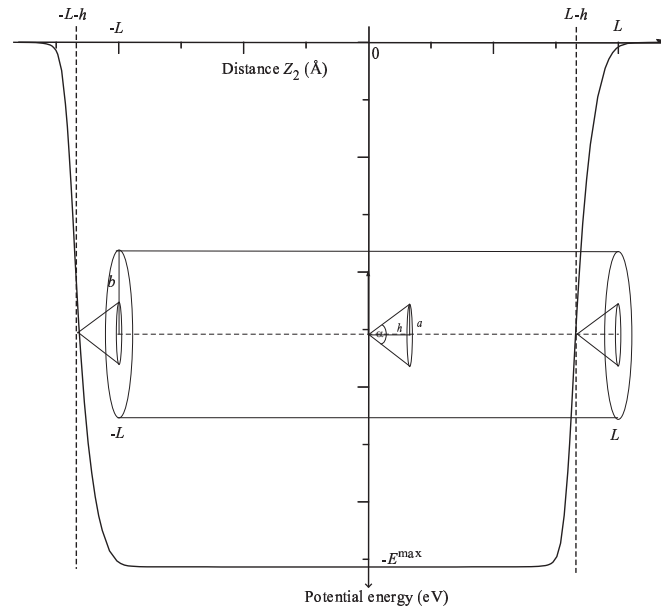


Figure 5.16: Potential energy for cone oscillating inside tube.

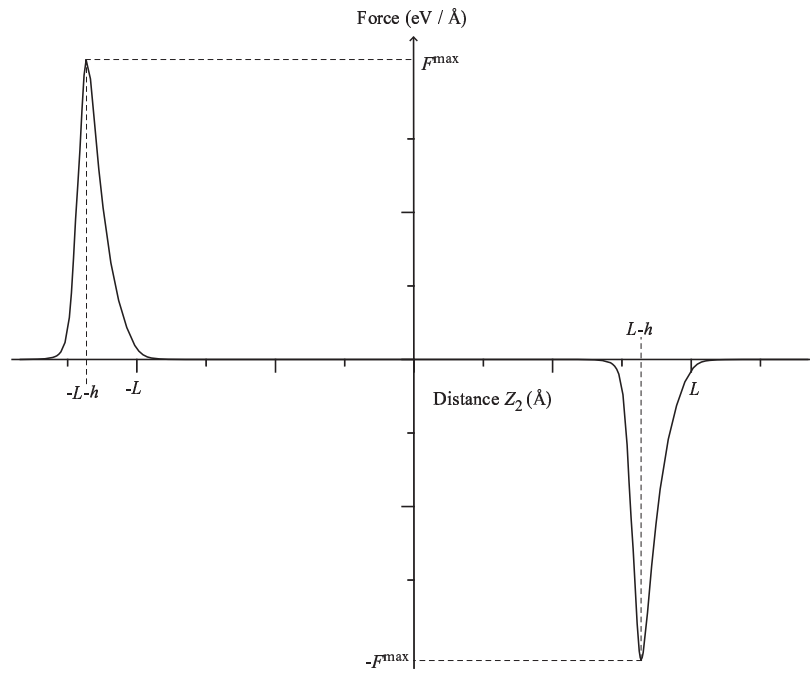


Figure 5.17: Force distribution for cone oscillating inside tube.



it can be deduced

$$M \frac{d^2 Z_2}{dt^2} = F_{Z_2}^{tot}(Z_2),$$

where  $Z_2$  is the distance between the vertex of the cone and the centre of the tube and  $M$  is the mass of the cone. The force distribution of the system can be approximated by two Dirac delta functions, as indicated in Figure 5.17, and from (5.8), it can be written as

$$M \frac{d^2 Z_2}{dt^2} = E_{max} [\delta(Z_2 + L + h) - \delta(Z_2 - L + h)]. \quad (5.9)$$

By multiplying both sides of (5.9) by  $dZ_2/dt$  and using the fact that  $dH(x)/dx = \delta(x)$ , equation (5.9) becomes

$$M \frac{d^2 Z_2}{dt^2} \frac{dZ_2}{dt} = E_{max} \frac{d}{dZ_2} [H(Z_2 + L + h) - H(Z_2 - L + h)] \frac{dZ_2}{dt}. \quad (5.10)$$

By integrating both sides of (5.10) with respect to  $t$  and since  $H(Z_2 + L + h) - H(Z_2 - L + h) = 1$  for  $-L - h \leq Z_2 \leq L - h$  and zero elsewhere, it may be deduced

$$\frac{M}{2} \left( \frac{dZ_2}{dt} \right)^2 = E_{max} + \frac{M}{2} v_0^2,$$

where  $v_0$  is the assumed initial velocity of the nanocone. This equation implies that the carbon nanocone travels inside the carbon nanotube at a constant speed  $dZ_2/dt = v = (2E_{max}/M + v_0^2)^{1/2}$  and therefore, the frequency is given by  $f = v/4L$ .

On assuming that the cone base radius  $a$  is 3.4 Å smaller than the tube radius  $b$ , which is the inter-spacing distance between two graphene sheets [36], the relation between the frequency and the length of the tube is shown. For a difference in the radii of more than 2.5 Å (see §5.5) a prescribed initial velocity  $v_0$  is not necessary, since a carbon nanocone which is initially at rest outside the carbon nanotube will be sucked into the tube due to the attractive force. The frequencies obtained are in the gigahertz range, which are 15 - 90 GHz, for the half-length of the tube between 100 - 300 Å for the five investigated structures of carbon nanocones. From the graph in Figure 5.18, a shorter tube provides a higher frequency, which is in accordance with the observations made by Liu *et al.* [59] for the oscillation of a C<sub>60</sub> fullerene inside a single-walled carbon nanotube. This is because of a decrease in the distance for the cone to travel between the tube ends. Moreover, the smaller the cone, the higher the frequency. Note that the word smaller cone is used to indicate the number

of carbon atoms, which depend on the disclination number of the pentagons, and a cone with five pentagons is the smallest cone of the five possible structures. The smaller cone has the lighter weight which increases the velocity and therefore results in a higher frequency. This result is also in agreement with the observation made by Zheng and Jiang [4] for multi-walled carbon nanotube oscillators.

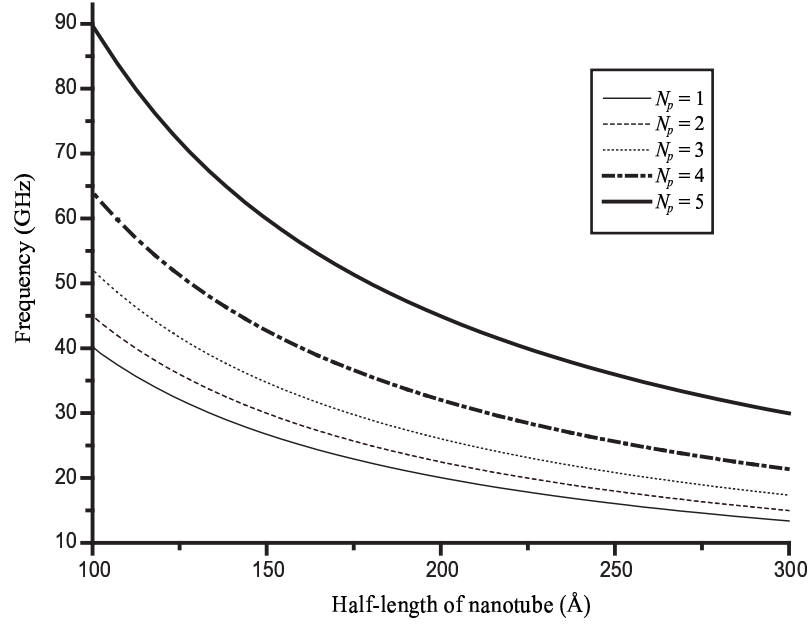


Figure 5.18: Variation of oscillatory frequency for five possible structures of carbon nanocones with respect to half-length of carbon nanotube.

## 5.7 Boron nitride nanocones

Boron nitride is a good semiconducting compound, and the large band gap in this material may produce better electronic properties than those of carbon structures [34]. There are two crystal structures for boron nitride, the cubic and the hexagonal structures, but only the hexagonal boron nitride, which is comparable to a carbon graphene sheet [33], is considered here

For carbon nanocones, there are five possible structures depending on the number of pentagons which are needed to close the vertex [9]. The five cone angles  $\alpha$  can be obtained from  $\sin(\alpha/2) = 1 - N_p/6$  where  $N_p$  is the number of pentagons. For boron nitride cones, Bourgeois *et al.* [85] investigate the conical structure of boron nitride using transmission electron microscopy and they measure their angles using an electron diffraction technique. From an analysis of the diffraction patterns,

they observe a layer of nanocones and propose two possible models, which are the monolayer boron nitride cones one inside the other and cones formed from helical overlapping sheets. Moreover, they find that an angle of  $84^\circ$  occurs at the apex because of a stable square ring at the vertex. Bourgeois *et al.* [86] also observe two other conical structures with apex angles of  $19.2^\circ$  and  $38.9^\circ$ , arising from  $300^\circ$  and  $240^\circ$  disclinations, respectively. They suggest that these two configurations arise because of the different stiffness in the chemical bonds of boron nitride compounds, and square rings which are the favoured ring defects in boron nitride. Furthermore, Han *et al.* [87] study conical nanotubes using high-resolution transmission electron microscopy and electron energy loss spectroscopy, and suggest that nested cones occur with the same apex angle as for boron nitride. Xu *et al.* [88] successfully synthesise conical helices of graphitic boron nitride and they examine theoretically their elastic properties. These structures hold considerable promise for potential applications in new-generation high performance composite materials.

The Lennard-Jones potential function is utilised by Lee [89] who determines gigahertz frequencies for boron nitride oscillators and finds that the frequencies generated by the boron nitride nanotubes are higher than those generated by the corresponding carbon nanotubes. Lee [89] also examines hybrid carbon-boron nitride nanotube oscillators by applying a well known mixing rule for the Lennard-Jones parameters.

In this study, equilibrium structures for two nested nanocones comprising either boron nitride or carbon-boron nitride are examined, again using the Lennard-Jones potential function and the continuum approximation. The analytical expressions obtained in the previous two sections are exploited and numerical results are determined for the equilibrium distance  $Z$  between two vertices and the perpendicular distance  $x$  between the inner cone vertex and the surface of the outer cone, as shown in Figure 5.19. For the hybrid carbon-boron nitride nanocones, the same numerical results are obtained irrespective of which cone is inside the other.

### 5.7.1 Model formation for boron nitride cones

In §5.4, the Lennard-Jones potential function and the continuum approximation are utilised to determine the energetically most favourable structures for nested

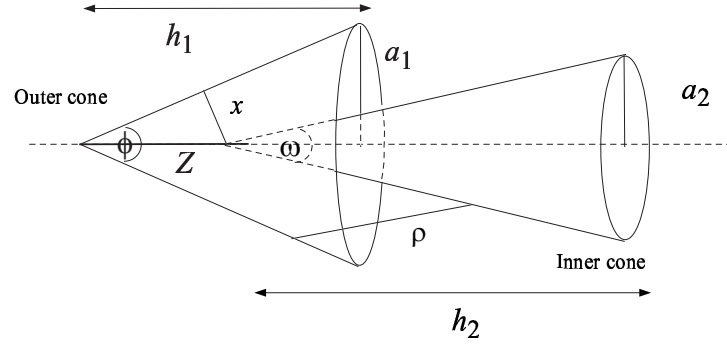


Figure 5.19: Geometry for any two nested nanocones.

cones. Here the results for both boron nitride and carbon-boron nitride cones are examined. Using the continuum approximation, the total potential energy of the system is obtained by performing double cone surface integrals. Two Lennard-Jones parameters, the well depth  $\epsilon = A^2/(4B)$  and the van der Waals diameter  $\sigma = (B/A)^{1/6}$ , for carbon, boron and nitrogen atoms are taken from Lee [89] and shown in Table 5.4 where  $A$  is the attractive constant and  $B$  is the repulsive constant. Note that the constants for boron nitride and carbon-boron nitride systems are obtained from the mixing rules which are given by  $\epsilon_{12} = \sqrt{\epsilon_1 \epsilon_2}$  and  $\sigma_{12} = (\sigma_1 + \sigma_2)/2$  [90].

Table 5.4: Lennard-Jones constants for boron nitride and carbon-boron nitride systems.

Interaction	$\epsilon$ (eV)	$\sigma$ (Å)	$A$ (Å <sup>-6</sup> )	$B$ (Å <sup>-12</sup> )
C - C	0.002635	3.369	15.412	22534.750
B - B	0.004116	3.453	27.907	47303.611
N - N	0.006281	3.365	36.475	52955.321
C - B	0.003293	3.411	20.748	32678.989
C - N	0.004068	3.367	23.710	34544.753
B - N	0.005085	3.410	31.921	50099.811
C - BN	0.003660	3.390	22.203	33668.474

Two cones, which do not necessarily have the same vertex angle, are assumed to be located co-axially, the distance between their vertices is denoted by  $Z$  and the perpendicular distance from the vertex of the inner cone to the surface of the outer cone at the equilibrium location is denoted by  $x$ , as illustrated in Figure 5.19. The outer cone has the apex angle  $\phi$  with base radius  $a_1$  and height  $h_1$ ,

and  $r_1 = \beta z_1$  where  $\beta = \tan(\phi/2)$ . The inner cone has the vertex angle  $\omega$  with base radius  $a_2$  and height  $h_2$ , and  $r_2 = \gamma z_2$  where  $\gamma = \tan(\omega/2)$ . With reference to a rectangular Cartesian coordinate system  $(x_1, y_1, z_1)$  with origin located at the vertex of the outer cone, a typical point on the outer cone surface has coordinates  $(r_1 \cos \theta_1, r_1 \sin \theta_1, z_1)$ . Similarly, with reference to the same rectangular Cartesian coordinate system  $(x_2, y_2, z_2)$ , a typical point on the inner cone surface has coordinates  $(r_2 \cos \theta_2, r_2 \sin \theta_2, Z + z_2)$ . The distance between two typical points on the outer and the inner cones is then given by  $\rho^2 = (\beta^2 + 1)z_1^2 + (\gamma^2 + 1)z_2^2 - 2z_1z_2(\beta\gamma + 1) - 2Z(z_1 - z_2) + Z^2 + 4\beta\gamma z_1z_2 \sin^2[(\theta_1 - \theta_2)/2]$ , and the total Lennard-Jones potential energy can be written as

$$E^{tot} = \eta_1 \eta_2 \left( \frac{a_1 a_2 \sqrt{(a_1^2 + h_1^2)(a_2^2 + h_2^2)}}{h_1^2 h_2^2} \right) \times \int_0^{h_2} \int_0^{h_1} \int_0^{2\pi} \int_0^{2\pi} z_1 z_2 \left( -\frac{A}{\rho^6} + \frac{B}{\rho^{12}} \right) d\theta_1 d\theta_2 dz_1 dz_2, \quad (5.11)$$

where  $\eta_1$  and  $\eta_2$  denote mean atomic surface densities of the outer and the inner cones, respectively. Analytical expressions for the  $\theta_1$  and  $\theta_2$  integrals can be evaluated either in terms of hypergeometric functions or Legendre functions, and the details of these calculations are referred to in §5.4. Again, the integrations with respect to  $z_1$  and  $z_2$  need to be performed numerically using the algebraic computer package MAPLE.

We note that for the total interaction energy between two carbon nanocones, the energy is simply obtained using (5.11) where  $A = A_{C-C}$ ,  $B = B_{C-C}$ , as given in Table 5.4. However, for the case of the interaction between two boron nitride cones, there are three different interactions which are B-B, N-N and B-N interactions, so that the total interaction energy can be obtained as

$$E^{tot} = \frac{\eta_1}{2} \frac{\eta_2}{2} E^*(A_{B-B}, B_{B-B}) + \frac{\eta_1}{2} \frac{\eta_2}{2} E^*(A_{N-N}, B_{N-N}) + 2 \frac{\eta_1}{2} \frac{\eta_2}{2} E^*(A_{B-N}, B_{B-N}), \quad (5.12)$$

where  $E^*(A, B)$  is defined by  $E^* = E^{tot}/(\eta_1 \eta_2)$  and  $E^{tot}$  is given in (5.11). Similarly, for the case of the interaction between carbon - boron nitride cones, there are two different interactions which are C-B and C-N interactions, so that the total interaction energy can be obtained as

$$E^{tot} = \eta_g \frac{\eta_1}{2} E^*(A_{C-B}, B_{C-B}) + \eta_g \frac{\eta_1}{2} E^*(A_{C-N}, B_{C-N}). \quad (5.13)$$

We comment that using (5.12) and (5.13) with different values of the constants  $A$  and  $B$  as shown in Table 5.4 results only in a minor effect on the numerical values for the total interaction energy. In other words, we may determine the total interaction energy of the system using (5.11) where  $A = A_{\text{B-N}}$  and  $B = B_{\text{B-N}}$  for the interaction between two boron nitride cones, and  $A = A_{\text{C-BN}}$  and  $B = B_{\text{C-BN}}$  for the interaction between carbon - boron nitride cones. In this thesis, we employ the later method to determine the interaction energy of the nanocone systems.

### 5.7.2 Numerical results for boron nitride cones

Following the work of Bourgeois *et al.* [85, 86], the apex angles  $\alpha$  assumed for the three different boron nitride cones which tend to occur in practice are  $19.2^\circ$ ,  $38.9^\circ$  and  $83.6^\circ$ . The height  $h$  is assumed to be  $50 \text{ \AA}$  which corresponds to base radii of  $8.338$ ,  $16.649$  and  $33.327 \text{ \AA}$ , respectively, which are determined from  $a = h \tan(\alpha/2)$ . Numerical values for the equilibrium distance  $Z$  between the two vertices and the perpendicular distance  $x$  at the equilibrium location between the vertex of the inner cone and the surface of the outer cone for any two of the above three boron nitride cones are presented in Table 5.5. Moreover, the other two vertex angles for boron nitride cones corresponding to the equivalent carbon nanocones are also considered and shown in Table 5.5. Corresponding values for any of the five possible carbon-boron nitride cones are shown in Table 5.6. For the carbon-boron nitride cones, the numerical results essentially depend on the outer cone angle and they indicate that the same results are obtained irrespective of which cone is inside the other.

For two identical cones, the equilibrium distance  $Z$  decreases with increasing cone angle, which is due to the repulsive force arising from the vertices. The interspacing distance  $x$  is found to be approximately  $3.4 \text{ \AA}$ , which is in excellent agreement with Bourgeois *et al.* [86] for nested cones. Furthermore, the equilibrium distance  $Z$  decreases for the case when the inner cone angle is smaller than that of the outer cone. This is because the inner cone can move closer to the outer vertex for the distance  $x$  to attain the value  $3.4 \text{ \AA}$ . In this case, the perpendicular distance  $x$  which is illustrated in Figure 5.19 is the shortest distance between the inner vertex and the outer wall. Consequently, the equilibrium distance  $Z$  is increased when the inner cone angle is larger than that of the outer cone, and the distance  $x$  between the

Table 5.5: Equilibrium distance  $Z$  (Å) between two vertices and the perpendicular distance  $x$  (Å) for boron nitride cones.

Outer angels Inner angles		19.2°	38.9°	60.0°	83.6°	112.9°
19.2°	$Z$	20.317	8.324	5.901	4.746	4.143
	$x$	3.388	2.772	2.951	3.163	3.453
38.9°	$Z$	34.378	10.708	5.823	4.718	4.097
	$x$	5.733	3.566	2.912	3.145	3.414
60.0°	$Z$	39.926	23.363	7.586	4.646	4.051
	$x$	6.658	7.780	3.793	3.097	3.376
83.6°	$Z$	42.800	30.344	17.873	6.146	3.995
	$x$	7.138	10.104	8.937	4.097	3.329
112.9°	$Z$	44.603	34.625	24.619	14.672	5.320
	$x$	7.438	11.530	12.310	9.779	4.434

Table 5.6: Equilibrium distance  $Z$  (Å) between two vertices and the perpendicular distance  $x$  (Å) for carbon-boron nitride cones.

Outer angels Inner angles		19.2°	38.9°	60.0°	83.6°	112.9°
19.2°	$Z$	20.188	8.278	5.863	4.732	4.101
	$x$	3.367	2.756	2.936	3.154	3.418
38.9°	$Z$	34.321	10.667	5.754	4.685	4.070
	$x$	5.724	3.552	2.877	3.123	3.392
60.0°	$Z$	39.873	23.316	7.554	4.630	4.025
	$x$	6.650	7.764	3.777	3.086	3.354
83.6°	$Z$	42.772	30.316	17.835	6.099	3.962
	$x$	7.133	10.095	8.918	4.065	3.302
112.9°	$Z$	44.560	34.598	24.592	14.642	5.282
	$x$	7.431	11.521	12.296	9.759	4.402

inner vertex and the outer wall is actually the greatest distance between the two surfaces.

The relation between the cone angles and the distance  $Z$  for boron nitride nanocones is shown in Figure 5.20 - 5.22. For two identical boron nitride cones at the equilibrium location, the system is observed to be more stable for the larger apex angle. This is because the large apex angle reduces the repulsive force arising from the vertex. In the case when the outer cone has a larger apex angle than the inner cone, the stability of the system also increases for increasing inner cone angle. On the other hand, the system is less stable at the equilibrium location if the outer cone angle is smaller than the inner cone. This indicates that nested cones are less likely to occur when the vertex angle of the outer cone is smaller than that of the inner cone. Also note that the energy profiles for the carbon-boron nitride nanocones are similar to those for boron nitride nanocones.

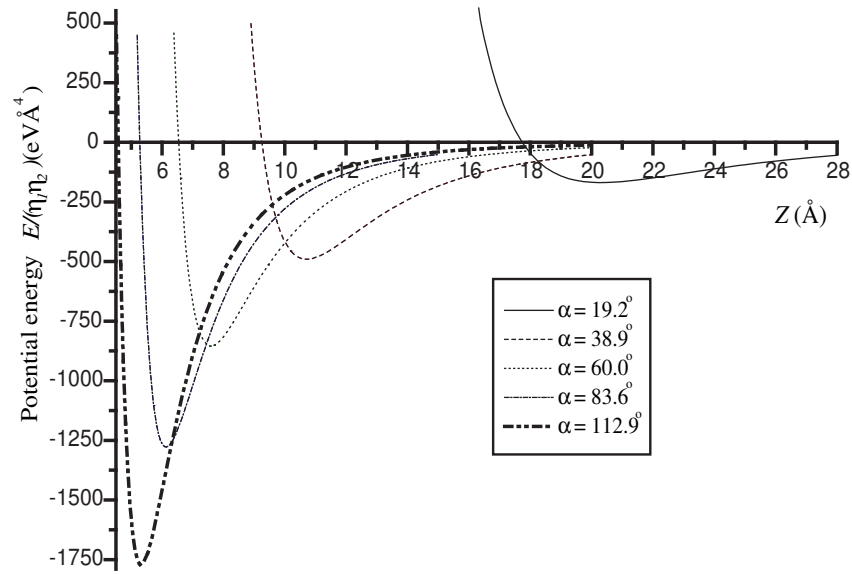


Figure 5.20: Potential energy versus the distance  $Z$  between two vertices for five identical possible boron nitride nanocones.



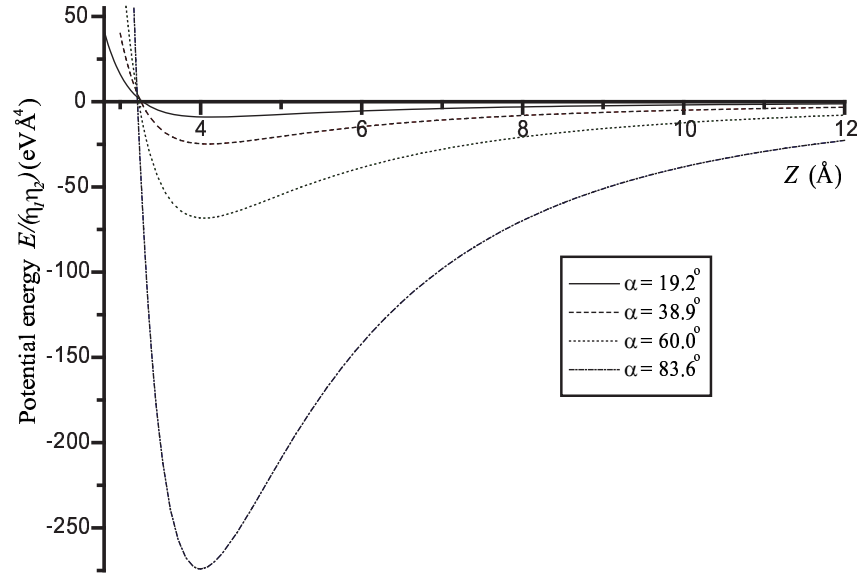


Figure 5.21: Potential energy versus the distance  $Z$  between two vertices for boron nitride cones when the outer cone angle  $\alpha = 112.9^\circ$  and the inner cone angles  $\alpha = 19.2^\circ, 38.9^\circ, 60.0^\circ$  and  $83.6^\circ$ .

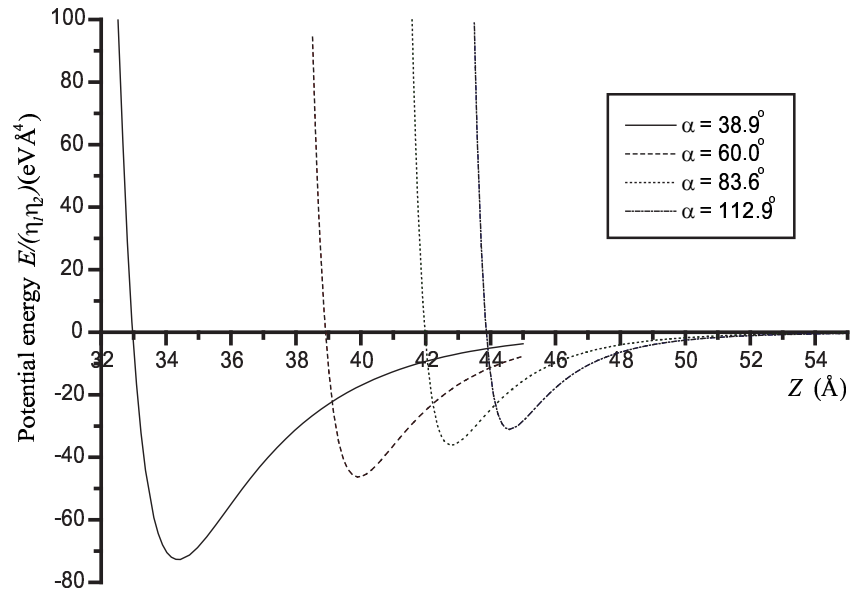


Figure 5.22: Potential energy versus the distance  $Z$  between two vertices for boron nitride cones when the outer cone angle  $\alpha = 19.2^\circ$  and the inner cone angles  $\alpha = 38.9^\circ, 60.0^\circ, 83.6^\circ$  and  $112.9^\circ$ .

## 5.8 Summary

This chapter considers three related problems of system of nanocones, which are (i) the potential energy for two carbon, two boron nitride and carbon-boron nitride nanocones for both cases of identical and non-identical cones, (ii) the suction energy for a carbon nanocone entering a carbon nanotube and (iii) the frequency of oscillation of a carbon nanocone moving co-axially within the interior of a carbon nanotube. Two types of nanocones, carbon and boron nitride, are investigated using the Lennard-Jones potential energy and the continuum approximation. Due to the lack of specific data for carbon nanocones, the known Lennard-Jones constants determined for plane sheets of carbon-carbon atoms are employed, and the mixing rule is used for the boron nitride cones.

In terms of carbon nanocones, the value  $3 \text{ \AA}$  for the distance between the two vertices at the equilibrium position for the system of two identical single-pentagon cones is obtained, and if this cone is paired with the other four possible cones this distance increases with decreasing cone angle or increasing number of pentagons. Moreover, in the case of two identical carbon nanocones, the equilibrium position moves away from the vertex as the cone angle is reduced. However, the equilibrium location is always inside the cone, hence nested double-cones from any two possible combinations of carbon nanocones might be constructed. For both boron nitride and carbon-boron nitride nanocones, all five possible vertex angles which occur for carbon nanocones are also examined. The interspacing between two monolayer cones is obtained to be approximately  $3.4 \text{ \AA}$  for both systems, and this result is in excellent agreement with the finding of Bourgeois *et al.* [86]. Furthermore, the equilibrium location always occurs with one cone inside the other, so that nested double-cones might also be expected to form in practice.

In terms of the suction behaviour, since the van der Waals force only operates at relatively short distances, a semi-infinite tube is used to model the open end of the carbon nanotube. The carbon cone is assumed initially at rest outside of the tube. The cone is sucked into the tube when the cone base radius and the tube radius differ by  $2.49 \text{ \AA}$  to  $2.54 \text{ \AA}$  for the cones which consist of one to five pentagons, and this is irrespective of the direction of the vertex. The maximum suction energy occurs when the radii differ by  $3.00 \text{ \AA}$  to  $3.05 \text{ \AA}$ .

The oscillatory behaviour is then examined, assuming that the carbon nanocone is located co-axially and that it is sucked into the tube by van der Waals forces alone. The potential energy can be assumed to be approximated by rectangular functions, and the corresponding force distribution can be approximated by two Dirac delta functions. The strong attractive forces at the ends of the tube ensure that the cone remains inside, so that it becomes an oscillator. Newton's second law neglecting the frictional force is employed to determine the frequency of the system. The frequencies obtained are in the gigahertz range, 15 to 90 GHz, for various values of the tube length, and are the same order of magnitude as for an oscillating co-axial carbon nanotubes. Moreover, the shorter the tube and the smaller the cone, the higher the frequency.

# Chapter 6

## Carbon onions

Experimentally, a wide variety of different shapes are obtained, including both spherical and spheroidal carbon onions. A spheroid is an ellipsoid with two equal axes and the term onion refers to a multi-layered composite structure. Assuming structures of either concentric spherical or ellipsoidal fullerenes comprising  $n$  layers, this study examines the interaction energy between adjacent shells for both spherical and spheroidal carbon onions. The Lennard-Jones potential together with the continuum approximation is employed to determine the equilibrium spacing between two adjacent shells. Analytical formulae for the potential energy, which may be expressed either in terms of hypergeometric or Legendre functions, are determined. The equilibrium spacing between shells is found to decrease for shells further out from the inner core owing to the decreasing curvature of the outer shells of a concentric structure.

### 6.1 Nomenclature

$\Phi$	is the van der Waals potential function
$\eta_1, \eta_2$	are the mean atomic number densities for the two surfaces
$\rho$	is the distance between two typical surface elements
$\sigma$	is the carbon-carbon covalent bond length
$A, B$	are the Lennard-Jones attractive and repulsive coefficients, respectively
$E^{tot}$	is the total interaction potential
$Z$	is the interspacing between two adjacent layers of carbon onion

## 6.2 Introduction

The special properties of nanostructures have not only led to proposals for many potential nano-devices [4, 5, 30] but also to the desire to create new carbon nanostructures, and the spherical and ellipsoidal carbon onions are examples of such structures. Carbon onions comprise multi-layer composite structures and here those of both spherical and spheroidal shapes are considered, note that a spheroid is simply an ellipsoid with two axes of equal length. Experimentally, electron beam irradiation methods are used to modify the multi-layers of carbon onions, but at present there are no procedures to predict the precise shape of the resulting structures. The major issue in this regard is the determination of the interspacing layer of such structures. Recently, molecular dynamics simulation techniques have been used to examine the formation of such nanostructures. This calculation may be performed using density functional theory and a tight binding method such as that described in [91] and [92]. However, rather than undertake such large scale calculations, elementary mechanical principles and classical mathematical modelling are employed here to investigate the interaction energies between adjacent shells of spherical and spheroidal carbon onions, which leads to the determination of the equilibrium spacings of such structures.

While there are a number of studies on spherical carbon onions [46, 47, 93], very little work has been undertaken for other forms of carbon onions. Kitahara *et al.* [94] employ an electron beam irradiation technique to experimentally create ellipsoidal carbon onions and they also investigate the stability of these structures by using molecular mechanics and molecular orbital calculations. Narita *et al.* [95] also utilise electron beam irradiation methods to produce tetrahedral carbon onions, and they determine their energy levels and the density of different states.

For spherical and spheroidal carbon onions, this chapter utilises the Lennard-Jones potential together with the continuum approximation to determine the potential energy between two adjacent layers. From the energy minimisation of the structure, this method can be used to predict the spacings between adjacent layers, and therefore the lateral and vertical dimensions for each layer of spherical and ellipsoidal carbon onions. Using curve fitting techniques, an expression for the equilibrium spacing for any two neighbouring layers of the carbon onions are obtained

and shown in §6.4. Finally, a summary of the results is given in §6.5.

### 6.3 Interaction energies between shells

Here the interaction energy between two adjacent shells of an ellipsoidal (or spherical) carbon onion is considered. The ellipsoidal carbon onion is assumed to comprise a family of concentric nested spheroidal fullerenes located co-axially, as shown in Figure 6.1.

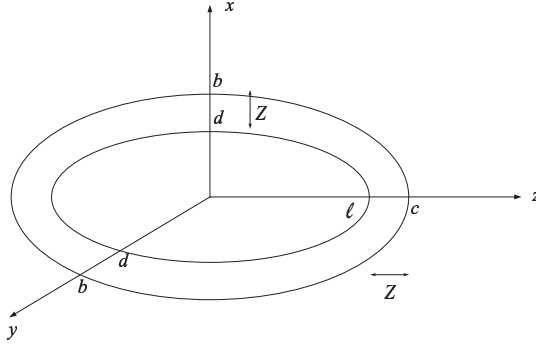


Figure 6.1: Double-shell ellipsoidal carbon onion

From Figure 6.1, with reference to the rectangular Cartesian coordinate system the parametric equations for the outer and inner spheroids are given by

$$(x_1, y_1, z_1) = (b \sin \phi_1 \cos \theta_1, b \sin \phi_1 \sin \theta_1, c \cos \phi_1),$$

and

$$(x_2, y_2, z_2) = (d \sin \phi_2 \cos \theta_2, d \sin \phi_2 \sin \theta_2, \ell \cos \phi_2),$$

respectively, where  $\theta_1, \theta_2 \in [0, 2\pi]$  and  $\phi_1, \phi_2 \in [0, \pi]$ . If the interspacing along the three coordinate axes between two neighbouring shells of the carbon onion is assumed to be given by  $Z$ , then it may be deduced  $\ell = c - Z$  and  $d = b - Z$ . The distance  $\rho$  between two typical surface elements on the inner and the outer spheroids is given by

$$\begin{aligned} \rho^2 &= (b \sin \phi_1 \cos \theta_1 - d \sin \phi_2 \cos \theta_2)^2 + (b \sin \phi_1 \sin \theta_1 - d \sin \phi_2 \sin \theta_2)^2 \\ &\quad + (c \cos \phi_1 - \ell \cos \phi_2)^2 \\ &= (b \sin \phi_1 - d \sin \phi_2)^2 + 4bd \sin \phi_1 \sin \phi_2 \sin^2[(\theta_1 - \theta_2)/2] + (c \cos \phi_1 - \ell \cos \phi_2)^2. \end{aligned}$$

For the continuum approach, the atoms are assumed to be uniformly distributed over the surface of the molecule, and a constant average atomic density which is simply the number of atoms divided by the surface area of the molecule is utilised. Thus, the total potential energy  $E^{tot}$  for the two molecules can be obtained by performing the surface integrals of a potential function over the two molecules, namely

$$E^{tot} = \eta_1 \eta_2 \int \int \Phi(\rho) d\Sigma_1 d\Sigma_2, \quad (6.1)$$

where  $\eta_1$  and  $\eta_2$  denote the mean surface densities of the outer and inner ellipsoidal fullerenes and  $\rho$  is the distance between the two surface elements  $\Sigma_1$  and  $\Sigma_2$  on the outer and inner spheroidal fullerenes, which are given respectively by

$$\begin{aligned} \Sigma_1 &= b \sin \phi_1 \sqrt{b^2 \cos^2 \phi_1 + c^2 \sin^2 \phi_1} d\theta_1 d\phi_1, \\ \Sigma_2 &= d \sin \phi_2 \sqrt{d^2 \cos^2 \phi_2 + \ell^2 \sin^2 \phi_2} d\theta_2 d\phi_2, \end{aligned}$$

and the integration is performed over the entire surface of the two ellipsoids. Further,  $\Phi(\rho)$  denotes the interatomic interaction potential for two typical single atoms located one on each ellipsoid and here the classical six-twelve Lennard-Jones potential is again adopted, so that the interaction energy (6.1) between shells of the ellipsoidal carbon onion takes the form

$$E^{tot} = \eta_1 \eta_2 \int_0^\pi \int_0^\pi \int_0^{2\pi} \int_0^{2\pi} \gamma \left( -\frac{A}{\rho^6} + \frac{B}{\rho^{12}} \right) d\theta_1 d\theta_2 d\phi_1 d\phi_2,$$

where  $\gamma = bd \sin \phi_1 \sin \phi_2 \sqrt{(b^2 \cos^2 \phi_1 + c^2 \sin^2 \phi_1)(d^2 \cos^2 \phi_2 + \ell^2 \sin^2 \phi_2)}$ . Further, the integrals  $J_n^*$  are defined as

$$J_n^* = \int_0^{2\pi} \int_0^{2\pi} \frac{d\theta_1 d\theta_2}{\rho^n} = \int_0^{2\pi} \int_0^{2\pi} \frac{d\theta_1 d\theta_2}{\{\lambda + \xi \sin^2[(\theta_1 - \theta_2)/2]\}^{n/2}},$$

where  $n = 6$  and  $12$ ,  $\lambda = (b \sin \phi_1 - d \sin \phi_2)^2 + (c \cos \phi_1 - \ell \cos \phi_2)^2$  and  $\xi = 4bd \sin \phi_1 \sin \phi_2$ . Note that none of the terms in  $\gamma$ ,  $\lambda$  and  $\xi$  depend on  $\theta_1$  or  $\theta_2$ . In Appendix A.1, the integrals  $J_n^*$  are evaluated either in terms of hypergeometric functions or Legendre functions. In terms of the hypergeometric function, it may

be deduced

$$J_6^* = \frac{4\pi^2}{(\lambda + \xi)^3} F\left(3, \frac{1}{2}; 1; \frac{\xi}{\lambda + \xi}\right),$$

$$J_{12}^* = \frac{4\pi^2}{(\lambda + \xi)^6} F\left(6, \frac{1}{2}; 1; \frac{\xi}{\lambda + \xi}\right).$$

Since these equations are degenerate hypergeometric functions (see Appendix E), they can be written as

$$J_6^* = \frac{4\pi^2}{\lambda^2 \sqrt{\lambda(\lambda + \xi)}} \left[ 1 - \frac{\xi}{\lambda + \xi} + \frac{3}{8} \left( \frac{\xi}{\lambda + \xi} \right)^2 \right],$$

$$J_{12}^* = \frac{4\pi^2}{\lambda^5 \sqrt{\lambda(\lambda + \xi)}} \left[ 1 - \frac{5}{2} \left( \frac{\xi}{\lambda + \xi} \right) + \frac{15}{4} \left( \frac{\xi}{\lambda + \xi} \right)^2 - \frac{25}{8} \left( \frac{\xi}{\lambda + \xi} \right)^3 \right. \\ \left. + \frac{175}{128} \left( \frac{\xi}{\lambda + \xi} \right)^4 - \frac{63}{256} \left( \frac{\xi}{\lambda + \xi} \right)^5 \right].$$

Thus, the total potential energy becomes

$$E^{tot} = \eta_1 \eta_2 \int_0^\pi \int_0^\pi \gamma(-AJ_6^* + BJ_{12}^*) d\phi_1 d\phi_2. \quad (6.2)$$

To obtain the final result for  $E^{tot}$ , the integral of (6.2) needs to be evaluated with respect to  $\phi_1$  and  $\phi_2$ , and these integrals are performed numerically. Although clearly complicated, numerical values for these integrals can be readily evaluated using the algebraic computer package MAPLE.

For the special case of the spherical carbon onion for which all three major axes are equal,  $d = \ell$  for the core and  $b = c$  for the outer shell. In this case, the interaction energy between shells can be obtained explicitly, and is given by

$$E_o = -P_6 + P_{12}, \quad (6.3)$$

where  $P_n$  ( $n = 6, 12$ ) are defined by

$$P_n = \frac{8\pi^2 b d C_n \eta_1 \eta_2}{(2 - n)} \left( \frac{1}{(b + d)^{n-2}} - \frac{1}{(b - d)^{n-2}} \right),$$

where  $C_6 = A$ ,  $C_{12} = B$  and again  $\eta_1$  and  $\eta_2$  represent the surface densities of carbon atoms on the outer and inner spherical fullerenes, respectively. The derivation of  $P_n$  can be found in Appendix C.



## 6.4 Numerical results

The algebraic computer package MAPLE is used to show graphically the relation between the potential energy and the interspacing between two neighbouring shells for spherical and ellipsoidal carbon onions. The attractive and repulsive constants  $A$  and  $B$  for graphitic carbon interactions are taken to be  $A = 17.4 \text{ eV}\text{\AA}^6$  and  $B = 29 \times 10^3 \text{ eV}\text{\AA}^{12}$  [36]. Due to the short range interaction of the van der Waals force, the interactions between adjacent layers is only taken into account for the calculation of the resultant potential energy [41].

For the spherical carbon onion, the 1st-shell, or the core, is assumed to be the spherical  $C_{60}$  fullerene, which has a radius of  $3.55 \text{ \AA}$ . This is consistent with experimental results, where the core of a fully formed spherical carbon onion has the diameter of  $7\text{-}10 \text{ \AA}$  [60]. From (6.3), upon substituting  $d = 3.55$ ,  $b$  is the radius of the 2nd-shell, which is the critical value for which the energy  $E_o/(\eta_1\eta_2)$  is minimum. Repeatedly, by using the radius of the  $(n - 1)$ th-shell as the value of  $d$  in (6.3), the radius of the  $n$ th-shell,  $b$ , is determined by minimising  $E_o/(\eta_1\eta_2)$ . Following this procedure, the radius for each shell of an eight-layer spherical carbon onion is obtained, as shown in Table 6.1. These values are the critical radii shown in Figure 6.2 for each shell. The spherical carbon onion comprising shells with radii shown in Table 6.1 are approximately the structure proposed by Kroto and McKay [96] which is the  $C_{60}@C_{240}@C_{540}@C_{960}@C_{1500}@...@C_N$  spherical carbon onion, where  $N$  is the number of carbon atoms in Goldberg fullerenes of  $I_h$  symmetry type I, given by  $N = 60n^2$  where  $n$  is an integer [27]. The average radii of  $C_N$  are referred to Table 6.2, which are taken from Itoh *et al.* [97] for  $C_{240}$ ,  $C_{540}$ ,  $C_{960}$ ,  $C_{2160}$  and  $C_{3840}$  and from Dunlap and Zope [98] for  $C_{1500}$ . For Goldberg fullerenes of  $I_h$  symmetry type I, the average radius is approximated by  $\bar{R} \approx 2.4\bar{\sigma}n$ , where  $\bar{\sigma}$  is the average bond length [47]. Using  $\bar{\sigma} = 1.421 \text{ \AA}$  and  $n = 7$ , the average radius of  $C_{2940}$  is obtained, as shown in Table 6.2.

Table 6.1: Radius of each shell for a spherical carbon onion predicted from minimisation of the energy  $E_o/(\eta_1\eta_2)$  (6.3) and assuming a  $C_{60}$  core.

$n$ th-shell	$C_{60}$	2nd	3rd	4th	5th	6th	7th	8th
Radius ( $\text{\AA}$ )	3.55	7.042	10.516	13.981	17.442	20.900	24.356	27.811

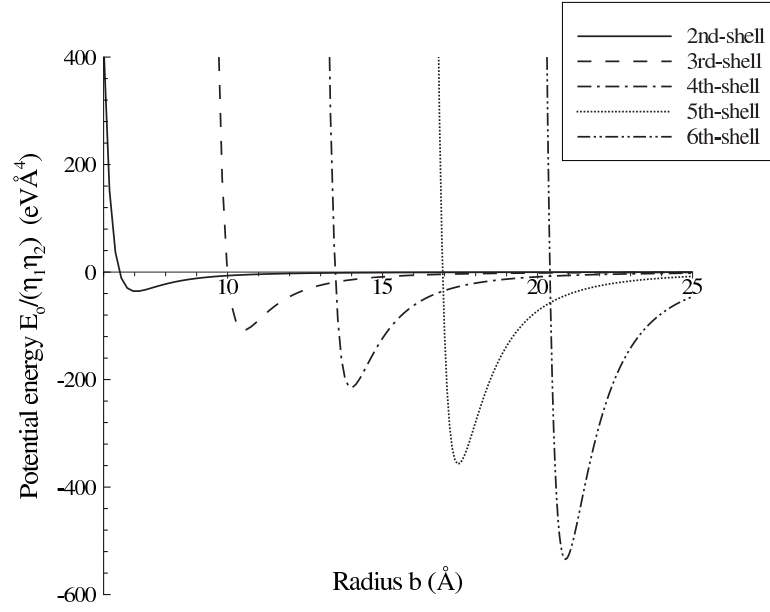


Figure 6.2: Potential energy profile for a spherical carbon onion showing the possible radii of the  $n$ th-shell for which the energy is minimum.

Table 6.2: Radii of spherical fullerenes  $C_N$ .

Fullerene	$C_{240}$	$C_{540}$	$C_{960}$	$C_{1500}$	$C_{2160}$	$C_{2940}$	$C_{3840}$
Radius (Å)	7.06	10.53	14.02	17.5225	20.95	23.8728	27.95

For spheroidal carbon onions, two cases are considered using  $C_{24}$  [93] and  $C_{80}$  [94] as the core. From (6.2) with the substitution  $c = \ell + Z$  and  $b = d + Z$ , the equilibrium distance  $Z$  between two adjacent layers may be obtained from minimisation of the energy  $E^{tot}/(\eta_1\eta_2)$ . Using a  $C_{80}$  ellipsoidal fullerene which has a lateral size  $\ell = 4.73$  Å and a vertical size  $d = 3.58$  Å [93] as the inner core, from (6.2) the equilibrium distance  $Z_{12}$  is determined which is the critical value shown in Figure 6.3 (—) that minimises the interaction energy between the 1st- and 2nd-shells. Knowing  $Z_{12}$  gives rise to the lateral and vertical sizes of the 2nd-shell, which then become  $\ell$  and  $d$  in the determination of  $Z_{23}$ . Repeatedly, the equilibrium spacing  $Z_{(n-1)n}$  for the  $(n-1)$ th- and  $n$ th-shells interaction is determined, and Figure 6.3 shows the relation between the energy  $E^{tot}/(\eta_1\eta_2)$  and the interspacing between two neighbouring shells for the ellipsoidal carbon onion with  $C_{80}$  as the core. The critical values that minimise the potential energy are the equilibrium distances between each layer of the ellipsoidal carbon onion. The lateral and vertical sizes for a five-shell ellipsoidal

carbon onion with  $C_{80}$  core are given in Table 6.3. Using a similar procedure to that described above, Table 6.4 gives the dimensions of the outer shells for the ellipsoidal carbon onion where  $C_{24}$  is the core. For the ellipsoidal carbon onions with a  $C_{80}$  core, the equilibrium interlayer spacing between neighbouring shells is approximately 3.4 Å. Further, from Terrones *et al.* [99], it can be found that the mean radii of  $C_{260}$ ,  $C_{560}$  and  $C_{980}$  are 7.662, 11.057 and 14.588 Å, respectively. As a result of Table 6.3, assuming  $C_{80}$  as a core gives rise to the carbon onion structure  $C_{80}@C_{260}@C_{560}@C_{980}@C_{1520}...@C_N$  where  $N = 20(m^2 + mn + n^2)$ . As such, this study confirms the possible creation of the nested chiral icosahedral fullerenes of type I symmetry as proposed by Terrones *et al.* [99].

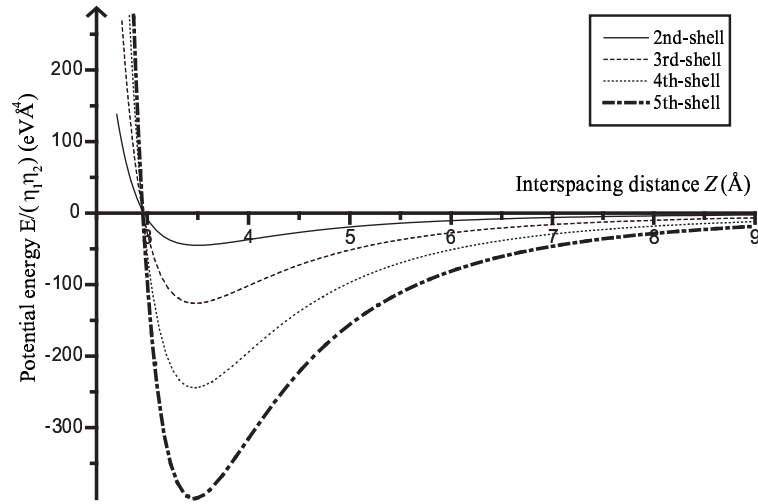


Figure 6.3: Potential energy profile for a five-shell  $C_{80}$  carbon onion.

Table 6.3: Lateral and vertical sizes for five-layer ellipsoidal carbon onion where  $C_{80}$  is the assumed inner core.

$n$ th-shell	$C_{80}$	2nd	3rd	4th	5th
Lateral radius (Å)	4.73	8.222	11.699	15.167	18.629
Vertical radius (Å)	3.58	7.072	10.549	14.017	17.479
Mean radius (Å)	4.155	7.647	11.124	14.542	18.054

From the tables, the values of the equilibrium spacing  $Z$  between two adjacent layers for both spherical and ellipsoidal carbon onions decrease the further away the shell is from the inner core, which results from the effect of decreasing the curvature of the spheroids. The high curvature of the inner shells means that for any atom

Table 6.4: Lateral and vertical sizes for five-layer ellipsoidal carbon onion where C<sub>24</sub> is the assumed inner core.

<i>n</i> th-shell	C <sub>24</sub>	2nd	3rd	4th	5th
Lateral radius (Å)	2.315	5.846	9.324	12.792	16.256
Vertical radius (Å)	1.665	5.196	8.674	12.142	15.606

on the surface, there can be more than one interacting atom on the neighbouring shell. Moreover, the shells which are further away from the inner core become more like a flat surface, for which the interaction energy of the neighbouring shells is approximately the equilibrium spacing of two graphite sheets. The equilibrium spacing between two adjacent layers is obtained approximately as 3.4 Å for both cases. This result is in excellent agreement with the observations made by Terrones *et al.* [99].

The relation between the equilibrium spacing between two adjacent shells is shown in Figure 6.4 for a spherical carbon onion. Using a first order exponential curve fitting technique from Microcal Origin 6.0 and the values of constants provided previously, an equation which describes the interspacing between each shell of a spherical carbon onion is obtained, namely

$$\text{Equilibrium spacing (Å)} = 3.455 + 0.131e^{-1.593n},$$

where  $n$  is the shell number.

For an ellipsoidal carbon onion, the relation between the spacing number and the equilibrium distance between each layer is shown in Figure 6.5. Again, using a first order exponential curve fitting technique from Microcal Origin 6.0 and the values of constants provided previously, the equations which describe the equilibrium spacing between any two neighbouring layers for the C<sub>24</sub> and C<sub>80</sub> ellipsoidal carbon onions are obtained, namely

$$\text{Equilibrium spacing for C}_{24} \text{ onion (Å)} = 3.458 + 0.757e^{-0.851n},$$

and

$$\text{Equilibrium spacing for C}_{80} \text{ onion (Å)} = 3.453 + 0.102e^{-2.061n},$$

where  $n$  is the shell number. Figure 6.5 shows that the large equilibrium spacing

between the 1st- and the 2nd-shells of  $C_{24}$  carbon onion occurs due to the unstable structure of  $C_{24}$  [93].

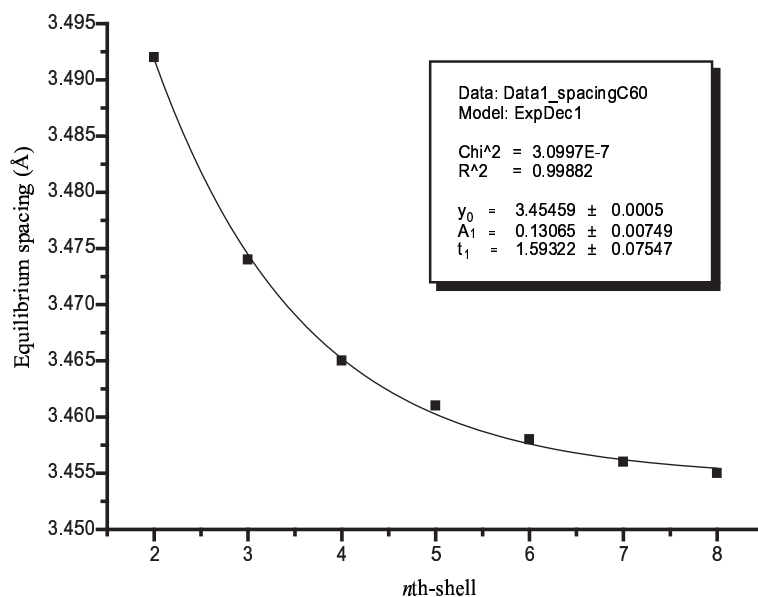


Figure 6.4: Equilibrium spacing between adjacent shells of spherical carbon onion assuming a  $C_{60}$  core.

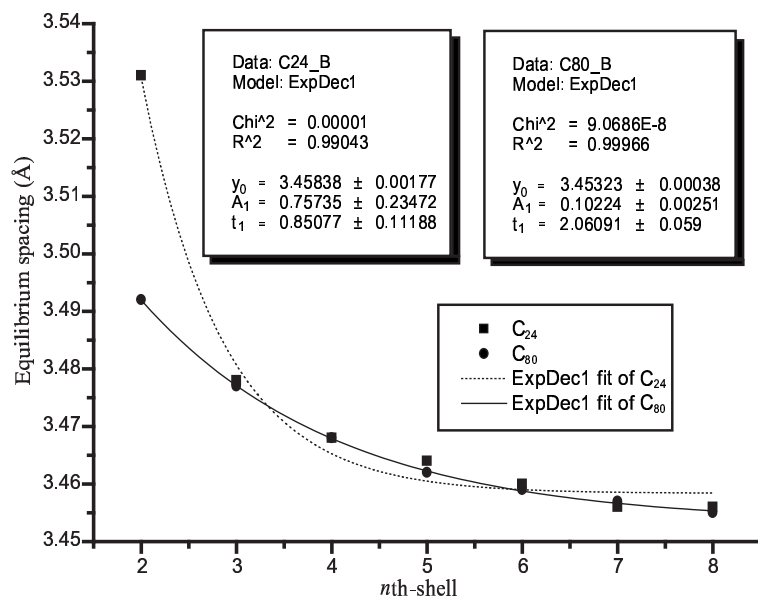


Figure 6.5: Equilibrium spacing between adjacent shells of spheroidal carbon onions assuming a  $C_{24}$  and a  $C_{80}$  core.

## 6.5 Summary

The interspacing between two adjacent layers of spherical and ellipsoidal carbon onions is considered here. The Lennard-Jones potential together with the continuum approximation is employed to determine the preferred position or the equilibrium distance for each layer of various carbon onions. The analysis gives rise to the possible dimensions for each shell of the carbon onions. Moreover, the equilibrium spacing is observed to decrease as the shell is further away from the inner core and this is due to the decreasing curvature for the larger spheroids. However, this is not the case when high temperatures and pressures are applied to the onion, as shown by Banhart and Ajayan [100]. Upon heating the particle up to 700°C and simultaneously irradiating it with electrons, the interlayer spacing in the onion is actually shown to decrease from the outside to the inside, indicating an increasing compressive stress towards the centre, giving rise to a diamond core. Finally, an approximate equation for the determination of the equilibrium spacing for any two adjacent layers of a spherical and an ellipsoidal carbon onion is presented.

## Part III

# Geometry of joining nanostructures

## Chapter 7

# Introduction to the geometry of joining nanostructures

Since the discovery of carbon nanostructures such as graphene sheets,  $C_{60}$  fullerenes and carbon nanotubes, a number of researchers have investigated the topological properties for such structures utilising Euler’s polyhedra theorem and computational molecular dynamics simulation [28, 101–103]. Kroto [101] proposes the basic empirical arguments for the stability of spherical carbon cages which mainly consist of pentagonal and hexagonal rings. By introducing the pentagonal, heptagonal and octagonal rings on the graphene sheet, Terrones and Terrones [28] and Terrones and Mackay [102] examine carbon nanostructures with various Euler characteristics. A defect on a carbon nanotube with a pentagon-heptagon pair as considered by Dunlap [104] is believed to strongly affect the electronic properties of carbon nanotubes [103, 105–108]. Furthermore, a pentagon-heptagon defect pair can be introduced to connect two different chiral nanotubes [104–106] or to change the helicity within a single tube [107].

For future nanoelectromechanical signalling, graphene sheets might be needed as the platform to transmit signals to other materials through joined carbon nanotubes. Thus connecting graphene sheets with carbon nanotubes is an interesting problem with potential applications, and to the author’s knowledge this problem has not previously been addressed in the literature. In Part III, two geometrical approaches, a variation in bond length and a variation in bond angle, are employed to determine the connection between a flat sheet and a tube open end, and the details for these two approaches are presented in §7.1. These two geometrical approaches are closely related to the bonded interaction energy for a small deformation system which is



detailed in §7.3. Euler’s polyhedra theorem, which is presented in §7.2, is utilised to determine the connected structure in terms of a geometrical point of view. Finally, an overview of this part is given in §7.4.

## 7.1 Least squares methods

From the work of Cox and Hill [11], the authors have exploited the idea that the basis of joined carbon nanostructures is an underlying requirement that each inter-atomic distance be as close as possible to the ideal carbon-carbon bond length. Accordingly, in [11] certain toroidal carbon nanostructures are constructed from elbows comprising sections of two distinct carbon nanotubes in such a way that the total squared deviation of all inter-atomic bond distances from the carbon-carbon bond length is minimised. The underlying hypothesis is that carbon nanostructures are formed in such a way that each inter-atomic bond length is as close as possible to the bond length, and indeed in [11] this procedure accurately produces certain toroidal molecules which are known to exist, along with numerous other predicted molecules. This leads us to ask, “To what extent is this least squares approach applicable to other carbon nanostructures?”, or equivalently “To what extent are carbon nanostructures dominated by geometric issues as well as energetic issues?” Although this approach appears to be geometric in nature, by trying to make each inter-atomic bond length as close as possible to the bond length, the requirement to minimise the energy is taken into account. In this thesis, two variation approaches, which are the variation in bond length and the variation in bond angle, are undertaken to consider the joining of two nanostructures, carbon and boron nitride, and the details of these two methods are given as follows.

### 7.1.1 Variation in bond length

To start, the  $i$ th terminal atoms at a join location are defined by the position vectors  $\mathbf{a}_i = (a_{xi}, a_{yi}, a_{zi})$  and  $\mathbf{b}_i = (b_{xi}, b_{yi}, b_{zi})$  for a sheet and a tube open end, respectively. The sheet is assumed to be located on the  $(x, y)$  plane (ie.  $a_{zi} = 0$ ) and it is allowed to move in both the  $x$ - and  $y$ -directions by distances  $X$  and  $Y$ , respectively, which can be either positive or negative. The atoms on the sheet are assumed to remain in the  $z = 0$  plane because here the bond angle is considered fixed. However, in the

variation of bond angle approach an out of plane displacement for the atoms on the sheet is incorporated. The position vector for the atoms at the defect sheet is given by  $\mathbf{a}_i = (a_{xi} + X, a_{yi} + Y, 0)$ . In terms of the atoms on the tube open end, the spacing between the tube and the sheet is assumed to be  $\ell$ , and the tube can be rotated about the  $z$ -axis through an angle  $\theta$ . Consequently, the position vector for the atoms at the tube open end can be written as  $\mathbf{b}_i = (b_{xi} \cos \theta - b_{yi} \sin \theta, b_{xi} \sin \theta + b_{yi} \cos \theta, \ell)$ . The Euclidean distance between the atoms at the junction is then given by

$$|\mathbf{a}_i - \mathbf{b}_i| = \{[a_{xi} + X - (b_{xi} \cos \theta - b_{yi} \sin \theta)]^2 + [a_{yi} + Y - (b_{xi} \sin \theta + b_{yi} \cos \theta)]^2 + \ell^2\}^{1/2}. \quad (7.1)$$

Given these distances between matching atoms, the procedure attempts to determine  $X$ ,  $Y$ ,  $\ell$  and  $\theta$  by minimising the least squares variation of these distances from the ideal bond length  $\sigma$ . Therefore, the objective function, given by (7.2) needs to be minimised,

$$f(X, Y, \ell, \theta) = \sum_i (|\mathbf{a}_i - \mathbf{b}_i| - \sigma)^2. \quad (7.2)$$

Throughout this study, the optimisation package in MAPLE is utilised to find the values for each parameter by minimising (7.2).

### 7.1.2 Variation in bond angle

In this subsection, the bond lengths are assumed to be fixed at  $\sigma$  and the bond angles at connection sites are varied so as to minimise the least square derivations from the physical bond angle for both the sheet and the tube. The bond length is assumed to be  $\sigma$ , the bond angles of the sheet are assumed to be  $120^\circ$ , and the bond angles on the tubes are taken from a new model of carbon nanotubes which properly incorporates curvature [109]. Since the atomic networks on both the sheet and the tube are formed from hexagonal rings, a general procedure is proposed to determine the position vectors of all atoms at the junction through the following steps:

1. Find the point  $\mathbf{M}$  which is the mid-point of  $\mathbf{A}_1$  and  $\mathbf{A}_2$ .
2. Find the vector  $\mathbf{U} = \mathbf{MA}_3$ .
3. Find the unit vector  $\hat{\mathbf{V}} = \mathbf{A}_1\mathbf{A}_2/|\mathbf{A}_1\mathbf{A}_2|$  which is perpendicular to  $\mathbf{U}$ .

4. Determine the vector  $\mathbf{W}$  which is perpendicular to both  $\mathbf{U}$  and  $\hat{\mathbf{V}}$  and has the same magnitude as  $\mathbf{U}$ ; namely  $\mathbf{W} = \mathbf{U} \times \hat{\mathbf{V}}$ .
5. The atom position is then given by  $\mathbf{M} + \mathbf{U} \cos \phi + \mathbf{W} \sin \phi$ .

Here,  $\mathbf{A}_1$ ,  $\mathbf{A}_2$  and  $\mathbf{A}_3$ , are the atoms positions as shown in Figure 7.1. The atom  $\mathbf{A}_3$ , which is the joining position, can move around a circular path and its position is determined by an angle  $\phi$ . Moreover, each bond length which joins between an atom on the tube to one on the sheet is restricted to be  $\sigma$ . Comment that in this approach the atoms can move out of plane (ie.  $a_{zi} \neq 0$ ). The number of parameters in each system depends on both the symmetry of the defect and the number of atoms at the tube open end which need to be joined.

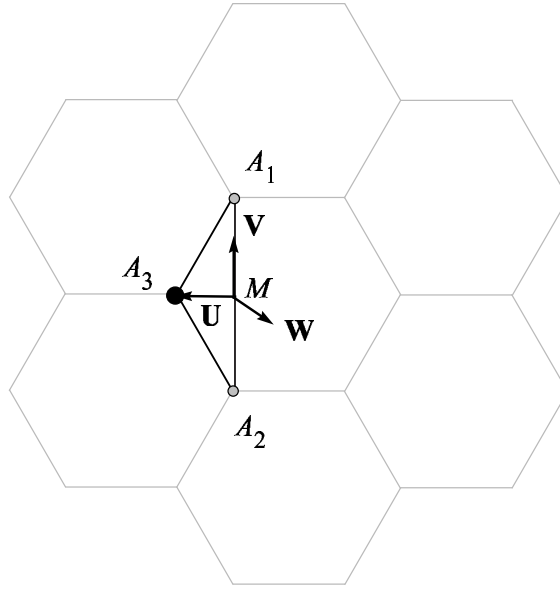


Figure 7.1: Position vectors for variation in bond angle approach.

We note that the variation in bond length and the variation in bond angle give very similar results because the bond angle approach automatically minimise the variation in bond length so that the two approaches are rather like a converging iterative procedure.

## 7.2 Euler's polyhedra theorem

Euler's polyhedra theorem, which involves the topological structure of the molecule, is considered here to investigate the connected configuration for two nanostructures.

Euler's polyhedra theorem states that

$$F + V - E = \chi, \quad (7.3)$$

where  $F$ ,  $V$  and  $E$  denote the numbers of faces, vertices and edges for the given polyhedron and  $\chi$  is the Euler characteristic. Note that any surface which is homeomorphic to a sphere has an Euler characteristic of 2, and further details of Euler's polyhedra theorem can be found in [110]. The notation  $P_n$  is used to denote the number of  $n$ -gonal sides, e.g.  $P_5$  is the number of pentagonal sides, and every atom is linked with three others in the  $sp^2$  structure, therefore three terms in (7.3) can be deduced

$$\begin{aligned} F &= P_4 + P_5 + P_6 + P_7 + P_8 + P_9 + P_{10}, \\ 3V &= 4P_4 + 5P_5 + 6P_6 + 7P_7 + 8P_8 + 9P_9 + 10P_{10}, \\ 2E &= 4P_4 + 5P_5 + 6P_6 + 7P_7 + 8P_8 + 9P_9 + 10P_{10}. \end{aligned} \quad (7.4)$$

By substituting (7.4) into (7.3) with  $\chi = 2$ , Euler's polyhedra theorem simplifies to

$$2P_4 + P_5 - P_7 - 2P_8 - 3P_9 - 4P_{10} = 12. \quad (7.5)$$

For example, a  $C_{60}$  fullerene is formed by pentagons and hexagons, and (7.5) implies that there are precisely twelve pentagons required to close the spherical shape. This is a result of the number of hexagonal sides  $P_6$  being an invariant of (7.5).

### 7.3 Bonded interaction for small deformations

A number of authors [13–16] adopt a numerical minimum energy principle such that the bonded potential energy for a small deformation is given by

$$E_{bonded} = \frac{1}{2} \sum_i \left( k_r (r - r_0)^2 + k_\phi (\phi - \phi_0)^2 + k_\tau [1 - \cos(n\tau - \tau_0)] \right), \quad (7.6)$$

where  $k_r$ ,  $k_\phi$  and  $k_\tau$  are certain bond stretching, bending angle and torsional constants, respectively,  $r_0$ ,  $\phi_0$  and  $\tau_0$  are equilibrium values of the bond length, bond angle and ideal phase angle for this bond type, respectively, and  $n$  is an integer relating to the periodicity of the bonding in  $sp^2$ ,  $n = 3$ . The parameters  $r$ ,  $\phi$  and  $\tau$  are shown in Figure 7.2. Ramani *et al.* [12] have reported all three force constants for

both carbon and hexagonal boron nitride, in the case of carbon, the force constants are obtained as  $k_r = 4.79 \text{ dyn cm}^{-1}$ ,  $k_\phi = 0.895 \text{ dyn cm}^{-1}$  and  $k_\tau = 0.156 \text{ dyn cm}^{-1}$ , and in the case of boron nitride, the force constants are obtained as  $k_r = 4.84 \text{ dyn cm}^{-1}$ ,  $k_\phi = 0.43 \text{ dyn cm}^{-1}$  and  $k_\tau = 0.156 \text{ dyn cm}^{-1}$ . Following their study, the bond stretching constant  $k_r$  is large, and is approximately five times and ten times larger than the bending angle constant  $k_\phi$  for carbon and boron nitride, respectively. In general, the variation in bond length approach corresponds to taking only the bond stretching energy. Similarly, the variation in bond angle approach corresponds to taking only the angle bending energy from equation (7.6) into account. Furthermore, according to [13–16], in terms of the relative magnitudes of the force constants, the torsional term plays only a minor effect on the system and it may be neglected. Therefore, the geometrical criteria are the more important underlying physical principles. Thus, the geometrical approaches adopted here correlate strongly to existing energy minimisation schemes.

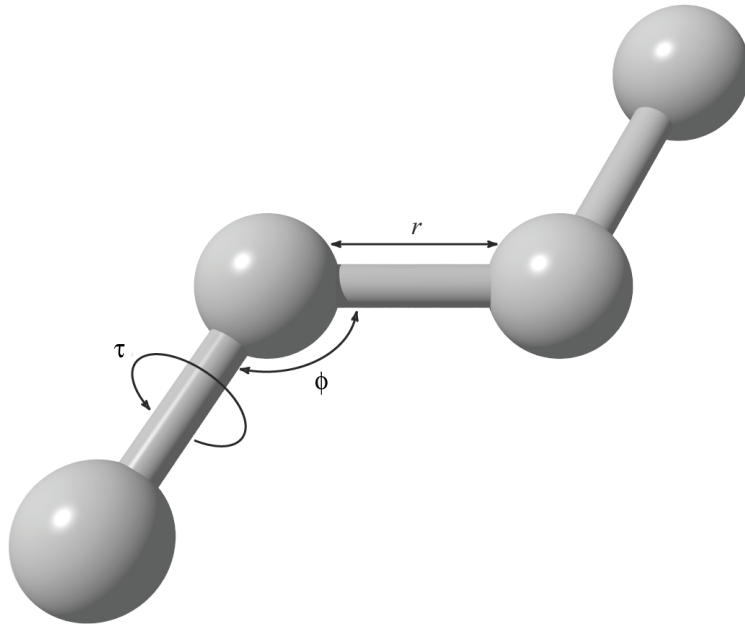


Figure 7.2: Definitions of variables  $r$ ,  $\phi$  and  $\tau$  for bonded potential energy given by equation (7.6).

## 7.4 Overview

Connecting structures from a geometrical point of view for both carbon and boron nitride are determined in Part III. Throughout this part, least squares methods, Euler's polyhedra theorem and the bonded interaction energy are employed to study the possible joined structures. Utilising the variation in bond length concept, in Chapter 8 a connecting of three distinct carbon nanotubes to form a torus is presented. In order to create an ideal transmission platform, connection between a carbon nanotube and a flat graphene sheet is investigated in Chapter 9. Furthermore, given that the energetically favourable bond in the hexagonal boron nitride network is the bond between the boron and the nitrogen atoms, boron nitride structures are formed from an even number of sides to each ring such as squares, hexagons and octagons. Therefore, the essential mathematical ideas for joining a sheet and a nanotube of boron nitride are presented in Chapter 10.

## Chapter 8

# Toroidal molecules formed from three distinct carbon nanotubes

In order to design nanotori for nanomechanical systems, perhaps involving oscillating components, precise physical parameters for the nanotori are needed. Toroidal shaped carbon molecules have been investigated previously and are constructed by connecting elbow sections formed from joining armchair and zigzag nanotubes through a pentagonal-heptagonal pair defects. In this chapter, this design is extended by constructing the elbow structures from three distinct carbon nanotubes. Since for a toroidal molecule, there is a constraint on the bend angles in the elbow sections to add up to  $360^\circ$ , particular elbow types which can accommodate this requirement are (5,0)-(4,4)-(7,0) and (3,3)-(6,0)-(4,4). A least squares approach for the bond length is adopted to minimise the variation from the ideal carbon-carbon bond length, which is taken to be  $\sigma = 1.42 \text{ \AA}$ . Moreover, formulae for the mean generating radius of the nanotori and the mean radius of the nanotubes are obtained from certain integral expressions. This geometrical approach can be directly related to certain numerical energy minimisation methods used by a number of authors [13–16].

### 8.1 Nomenclature

$\phi_1, \phi_2$  are the elbow bend angles between tubes A and B, and tubes B and C, respectively

$\sigma$  is the carbon-carbon covalent bond length

$R_1, R_2$  are the distances from the centres of a nanotorus to the elbow corners of

tubes A and B, and tubes B and C, respectively

$\mathbf{a}_i, \mathbf{b}_i, \mathbf{c}_i$  are the positions of terminal atoms on tubes A, B and C, respectively

$a$  is the representative tube radius for an ideal nanotorus

$a_1, a_2, a_3$  are the radii of tubes A, B and C, respectively

$c$  is the representative generating radius for an ideal nanotorus

$k, k'$  are the elliptic modulus and complementary modulus, respectively

$\ell_1, \ell_2, \ell_3$  are the half lengths of tubes A, B and C, respectively

$n$  is the number of elbow sections

$r_1, r_2, r_3$  are the perpendicular distances from the centre of a nanotorus to tube A, B and C sections, respectively

## 8.2 Introduction

Dunlap [111] first proposed the torus as a stable form of graphitic carbon. He constructs toroidal molecules by joining two different carbon nanotubes with matching radii and introduces the pentagon-heptagon pair [104, 111, 112]. Moreover, Dunlap [104, 111, 112] predicts that the molecule comprises twelve connecting sections occurring for the  $360^\circ$  turn, and therefore the tubule bend angle is  $30^\circ$  for each section. The energetic stability of molecules that are constructed based on the  $C_{60}$  fullerene and carbon nanotube structures are investigated by Itoh *et al.* [113], Ihara *et al.* [114] and Itoh and Ihara [115]. They find that these structures are more thermodynamically stable [114, 116] and such toroidal shapes are expected to be physically more interesting than those of the two original structures [115]. Although these theoretically proposed structures have not been confirmed by experiment [117], they are believed to give rise to fascinating electrical, magnetic and elastic properties arising from the pattern of the hexagonal rings [116].

In a recent paper Cox and Hill [11] show that certain toroidal molecules may be constructed from two types of carbon nanotubes, such that the bend angle and the two nanotube lengths are determined by minimising the total squared deviations



of the inter-atomic spacings from the ideal spacing  $\sigma = 1.42$  Å. This procedure generates certain toroidal shaped molecules previously known to exist, along with numerous other toroidal molecular structures. The question arises as to the generality of the procedure, and whether or not other toroidal shaped molecules are determined, such as ones constructed from three distinct nanotubes.

This chapter examines the geometry of the basic repeatable units, comprising three distinct carbon nanotubes, which are needed to assemble the toroidal molecule. Following [11], these repeating units are joined according to the least squares minimisation of the deviations of the inter-atomic spacing from the ideal spacing  $\sigma = 1.42$  Å. In this study, all the carbon nanotube sections are assumed to be either zigzag or armchair. This is because from previous studies only these two types of nanotubes are thought to form nanotori [104, 111, 112, 118]. In addition, there is no experimental evidence to indicate that chiral tubes can be formed into toroidal structures [117]. The model formation for the elbow comprising three distinct carbon nanotubes is presented in the following section. In §8.4, the toroidal molecules constructed by connecting  $n$  elbows are determined, and formulae for a representative radius of such tori and a representative radius of the toroidal tube are also given. The results and discussion are presented in §8.5, and a summary is made in §8.6.

### 8.3 Model formation for an elbow

The elbow structure required for toroidal molecules is investigated here by joining three distinct carbon nanotubes of lengths  $2\ell_1$ ,  $2\ell_2$  and  $2\ell_3$  utilising the least squares in bond length approach. Only zigzag and armchair carbon nanotubes are examined. The proposed model assumes that the basic repeating unit comprises tubes A and C as half unit lengths and tube B as one unit length. Further, it is assumed that the origin  $O$  of a rectangular Cartesian coordinate system  $(x, y, z)$  is located at the central point of tube B, such that the axis of tube B is aligned along the  $z$ -axis, as illustrated in Figure 8.1.

The  $i$ th terminal atom at a join location is defined by position vectors  $\mathbf{a}_i = (a_{ix}, a_{iy}, a_{iz})$ ,  $\mathbf{b}_i = (b_{ix}, b_{iy}, b_{iz})$  and  $\mathbf{c}_i = (c_{ix}, c_{iy}, c_{iz})$  for tubes A, B and C, respectively. At the junction of tubes A and B with  $x'$ -axis as shown in Figure 8.2(a), a translation of the tube B in the negative  $z$ -direction is performed by a length  $\ell_{2A}$ ,

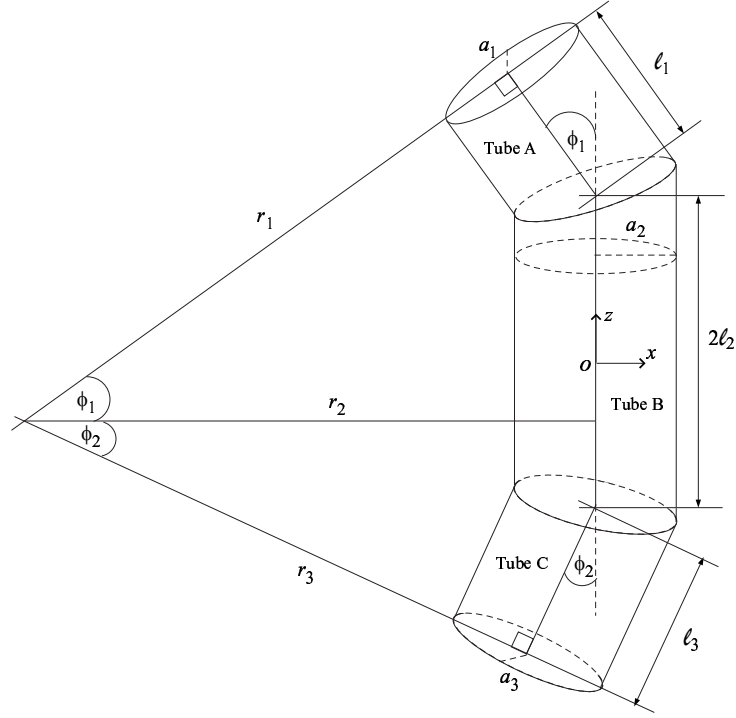


Figure 8.1: Basic double elbow unit formed from three nanotube sections.

where  $2\ell_2 = \ell_{2A} + \ell_{2B}$  and  $\ell_{2B}$  is as defined later in the text. Tube A is also translated in the positive  $z$ -direction by a length  $\ell_1$  and rotated by an angle  $\phi_1$  about the  $y'$ -axis. Therefore, the Euclidean distance between the atoms at the junction is given by

$$|\mathbf{a}_i - \mathbf{b}_i| = \{[a_{ix} \cos \phi_1 + (a_{iz} + \ell_1) \sin \phi_1 - b_{ix}]^2 + (a_{iy} - b_{iy})^2 \\ [(a_{iz} + \ell_1) \cos \phi_1 - a_{ix} \sin \phi_1 - (b_{iz} - \ell_{2A})]^2\}^{1/2}.$$

Similarly, at the junction of tubes B and C with  $x''$ -axis as shown in Figure 8.2(b), tube B is translated in the positive  $z$ -direction by a length  $\ell_{2B}$ , tube C is translated in the negative  $z$ -direction by a length  $\ell_3$  and rotated by an angle  $\phi_2$  about the  $y''$ -axis. The distance between the atoms at the join location is then given by

$$|\mathbf{c}_i - \mathbf{b}_i| = \{[c_{ix} \cos \phi_2 + (c_{iz} - \ell_3) \sin \phi_2 - b_{ix}]^2 + (c_{iy} - b_{iy})^2 \\ [(c_{iz} - \ell_3) \cos \phi_2 - c_{ix} \sin \phi_2 - (b_{iz} + \ell_{2B})]^2\}^{1/2}.$$

Given these distances between matching atoms, the procedure is to determine  $\ell_1, \ell_2, \ell_3, \phi_1$  and  $\phi_2$  by minimising the least squares variation of these distances from the ideal carbon-carbon bond length which is taken to be  $\sigma = 1.42 \text{ \AA}$ . Consequently,

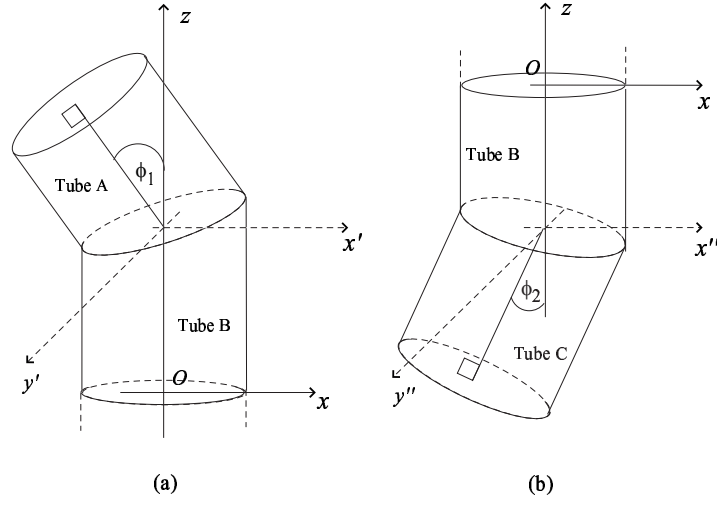


Figure 8.2: Cartesian coordinate system for two single nanotube elbows.

this approach is seeking to minimise the following objective functions,

$$f(\ell_1, \ell_{2A}, \phi_1) = \sum_i (|\mathbf{a}_i - \mathbf{b}_i| - \sigma)^2,$$

$$g(\ell_{2B}, \ell_3, \phi_2) = \sum_j (|\mathbf{c}_j - \mathbf{b}_j| - \sigma)^2.$$

Given that the parameters  $\ell_1, \ell_2, \ell_3, \phi_1$  and  $\phi_2$  are determined, the basic repeating unconstrained elbow unit can be obtained and is illustrated in Figure 8.3. However, in the case of a nanotorus, an even number of elbow sections are required to form a symmetrical torus, so that the angles  $\phi_1$  and  $\phi_2$  must be constrained to the value  $\phi_1 + \phi_2 = 180^\circ/n$  where  $n \in \{2, 3, 4, \dots\}$ . So in this case, the objective function becomes

$$F(\ell_1, \ell_{2A}, \ell_{2B}, \ell_3, \phi_1) = f(\ell_1, \ell_{2A}, \phi_1) + g(\ell_{2B}, \ell_3, 180^\circ/n - \phi_1).$$

In consequence, with this additional constraint, slightly different values for  $\ell_1, \ell_2$  and  $\ell_3$  might be obtained. The resulting nanotorus structure is achieved by translating the elbow in the  $x$ -direction by a distance  $r_2$  which is obtained by the procedure given in the following section.

## 8.4 Model formation for a toroidal molecule

In this section, nanotoroidal structures formed from the elbows determined in §8.3 are investigated here. A representative radius of the toroidal shapes is determined

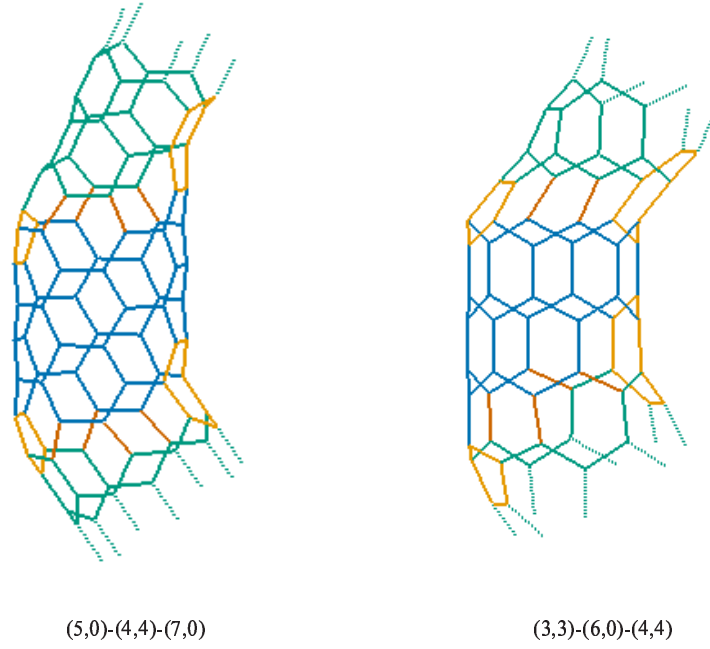


Figure 8.3: Elbows formed from three distinct nanotube sections.

by connecting the basic elbow units with  $\phi_1$  and  $\phi_2$  constrained for the  $360^\circ$  turn. Firstly, the upper quadrilateral shown in Figure 8.4 is considered which comprises four sides, namely  $r_1, \ell_1, \ell_{2A}$  and  $r_2$ , and the configuration also depend on the angle  $\phi_1$ . On using the compound angle formula for sine which can be deduced

$$\sin \phi_1 = \sin \theta_1 \cos \theta_{2A} + \sin \theta_{2A} \cos \theta_1 = (\ell_1 r_2 + \ell_{2A} r_1) / R_1^2,$$

and therefore,

$$r_1 = (R_1^2 \sin \phi_1 - \ell_1 r_2) / \ell_{2A}. \quad (8.1)$$

Similarly, from the compound angle formula for cosine,

$$\cos \phi_1 = \cos \theta_1 \cos \theta_{2A} - \sin \theta_1 \sin \theta_{2A} = (r_1 r_2 - \ell_1 \ell_{2A}) / R_1^2,$$

and therefore,  $r_1$  simplifies to become

$$r_1 = (R_1^2 \cos \phi_1 + \ell_1 \ell_{2A}) / r_2. \quad (8.2)$$

By equating equations (8.1) and (8.2),  $r_2$  can be rearranged and is given by

$$r_2 R_1^2 \sin \phi_1 = \ell_{2A} R_1^2 \cos \phi_1 + \ell_1 (r_2^2 + \ell_{2A}^2),$$

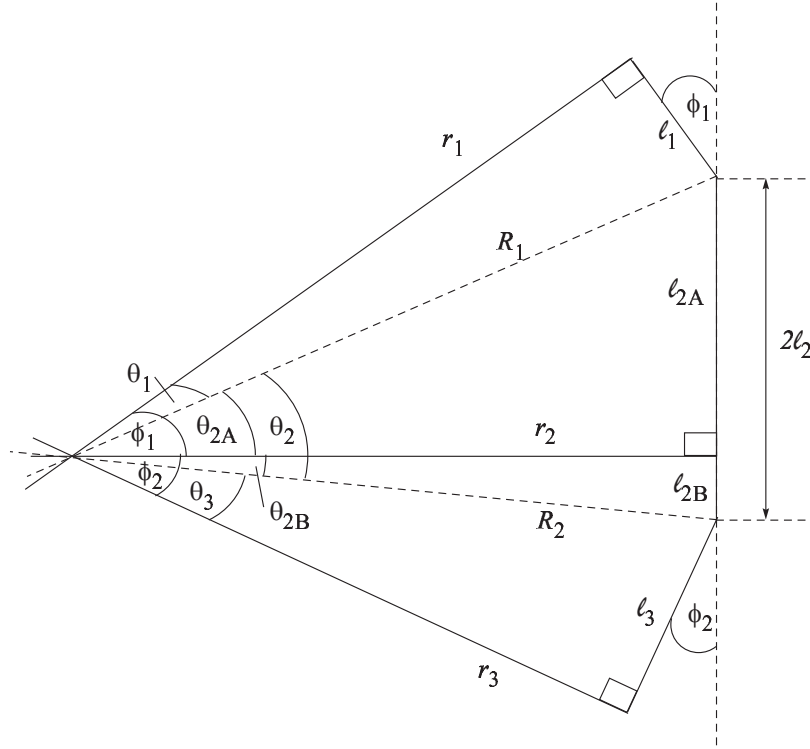


Figure 8.4: Elbow skeleton formed from three distinct nanotube sections.

where  $R_1^2 = r_2^2 + \ell_{2A}^2$  is strictly positive. By dividing by  $R_1^2$  and rearranging,  $r_2$  simplifies to obtain

$$r_2 = \ell_{2A} \cot \phi_1 + \ell_1 \csc \phi_1, \quad (8.3)$$

and likewise

$$r_1 = \ell_1 \cot \phi_1 + \ell_{2A} \csc \phi_1.$$

By precisely the same process for the quadrilateral comprising the sides  $r_2, \ell_{2B}, \ell_3$  and  $r_3$ ,  $r_2$  and  $r_3$  can be deduced

$$r_2 = \ell_{2B} \cot \phi_2 + \ell_3 \csc \phi_2, \quad (8.4)$$

$$r_3 = \ell_3 \cot \phi_2 + \ell_{2B} \csc \phi_2.$$

The parameters  $\ell_{2A}$  and  $\ell_{2B}$  can be rearranged from (8.3) and (8.4), respectively,

$$\ell_{2A} = \frac{r_2 - \ell_1 \csc \phi_1}{\cot \phi_1} = r_2 \tan \phi_1 - \ell_1 \sec \phi_1,$$

$$\ell_{2B} = \frac{r_2 - \ell_3 \csc \phi_2}{\cot \phi_2} = r_2 \tan \phi_2 - \ell_3 \sec \phi_2.$$

Since  $2\ell_2 = \ell_{2A} + \ell_{2B}$ , therefore

$$r_2 = \frac{\ell_1 \sec \phi_1 + 2\ell_2 + \ell_3 \sec \phi_2}{\tan \phi_1 + \tan \phi_2}. \quad (8.5)$$

By substituting (8.5) into the above equations,  $r_1$  and  $r_3$  are obtained

$$r_1 = \ell_1 \cot(\phi_1 + \phi_2) + 2\ell_2 \csc(\phi_1 + \phi_2) \cos \phi_2 + \ell_3 \csc(\phi_1 + \phi_2), \quad (8.6)$$

$$r_3 = \ell_1 \csc(\phi_1 + \phi_2) + 2\ell_2 \csc(\phi_1 + \phi_2) \cos \phi_1 + \ell_3 \cot(\phi_1 + \phi_2). \quad (8.7)$$

These two formulae provide the appropriate generalisation of those given in Cox and Hill [11] for the case of two distinct tubes. The corresponding equations given in Cox and Hill [11] can be obtained from (8.6) and (8.7) with the formal identification  $\ell_2 \equiv \phi_2 \equiv 0$ .

To calculate a representative radius  $a$  and a representative generating radius  $c$  in terms of the perpendicular distances  $r_1$ ,  $r_2$  and  $r_3$ , the integral formula for a mean radius  $\bar{r}$  of a circle is utilised, which is given by

$$\bar{r}\phi_0 = \int_0^{\phi_0} r(\phi) d\phi.$$

For a right-angled triangle which consists of  $r_1$ ,  $\ell_1$  and  $R_1$  sides,  $\phi_0$  and  $r$  are obtained as  $\phi_0 = \tan^{-1}(\ell_1/r_1)$  and  $r(\phi) = r_1 \sec \phi$  and it can be deduced

$$\bar{r}_1\theta_1 = r_1 \int_0^{\tan^{-1}(\ell_1/r_1)} \sec \phi d\phi = r_1 \ln \left( \frac{\ell_1}{r_1} + \frac{\sqrt{\ell_1^2 + r_1^2}}{r_1} \right).$$

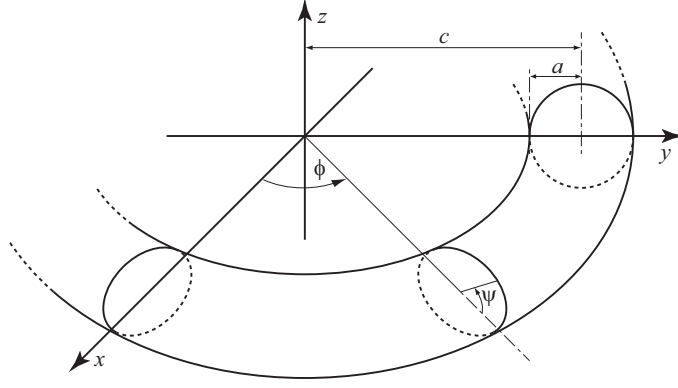
Since  $\sinh^{-1} x = \ln(x + \sqrt{x^2 + 1})$ , therefore  $\bar{r}_1\theta_1$  simplifies to obtain

$$\bar{r}_1\theta_1 = r_1 \sinh^{-1}(\ell_1/r_1).$$

The same procedure is repeated to obtain the mean radii for  $r_2$  and  $r_3$  and finally by averaging, the representative toroidal generating radius  $c$  is obtained to be given by

$$c = \{r_1 \sinh^{-1}(\ell_1/r_1) + r_2 [\sinh^{-1}(\ell_{2A}/r_2) + \sinh^{-1}(\ell_{2B}/r_2)] + r_3 \sinh^{-1}(\ell_3/r_3)\} / (\phi_1 + \phi_2). \quad (8.8)$$

This process is then extended to determine a representative expression for the representative tube radius  $a$ . Here a surface integral for a torus is undertaken to determine such a radius. The surface element for the tube is obtained by transforming

Figure 8.5: Toroidal coordinate system  $(a, \phi, \psi)$ .

the toroidal coordinate system  $(a, \phi, \psi)$  into a Cartesian coordinate system via

$$x = (c + a \cos \psi) \cos \phi, \quad y = (c + a \cos \psi) \sin \phi, \quad z = a \sin \psi,$$

where  $c$  and  $a$  denote the mean radii for the torus and the tube, and  $\phi$  and  $\psi$  are the torus and the tube angles, respectively (see Figure 8.5). By using the Jacobian matrix, the surface element integral for the torus can then be written as

$$\int_0^{\phi_0} \int_0^{2\pi} b(\phi, \psi) [r(\phi) + b(\phi, \psi) \cos \psi] d\psi d\phi = 2\pi \bar{b} \phi_0 c,$$

where  $b(\phi, \psi)$  is the radius of the tube, and as before  $r(\phi)$  is the torus generating radius. For the section of tube A,  $\theta_1 = \tan^{-1}(\ell_1/r_1)$ ,  $r(\phi) = r_1 \sec \phi$  and  $b(\phi, \psi) = a_1 \sqrt{\sec^2 \phi \cos^2 \psi + \sin^2 \psi}$ , it can be deduced

$$\begin{aligned} \bar{a}_1 &= \frac{1}{2\pi c \theta_1} \int_0^{\theta_1} \int_0^{2\pi} a_1 r_1 \sec \phi \sqrt{\sec^2 \phi \cos^2 \psi + \sin^2 \psi} d\psi d\phi, \\ &= \frac{a_1 r_1}{2\pi c \theta_1} \int_0^{\theta_1} \int_0^{2\pi} \frac{\sqrt{1 - \sin^2 \phi \sin^2 \psi}}{\cos^2 \phi} d\psi d\phi. \end{aligned}$$

Upon the substitution of  $k = \sin \phi$ , the above integral can be written as

$$\bar{a}_1 = \frac{2a_1 r_1}{\pi c \theta_1} \int_0^{\pi/2} \int_0^{\ell_1/R_1} \frac{\sqrt{1 - k^2 \sin^2 \psi}}{k'^3} dk d\psi = \frac{2a_1 r_1}{\pi c \theta_1} \int_0^{\ell_1/R_1} \frac{E(k)}{k'^3} dk,$$

where  $E(k)$  is the complete elliptic integral of the second kind with modulus  $k$  and  $k' = \sqrt{1 - k^2}$  is the complementary modulus. Using these definitions with equivalent expressions for tubes B and C and then combining, the following formula may be

derived for the representative tube radius

$$a = \frac{2}{\pi c(\phi_1 + \phi_2)} \{a_1 r_1 h(\ell_1/R_1) + a_2 r_2 [h(\ell_{2A}/R_1) + h(\ell_{2B}/R_2)] + a_3 r_3 h(\ell_3/R_2)\}, \quad (8.9)$$

where

$$h(x) = \int_0^x \frac{E(k)}{k^3} dk. \quad (8.10)$$

The analytical expression in terms of an infinite series for (8.10) can be found in Appendix A of Cox and Hill [11], and is given by

$$\begin{aligned} h(x) = & \frac{3\pi x}{8r} + \frac{\pi}{8} \sin^{-1} x + \frac{\pi}{2} \sum_{m=1}^{\infty} \left( \frac{-\frac{1}{2}}{m+1} \right)^2 \left\{ \frac{(2m-1)!!}{2^m m!} \sin^{-1} x \right. \\ & \left. - \frac{x^{2m+1}}{(2m+1)r} \left[ 1 + \left( \frac{r^2}{x^2} \right) \sum_{k=0}^{m-1} \frac{(m-k-1)!(2m+1)!!}{2^{k+1} m! (2m-2k-1)!!} \left( \frac{1}{x} \right)^{2k} \right] \right\}, \end{aligned}$$

where  $r = (1-x^2)^{1/2}$  and the double factorial  $(2n-1)!!$  denotes  $(2n-1)(2n-3) \cdots 5 \cdot 3$ .

The above procedures for the determination of the representative parameters  $a$  and  $c$  are by no means unique, but appear as the most natural and simplest for the determination of these quantities.

## 8.5 Results and discussion

In this section, elbows made from the smallest possible nanotube sections are determined. By precisely the same procedure as that given in [11], the basic parameter for elbows are given in Table 8.1. The smallest possible nanotube sections which can be formed from the elbows are referred to as the base unit, and other possible structures can be obtained by adding further incremental units. The same nomenclature formulated in [11] for toroidal shaped molecules is employed by utilising the notation  $N(n, m)_p$  where  $(n, m)$  refers to a section of nanotube which is constructed from  $p$  atoms and  $N$  is a number of base units.

Numerical results from the least squares procedure when applied to various distinct nanotube elbows are presented here. Two different elbow structures, which are (5,0)-(4,4)-(7,0) and (3,3)-(6,0)-(4,4), are considered. Using the new polyhedral faceted model for carbon nanotubes which incorporates curvature [109] and the value of the bond length  $\sigma = 1.42 \text{ \AA}$ , the tube radii are obtained. Once the atom positions are determined, the physical parameters  $\ell_1, \ell_2, \ell_3, \phi_1$  and  $\phi_2$  are determined



Table 8.1: Fundamental parameters for nanotube elbows formed from three distinct carbon nanotube sections.

Nanotube	Radius (Å)	Base unit	Incremental unit	
		Number atoms	Number atoms	Length (Å)
(5,0)	2.0551	17	+20	+4.7986
(4,4)	2.7582	48	+16	+2.4380
(7,0)	2.8094	19	+28	+4.2230
(3,3)	2.0965	12	+12	+2.4206
(6,0)	2.4298	32	+24	+4.1580
(4,4)	2.7582	24	+16	+2.4380

by the minimisation process, both for no constraints and again with the constraint  $\phi_1 + \phi_2 = 180^\circ/n$  where  $n \in \{2, 3, 4, \dots\}$ . In Table 8.2, the results for the unconstrained case and the constrained case when  $\phi_1 + \phi_2 = 60^\circ$  (that is  $n = 3$ ) for two different nanotori are presented. Note that the sum of the angles  $\phi_1$  and  $\phi_2$  needs to be exactly or close to a common factor of  $360^\circ$  for toroidal structures, and there is only one case arising for these particular two structures. Moreover, there is no straightforward procedure to choose the elbow structures for which  $\phi_1 + \phi_2 \simeq 180^\circ/n$ , so that only (5,0)-(4,4)-(7,0) and (3,3)-(6,0)-(4,4) are presented here.

Table 8.2: Bend angles and base unit section for nanotube elbows.

	Elbow type	
	(5,0)-(4,4)-(7,0)	(3,3)-(6,0)-(4,4)
$\phi_1 + \phi_2$ unconstrained		
$\phi_1(^\circ)$	25.59	31.38
$\phi_2(^\circ)$	36.00	33.80
$\ell_1(\text{Å})$	3.7089	3.2202
$\ell_2(\text{Å})$	3.6571	2.4085
$\ell_3(\text{Å})$	3.1727	2.3430
$\phi_1 + \phi_2 = 60^\circ$		
$\phi_1(^\circ)$	24.00	26.20
$\phi_2(^\circ)$	36.00	33.80
$\ell_1(\text{Å})$	3.3396	3.2716
$\ell_2(\text{Å})$	3.6571	2.4085
$\ell_3(\text{Å})$	3.1727	2.3430

Using the parameters for the constrained elbows, the toroidal parameters  $r_1, r_2$  and  $r_3$  from equations (8.6), (8.5) and (8.7) are calculated, and values for the mean

torus generating radius  $c$  and mean tube radius  $a$  are derived from the expressions (8.8) and (8.9). These results are presented in Table 8.3. Two of these nanotori are illustrated graphically in Figure 8.6 and Figure 8.7. In Figure 8.6, the toroidal structure of  $3(5,0)_{17}6(4,4)_{48}3(7,0)_{19}$  is depicted, which can be referred to as a  $C_{396}$  molecule, and also in Figure 8.7, the toroidal structure of  $3(3,3)_{12}6(6,0)_{32}3(4,4)_{24}$  is shown, which can be referred to as a  $C_{300}$  molecule.

Table 8.3: Physical parameters of two specific toroidal structures.

Toroidal structures	$r_1$ (Å)	$r_2$ (Å)	$r_3$ (Å)	$c$ (Å)	$a$ (Å)
$3(5,0)_{17}6(4,4)_{48}3(7,0)_{19}$	12.4239	12.7083	13.4038	12.9935	2.6209
$3(3,3)_{12}6(6,0)_{32}3(4,4)_{24}$	9.2163	9.7138	10.1213	9.7980	2.4780

## 8.6 Summary

The principle contribution of this study is applying a least squares approach to determine the basic elbow unit and toroidal structures formed from three distinct carbon nanotubes. Within each constituent nanotube structure, the relative atom positions are assumed to remain unchanged. The connection to adjacent atoms on each of the two sections is assumed to be as close as possible to the carbon-carbon bond length, taken to be  $\sigma = 1.42$  Å. The variation in the bond length is minimised which gives rise to the physical parameters, namely the bend angles,  $\phi_1$  and  $\phi_2$ , and the half-lengths  $\ell_1, \ell_2$  and  $\ell_3$ . We comment that this minimisation procedure ignores angle bending because the bending force constant is small relative to the bond length constant. There are two approaches in the minimisation routines, which are the unconstrained and constrained cases for the bend angles. In terms of the unconstrained procedure, all the physical parameters are allowed to attain their optimum values themselves which are necessary to form the elbow structures. However, in such a procedure there is no guarantee that the elbow sections can be joined to each other and form a toroidal shaped structure with a  $360^\circ$  turn. Therefore, the analysis is repeated with the angles  $\phi_1$  and  $\phi_2$  constrained to the value  $\phi_1 + \phi_2 = 180^\circ/n$  where  $n \in \{2, 3, 4, \dots\}$ .

Here, two distinct elbows are considered which are (5,0)-(4,4)-(7,0) and (3,3)-(6,0)-(4,4), and all the physical parameters are given in Table 8.2. Since the principal

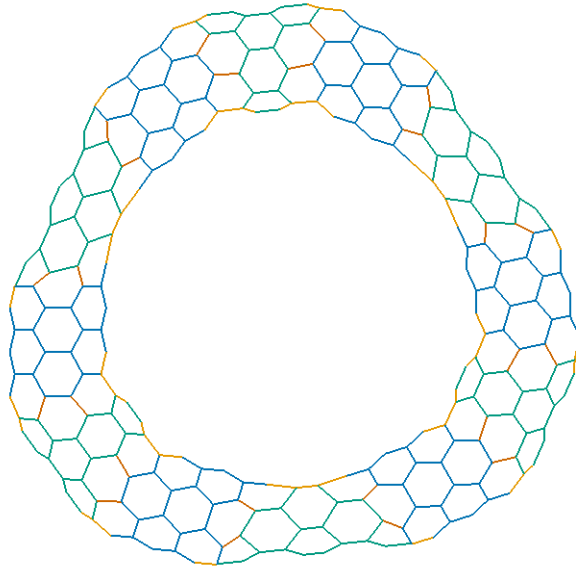


Figure 8.6: Nanotorus formed from  $3(5,0)_{17}6(4,4)_{48}3(7,0)_{19}$  where  $\phi_1 + \phi_2 = 60^\circ$ .

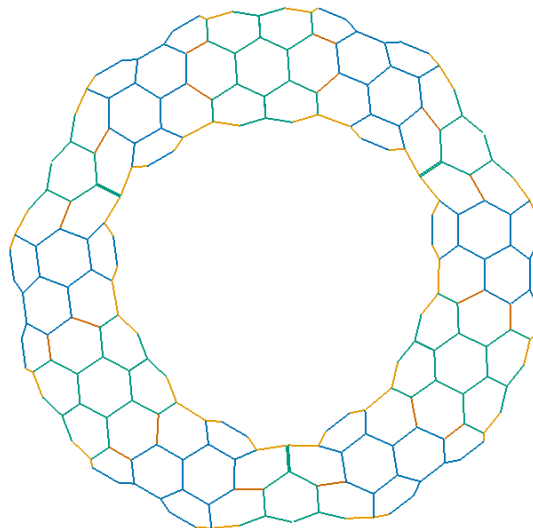


Figure 8.7: Nanotorus formed from  $3(3,3)_{12}6(6,0)_{32}3(4,4)_{24}$  where  $\phi_1 + \phi_2 = 60^\circ$ .

aim is to construct toroidal molecules by joining elbow sections, the bend angles must sum to  $360^\circ$ . The two elbows which are studied here correspond to cases for which  $360/(\phi_1 + \phi_2)$  is approximately an integer.

Following the analysis of two elbow types [11], toroidal shaped molecules are then investigated. A straightforward procedure is established to determine the mean generating toroidal radius  $c$  and the mean tube radius  $a$ . Once the bend angles and tube lengths are obtained, the perpendicular lengths from the torus centre can be determined, as given in Table 8.3. Such theoretical structures have yet to be confirmed either experimentally or by molecular dynamics simulations, nonetheless their theoretical existence is a first step in understanding the complex geometrical structures of such molecules.

# Chapter 9

## Joining carbon nanotubes and flat graphene sheets

In order to transmit signals from future nanoelectromechanical graphene sheets to other materials, connections with carbon nanotubes are required. Here, three particular perpendicular connections of carbon nanotubes are examined employing two simple distinct least squares approaches and using Euler's polyhedra theorem. Firstly, for (8,0) and (4,4) carbon nanotubes, a least squares approach is applied to the bond lengths. Sixteen distinct defects and two possible orientations for the armchair tube (4,4) are identified. Assuming that only pentagons, hexagons, heptagons and occasionally octagons are accepted, the number of possibilities is greatly reduced. By excluding octagonal rings, the number of possible configurations may be further reduced to only one and two most likely configurations for the zigzag (8,0) and the armchair (4,4) tubes, respectively. Secondly, for (6,0) and (8,0) carbon nanotubes, a least squares approach is applied to bond angles, and for one particular (8,0) junction, the two least squares approaches are shown to produce similar structures in terms of atom locations. These geometric approaches can be formally related directly to certain numerical energy minimisation methods used by a number of authors [13–16].

### 9.1 Nomenclature

$\sigma$	is the carbon-carbon covalent bond length
$\theta$	is the rotational angle of the carbon nanotube
$L$	is the spacing between the carbon nanotube and the graphene sheet,

equivalent to  $\ell + \sigma(\sqrt{3}\sin\phi\cos\omega - 1)$  where  $\phi$  is the bond half-angle and  $\omega$  is the angle of incline [109]

$P_n$  is the number of  $n$ -gonal sides

$X, Y$  are the translation distances in the  $x$ - and  $y$ -directions, respectively

$\mathbf{a}_i, \mathbf{b}_i$  are the positions of terminal atoms on the graphene sheet and the carbon nanotube, respectively

$\ell$  is the spacing between the graphene sheet and the carbon nanotube in the positive  $z$ -direction

## 9.2 Introduction

As a first step to examine the joining of two different carbon nanotubes, the radius of one tube is assumed to be much larger than the radius of the other. This line of reasoning leads to the notion of joining a tube to a flat graphene sheet. The basic idea of connecting a graphene sheet to a tube is also involved in the root-growth process for single-walled nanotubes [119–122], where the tubes are grown from the base metal-catalyst. Gavillet *et al.* [119] investigate the catalytic growth of single-walled carbon nanotubes using high-resolution transmission electron microscopy. Utilising quantum molecular dynamics simulation, they also find that hexagons and pentagons occur at the connection, but there are difficulties arising from computational limitations. Maiti *et al.* [122] use Euler’s polyhedra theorem and undertake molecular dynamics calculations to determine the polygons which occur at the base of the nanotube during the growth process. In terms of stability, they obtain results relating the type of polygonal rings occurring in Euler’s polyhedra theorem and the energy at the growth site.

Here, the approach of [11] is developed with reference to the perpendicular joining of a plane graphene sheet to three particular carbon nanotubes. For this problem, two least squares approaches are employed, which are the variation in the bond length as in [11], and an alternative idea which is fixing all bond lengths to be exactly the assumed bond length  $\sigma$  and minimising the variation in the bond angle as mentioned in §7.1. In the following section, the connecting of a zigzag (8,0) and

an armchair (4,4) carbon nanotube with sixteen different defect sites on a graphene sheet are examined by the variation in the bond length. For the ideal case of connecting a (6,0) tube with a symmetric defect, the variation in the bond angle is exploited using a least squares method to determine the connecting structure, which is presented in §9.4. The polygons which occur at the junction are determined and are shown to be consistent with Euler's polyhedra theorem in §9.5. Additionally, the most likely structure for the (8,0) tube and the sheet as determined from §9.5 is investigated using the bond angle variation method, and it is found that the two arrangements using least squares are very similar in terms of atom locations. Finally, a summary is presented in §9.6.

### 9.3 Variation in the bond length

The possibility of connecting zigzag (8,0) and armchair (4,4) nanotubes with a flat graphene sheet is investigated here by fixing the atom positions on the tube end and the graphene sheet. Then the variation in distance between an atom on the tube open end and an atom on the sheet from the bond length  $\sigma$  between two carbon atoms, taken to be 1.42 Å, is minimised. In both cases, there are eight atoms which are connected to the tube by two carbon bonds so that they require one other bond to complete the  $sp^2$  structure. Consequently, the defect on the graphene sheet must have eight atoms and each require one further bond to complete the structure. In Figure 9.1, sixteen possible defects are depicted to which the (8,0) and the (4,4) tubes might be joined. The first atom on the sheet is denoted by a black square and atoms indicated by grey circles are numbered sequentially and counterclockwise from the first atom. Because of the symmetric locations of all atoms on the open end of the zigzag tube, there are sixteen possible configurations denoted by an integer  $\#n$  from 1 to 16, corresponding to the sixteen possible defects. For the armchair tube, there are two connected forms for the adjacent atoms on the tube end which are either connected by three bonds, as in the first atom to the second atom, or by a single bond, as in the second atom to the third atom. This pattern alternates around the tube end as depicted in Figure 9.1. Therefore, the joining of the first atom on the tube with the first atom on the sheet is denoted by  $\#n$ -a and the joining of the second atom on the tube with the first atom on the sheet is denoted by  $\#n$ -b where

$\#n$  is again an integer from 1 to 16 corresponding to the 16 possible defects.

As in §7.1.1, the variation in bond length for joining a flat graphene sheet and a carbon nanotube can be determined. In a Cartesian coordinate system, the graphene sheet is assumed to be located in the  $(x, y)$  plane and the  $i$ th atom on the sheet is assumed to have the position vector  $\mathbf{a}_i = (a_{xi} + X, a_{yi} + Y, 0)$  where  $i = 1, 2, 3, \dots, 8$ . The sheet is allowed to move in both  $x$ - and  $y$ -directions by distances  $X$  and  $Y$ , respectively, which can be either positive or negative. To keep the approach as simple as is possible, the atoms in the graphene sheet are assumed to remain in the  $z = 0$  plane. A refinement of the present approach would be to assume a displacement  $Z$  out of the  $z = 0$  plane, but this additional complexity makes no substantial qualitative changes to the final geometric structure obtained, and in this section  $z = 0$  is adopted because the bond angle is considered fixed.

The position vector of the  $i$ th atom on the tube open end is assumed to be given by  $\mathbf{b}_i = (b_{xi}, b_{yi}, \ell)$  where  $\ell$  is the spacing between the tube and the sheet in the positive  $z$ -direction. In addition, the tube can be rotated by an angle  $\theta$ . The distance between the atom on the tube end and the atom on the sheet is then given by

$$|\mathbf{a}_i - \mathbf{b}_i| = \{[(a_{xi} + X) - (b_{xi} \cos \theta - b_{yi} \sin \theta)]^2 + [(a_{yi} + Y) - (b_{xi} \sin \theta + b_{yi} \cos \theta)]^2 + \ell^2\}^{1/2}.$$

Using the least squares method, this study aims to determine  $X$ ,  $Y$ ,  $\ell$  and  $\theta$  which minimises the function

$$f(X, Y, \ell, \theta) = \sum_{i=1}^8 (|\mathbf{a}_i - \mathbf{b}_i| - \sigma)^2. \quad (9.1)$$

Using the algebraic computer package MAPLE, the numerical values for the least squares function  $f$  defined by (9.1) and the distance  $\ell$  are presented in Table 9.1 and Table 9.2 for the zigzag and the armchair tubes, respectively, where the radii of the tubes are taken from [109]. The global minimum values for the least squares are first graphed to ensure a genuine global minimum and the optimisation package in MAPLE is then utilised to find the values for each parameter which gives the minimum.



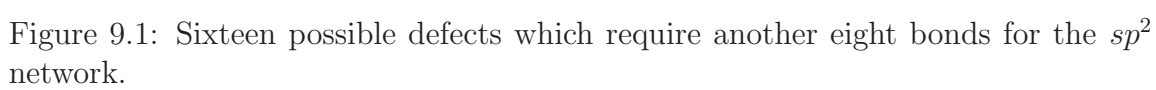


Table 9.1: Values of least square function  $f$  ( $\text{\AA}^2$ ) and distance  $\ell$  ( $\text{\AA}$ ) for 16 configurations of an (8,0) tube and corresponding polygons  $P_n$  where  $n$  is number of sides.

Configurations #	$f$	$\ell$	$P_5$	$P_6$	$P_7$	$P_8$	$P_9$
1	0.0239	1.3243	-	4	2	2	-
2	0.2092	1.1663	1	3	1	3	-
3	0.0018	1.3027	-	4	2	2	-
4	0.0676	0.9471	1	2	3	2	-
5	1.2631	0.0010	2	-	4	2	-
6	0.0817	1.3218	-	2	6	-	-
7	0.0729	1.1823	1	1	5	1	-
8	0.0020	1.3500	1	2	3	2	-
9	0.0592	1.3349	2	2	-	4	-
10	0.0793	1.2210	2	1	2	3	-
11	0.5513	0.9560	2	-	5	-	1
12	0.2498	0.9191	2	-	4	2	-
13	0.0404	1.1951	2	1	2	3	-
14	0.6005	0.9841	3	-	2	2	1
15	0.5262	0.9482	3	-	2	2	1
16	0.5284	0.9227	4	-	-	2	2

## 9.4 Variation in the bond angle

In this section, a second approach for joining a carbon nanotube to a graphene sheet is examined, the variation of the bond angle method as described in §7.1.2. For the graphene sheet, the bond angle is assumed to be  $120^\circ$ , while the bond angle for the carbon nanotube is again taken from [109]. Firstly, the case of a (6,0) carbon nanotube connecting with a six-fold type symmetric defect shown in Figure 9.2 is considered. Due to the six-fold type symmetry of the configuration, there is only one joining site that needs to be considered for which atom  $A_3$  on the sheet connects with atom  $C$  on the tube. Moreover, atoms  $A_1$  and  $A_2$  are assumed to be fixed but atom  $A_3$  can move around a circular path and its position is determined by an angle  $\theta$ . The five steps for determining atom positions at the connection site can be found in §7.1.2. In terms of a graphene sheet and on assuming that the bond length  $\sigma$  is  $1.42 \text{ \AA}$ , the bond angle is  $120^\circ$  and from the diagram in Figure 9.2, the coordinates

Table 9.2: Values of least square function  $f$  ( $\text{\AA}^2$ ) and distance  $\ell$  ( $\text{\AA}$ ) for 32 configurations of a (4,4) tube and corresponding polygons  $P_n$  where  $n$  is the number of sides. By symmetry #1-a and #1-b are equivalent.

Configurations #	$f$	$\ell$	$P_4$	$P_5$	$P_6$	$P_7$	$P_8$	$P_9$	$P_{10}$
1-a	0.0526	1.1548	-	2	1	3	1	1	-
1-b	0.0526	1.1548	-	2	1	3	1	1	-
2-a	0.0638	1.1501	-	1	2	4	-	1	-
2-b	0.0528	1.1798	1	2	-	2	1	2	-
3-a	0.4494	1.2208	-	4	-	-	2	2	-
3-b	0.0643	1.1157	-	-	2	6	-	-	-
4-a	0.3751	1.0544	-	2	3	-	1	2	-
4-b	0.0847	0.9834	1	-	1	4	2	-	-
5-a	0.0435	0.6723	-	-	6	-	-	2	-
5-b	0.2458	0.6746	2	-	-	2	4	-	-
6-a	0.5177	1.1151	-	-	4	2	2	-	-
6-b	0.3802	1.1098	-	2	2	-	4	-	-
7-a	0.3132	1.0767	1	-	3	1	2	1	-
7-b	0.2498	1.1093	-	1	3	1	3	-	-
8-a	0.0273	1.1968	-	-	3	4	1	-	-
8-b	0.1637	1.2151	1	2	1	-	2	2	-
9-a	0.0127	1.2968	-	-	2	6	-	-	-
9-b	0.0161	1.3612	2	2	-	-	-	4	-
10-a	0.0687	1.1979	1	-	2	3	1	1	-
10-b	0.0393	1.1624	1	1	2	1	1	2	-
11-a	0.0272	1.1240	2	-	2	-	3	-	1
11-b	0.5537	1.0920	-	-	5	-	3	-	-
12-a	0.0430	0.6309	2	-	2	-	2	2	-
12-b	0.1764	1.0026	-	-	4	2	2	-	-
13-a	0.2451	0.8439	2	-	2	1	-	3	-
13-b	0.0425	1.1583	-	1	2	3	2	-	-
14-a	0.0176	0.7303	2	-	1	2	2	-	1
14-b	0.2985	1.1284	1	-	4	-	1	2	-
15-a	0.0494	1.0936	3	-	1	-	1	2	1
15-b	0.4425	1.1057	-	-	4	2	2	-	-
16-a	0.0561	1.0353	4	-	-	-	-	2	2
16-b	0.3448	1.1007	-	-	4	2	2	-	-

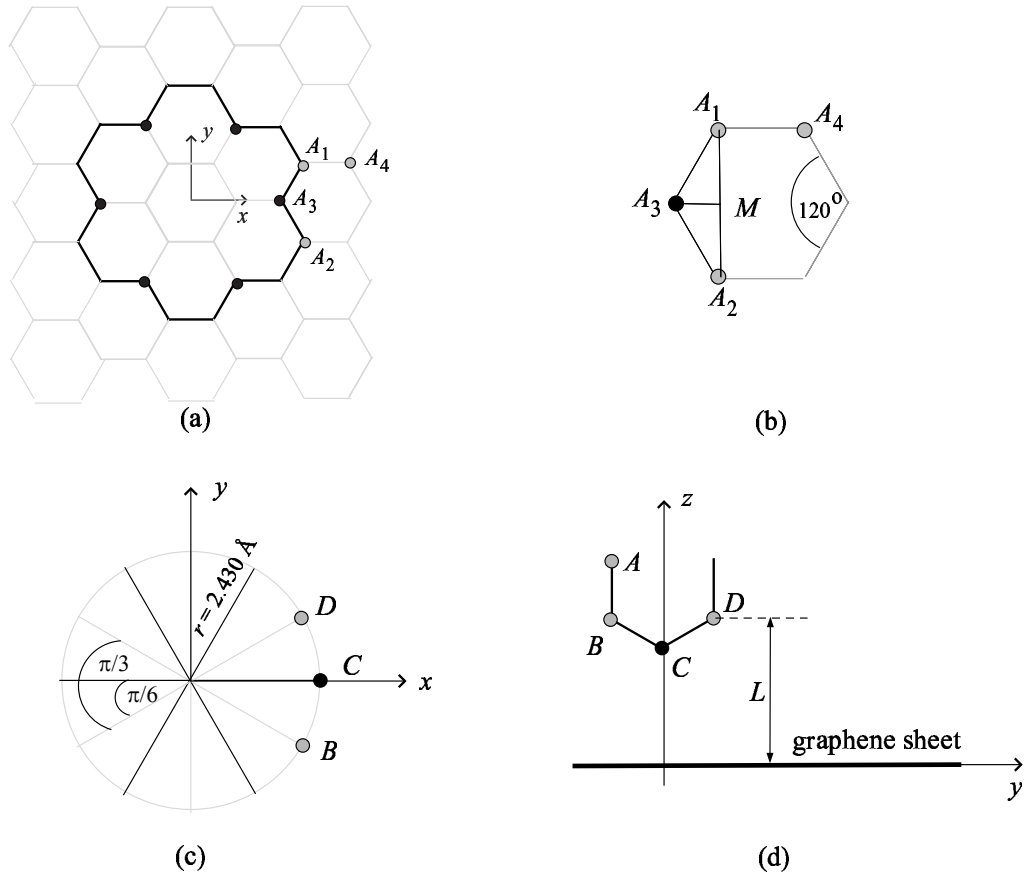


Figure 9.2: Model formation for joining a (6,0) tube with most symmetric defect where (a) and (b) are for a graphene sheet and (c) and (d) are for a (6,0) tube.

for the atoms  $A_1$ ,  $A_2$ ,  $A_3$  and  $A_4$  are given by

$$\begin{aligned} \mathbf{A}_1 &= \sigma \left( \frac{5}{2}, \frac{\sqrt{3}}{2}, 0 \right), & \mathbf{A}_2 &= \sigma \left( \frac{5}{2}, -\frac{\sqrt{3}}{2}, 0 \right), \\ \mathbf{A}_3 &= \sigma \left( \frac{5}{2} - \frac{1}{2} \cos \theta, 0, \frac{1}{2} \sin \theta \right), & \mathbf{A}_4 &= \sigma \left( \frac{7}{2}, \frac{\sqrt{3}}{2}, 0 \right). \end{aligned}$$

By precisely the same procedure, the coordinates for the atoms  $A$ ,  $B$ ,  $C$  and  $D$  on the tube can be expressed as

$$\begin{aligned} \mathbf{A} &= (2.105, -1.215, L + 1.42), & \mathbf{B} &= (2.105, -1.215, L), \\ \mathbf{C} &= (2.105 + 0.735 \sin \phi, 0, L - 0.735 \cos \phi), & \mathbf{D} &= (2.105, 1.215, L), \end{aligned}$$

where the atom  $C$  moves around a circular path given by the angle  $\phi$  and  $L$  is the spacing between the tube and the sheet as shown in Figure 9.2(d). Noting that  $L = \ell + 0.659 \text{ \AA}$  where  $\ell$  is defined in §9.3. Again following the work of Cox and Hill [109] the radius of the (6,0) tube is  $2.430 \text{ \AA}$  and the bond angle is given by  $117.65^\circ$ .

The variations of  $\theta$  and  $\phi$  from the normal physical bond angles, which are  $120^\circ$  and  $117.65^\circ$  are minimised where each bond length which joins between an atom of the tube to one on the sheet is restricted to be  $1.42 \text{ \AA}$ . Therefore, the constraints are the maximum distances of the hexagonal network which are  $|\mathbf{AC}| = |\mathbf{BA}_3| = 2.474 \text{ \AA}$  and  $|\mathbf{CA}_1| = |\mathbf{A}_3\mathbf{A}_4| = 2.460 \text{ \AA}$ . Using the optimisation package in MAPLE, all parameters are obtained as  $\theta = 30.73^\circ$ ,  $\phi = 9.39^\circ$  and  $L = 2.315 \text{ \AA}$ , and the three-dimensional figure is depicted in Figure 9.3 where the dashed and solid lines represent bonds in the background and foreground, respectively.

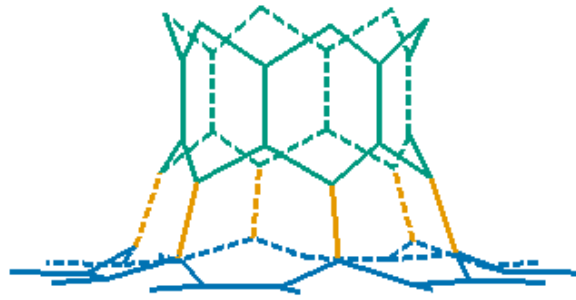


Figure 9.3: Three dimensional illustration for a (6,0) tube perpendicularly connected to a graphene sheet.

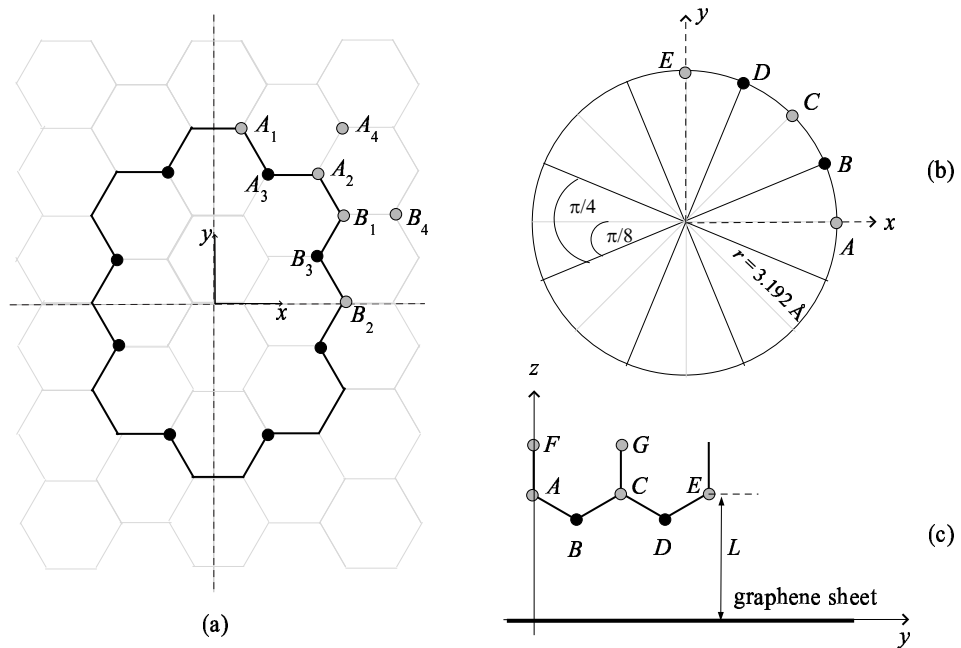


Figure 9.4: Model formation for joining an (8,0) tube with defect #6 where (a) is for a graphene sheet and (b) and (c) are for an (8,0) tube.

The same method is exploited to examine the joining of the (8,0) tube with defect #6 identified as the most likely configuration, which details of the classification can be found in §9.5. Since the defect #6 has four-fold symmetry, only the atoms in the first quadrant are examined and the positions of every atom are shown in Figure 9.4. Note that the spacing  $L$ , illustrated in Figure 9.4(c), is equivalent to  $L = \ell + 0.681$  Å where  $\ell$  is defined in §9.3. The calculation of the circular paths are examined and the coordinates for each atom are then given by:

$$\begin{aligned}\mathbf{A}_1 &= \sigma\left(\frac{1}{2}, 2\sqrt{3}, 0\right), & \mathbf{A}_2 &= \sigma\left(2, \frac{3\sqrt{3}}{2}, 0\right), \\ \mathbf{A}_3 &= \sigma\left(\frac{5}{4} - \frac{1}{4}\cos\theta_1, \frac{7\sqrt{3}}{4} - \frac{\sqrt{3}}{4}\cos\theta_1, \frac{1}{2}\sin\theta_1\right), & \mathbf{A}_4 &= \sigma\left(\frac{5}{2}, 2\sqrt{3}, 0\right), \\ \mathbf{B}_1 &= \sigma\left(\frac{5}{2}, \sqrt{3}, 0\right), & \mathbf{B}_2 &= \sigma\left(\frac{5}{2}, 0, 0\right), \\ \mathbf{B}_3 &= \sigma\left(\frac{5}{2} - \frac{1}{2}\cos\theta_2, \frac{\sqrt{3}}{2}, \frac{1}{2}\sin\theta_2\right), & \mathbf{B}_4 &= \sigma\left(\frac{7}{2}, \sqrt{3}, 0\right),\end{aligned}$$

$$\mathbf{A} = (3.192, 0, L),$$

$$\begin{aligned}\mathbf{B} &= (2.725 + 0.224\cos\phi_1 + 0.629\sin\phi_1, 1.129 + 0.093\cos\phi_1 + 0.261\sin\phi_1, \\ &\quad L - 0.681\cos\phi_1 + 0.243\sin\phi_1),\end{aligned}$$

$$\mathbf{C} = (2.257, 2.257, L),$$

$$\begin{aligned}\mathbf{D} &= (1.129 + 0.093\cos\phi_2 + 0.261\sin\phi_2, 2.725 + 0.224\cos\phi_2 + 0.629\sin\phi_2, \\ &\quad L - 0.681\cos\phi_2 + 0.243\sin\phi_2),\end{aligned}$$

$$\mathbf{E} = (0, 3.192, L), \quad \mathbf{F} = (3.192, 0, L + 1.42), \quad \mathbf{G} = (2.257, 2.257, L + 1.42),$$

where the radius of the (8,0) tube is 3.192 Å and the bond angle is given by  $118.70^\circ$  [109]. The computer package MAPLE is also employed to minimise the bond angles of the system with the set of the constraints  $|\mathbf{FB}| = |\mathbf{AB}_3| = |\mathbf{GD}| = |\mathbf{CA}_3| = 2.468$  Å and  $|\mathbf{B}_4\mathbf{B}_4| = |\mathbf{BB}_1| = |\mathbf{A}_3\mathbf{A}_4| = |\mathbf{DA}_2| = 2.460$  Å, where  $|\mathbf{BB}_3| = |\mathbf{DA}_3| = 1.42$  Å. For this configuration, the parameters are obtained as  $L = 2.222$  Å,  $\theta_1 = 38.85^\circ$ ,  $\theta_2 = 17.16^\circ$ ,  $\phi_1 = -42.29^\circ$  and  $\phi_2 = 2.53^\circ$  and the three-dimensional figure is presented in Figure 9.5(a). The corresponding structure previously obtained by minimisation of the bond length is shown in Figure 9.5(b), and it is clear that the two approaches give closely related structures in terms of atom locations. In order

to give a more mathematical measure for the difference between the atom locations of these two structures, the mean absolute error is determined, defined by

$$Error = \frac{1}{n} \sum_{i=1}^n |\mathbf{r}_{1i} - \mathbf{r}_{2i}|, \quad (9.2)$$

where in this case  $n = 16$  and  $Error = 0.372 \text{ \AA}$  (26.19% of bond length). Moreover, the difference in the spacing between the (8,0) tube and the graphene sheet in terms of  $L$  is obtained as  $0.22 \text{ \AA}$ . Therefore, in this case the two approaches give similar outcomes.

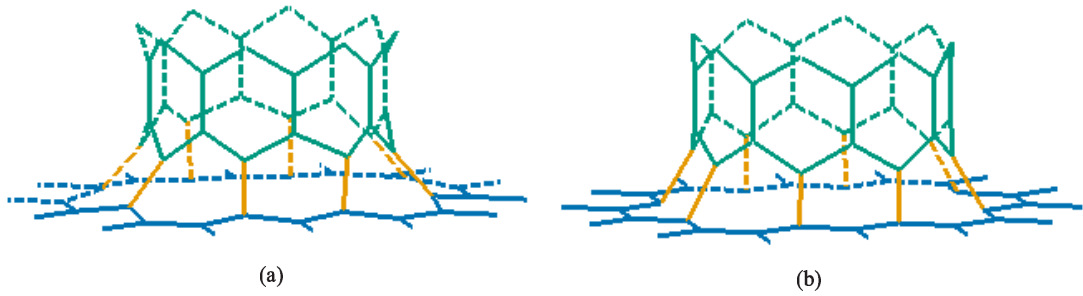


Figure 9.5: Three dimensional illustrations for an (8,0) connection with a graphene sheet by (a) variation in bond angle and (b) variation in bond length.

## 9.5 Results and discussion

Euler's polyhedra theorem is utilised here to examine the joining of a graphene sheet and a carbon nanotube. The details for Euler's theorem are presented in §7.2, and here the zigzag (8,0) and the armchair (4,4) tube, which topologically can be considered to be capped at one end with a hemispherical  $C_{60}$  fullerene comprising six pentagons, are considered. In order to maintain the Euler characteristic of any shape that a nanotube is joined to, the connection must necessarily become the six pentagons with the six heptagons or an equivalent number of other polygons. Therefore, the polygons which occur at the junction of the tube and the graphene sheet must satisfy

$$-2P_4 - P_5 + P_7 + 2P_8 + 3P_9 + 4P_{10} = 6, \quad (9.3)$$

and this equation is confirmed by the results in Table 9.1 and Table 9.2. Note that (9.3) is also true for any surface comprising of only hexagonal sides, e.g. connecting

a nanotube to a section of another nanotube to form a T-junction [108]. However, the square ring is very unstable for the carbon network [101] and heptagons and octagons can be introduced into the system [102], therefore there are twelve and eleven possible configurations for joining the (8,0) and the (4,4) tubes with the graphene sheet, respectively. Nevertheless, defects in a nanotube are experimentally observed with only pentagonal and heptagonal rings [103], and imposing this experimental requirement leaves only configuration #6 for the zigzag tube. Figure 9.6(a) illustrates the three-dimensional structure, where the solid lines are for foreground bonds and the dashed lines indicate hidden or background bonds. In a least squares sense, the configuration #3 gives the minimum value of  $f$ , which is  $0.0018 \text{ \AA}^2$ , and therefore this configuration might also be accepted despite the existence of octagonal rings as shown in Figure 9.6(b). Similarly by considering only pentagons and heptagons, the #3-b and #9-a configurations for the armchair (4,4) tube might be the most likely occurring structures. These structures coincide with the findings of Menon and Srivastava [108] for the T-junction of two carbon nanotubes. The three-dimensional illustrations for these two configurations are presented in Figure 9.7, where the solid lines are for foreground bonds and the dashed lines indicate hidden or background bonds. Noting that, the #9-a defect configuration (see Figure 9.7(b)) is more likely from a comparison of the values of the least squares function given in equation (9.1).

From these results, the joining of (8,0) tube to the defect #6 and the joining of (4,4) tube to the defect #9-a are the most likely to occur. In Table 9.3 and Table 9.4, numerical values of the atom positions in the Cartesian coordinate system are presented for the purpose of future comparisons. The configurations given are the sixteen atom positions at the junctions after the optimisation process for the (8,0) and the (4,4) tubes with the #6 and the #9-a defects, respectively. Note that the atom positions on the tubes are calculated from the new model for carbon nanotubes [109] and the atom positions on the graphene sheet are evaluated as usual, and for these two particular configurations  $X$ ,  $Y$  and  $\theta$  can be taken to be zero by an appropriate choice of the coordinate axes, as might be expected from the symmetries of both configurations.



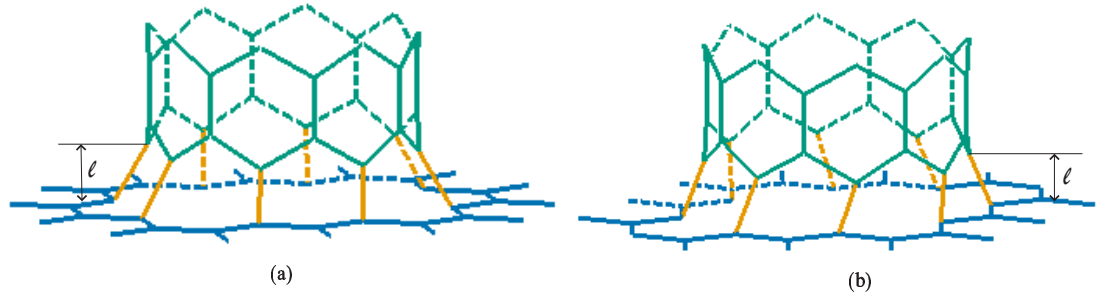


Figure 9.6: Connecting an (8,0) tube with a graphene sheet for the defect configurations (a) #6 and (b) #3.

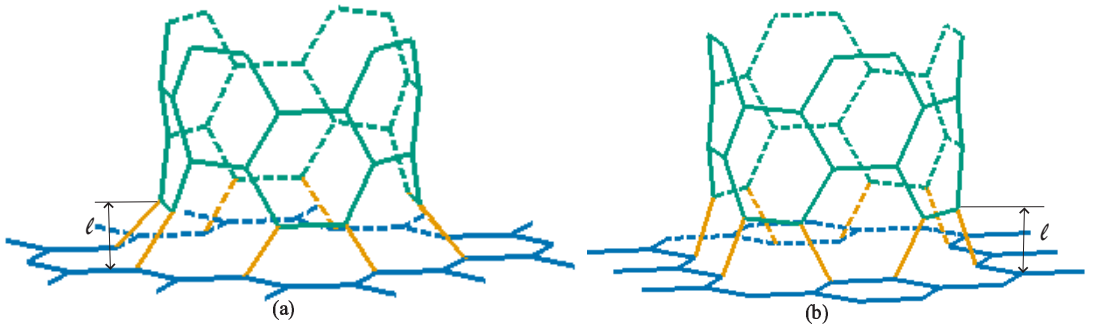


Figure 9.7: Connecting a (4,4) tube with a graphene sheet for (a) #3-b and (b) #9-a configurations. The second configuration has the smallest variation in bond length in a least squares sense.

Table 9.3: Eight coordinate positions for joining an (8,0) tube with defect #6 using the variation in bond length method.

Positions	1	2	3	4	5	6	7	8
(8,0) tube								
$x$	2.949	2.949	1.222	-1.222	-2.949	-2.949	-1.222	1.222
$y$	-1.222	1.222	2.949	2.949	1.222	-1.222	-2.949	-2.949
$z$	1.322	1.322	1.322	1.322	1.322	1.322	1.322	1.322
#6 sheet								
$x$	2.840	2.840	1.420	-1.420	-2.840	-2.840	-1.420	1.420
$y$	-1.230	1.230	3.689	3.689	1.230	-1.230	-3.689	-3.689
$z$	0	0	0	0	0	0	0	0

Table 9.4: Eight coordinate positions for joining a (4,4) tube with defect #9-a using the variation in bond length method.

Positions	1	2	3	4	5	6	7	8
(4,4) tube								
$x$	2.389	1.379	-1.379	-2.389	-2.389	-1.379	1.379	2.389
$y$	1.379	2.389	2.389	1.379	-1.379	-2.389	-2.389	-1.379
$z$	1.297	1.297	1.297	1.297	1.297	1.297	1.297	1.297
#9-a sheet								
$x$	2.840	0.710	-0.710	-2.840	-2.840	-0.710	0.710	2.840
$y$	1.230	2.460	2.460	1.230	-1.230	-2.460	-2.460	-1.230
$z$	0	0	0	0	0	0	0	0

## 9.6 Summary

Two distinct least square approaches are utilised in this chapter to determine the perpendicular joining of three particular carbon nanotubes to a flat graphene sheet. Firstly, all possible structures for connecting the zigzag (8,0) and the armchair (4,4) carbon nanotubes to a flat graphene sheet are determined. Here, the least squares method is employed to minimise the variation in bond length at each inter-atomic junction from the bond length between two carbon atoms. There are eight carbon atoms at the open end of both (8,0) and (4,4) tubes which require the other bond to satisfy the  $sp^2$  network, and therefore sixteen defect patterns in the graphene sheet are identified. Furthermore, an adjacent atom on the armchair tube end is bonded either by three bonds or a single bond so that there are in total thirty-two configurations that connect the armchair tube and the sheet. There are sixteen structures for joining the zigzag tube due to the symmetric locations of the atoms on the tube end. From a topological point of view, Euler's polyhedra theorem is utilised to prescribe the polygons which occur at the junction. In order to maintain the Euler characteristic by connecting the nanotube, (9.3) must be satisfied. This applies for all cases when a carbon nanotube is connected to a surface comprising of only hexagonal sides. For reasons of stability, the only carbon rings realizable are pentagonal, hexagonal, heptagonal and octagonal, and by imposing this the number of configurations is reduced to twelve and eleven for the zigzag and the armchair tubes, respectively. Furthermore, octagonal rings are considered less likely to occur, and therefore only configuration #6 for the zigzag tube and #3-b and

#9-a for the armchair tube might be expected to be found in practice. The result of the least squares analysis indicates that the junction which is most favoured is the configurations #3 for the zigzag and #9-a for the armchair, which are illustrated in Figure 9.6(b) and Figure 9.7(b).

In terms of the least squares bond angle approach, which assumes that all bond lengths are fixed to be  $\sigma = 1.42 \text{ \AA}$ , a simple example for joining a flat graphene sheet to a (6,0) carbon nanotube is presented, which is the most symmetric possibility for the defect. Subsequently, for the (8,0) tube and the defect structure #6, which is believed to be the most favoured configuration, a least squares bond angle approach is undertaken. The structure obtained for the (8,0) and the sheet is shown to be very similar in terms of atom locations to that found using the bond length approach.

# Chapter 10

## Joining boron nitride nanotubes and flat sheets

Since boron nitride nanostructures are considered to be good electronic materials [34], in this chapter and with reference to the same problem in Chapter 9, the classification of defect geometries for combining boron nitride structures is elucidated. Specifically, possible joining structures between a boron nitride nanotube and a flat sheet of hexagonal boron nitride are determined. Firstly, the appropriate defect configurations are investigated on which the tube can be connected, given that the energetically favourable rings for boron nitride structures are rings with an even number of sides. A new formula  $E = 6 + 2J$  relating the number of edges  $E$  and the number of joining positions  $J$  is established for each defect, and the number of possible distinct defects is related to the so-called necklace and bracelet problems of combinatorial theory. Two least squares approaches, which are the variation in bond length and the variation in bond angle, are also employed to determine the perpendicular connection of both zigzag and armchair boron nitride nanotubes with a boron nitride sheet. Here, three boron nitride tubes, which are (3,3), (6,0) and (9,0) tubes, are joined with the sheet, and Euler's theorem is used to verify geometrically that the connected structures are sound, and their relationship with the bonded potential energy function approach is discussed. For zigzag tubes  $(n, 0)$ , it is proved that such connections investigated here are possible only for  $n$  divisible by 3. The essential mathematical ideas elucidated here are relevant to combining all boron nitride nanostructures and are quite different to those required for connecting the corresponding carbon structures.

## 10.1 Nomenclature

$\phi(d)$	is the Euler's totient function
$\sigma$	is the boron-nitrogen covalent bond length
$\theta$	is the rotational angle of the boron nitride nanotube
$E$	is the number of edges of the polyhedron
$F$	is the number of faces of the polyhedron
$J$	is the number of joining position between the boron nitride sheet and the boron nitride nanotube
$P_n$	is the number of $n$ -gonal sides
$V$	is the number of vertices of the polyhedron
$V_r, V_\theta$	are the variation summations of bond length and bond angle, respectively
$\mathbf{a}_i, \mathbf{b}_i$	are the positions of terminal atoms on the boron nitride sheet and the boron nitride nanotube, respectively
$\ell$	is the spacing between the boron nitride sheet and the boron nitride nanotube in the positive $z$ -direction

## 10.2 Introduction

Boron nitride is a binary chemical compound consisting of equal number of boron and nitrogen atoms with various polymorphic forms. The diamond-like polymorph of boron nitride is one of the hardest materials known. The hexagonal structure of boron nitride is geometrically similar to that of graphite in carbon structures [33, 123], and in the periodic table, boron and nitrogen are adjacent to carbon [33]. With excellent stability and thermal conductivity, boron nitride can be used in vacuum technology, the nuclear energy industry, and for the development of X-rays and lubrication [35].

As with carbon nanostructures, boron nitride nanostructures such as nanotubes and fullerene-like structures have been widely investigated, with Rubio *et al.* [34]

being the first to study a boron nitride nanotube. These authors find that the electronic properties of boron nanotubes are independent of both their chirality and the tube radii, and all nanotubes are semiconducting materials. Employing an arc discharge technique, Terrone *et al.* [124] synthesise boron nitride nanotubes and find that the ratio of boron to nitrogen atoms is approximately one to one. A number of studies show that the most energetically favourable bond in the hexagonal boron nitride network is the bond between the boron and the nitrogen atoms (see for example [125–130]). Consequently, boron nitride structures are formed from an even number of sides to each ring with the atom species alternating, and these rings are normally squares, hexagons and octagons.

In order to transmit signals to future nanoelectromechanical devices, connections between a platform and other nanostructures may need to be considered. Given the consistent electronic properties of boron nitride nanostructures, a hexagonal boron nitride sheet can be considered as the platform for such devices. Since the electronic properties of boron nitride nanotubes do not depend on their physical configurations, this material is a good candidate to transmit signals to other materials. With this in mind, the perpendicular joining configurations between a boron nitride tube with a hexagonal boron nitride plane sheet is investigated.

The first question which arises is how defects are determined to which the tube can be joined such that all the polygons at the junction comprise rings which all have an even number of sides, such as squares, hexagons and octagons. Firstly, the relation between the number of edges, which form the defect, and the number of atoms on the defect, that can be joined with the tube, are determined. Since a closed defect is required, it is clear that the total angle of such a defect needs to comprise a complete  $360^\circ$  turn. Therefore, each of the six edges of a hexagonal lattice are assigned the angle values as shown in Figure 10.1. Furthermore, all possible defect structures that can be joined with the tube open end are examined, and the distinct number of possible defects relates to the so-called necklace and bracelet problems of combinatorics.

After the geometric analysis, the least squares minimisation method is further utilised to examine the perpendicular joining of a boron nitride nanotube and a flat boron nitride sheet. Here, variations in both bond length and bond angle are

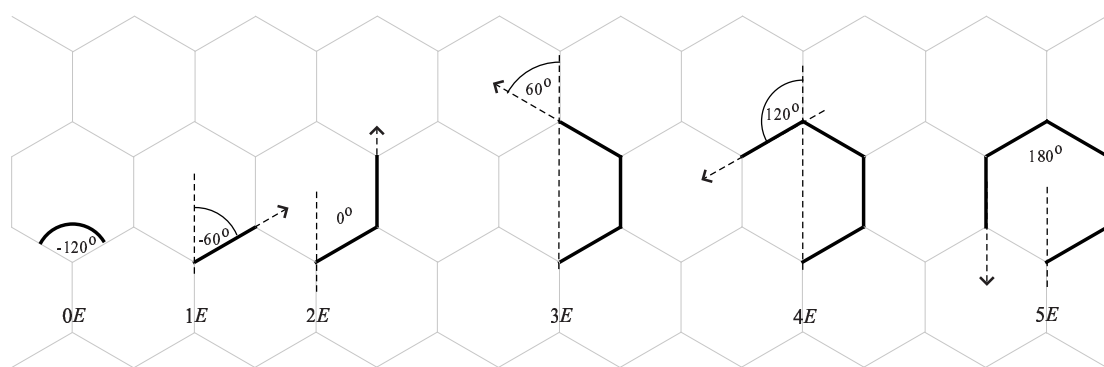


Figure 10.1: Angle values defined by each of the six sides of a hexagonal lattice.

studied as described in §7.1. In the first method, the distance between an atom on the tube open end and an atom on the sheet from the ideal bond length, taken to be  $\sigma = 1.45 \text{ \AA}$ , is minimised. In the latter technique, all bond lengths are assumed to be fixed to be exactly the assumed bond length  $\sigma$  and the variation in the bond angle at the connecting site is minimised. Both of these geometric approaches can be directly related to certain numerical energy minimisation methods used by a number of authors [13–16] as discussed in §7.3. Moreover, Euler’s polyhedra theorem is applied for all connected configurations to verify that rings with an even number of sides occur at the junction.

In the following two sections, a procedure to classify the defect configurations on hexagonal boron nitride sheet to which the boron nitride nanotubes can be joined is proposed. Using the two variation methods presented in §7.1, connected structures are discussed in §10.6 which involve in Euler’s polyhedra theorem and the bonded interaction energy. A summary of results is presented in §10.7.

### 10.3 Defect classification

In this and the following sections, the appropriate defect structures on a hexagonal boron nitride sheet to which boron nitride nanotubes can be perpendicularly joined such that the connected structures also satisfy Euler’s polyhedra theorem are determined. All the atoms are assumed to require the  $sp^2$  configuration to form an even number-sided polygonal ring network. Compared to the previous study on carbon nanotube connections in Chapter 9, there are less possible defect configurations for boron nitride structures, due to the even number side rings being energetically

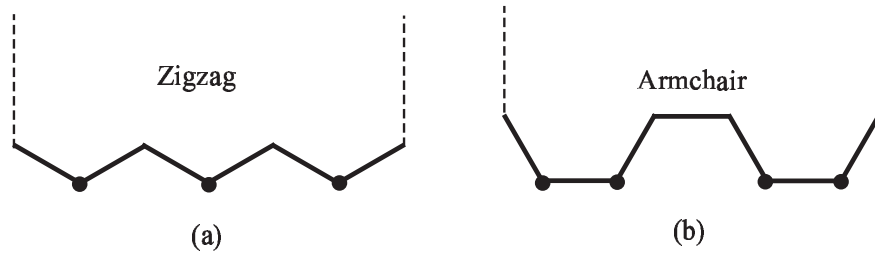


Figure 10.2: Atoms at open end of (a) a zigzag tube and (b) an armchair tube.

more favourable. One implication of this constraint is that a zigzag tube where two adjacent atoms at the tube open end are connected by two bonds, as shown in Figure 10.2(a), must join to a defect which has an even number of bonds joining between the two nearest atoms in order to complete the  $sp^2$  structure. Likewise, two adjacent atoms on the open end of an armchair tube have either one or three bonds connecting them, as shown in Figure 10.2(b), and therefore an armchair tube must join to a defect which has an odd number of bonds joining nearest atoms.

Initially, the relationship between the number of edges and the number of atoms for any defect which will bond to the open end of the nanotube to complete the  $sp^2$  structure is determined. In Figure 10.3, some typical defects are depicted and all the connecting positions for each defect are shown, where atoms are denoted by either black dots or gray squares depending on whether they require one or two bonds to complete the  $sp^2$  structure, respectively. Consequently, there is one joining position for the black dot and there are two joining positions for the gray square. In the case that two hexagons share a side, the edges need to be counted twice. Therefore, the number of edges and the number of joins which correspond to the defects in Figure 10.3 are presented in Table 10.1. It can be seen that the number of edges ( $E$ ) depends on the number of joining positions ( $J$ ) which can be written as

$$E = 6 + 2J. \quad (10.1)$$

Next, defects are determined such that all atoms which need to be joined with the tube are connected by either an odd or even number of bonds, and this problem leads one to consider the angles of the sides for a hexagonal ring. There are six possible angles with respect to an atom position corresponding to the six sides of the hexagon as shown in Figure 10.1, and note that the angles are defined in a counter-clockwise



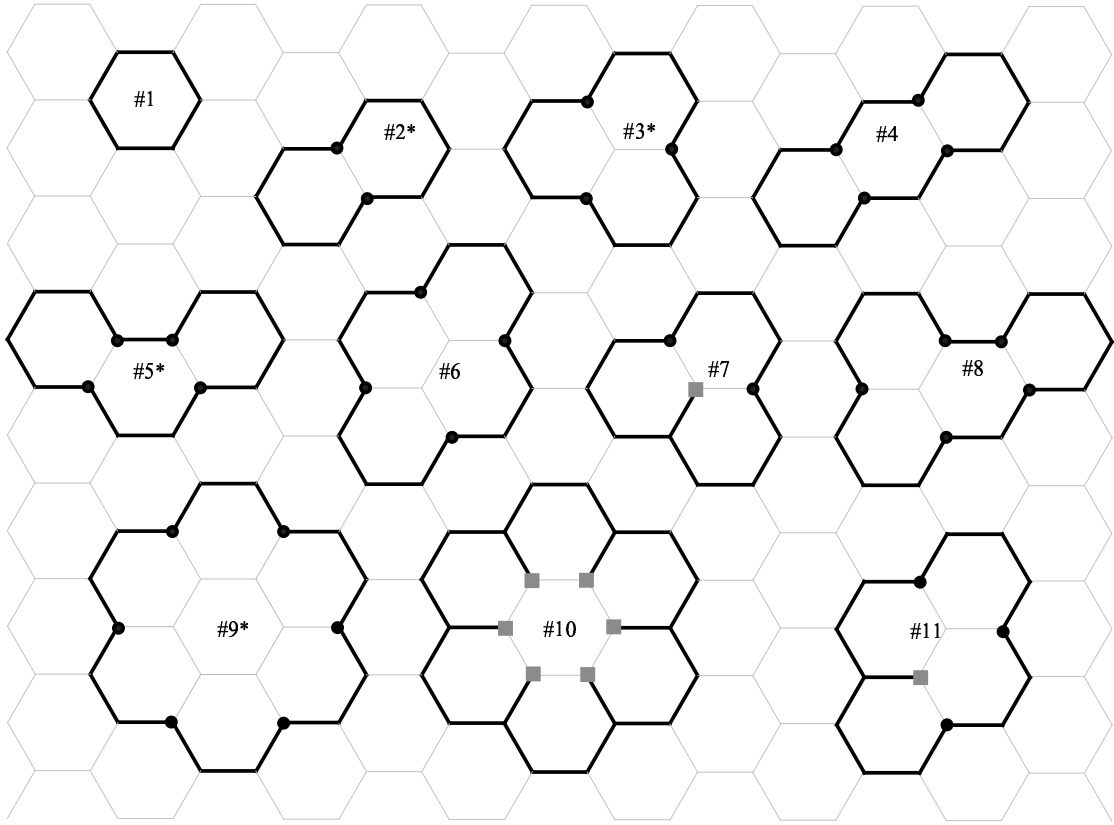


Figure 10.3: Some typical defects showing the number of edges and the number of atoms that can be joined (those marked \* are possible boron nitride defects).

direction. In other words, each angle is related to the number of bonds connecting between two adjacent atoms. Consequently, for an armchair (zigzag) tube which requires an odd (even) number of bonds for the defect, the defect structure needs to be constructed with  $1E, 3E$  and  $5E$  ( $0E, 2E$  and  $4E$ ) edges as defined in Figure 10.1. Note that for convenience, the number of edges  $1E, 2E, 3E, 4E, 5E, 6E$  are simply referred to by the integers 1, 2, 3, 4, 5, 6 in order to construct the sequences examined in §10.4. At any joining position there are three possible paths to choose from to form the defect, and the angle between two of them is  $-120^\circ$  in a clockwise direction. Moreover, in every moving step (side), the angle will change by  $60^\circ$ . Hence, this can be written as  $-120J + 60E$ . From the fact that the defect must be closed, the total angle obtained by joining the sides of the hexagonal lattice needs to make a complete  $360^\circ$  turn and from (10.1), it can be deduced

$$-120^\circ J + 60^\circ(6 + 2J) = 360^\circ, \quad (10.2)$$

which indicates that the total angle of the system will always be  $360^\circ$ , but note that a

Table 10.1: Relation between the number of edges ( $E$ ) and number of joins ( $J$ ) for defects (those marked \* are possible boron nitride defects).

Configuration	Number of edges	Number of joins
#1	6	0
#2*	10	2
#3*	12	3
#4	14	4
#5*	14	4
#6	14	4
#7	14	4
#8	16	5
#9*	18	6
#10	30	12
#11	16	5

turn of  $360^\circ$  only satisfies the rotational requirement but not necessarily the translational condition that the two end points meet. Alternatively, this argument leading to equation (10.2) may be viewed as a formal derivation of equation (10.1). In the next section, combinatorial theory for the so-called necklace and bracelet problems is employed to determine the distinct defect configurations for both armchair and zigzag boron nitride tubes.

## 10.4 Combinatorial theory and possible defects

Only the sequence of 1, 3, 5 and 0, 2, 4 for an armchair  $(n, n)$  and a zigzag  $(n, 0)$  boron nitride tube, respectively, can be used, so as to add up to the value of  $E$  defined by (10.1), where  $J$  is  $2n$  for an armchair tube and  $n$  for a zigzag tube. Moreover, the number of terms in the sequence must be equal to  $2n$  and  $n$  for the armchair and the zigzag tubes.

For example, for a (6,0) tube  $E$  is obtained as  $E = 18$  and six terms chosen from 0, 2, 4 are needed to form a sequence. In this case, there are two distinct ways to generate the sequences, which are  $[4, 4, 4, 2, 2, 2]$  and  $[4, 4, 4, 4, 2, 0]$ . The permutations of these two sets of data, ignoring rotationally symmetric representations, are required from which all possible defects are determined, and they are given respectively by

$$\{4, 4, 4, 2, 2, 2\}, \quad \{4, 4, 2, 4, 2, 2\}, \quad \{4, 4, 2, 2, 4, 2\}, \quad \{4, 2, 4, 2, 4, 2\},$$

and

$$\{4, 4, 4, 4, 2, 0\}, \quad \{4, 4, 4, 4, 0, 2\}, \quad \{4, 4, 4, 2, 4, 0\}, \quad \{4, 4, 4, 0, 4, 2\}, \quad \{4, 4, 2, 4, 4, 0\},$$

noting that square brackets is used to designate the unordered combination, while the curly braces designate a particular ordering of the permutation. After a rotation, the second and the third permutations in the first group have a mirror image or flip symmetry property. Similarly, the first and the second permutations, and the third and the fourth permutations in the second group also have a mirror image or flip symmetry property after a rotation. Once the defects are determined, the mirror image symmetry configurations will provide the same structure when the tube is joined, and therefore they can be ignored.

This problem is closely related to necklace permutations representing the number of distinct ways in which a  $k$  bead necklace of  $i$  colours can be made. Following the work of Knuth [131] and Ruskey and Sawada [132], the expression for the necklace permutation may be written

$$N(k_1, k_2, \dots, k_i) = \frac{1}{k} \sum_{d|\gcd(k_1, k_2, \dots, k_i)} \phi(d) \left( \frac{(k/d)!}{(k_1/d)!(k_2/d)! \dots (k_i/d)!} \right), \quad (10.3)$$

where  $k = k_1 + k_2 + \dots + k_i$  and  $\phi(d)$  is Euler's totient function given by

$$\phi(d) = d \prod_{p|d} \left( 1 - \frac{1}{p} \right),$$

where the product ranges only over all distinct primes  $p$  which divide  $d$ . In the case where there are only  $j$  beads of black and  $k - j$  beads of white for the necklace, the expression (10.3) simplifies to become

$$N(k, j) = \frac{1}{k} \sum_{d|(k, j)} \phi(d) \binom{k/d}{j/d}, \quad (10.4)$$

where  $d$  denotes all common divisors of  $k$  and  $j$  and the last term is the usual binomial coefficient.

However, due to the symmetry of the joining nanotubes, the mirror image symmetric configurations need not be considered, and this problem is referred to as the bracelet permutation, which is a necklace permutation which remains unchanged when flipped over. To the author's knowledge, there is no general formula to de-

termine the necklace permutations for a  $k$  bead bracelet of  $i$  colours. Nevertheless, Bower [133] has developed a sequence for  $k$  beads of  $j$  black and  $k - j$  white beads which can be found in A052307 [133] and can be written as

$$B(k, j) = \frac{1}{2} \left( N(k, j) + T(k, j) \right),$$

where  $N(k, j)$  is defined in (10.4) and

$$\begin{aligned} T(k, j) &= \binom{k/2}{j/2} && k \text{ and } j \text{ are even,} \\ &= \binom{(k-2)/2}{(j-1)/2} && k \text{ is even and } j \text{ is odd,} \\ &= \binom{(k-1)/2}{j/2} && k \text{ is odd and } j \text{ is even,} \\ &= \binom{(k-1)/2}{(j-1)/2} && k \text{ and } j \text{ are odd.} \end{aligned}$$

Here, the algebraic computer package MAPLE is utilised to determine the defect possibilities by undertaking the bracelet permutations for beads of three colours. Firstly, all bracelet permutations are determined for both armchair and zigzag boron nitride nanotubes for every possible form of sequences. Given that the defects are required to close a circuit, the number of permutations is reduced, and only the number of the closed circuit defects are presented in Table 10.2. Clearly some of the defects do not have a physically sensible structure for which to join an open end of a circular tube, and such defects will not occur in practice. Since the number of physically appropriate defects rapidly increases for increasing  $n$  for armchair  $(n, n)$  and zigzag  $(n, 0)$  tubes, in Figure 10.4, only the defects which are most likely to occur physically corresponding to certain values of  $n$  are depicted.

Table 10.2: Number of possible defects for zigzag  $(n, 0)$  and armchair  $(n, n)$  boron nitride tubes.

Zigzag tube	Number of defects	Armchair tube	Number of defects
(3,0)	1	(3,3)	4
(6,0)	2	(4,4)	5
(9,0)	7	(5,5)	17
(12,0)	35	(6,6)	40
(15,0)	231	(7,7)	138
		(8,8)	422

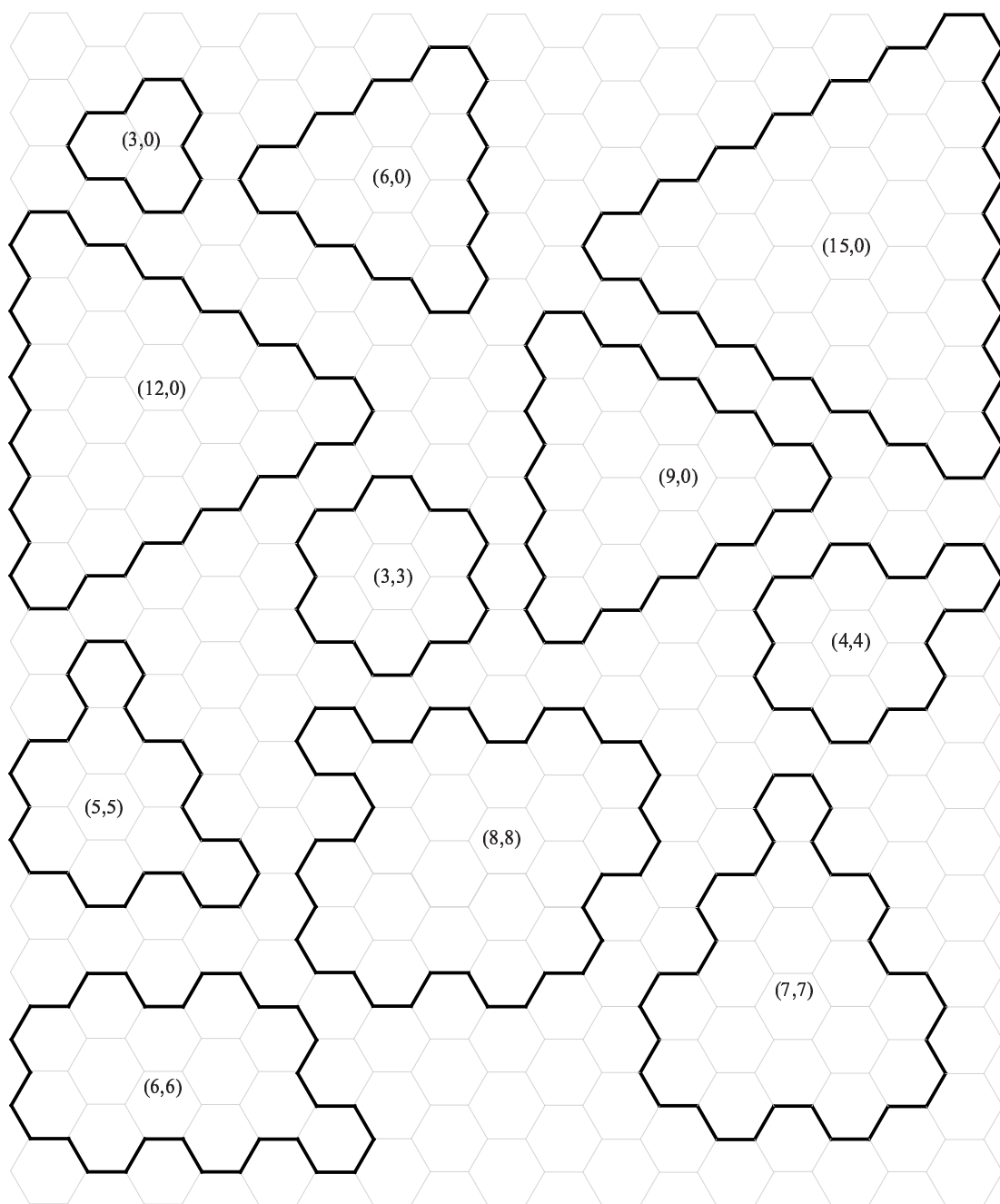


Figure 10.4: Most likely physical defects for various zigzag and armchair nanotubes.

Numerical results indicate that defects for the zigzag  $(n, 0)$  tubes only occur if  $n$  is divisible by 3, a result which can be formally established as follows. To begin, the defect for the smallest zigzag tube which is the  $(3, 0)$  tube is determined, and subsequently this defect is extended to that for  $(6, 0)$  as shown in Figure 10.4, and so on. The smallest closed circuit defect corresponding to the  $(3, 0)$  tube is a closed circuit defect  $\{4, 4, 4\}$ , as shown in Figure 10.4. The aim is to add edges to this defect such that the complete circuit defect is still closed and comprises only an even number of edges between adjacent atoms. As previously noted, zigzag tubes require a defect which comprise only 0, 2, and 4 edges between connecting atoms. Given that boron and nitrogen atoms are alternately bonded to form a hexagonal lattice, two triangular sublattices may be thought of as the basis units super-imposing to form such a hexagonal network. In Figure 10.5(a), the directional vectors for 2 and 4 are observed to be in opposite directions, and are provided three different directions for the three sides of the triangular lattices. Consequently, any closed circuit system will be invariant under translation when adding one of 2 and one of 4 in opposite directions. Likewise, a closed circuit will be rotationally invariant by adding one of 0 and one of 4 into the system, since the  $-120^\circ$  of 0 and  $120^\circ$  of 4 will balance each other out, as shown in Figure 10.5(b). Accordingly, there are three possibilities to add the set of  $[0, 2, 4]$  to any closed circuit such that the new defect will still be valid for a zigzag boron nitride tube and these are:

1. add three 2's in distinct directions,
2. add three 4's in distinct directions, and three 0's to maintain the rotational invariance,
3. add one 2 in the opposite direction to one 4, and one 0 to maintain the rotational invariance.

For the above three possibilities, it can be seen that if three of 2 are added to make a complete circuit, the defect is invariant under translation, and the defect is automatically invariant under rotations since the rotational angle of 2 is  $0^\circ$ . Similarly, by adding three 0's and three 4's provides the zero rotational angle for the defect, and three 4's also provide the closed circuit defect which maintains the translational property. Finally, the directional vectors of 2 and 4 are in opposite

directions and the system maintains the translational property by adding one of each, and one 0 is required to maintain the rotational property.

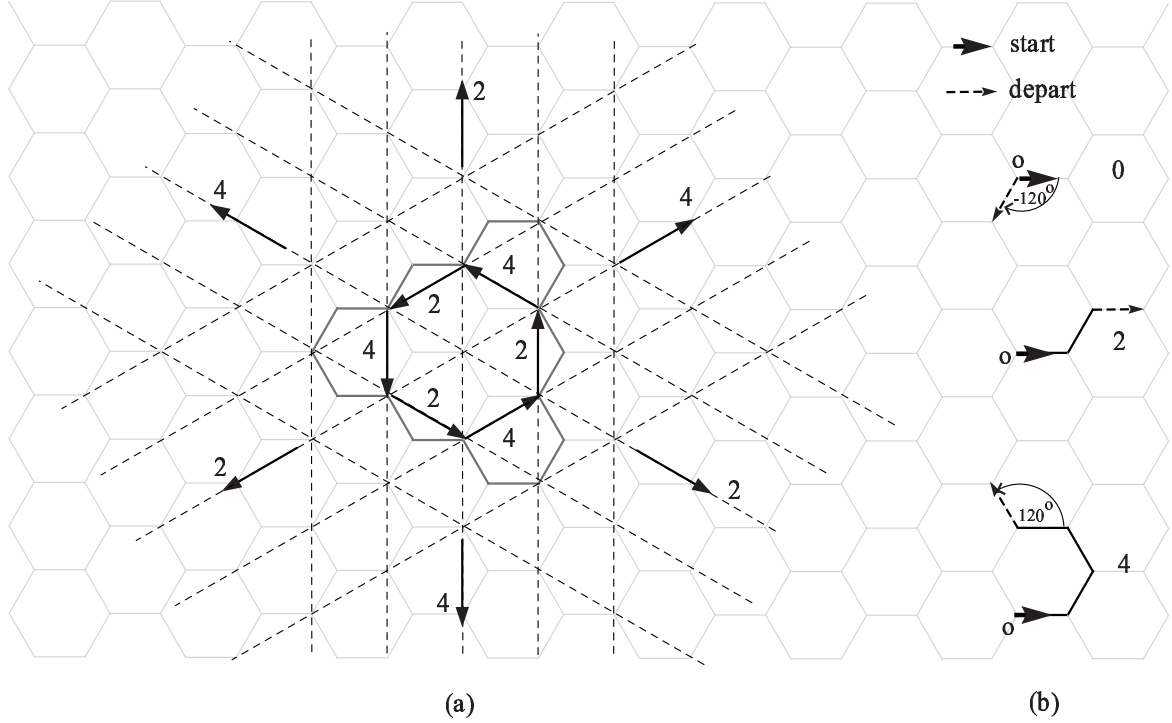


Figure 10.5: Hexagonal lattice formed from two triangular sublattices for boron nitride network, (a) translational vectors and (b) rotational angles.

Now, if  $x, y$  and  $z$  are assigned to be the respective number of each of these possibilities present in a given defect, it can be shown that

$$\begin{aligned} \text{number of 0's} &= 3y + z, \\ \text{number of 2's} &= 3x + z, \\ \text{number of 4's} &= 3 + 3y + z, \end{aligned}$$

where the smallest defect for the zigzag tube is  $\{4, 4, 4\}$ , which is added for the number of 4's in the last equation. Then, by addition of the above, it can be deduced

$$(n/3) = 1 + x + 2y + z, \quad (10.5)$$

and therefore  $n$  must be divisible by 3 for a zigzag boron nitride tube. Alternatively, (10.5) may be derived from (10.1) which becomes  $E = 2(3x + z) + 4(3 + 3y + z)$ . Since  $E = 6 + 2J$  and  $J = n$  for a zigzag tube, one can deduce (10.5).

## 10.5 Two least squares approaches

Following the methodology of [11] and §7.1, two least squares approaches, the variation in bond length and the variation in bond angle, are employed here to determine the perpendicular connecting structures between a boron nitride nanotube and a hexagonal boron nitride sheet. The ideal bond length between boron and nitrogen atoms is assumed to be  $\sigma = 1.45 \text{ \AA}$  [33, 34], and all atoms are connected by the  $sp^2$  structure. In this study, all the atom positions and bond angles for the boron nitride tube are calculated using the same routine as that used by Cox and Hill [109], which provides a new geometric model of carbon nanotubes, but where the bond length here is taken to be  $\sigma = 1.45 \text{ \AA}$ .

A brief review for the variation in bond length approach is given here. The  $i$ th terminal atoms at a join location is defined by the position vectors  $\mathbf{a}_i = (a_{xi}, a_{yi}, a_{zi})$  and  $\mathbf{b}_i = (b_{xi}, b_{yi}, b_{zi})$  for a sheet and a tube open end, respectively. The boron nitride sheet is assumed to be located in the  $(x, y)$  plane  $z = 0$ , and it is allowed to move in both  $x$ - and  $y$ -directions by distances  $X$  and  $Y$ , respectively, which can be either positive or negative. The position vector for the atoms at the defect on the boron nitride sheet is given by  $\mathbf{a}_i = (a_{xi} + X, a_{yi} + Y, 0)$ . In terms of the atoms on the tube open end, the spacing between the tube and the sheet is assumed to be  $\ell$ , and the tube can be rotated about the  $z$ -axis through an angle  $\theta$ . Consequently, the position vector for the atoms at the tube open end can be written as  $\mathbf{b}_i = (b_{xi} \cos \theta - b_{yi} \sin \theta, b_{xi} \sin \theta + b_{yi} \cos \theta, \ell)$ . Therefore, Euclidean distance between the atoms is obtained, as given by (7.1), and the objective function (7.2) needs to be determined.

Again, only a brief summary for the variation in bond angle method is presented, and full details can be found in §7.1.2. For this approach, the bond lengths are assumed to be fixed at  $\sigma$  and the bond angles at connection sites are varied so as to minimise the least square deviations from the physical bond angle values for both the sheet and the tube. The boron-nitrogen bond length is taken to be  $\sigma = 1.45 \text{ \AA}$ , the bond angles of the boron nitride sheet are assumed to be  $120^\circ$ , and the bond angles on the boron nitride tubes are taken from the new model of carbon nanotubes [109]. A five steps procedure for determining the position vectors for all atoms at the junction is presented in §7.1.2.



## 10.6 Results and discussion

Once a number of appropriate defects are determined, both the variation in bond length and the variation in bond angle approaches are undertaken to determine the most likely connected structures for the tube and the sheet of boron nitride. Here, some examples of such structures are demonstrated where (3,3), (6,0) and (9,0) boron nitride nanotubes are joined to the defects shown in Figure 10.6(a), (b) and (c), which are those where the geometry of the defect corresponds to the circular cross-section of the tube open end. All numerical calculations are carried out using the algebraic computer package MAPLE. Three dimensional figures for the (3,3), (6,0) and (9,0) boron nitride tubes joined with the hexagonal boron nitride sheets are illustrated in Figure 10.7 - 10.9 for both approaches.

In terms of polygonal rings which occur at the connection site, Euler's polyhedra theorem is utilised to verify that the proposed structures are geometrically sound. Euler's polyhedra theorem states that

$$F + V - E = \chi,$$

where  $F$ ,  $V$  and  $E$  denote the numbers of faces, vertices and edges for the given polyhedron and  $\chi$  is the Euler characteristic. For the sheet, letting  $P_n$  be the number of  $n$ -gon sides and every atom is linked with three others in the  $sp^2$  structure, Euler's theorem states that

$$2P_4 + P_5 - P_7 - 2P_8 = 0, \quad (10.6)$$

where any surface which is homeomorphic to a flat sheet has an Euler characteristic of 0. Given that only an even number of side rings are most energetically favourable,  $P_5$  and  $P_7$  are zero. For the junction, once the sheet is joined with the tube three  $P_4$ 's are required to form a cap at the unjoined end of the tube to provide the closed structure, and therefore the equation corresponding to (10.6) is obtained

$$P_8 - P_4 = 3. \quad (10.7)$$

For all three cases examined here, three octagonal rings, zero square rings and  $n$  hexagonal rings occur at the connection site. These results all satisfy Euler's polyhedra theorem since hexagons do not arise in equation (10.7) and the three

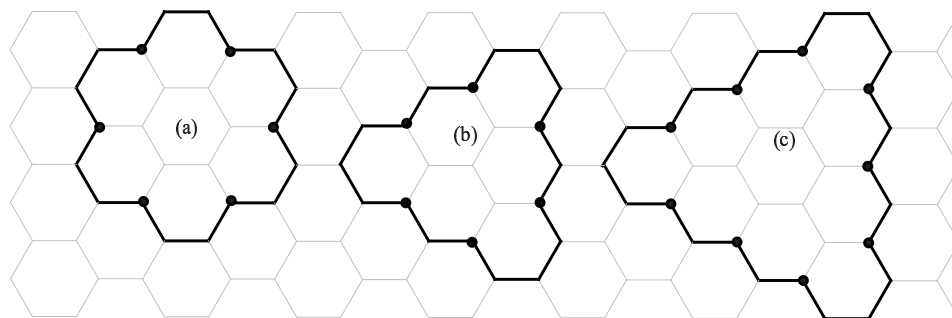


Figure 10.6: Defect configurations for (a) (3,3), (b) (6,0) and (c) (9,0) boron nitride nanotubes.

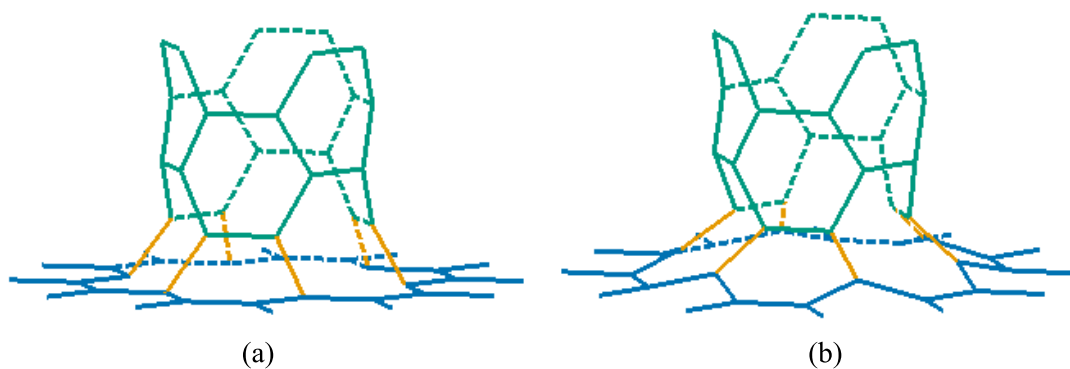


Figure 10.7: (3,3) nanotube connected with a hexagonal boron nitride sheet by (a) variation in bond length and (b) variation in bond angle.

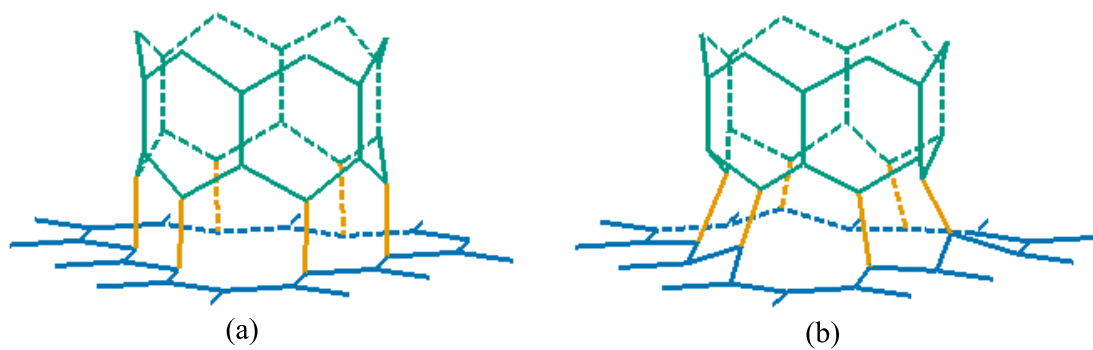


Figure 10.8: (6,0) nanotube connected with a hexagonal boron nitride sheet by (a) variation in bond length and (b) variation in bond angle.

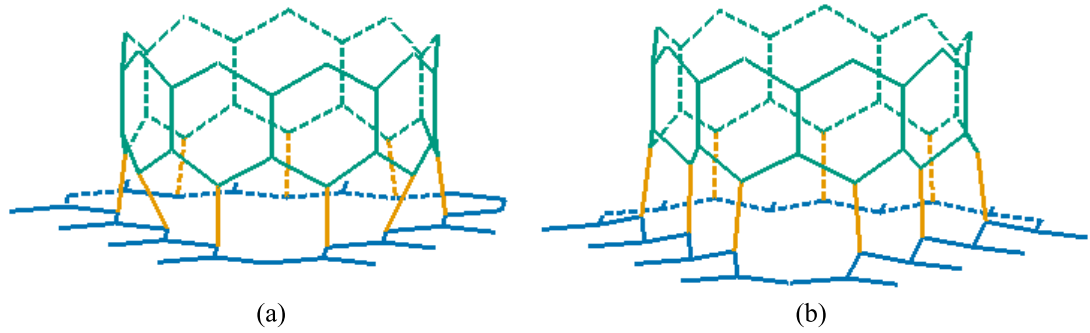


Figure 10.9: (9,0) nanotube connected with a hexagonal boron nitride sheet by (a) variation in bond length and (b) variation in bond angle.

nanotubes can be considered to be capped at one end with the polygonal network, which also satisfies Euler's polyhedra theorem, so that three octagons are required to form a closed structure.

A number of authors [13–16] adopt a numerical minimum energy principle such that the bonded potential energy for small deformations is given by (7.6). The numerical values for the variation of bond stretching as well as the percentage difference from the assumed bond length 1.45 Å, and the bending angle as well as the percentage difference from the assumed bond angle 120° for all three examples in this study are given in Table 10.3. It is clear from (7.6) that the energy of the system is linearly dependent on the force constants, and all the force constants are positive. Therefore, the energy of the systems may be compared by separately considering the various summations in equation (7.6) for which

$$V_r = \sum_i (r - r_0)^2, \quad V_\theta = \sum_i (\theta - \theta_0)^2.$$

In terms of the variation in bond length, all bond lengths on the tube and the sheet are fixed. However, the bond lengths which connect between the atoms at the tube open end and the atoms on the sheet may vary from the assumed bond length, and the bond angles at the connection sites may also vary. This means that the variation in bond length approach affects both the bond stretching and the bending angle terms in the energy equation. On the other hand, all the bond lengths are fixed for the variation in bond angle approach and only the bond angle varies, therefore the bond stretching term will always be zero. The differences between (a) and (b) in Table 10.3 arise from the fact that for (a) the sheet atoms are fixed in the plane,

while for (b) the sheet atoms are allowed to move. With these considerations in mind, it can be said that the variation in bond angle approach (b) gives rise to more stable structures than those arising from the variation in bond length approach (a). In addition, the percentage differences are very small so that the harmonic terms in (7.6) are valid.

Table 10.3: Numerical values for the sum of squared derivations (percentage differences) for joining (3,3), (6,0) and (9,0) boron nitride tubes with a boron nitride sheet by the variation in bond length (a) and the variation in bond angle (b).

Values	(3,3)		(6,0)		(9,0)	
	(a)	(b)	(a)	(b)	(a)	(b)
$V_r$ ( $\text{\AA}^2$ )	0	0	0	0	0.064	0
Percentage difference (%)	0	0	0	0	0.49	0
$V_\theta$ ( $^\circ^2$ )	78.048	43.859	171.782	49.135	179.760	21.717
Percentage difference (%)	1.08	1.02	3.98	1.14	2.77	0.35

Some of the numerical data for the determination of the possible defect configurations, and the least squares approach for the variation in bond length to find the best defect configuration for both zigzag and armchair boron nitride tubes are examined. Using combinatorial theory, all possible defects can be obtained. However, some of them, such as those shown in Figure 10.10 are thought to be less likely to be joined with a tube, than those shown in Figure 10.11 which are believed to be physically more reasonable. Subsequently, only the quasi-circular defects such as those shown in Figure 10.11 are examined. In Table 10.4 and Table 10.5, the value for the function  $f$  defined in (7.2) and the interspacing between the sheet and the tube  $\ell$  for zigzag and armchair tubes are respectively presented for certain defects which are considered to be physically more likely to occur.

## 10.7 Summary

With reference to the particular problem of the perpendicular connecting of boron nitride nanotubes with a boron nitride sheet, this chapter considers two aspects of defect classification and connection for combining boron nitride structures. Given that rings with an even number of sides are energetically favourable for boron nitride nanostructures, the most appropriate defect configurations on the sheet need to be

determined. The number of possible distinct defect configurations is related to the necklace and bracelet problems of combinatorial theory. The necklace permutation method is employed to classify all distinct closed defect possibilities where an arm-chair (zigzag) tube requires all odd (even) number of bonds connecting between two adjacent atoms at the defect site. Since additional mirror image symmetrical defects can be neglected, the bracelet permutation concept is utilised to quantify the most physically meaningful defects.

Once the defects are obtained, two distinct least squares approaches are employed to determine the connected structures for the tube and the sheet of boron nitride. Firstly, the variation in bond length is exploited to minimise the inter-atomic distance from the assumed bond length  $\sigma = 1.45 \text{ \AA}$  between an atom at the tube open end and one at the defect on the sheet. In this case, all atoms are assumed to remain in their own positions on the perfect tube and the perfect sheet structures. However, the tube is allowed to rotate about its axis and to move in the axial direction, while the sheet is assumed to be fixed in the plane. Secondly, the least squares bond angle approach is examined, which assumes that all the bond lengths are fixed to be  $\sigma = 1.45 \text{ \AA}$ . The atoms at the joining positions for both at the tube end and at the defect can move around a defined circular path to determine the most suitable locations to be connected.

Three examples of perpendicular joining boron nitride nanotubes, (3,3), (6,0) and (9,0) tubes, and the most symmetrical defects are used to illustrate such approaches. Using the algebraic computer package MAPLE, three dimensional illustrations for all cases of the two variation approaches are depicted, and Euler's polyhedra theorem is utilised to verify that the connected structures are geometrically acceptable. Furthermore, the bonded potential energy for small deformations is evaluated to determine a measure of the stability of the system. Since the value for the bond stretching constant is significantly larger than that of the bending angle and from the least squares calculations, this are led to conclude that the minimisation of the bond angle procedure provides lower energy values than the minimisation of the bond length procedure, so that the former most likely provides a better model for physically occurring molecular structures.

Table 10.4: Values of least squares function  $f$  ( $\text{\AA}^2$ ) defined by (7.2) and distance  $\ell$  ( $\text{\AA}$ ) for joining zigzag boron nitride tubes with some defects.

Defect configurations	$f$	$\ell$
(3,0) tube		
{4, 4, 4}	0	1.445614
(6,0) tubes		
{4, 2, 4, 2, 4, 2}	0	1.449434
{4, 4, 2, 4, 4, 0}	0.000677	0.250835
(9,0) tubes		
{4, 2, 2, 4, 2, 2, 4, 2, 2}	0.019121	0.421028
{4, 2, 4, 2, 2, 4, 2, 4, 0}	0.580765	0.679539
{4, 4, 0, 4, 2, 4, 2, 4, 0}	3.419328	0
{4, 4, 0, 4, 4, 0, 4, 4, 0}	5.949885	0
(12,0) tubes		
{4, 2, 2, 2, 4, 2, 2, 2, 4, 2, 2, 2}	0.309083	1.244449
{4, 2, 4, 2, 2, 2, 4, 2, 2, 4, 2, 0}	4.255253	0
{4, 2, 2, 4, 2, 2, 2, 4, 2, 2, 4, 0}	1.432916	1.019704
{4, 2, 4, 0, 4, 2, 2, 4, 2, 2, 4, 0}	3.142780	0.448532
{4, 2, 4, 0, 4, 2, 4, 0, 4, 2, 4, 0}	4.072747	0.278195
{4, 4, 0, 4, 2, 4, 0, 4, 4, 0, 4, 0}	15.904065	0
(15,0) tubes		
{4, 2, 2, 2, 2, 4, 2, 2, 2, 2, 4, 2, 2, 2, 2}	0.915522	1.046673
{4, 2, 2, 4, 2, 2, 2, 2, 4, 2, 2, 2, 4, 2, 0}	7.126194	0
{4, 2, 2, 2, 4, 2, 2, 2, 2, 4, 2, 2, 2, 4, 0}	1.933119	0.907544
{4, 2, 2, 4, 0, 4, 2, 2, 2, 4, 2, 2, 2, 4, 0}	2.543159	0.610721
{4, 2, 4, 0, 4, 2, 2, 4, 0, 4, 2, 2, 4, 2, 0}	8.875528	0
{4, 2, 2, 4, 0, 4, 2, 2, 4, 0, 4, 2, 2, 4, 0}	2.289527	0
{4, 2, 4, 0, 4, 2, 2, 4, 0, 4, 2, 4, 0, 4, 0}	14.082357	0
{4, 4, 0, 4, 0, 4, 2, 4, 0, 4, 2, 4, 0, 4, 0}	32.531784	0
{4, 4, 0, 4, 0, 4, 4, 0, 4, 0, 4, 4, 0, 4, 0}	54.061449	0

Table 10.5: Values of least squares function  $f$  ( $\text{\AA}^2$ ) defined by (7.2) and distance  $\ell$  ( $\text{\AA}$ ) for joining armchair boron nitride tubes with some defects.

Defect configurations	$f$	$\ell$
(3,3) tubes		
{3, 3, 3, 3, 3, 3}	0	1.450000
{5, 1, 5, 1, 5, 1}	0.000042	1.235115
(4,4) tube		
{5, 1, 3, 3, 3, 3, 3, 1}	0.028538	1.147819
(5,5) tubes		
{3, 3, 3, 3, 1, 3, 3, 3, 3, 1}	0.449559	0.959827
{5, 1, 3, 3, 3, 3, 1, 5, 1, 1}	0.980817	0.798733
{5, 1, 3, 3, 3, 1, 5, 1, 3, 1}	0.292789	1.097115
{5, 1, 3, 3, 1, 5, 1, 3, 3, 1}	0.906751	1.032654
{5, 1, 5, 1, 1, 5, 1, 5, 1, 1}	4.507192	0
(6,6) tubes		
{3, 3, 3, 1, 3, 3, 3, 1, 3, 3, 3, 1}	0.511011	1.223435
{5, 1, 3, 3, 3, 1, 3, 3, 3, 3, 1, 1}	2.132008	0.816330
{5, 1, 3, 3, 1, 3, 3, 3, 3, 1, 3, 1}	0.397135	0
{5, 1, 3, 3, 3, 1, 5, 1, 1, 5, 1, 1}	1.966639	0.439799
{5, 1, 3, 1, 5, 1, 3, 1, 5, 1, 3, 1}	0.774044	1.007332
(7,7) tubes		
{3, 3, 3, 3, 1, 3, 3, 1, 3, 3, 3, 3, 1, 1}	5.627837	0
{3, 3, 3, 3, 1, 3, 1, 3, 3, 3, 3, 1, 3, 1}	4.919751	0
{3, 3, 3, 1, 3, 3, 1, 3, 3, 3, 1, 3, 3, 1}	1.483391	1.119239
{5, 1, 3, 3, 1, 3, 3, 3, 1, 3, 3, 3, 1, 1}	1.634777	0.930209
{5, 1, 3, 1, 3, 3, 3, 1, 3, 3, 3, 1, 3, 1}	0.905888	0.982272
{5, 1, 3, 1, 5, 1, 1, 5, 1, 3, 1, 5, 1, 1}	3.977454	0
(8,8) tubes		
{3, 3, 3, 3, 1, 3, 1, 3, 3, 3, 1, 3, 3, 3, 1, 1}	8.093382	0.449886
{3, 3, 3, 1, 3, 3, 1, 3, 3, 1, 3, 3, 3, 1, 3, 1}	1.808325	1.020557
{5, 1, 3, 3, 1, 3, 3, 1, 3, 3, 3, 1, 3, 3, 1, 1}	4.099844	0.776275
{5, 1, 3, 1, 3, 3, 3, 1, 3, 3, 1, 3, 3, 3, 1, 1}	1.742843	0.902405
{5, 1, 3, 3, 1, 3, 3, 3, 1, 3, 3, 1, 5, 1, 1, 1}	6.940624	0
{5, 1, 3, 3, 1, 3, 3, 3, 1, 3, 1, 5, 1, 3, 1, 1}	5.301284	0
{5, 1, 3, 1, 5, 1, 1, 3, 3, 3, 1, 3, 3, 3, 1, 1}	5.726062	0.846815
{5, 1, 3, 1, 5, 1, 1, 5, 1, 1, 5, 1, 1, 5, 1, 1}	12.354890	0

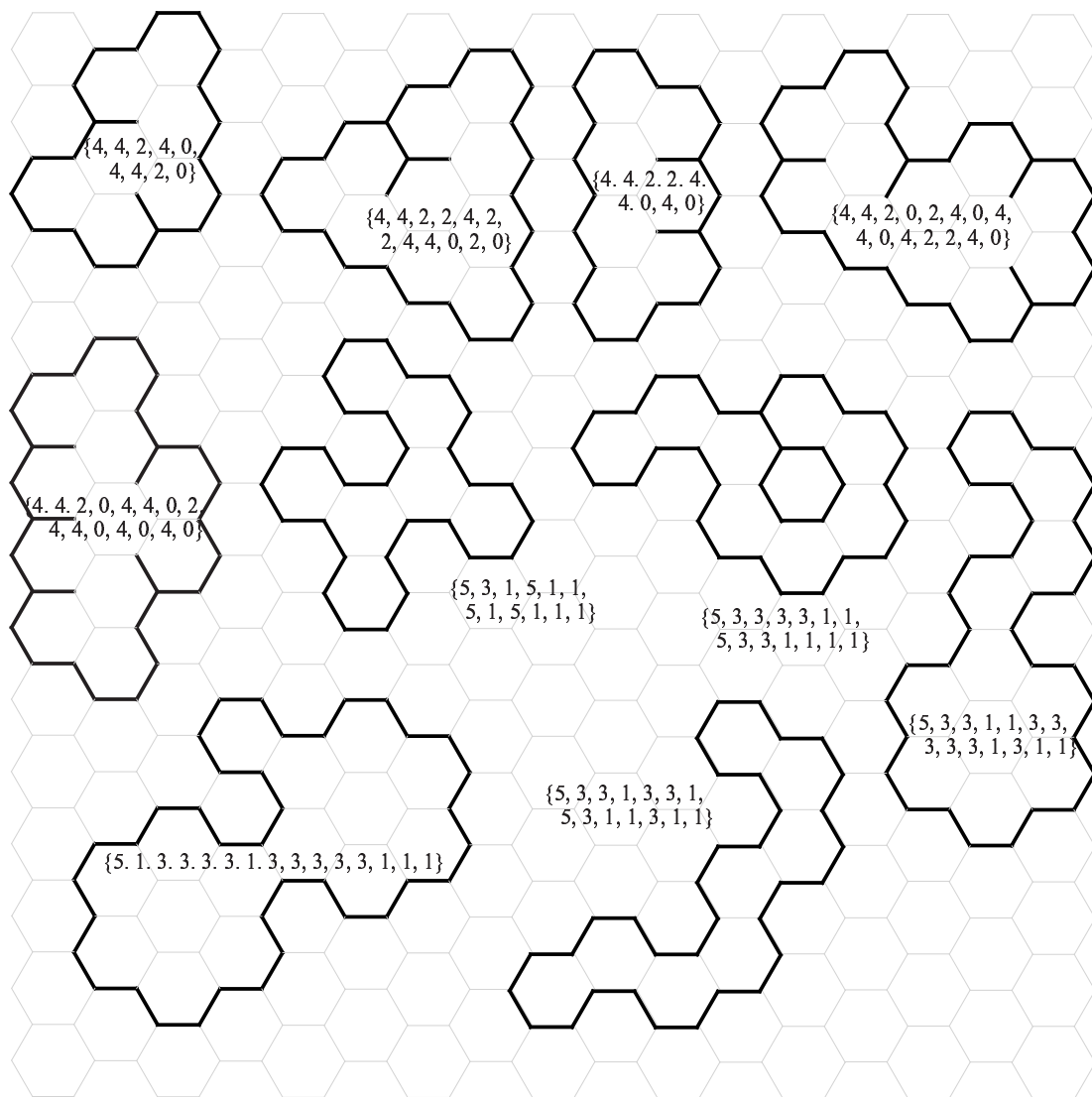


Figure 10.10: Some typical defect configurations considered to be non-physical.



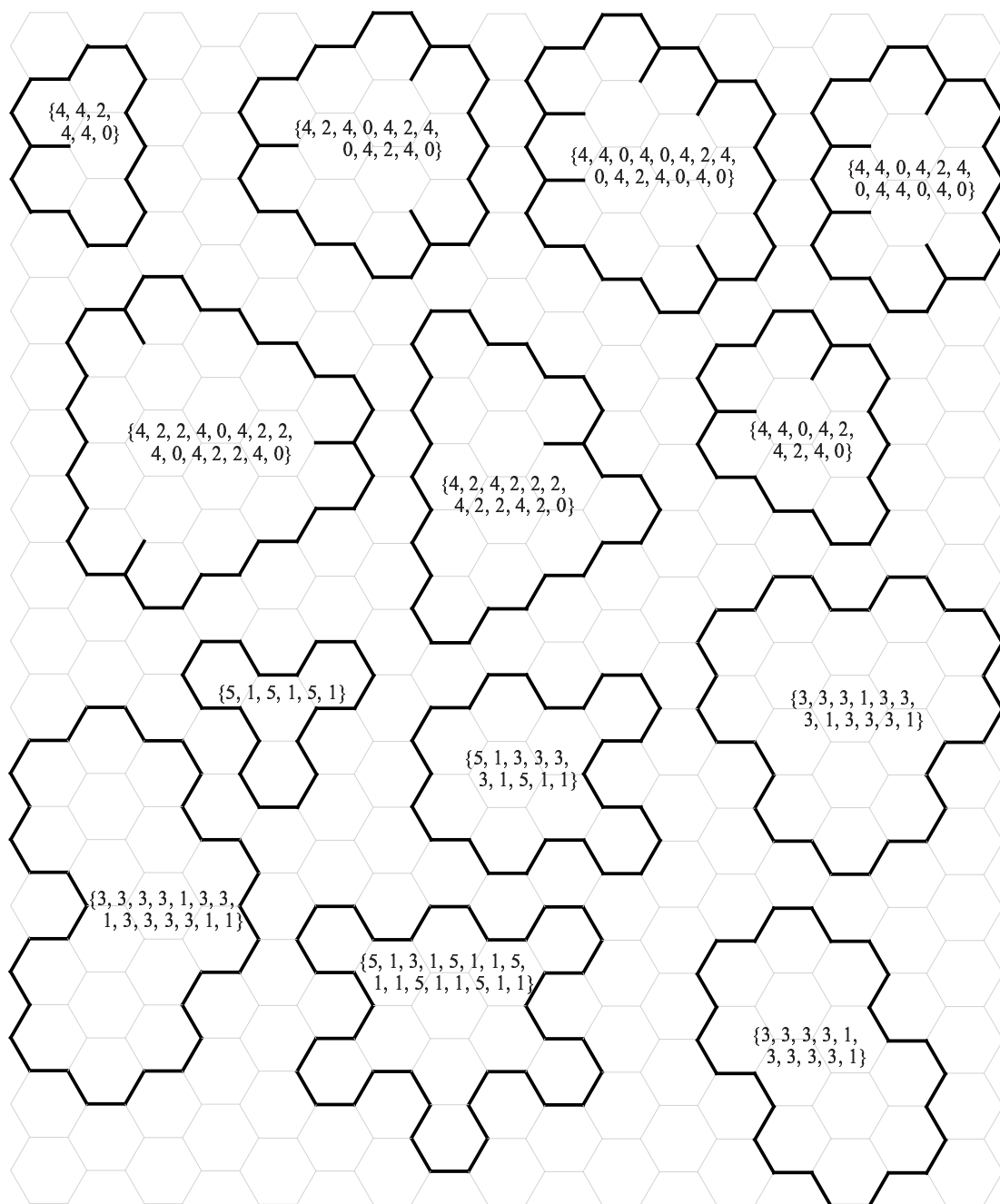


Figure 10.11: Some quasi-circular defects considered to more likely candidates to be joined with a nanotube.

## Part IV

# Transversely isotropic linearly elastic materials

# Chapter 11

## Introduction to transversely isotropic linearly elastic materials

The discovery of carbon nanotubes by Iijima [32] has led to the possible creation of many new nanoscale devices such as nano-oscillators. The aim of Part IV is to investigate the wave-like deformation on the tube wall of a double-walled carbon nanotube when the inner tube oscillates. In this study, carbon nanotubes are assumed to be transversely isotropic materials and by using the resultant force distribution determined in Chapter 3, the deformations are determined. In §11.1, a background study of elasticity for carbon nanotubes is introduced and an overview of Part IV is given in §11.2.

### 11.1 Elasticity of carbon nanotubes

Carbon nanotubes are capable of being realised to be perfectly elastic materials in the sense that they return to their original configurations when the applied loads are released [17]. There are many experiments and molecular dynamics simulations which study their elastic properties (see for example, [15, 17–21, 134]). Yu *et al.* [18] study multi-walled carbon nanotubes under load, and obtain values in the range of 270–950 GPa for the Young’s modulus. Alternatively, Zhao *et al.* [19] use quantum mechanical and molecular mechanical calculations to model the deformation in carbon nanotubes under an applied load. They determine a value in the order of 1 TPa for the Young’s modulus, which is much higher than values proposed in previous investigations. These authors suggest that carbon nanotubes are the strongest known material. Lu [20] presents values of elastic moduli using constant-force models for both single-walled and multi-walled carbon nanotubes, as well as for nanoropes. He

finds that the elastic properties are insensitive to the helicity, radius and number of walls. Tersoff and Ruoff [135], Popov *et al.* [136], Thostenson and Chou [137] and Shen and Li [21, 134] propose that carbon nanotubes might be modelled as a transversely isotropic linearly elastic material. Shen and Li [21, 134] also study the deformation of carbon nanotubes under loading and obtain values for the elastic constants and elastic moduli. Jin and Yuan [15] use molecular dynamics simulations as well as the Lennard-Jones potential to study the elastic properties of single-walled carbon nanotubes. They determine the elastic moduli using energy and force approaches which give rise to approximately the same numerical values as Shen and Li [21, 134].

In terms of the development of the theory for transversely isotropic linearly elastic materials, Elliott [22] is the first to introduce a general three dimensional solution for such materials. He finds that the solutions for displacements and stresses can be described in terms of two harmonic functions, and subsequently many researchers examine the physical properties of such materials. Moreover, Elliott [138] solves the problems of the rigid conical punch, rigid spherical ball indentation, cylindrical punch and a disk-shaped ‘Griffith’ crack in solids under tension. The line force in an infinite plate, elliptical crack and punch and isolated force with plane boundary are studied by Shield [23]. Payne and Green [24] modify these transversely isotropic solutions and introduce another potential function for curvilinear coordinates, which corresponds to Mehler’s expansion theorem. They also study the punch problem, the Boussinesq problem and crack problems for both pressure prescribed and displacement prescribed cases. Furthermore, Selvadurai [25] studies a rigid disc inclusion embedded in a transversely isotropic elastic medium of infinite extent. He considers the displacement and stress equations with no body force and shows that in general there are three potential functions  $\phi_1(r, \theta, z)$ ,  $\phi_2(r, \theta, z)$  and  $\psi(r, \theta, z)$  needed for the solution of transversely isotropic materials.

## 11.2 Overview

In Part IV, the phenomenon of nanoscale oscillators is investigated, and in particular the generation of a wave-like formation on the outer surface of a double-walled carbon nanotube arising from the motion of an oscillating inner tube is examined.

In the following chapter, the basic governing equations for transversely isotropic linearly elastic materials are formulated. Chapter 13 presents the model formulation and the analysis of assumed solutions for the displacements and stresses, and the key mathematical solution details are outlined. Values for the elastic constants for single-walled and multi-walled carbon nanotubes are discussed in Chapter 13, and detailed tables of numerical values are listed in Appendix G.

## Chapter 12

# Governing equations for transversely isotropic linearly elastic material

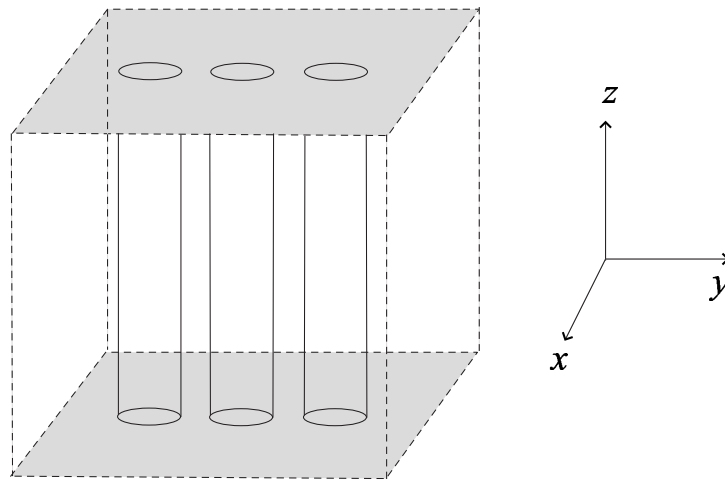


Figure 12.1: Diagram for transversely isotropic materials.

Transversely isotropic materials possess a single axis about which the material is isotropic, but it is not isotropic with respect to any other axis. In other words, transversely isotropic materials have the same properties in one plane,  $x - y$  plane, but which differ in the normal direction to this plane, the  $z$ -direction, which is illustrated in Figure 12.1. Such a constitutive assumption has been proposed for carbon nanotubes (see for example [20, 21]). Isotropic materials are a particular case of transversely isotropic materials, and for linearly elastic materials a good deal is known about isotropic materials. Accordingly, results are frequently specialised to the well known version arising from isotropic linearly elastic materials. We comment that isotropic in materials engineering refers to materials which have the same

mechanical properties in all crystallographic directions, not in all directions, for example a material of cubic symmetry will behave the same in each of the face directions which differ from the vertex directions. While homogeneous materials will have the same mechanical properties in any direction as in a sphere.

## 12.1 Nomenclature

$\varepsilon_{ij}$	are elements of the strain tensor
$\phi, \phi_1, \phi_2$	are the assumed harmonic solutions
$\lambda, \mu$	are the Lamé constants
$\mu'$	is the shear modulus in the longitudinal direction
$\nu, \nu'$	are the Poisson's ratios in the transverse plane and in the longitudinal direction, respectively
$\sigma_{ij}$	are elements of the Cauchy stress tensor
$\tau$	is the coefficient of tangential friction
$\psi$	is an harmonic function
$C_{k\ell}$	are the elastic constants
$E, E'$	are the Young's moduli in the transverse plane and in the longitudinal direction, respectively
$a, b$	are the radii of the inner and the outer carbon nanotubes, respectively
$r, \theta, z$	are a system of cylindrical coordinates
$u, v, w$	are the displacements in Cartesian coordinates $x, y, z$ , respectively
$x, y, z$	are a system of Cartesian coordinates

## 12.2 Hooke's law for transversely isotropic linearly elastic materials

For transversely isotropic linearly elastic materials, the stiffness matrix can be written in the form

$$\begin{bmatrix} \sigma_{xx} \\ \sigma_{yy} \\ \sigma_{zz} \\ \sigma_{yz} \\ \sigma_{zx} \\ \sigma_{xy} \end{bmatrix} = \begin{bmatrix} C_{11} & C_{12} & C_{13} & 0 & 0 & 0 \\ C_{12} & C_{11} & C_{13} & 0 & 0 & 0 \\ C_{13} & C_{13} & C_{33} & 0 & 0 & 0 \\ 0 & 0 & 0 & 2C_{44} & 0 & 0 \\ 0 & 0 & 0 & 0 & 2C_{44} & 0 \\ 0 & 0 & 0 & 0 & 0 & C_{11} - C_{12} \end{bmatrix} \begin{bmatrix} \varepsilon_{xx} \\ \varepsilon_{yy} \\ \varepsilon_{zz} \\ \varepsilon_{yz} \\ \varepsilon_{zx} \\ \varepsilon_{xy} \end{bmatrix}, \quad (12.1)$$

where  $C_{kl}$  ( $k, l = 1, 2, 3, 4$ ) denote certain constants,  $\sigma_{ij}$  ( $i, j = 1, 2, 3$ ) denote the Cauchy stress tensor in Cartesian coordinates  $x_j$  ( $j = 1, 2, 3$ ) =  $(x, y, z)$  and here the strain tensor  $\varepsilon_{ij}$  are defined by

$$\varepsilon_{ij} = \frac{1}{2} \left( \frac{\partial u_i}{\partial x^j} + \frac{\partial u_j}{\partial x^i} \right), \quad (i, j = 1, 2, 3),$$

where  $u_i(x, y, z)$  ( $i = 1, 2, 3$ ) denote the three displacements  $(u, v, w)$ . Explicitly in terms of  $(x, y, z)$ , the strain tensor can be written as

$$\begin{aligned} \varepsilon_{xx} &= \frac{\partial u}{\partial x}, & \varepsilon_{yy} &= \frac{\partial v}{\partial y}, & \varepsilon_{zz} &= \frac{\partial w}{\partial z}, \\ \varepsilon_{yz} &= \frac{1}{2} \left( \frac{\partial v}{\partial z} + \frac{\partial w}{\partial y} \right), & \varepsilon_{zx} &= \frac{1}{2} \left( \frac{\partial w}{\partial x} + \frac{\partial u}{\partial z} \right), & \varepsilon_{xy} &= \frac{1}{2} \left( \frac{\partial u}{\partial y} + \frac{\partial v}{\partial x} \right), \end{aligned} \quad (12.2)$$

and this notation is adopted by Fung [139], page 94, Sokolnikoff [140], page 22 and Landau and Lifshitz [141], page 3. However, some authors employ the notation referred to as the engineering strain such as Ding *et al.* [142], page 4, Lure [143], page 9, and Tran-Cong [144], page 2, which are given by

$$\begin{aligned} \varepsilon_{xx} &= \frac{\partial u}{\partial x}, & \varepsilon_{yy} &= \frac{\partial v}{\partial y}, & \varepsilon_{zz} &= \frac{\partial w}{\partial z}, \\ \gamma_{yz} &= \left( \frac{\partial v}{\partial z} + \frac{\partial w}{\partial y} \right), & \gamma_{zx} &= \left( \frac{\partial w}{\partial x} + \frac{\partial u}{\partial z} \right), & \gamma_{xy} &= \left( \frac{\partial u}{\partial y} + \frac{\partial v}{\partial x} \right), \end{aligned}$$



while others, such as Elliott [22], Green and Zerna [145], page 176, Love [146], page 38, and Rekach [147], page 25, employ the strain tensor

$$\begin{aligned} e_{xx} &= \frac{\partial u}{\partial x}, & e_{yy} &= \frac{\partial v}{\partial y}, & e_{zz} &= \frac{\partial w}{\partial z}, \\ e_{yz} &= \left( \frac{\partial v}{\partial z} + \frac{\partial w}{\partial y} \right), & e_{zx} &= \left( \frac{\partial w}{\partial x} + \frac{\partial u}{\partial z} \right), & e_{xy} &= \left( \frac{\partial u}{\partial y} + \frac{\partial v}{\partial x} \right). \end{aligned}$$

We comment that the last two equations have the same definitions but differ only in the notations for the strain tensor. Throughout the present work, the notation (12.2) for the strain tensor is consistently adopted.

For transversely isotropic linearly elastic materials, the notations which are inverse to (12.1) (i.e. the so-called compliance matrix) becomes

$$\begin{bmatrix} \varepsilon_{xx} \\ \varepsilon_{yy} \\ \varepsilon_{zz} \\ \varepsilon_{yz} \\ \varepsilon_{zx} \\ \varepsilon_{xy} \end{bmatrix} = \begin{bmatrix} S_{11} & S_{12} & S_{13} & 0 & 0 & 0 \\ S_{12} & S_{11} & S_{13} & 0 & 0 & 0 \\ S_{13} & S_{13} & S_{33} & 0 & 0 & 0 \\ 0 & 0 & 0 & S_{44}/2 & 0 & 0 \\ 0 & 0 & 0 & 0 & S_{44}/2 & 0 \\ 0 & 0 & 0 & 0 & 0 & S_{11} - S_{12} \end{bmatrix} \begin{bmatrix} \sigma_{xx} \\ \sigma_{yy} \\ \sigma_{zz} \\ \sigma_{yz} \\ \sigma_{zx} \\ \sigma_{xy} \end{bmatrix}. \quad (12.3)$$

Poisson's ratio and Young's modulus in the transverse plane and Poisson's ratio, Young's modulus and shear modulus in the longitudinal directions; namely  $\nu$ ,  $E$  and  $\nu'$ ,  $E'$ ,  $\mu'$ , respectively, are expressed as

$$\begin{aligned} \varepsilon_{xx} &= \frac{1}{E}(\sigma_{xx} - \nu\sigma_{yy}) - \frac{\nu'}{E'}\sigma_{zz}, & \varepsilon_{xz} &= \frac{1}{2\mu'}\sigma_{xz}, \\ \varepsilon_{yy} &= \frac{1}{E}(-\nu\sigma_{xx} + \sigma_{yy}) - \frac{\nu'}{E'}\sigma_{zz}, & \varepsilon_{yz} &= \frac{1}{2\mu'}\sigma_{yz}, \\ \varepsilon_{zz} &= -\frac{\nu'}{E'}(\sigma_{xx} + \sigma_{yy}) + \frac{1}{E'}\sigma_{zz}, & \varepsilon_{xy} &= \frac{1+\nu}{E}\sigma_{xy}, \end{aligned}$$

as well as the following values for the constants  $S_{ij}$

$$S_{11} = \frac{1}{E}, \quad S_{12} = -\frac{\nu}{E}, \quad S_{13} = -\frac{\nu'}{E'}, \quad S_{33} = \frac{1}{E'}, \quad S_{44} = \frac{1}{\mu'}.$$

The constants  $C_{ij}$  can be shown to be given by the expressions

$$\begin{aligned} C_{11} &= \Delta \frac{(E\nu'^2 - E')}{(1 + \nu)}, & C_{12} &= -\Delta \frac{(E'\nu + E\nu'^2)}{(1 + \nu)}, \\ C_{13} &= -\Delta E'\nu', & C_{33} &= \Delta \frac{E'^2}{E}(\nu - 1), & C_{44} &= \mu', \end{aligned} \quad (12.4)$$

where the quantity  $\Delta$  is defined by

$$\Delta = \frac{E}{(E'\nu - E' + 2E\nu'^2)}.$$

In cylindrical coordinates  $(r, \theta, z)$  the stiffness matrix involves the same constants as in Cartesian coordinates, and is given by

$$\begin{bmatrix} \sigma_{rr} \\ \sigma_{\theta\theta} \\ \sigma_{zz} \\ \sigma_{\theta z} \\ \sigma_{rz} \\ \sigma_{r\theta} \end{bmatrix} = \begin{bmatrix} C_{11} & C_{12} & C_{13} & 0 & 0 & 0 \\ C_{12} & C_{11} & C_{13} & 0 & 0 & 0 \\ C_{13} & C_{13} & C_{33} & 0 & 0 & 0 \\ 0 & 0 & 0 & 2C_{44} & 0 & 0 \\ 0 & 0 & 0 & 0 & 2C_{44} & 0 \\ 0 & 0 & 0 & 0 & 0 & C_{11} - C_{12} \end{bmatrix} \begin{bmatrix} \varepsilon_{rr} \\ \varepsilon_{\theta\theta} \\ \varepsilon_{zz} \\ \varepsilon_{\theta z} \\ \varepsilon_{rz} \\ \varepsilon_{r\theta} \end{bmatrix}. \quad (12.5)$$

### 12.3 Hooke's law for isotropic linearly elastic materials

For isotropic linearly elastic materials the stiffness matrix (12.1) and compliance matrix (12.3) become

$$\begin{bmatrix} \sigma_{xx} \\ \sigma_{yy} \\ \sigma_{zz} \\ \sigma_{yz} \\ \sigma_{zx} \\ \sigma_{xy} \end{bmatrix} = \frac{E}{(1 + \nu)(1 - 2\nu)} \begin{bmatrix} 1 - \nu & \nu & \nu & 0 & 0 & 0 \\ \nu & 1 - \nu & \nu & 0 & 0 & 0 \\ \nu & \nu & 1 - \nu & 0 & 0 & 0 \\ 0 & 0 & 0 & 1 - 2\nu & 0 & 0 \\ 0 & 0 & 0 & 0 & 1 - 2\nu & 0 \\ 0 & 0 & 0 & 0 & 0 & 1 - 2\nu \end{bmatrix} \begin{bmatrix} \varepsilon_{xx} \\ \varepsilon_{yy} \\ \varepsilon_{zz} \\ \varepsilon_{yz} \\ \varepsilon_{zx} \\ \varepsilon_{xy} \end{bmatrix},$$

$$\begin{bmatrix} \varepsilon_{xx} \\ \varepsilon_{yy} \\ \varepsilon_{zz} \\ \varepsilon_{yz} \\ \varepsilon_{zx} \\ \varepsilon_{xy} \end{bmatrix} = \frac{1}{E} \begin{bmatrix} 1 & -\nu & -\nu & 0 & 0 & 0 \\ -\nu & 1 & -\nu & 0 & 0 & 0 \\ -\nu & -\nu & 1 & 0 & 0 & 0 \\ 0 & 0 & 0 & 1+\nu & 0 & 0 \\ 0 & 0 & 0 & 0 & 1+\nu & 0 \\ 0 & 0 & 0 & 0 & 0 & 1+\nu \end{bmatrix} \begin{bmatrix} \sigma_{xx} \\ \sigma_{yy} \\ \sigma_{zz} \\ \sigma_{yz} \\ \sigma_{zx} \\ \sigma_{xy} \end{bmatrix},$$

where  $\nu$  is the Poisson's ratio and  $E$  is the Young's modulus. Alternatively, these relations can be expressed as

$$\varepsilon_{ij} = \frac{1+\nu}{E} \sigma_{ij} - \frac{\nu}{E} \delta_{ij} \sigma_{kk}, \quad (12.6)$$

$$\sigma_{ij} = \frac{E}{1+\nu} \varepsilon_{ij} + \frac{\nu E}{(1-2\nu)(1+\nu)} \delta_{ij} \varepsilon_{kk},$$

and in terms of the Lamé constants  $\lambda$  and  $\mu$  defined by

$$\lambda = \frac{\nu E}{(1-2\nu)(1+\nu)}, \quad \mu = \frac{E}{2(1+\nu)},$$

(12.6) becomes

$$\sigma_{ij} = 2\mu \varepsilon_{ij} + \lambda \delta_{ij} \varepsilon_{kk}.$$

## 12.4 Equilibrium equations for transversely isotropic linearly elastic materials

### 12.4.1 Cartesian coordinates $(x, y, z)$

The equilibrium equations for a force balance in Cartesian coordinates are

$$\begin{aligned} \frac{\partial \sigma_{xx}}{\partial x} + \frac{\partial \sigma_{yx}}{\partial y} + \frac{\partial \sigma_{zx}}{\partial z} + f_x &= 0, \\ \frac{\partial \sigma_{xy}}{\partial x} + \frac{\partial \sigma_{yy}}{\partial y} + \frac{\partial \sigma_{zy}}{\partial z} + f_y &= 0, \\ \frac{\partial \sigma_{xz}}{\partial x} + \frac{\partial \sigma_{yz}}{\partial y} + \frac{\partial \sigma_{zz}}{\partial z} + f_z &= 0. \end{aligned} \quad (12.7)$$

The equilibrium equations can be also concisely written in tensor form

$$\frac{\partial \sigma_{ij}}{\partial x_i} + f_j = 0.$$

If this equation involves an acceleration, it becomes the equation of motion, i.e.

$$\frac{\partial \sigma_{ij}}{\partial x_i} + f_j = \rho \frac{d^2 u_i}{dt^2},$$

where  $u_i$  ( $i=1,2,3$ ) denotes displacements. From (12.1), the stress equations are given explicitly by

$$\begin{aligned} \sigma_{xx} &= C_{11}\varepsilon_{xx} + C_{12}\varepsilon_{yy} + C_{13}\varepsilon_{zz}, & \sigma_{yy} &= C_{12}\varepsilon_{xx} + C_{11}\varepsilon_{yy} + C_{13}\varepsilon_{zz}, \\ \sigma_{zz} &= C_{13}(\varepsilon_{xx} + \varepsilon_{yy}) + C_{33}\varepsilon_{zz}, & \sigma_{yz} &= 2C_{44}\varepsilon_{yz}, \\ \sigma_{xz} &= 2C_{44}\varepsilon_{xz}, & \sigma_{xy} &= (C_{11} - C_{12})\varepsilon_{xy}. \end{aligned}$$

From (12.1) and (12.7), three equilibrium equations in terms of displacements are obtained and then given by

$$\begin{aligned} C_{11} \frac{\partial^2 u}{\partial x^2} + \frac{(C_{11} - C_{12})}{2} \frac{\partial^2 u}{\partial y^2} + C_{44} \frac{\partial^2 u}{\partial z^2} + \frac{\partial}{\partial x} \left( \frac{(C_{11} - C_{12})}{2} \frac{\partial v}{\partial y} + (C_{13} + C_{44}) \frac{\partial w}{\partial z} \right) &= 0, \\ \frac{(C_{11} - C_{12})}{2} \frac{\partial^2 v}{\partial x^2} + C_{11} \frac{\partial^2 v}{\partial y^2} + C_{44} \frac{\partial^2 v}{\partial z^2} + \frac{\partial}{\partial y} \left( \frac{(C_{11} + C_{12})}{2} \frac{\partial u}{\partial x} + (C_{13} + C_{44}) \frac{\partial w}{\partial z} \right) &= 0, \\ C_{44} \left( \frac{\partial^2 w}{\partial x^2} + \frac{\partial^2 w}{\partial y^2} \right) + C_{33} \frac{\partial^2 w}{\partial z^2} + (C_{13} + C_{44}) \frac{\partial}{\partial z} \left( \frac{\partial u}{\partial z} + \frac{\partial v}{\partial y} \right) &= 0. \end{aligned} \quad (12.8)$$

On assuming that

$$u = \frac{\partial \phi}{\partial x}, \quad v = \frac{\partial \phi}{\partial y}, \quad w = k \frac{\partial \phi}{\partial z},$$

is a solution of the equilibrium equations for some function  $\phi(x, y, z)$ , (12.8) becomes

$$\begin{aligned} C_{11} \left( \frac{\partial^2 \phi}{\partial x^2} + \frac{\partial^2 \phi}{\partial y^2} \right) + [C_{44} + k(C_{13} + C_{44})] \frac{\partial^2 \phi}{\partial z^2} &= 0, \\ C_{11} \left( \frac{\partial^2 \phi}{\partial x^2} + \frac{\partial^2 \phi}{\partial y^2} \right) + [C_{44} + k(C_{13} + C_{44})] \frac{\partial^2 \phi}{\partial z^2} &= 0, \\ [kC_{44} + (C_{13} + C_{44})] \left( \frac{\partial^2 \phi}{\partial x^2} + \frac{\partial^2 \phi}{\partial y^2} \right) + kC_{33} \frac{\partial^2 \phi}{\partial z^2} &= 0. \end{aligned}$$

These equations will be identical if

$$\frac{C_{44} + k(C_{13} + C_{44})}{C_{11}} = \frac{kC_{33}}{kC_{44} + (C_{13} + C_{44})} = \vartheta,$$

where  $\vartheta$  is a constant. From this equation, the quadratic equation for  $k$  is obtained which is

$$C_{44}(C_{13} + C_{44})k^2 + [C_{44}^2 + (C_{13} + C_{44})^2 - C_{11}C_{33}]k + C_{44}(C_{13} + C_{44}) = 0, \quad (12.9)$$

and if  $k_1$  and  $k_2$  are the solutions of (12.9) then  $\vartheta_i$  ( $i = 1, 2$ ) are given by

$$\vartheta_i = \frac{C_{44} + k_i(C_{13} + C_{44})}{C_{11}} = \frac{k_i C_{33}}{k_i C_{44} + (C_{13} + C_{44})}, \quad (i = 1, 2), \quad (12.10)$$

and  $\phi_i(x, y, z)$  satisfies the equation

$$\nabla^2 \phi + \vartheta_i \frac{\partial^2 \phi}{\partial z^2} = 0, \quad (i = 1, 2),$$

where  $\nabla^2 = \frac{\partial^2}{\partial x^2} + \frac{\partial^2}{\partial y^2}$ . (12.9) can be simplified to give

$$k^2 + (2 + \beta)k + 1 = 0,$$

where  $\beta = (C_{13}^2 - C_{11}C_{33})/(C_{44}(C_{44} + C_{13}))$ , and the displacements become

$$u = \frac{\partial}{\partial x}(\phi_1 + \phi_2), \quad v = \frac{\partial}{\partial y}(\phi_1 + \phi_2), \quad w = \frac{\partial}{\partial z}(k_1 \phi_1 + k_2 \phi_2). \quad (12.11)$$

In linear elasticity, the super position principle plays an important role, so that if two solutions for the displacement for transversely isotropic linearly elastic materials are linearly independent to each other, then adding the two solutions gives rise a more general solution of the system. Assuming that

$$u = \frac{\partial \psi}{\partial y}, \quad v = -\frac{\partial \psi}{\partial x}, \quad w = 0, \quad (12.12)$$

is a solution where  $\psi$  is a harmonic function (12.8) becomes

$$\begin{aligned} \frac{(C_{11} - C_{12})}{2} \left( \frac{\partial^2 \psi}{\partial x^2} + \frac{\partial^2 \psi}{\partial y^2} \right) + C_{44} \frac{\partial^2 \psi}{\partial z^2} &= 0, \\ \frac{(C_{11} - C_{12})}{2} \left( \frac{\partial^2 \psi}{\partial x^2} + \frac{\partial^2 \psi}{\partial y^2} \right) + C_{44} \frac{\partial^2 \psi}{\partial z^2} &= 0, \\ (C_{13} + C_{44}) \frac{\partial}{\partial z} \left( \frac{\partial^2 \psi}{\partial z \partial y} - \frac{\partial^2 \psi}{\partial z \partial y} \right) &= 0. \end{aligned} \quad (12.13)$$

Since (12.13)<sub>3</sub> is always true for  $\psi \neq 0$ , on introducing  $\vartheta_3$  such that

$$\frac{2C_{44}}{C_{11} - C_{12}} = \vartheta_3, \quad (12.14)$$

$\psi$  satisfies the equation

$$\nabla^2 \psi + \vartheta_3 \frac{\partial^2 \psi}{\partial z^2} = 0.$$

For the isotropic case,  $k_1 = k_2 = 1$  and  $\vartheta_1 = \vartheta_2 = \vartheta_3 = 1$ , where the passage to this limit has to be done carefully.

Thus, by superposition of the two solution (12.11) and (12.12), the displacements in Cartesian coordinates for a transversely isotropic linearly elastic material are given by

$$u = \frac{\partial}{\partial x}(\phi_1 + \phi_2) + \frac{\partial \psi}{\partial y}, \quad v = \frac{\partial}{\partial y}(\phi_1 + \phi_2) - \frac{\partial \psi}{\partial x}, \quad w = \frac{\partial}{\partial z}(k_1 \phi_1 + k_2 \phi_2),$$

and the stress equations in terms of the functions  $\phi_1(x, y, z)$ ,  $\phi_2(x, y, z)$  and  $\psi(x, y, z)$  are obtained from the relations of strain, displacements solutions, and equation (12.1) as the following:

$$\begin{aligned} \sigma_{xx} &= C_{11} \frac{\partial^2}{\partial x^2}(\phi_1 + \phi_2) + C_{12} \frac{\partial^2}{\partial y^2}(\phi_1 + \phi_2) + (C_{11} - C_{12}) \frac{\partial^2 \psi}{\partial x \partial y} \\ &\quad + C_{13} \frac{\partial^2}{\partial z^2}(k_1 \phi_1 + k_2 \phi_2), \end{aligned}$$

$$\begin{aligned}
\sigma_{yy} &= C_{12} \frac{\partial^2}{\partial x^2} (\phi_1 + \phi_2) + C_{11} \frac{\partial^2}{\partial y^2} (\phi_1 + \phi_2) - (C_{11} - C_{12}) \frac{\partial^2 \psi}{\partial x \partial y} \\
&\quad + C_{13} \frac{\partial^2}{\partial z^2} (k_1 \phi_1 + k_2 \phi_2), \\
\sigma_{zz} &= C_{13} \left[ \frac{\partial^2}{\partial x^2} (\phi_1 + \phi_2) + \frac{\partial^2}{\partial y^2} (\phi_1 + \phi_2) \right] + C_{33} \frac{\partial^2}{\partial z^2} (k_1 \phi_1 + k_2 \phi_2), \\
\sigma_{yz} &= C_{44} \left[ (1 + k_1) \frac{\partial^2 \phi_1}{\partial y \partial z} + (1 + k_2) \frac{\partial^2 \phi_2}{\partial y \partial z} \right] - C_{44} \frac{\partial^2 \psi}{\partial x \partial z}, \\
\sigma_{xz} &= C_{44} \left[ (1 + k_1) \frac{\partial^2 \phi_1}{\partial x \partial z} + (1 + k_2) \frac{\partial^2 \phi_2}{\partial x \partial z} \right] + C_{44} \frac{\partial^2 \psi}{\partial x \partial z}, \\
\sigma_{xy} &= (C_{11} - C_{12}) \frac{\partial^2}{\partial x \partial y} (\phi_1 + \phi_2) - \frac{(C_{11} - C_{12})}{2} \left[ \frac{\partial^2 \psi}{\partial x^2} - \frac{\partial^2 \psi}{\partial y^2} \right].
\end{aligned}$$

### 12.4.2 Cylindrical polar coordinates $(r, \theta, z)$

In cylindrical polar coordinates  $(r, \theta, z)$ , the equilibrium equations can be written in vector form as follows:

$$\begin{aligned}
\frac{\partial \sigma_{rr}}{\partial r} + \frac{1}{r} \frac{\partial \sigma_{r\theta}}{\partial \theta} + \frac{\partial \sigma_{rz}}{\partial z} + \frac{\sigma_{rr} - \sigma_{\theta\theta}}{r} + F_r &= 0, \\
\frac{\partial \sigma_{r\theta}}{\partial r} + \frac{1}{r} \frac{\partial \sigma_{\theta\theta}}{\partial \theta} + \frac{\partial \sigma_{\theta z}}{\partial z} + \frac{2}{r} \sigma_{r\theta} + F_\theta &= 0, \\
\frac{\partial \sigma_{rz}}{\partial r} + \frac{1}{r} \frac{\partial \sigma_{\theta z}}{\partial \theta} + \frac{\partial \sigma_{zz}}{\partial z} + \frac{1}{r} \sigma_{rz} + F_z &= 0,
\end{aligned} \tag{12.15}$$

and the strain relations in term of displacements for transversely isotropic materials are

$$\begin{aligned}
\varepsilon_{rr} &= \frac{\partial u}{\partial r}, & \varepsilon_{\theta\theta} &= \frac{1}{r} \frac{\partial v}{\partial \theta} + \frac{u}{r}, & \varepsilon_{zz} &= \frac{\partial w}{\partial z}, \\
\varepsilon_{r\theta} &= \frac{1}{2} \left( \frac{1}{r} \frac{\partial u}{\partial \theta} + \frac{\partial v}{\partial r} - \frac{v}{r} \right), & \varepsilon_{rz} &= \frac{1}{2} \left( \frac{\partial w}{\partial r} + \frac{\partial u}{\partial z} \right), & \varepsilon_{\theta z} &= \frac{1}{2} \left( \frac{\partial v}{\partial z} + \frac{1}{r} \frac{\partial w}{\partial \theta} \right).
\end{aligned} \tag{12.16}$$

where  $(u, v, w) = (u_r, u_\theta, u_z)$ . From the matrix for Hooke's law (12.5), the stress equations are

$$\begin{aligned}\sigma_{rr} &= C_{11}\varepsilon_{rr} + C_{12}\varepsilon_{\theta\theta} + C_{13}\varepsilon_{zz}, & \sigma_{\theta\theta} &= C_{12}\varepsilon_{rr} + C_{11}\varepsilon_{\theta\theta} + C_{13}\varepsilon_{zz}, \\ \sigma_{zz} &= C_{13}(\varepsilon_{rr} + \varepsilon_{\theta\theta}) + C_{33}\varepsilon_{zz}, & \sigma_{\theta z} &= 2C_{44}\varepsilon_{\theta z}, \\ \sigma_{rz} &= 2C_{44}\varepsilon_{rz}, & \sigma_{r\theta} &= (C_{11} - C_{12})\varepsilon_{r\theta}.\end{aligned}\tag{12.17}$$

From these relations, the equilibrium equations (12.15) for transversely isotropic materials can be written as

$$\begin{aligned}& C_{11}\frac{\partial^2 u}{\partial r^2} + \frac{(C_{11} - C_{12})}{2}\frac{1}{r^2}\frac{\partial^2 u}{\partial \theta^2} + C_{44}\frac{\partial^2 u}{\partial z^2} + \frac{(C_{11} + C_{12})}{2}\frac{1}{r}\frac{\partial^2 v}{\partial r \partial \theta} + (C_{13} + C_{44})\frac{\partial^2 w}{\partial r \partial z} \\ & + C_{11}\frac{1}{r}\frac{\partial u}{\partial r} - \frac{(3C_{11} - C_{12})}{2}\frac{1}{r^2}\frac{\partial v}{\partial \theta} - C_{11}\frac{1}{r^2}u + F_r = 0, \\ & \frac{(C_{11} - C_{12})}{2}\frac{\partial^2 v}{\partial r^2} + C_{11}\frac{1}{r^2}\frac{\partial^2 v}{\partial \theta^2} + C_{44}\frac{\partial^2 v}{\partial z^2} + \frac{(C_{11} + C_{12})}{2}\frac{1}{r}\frac{\partial^2 u}{\partial r \partial \theta} + (C_{13} + C_{44})\frac{1}{r}\frac{\partial^2 w}{\partial \theta \partial z} \\ & + \frac{(3C_{11} - C_{12})}{2}\frac{1}{r^2}\frac{\partial u}{\partial \theta} + \frac{(C_{11} - C_{12})}{2}\frac{1}{r}\frac{\partial v}{\partial r} - \frac{(C_{11} - C_{12})}{2}\frac{1}{r^2}v + F_\theta = 0, \\ & C_{44}\frac{\partial^2 w}{\partial r^2} + C_{44}\frac{1}{r^2}\frac{\partial^2 w}{\partial \theta^2} + C_{33}\frac{\partial^2 w}{\partial z^2} + (C_{13} + C_{44})\frac{\partial^2 u}{\partial r \partial z} + (C_{13} + C_{44})\frac{1}{r}\frac{\partial^2 v}{\partial \theta \partial z} \\ & + (C_{13} + C_{44})\frac{1}{r}\frac{\partial u}{\partial z} + C_{44}\frac{1}{r}\frac{\partial w}{\partial r} + F_z = 0,\end{aligned}\tag{12.18}$$

where  $C_{kl}$  are the constants appearing in Hooke's law as given by (12.1). Following the same strategy as in Cartesian coordinates, the general solutions are obtained in form of

$$u = \frac{\partial}{\partial r}(\phi_1 + \phi_2) + \frac{1}{r}\frac{\partial \psi}{\partial \theta}, \quad v = \frac{1}{r}\frac{\partial}{\partial \theta}(\phi_1 + \phi_2) - \frac{\partial \psi}{\partial r}, \quad w = \frac{\partial}{\partial z}(k_1\phi_1 + k_2\phi_2),\tag{12.19}$$

where  $k_1$  and  $k_2$  are the roots of (12.9) which correspond to  $\vartheta_1$  and  $\vartheta_2$  in (12.10).

Following (12.1), the strain relations and the displacement solution (12.19), the



stress equations in term of displacements can be written as

$$\begin{aligned}
\frac{\sigma_{rr}}{C_{44}} &= -(1+k_1)\frac{\partial^2\phi_1}{\partial z^2} - (1+k_2)\frac{\partial^2\phi_2}{\partial z^2} - \frac{2}{\vartheta_3}\left[\left(\frac{1}{r}\frac{\partial}{\partial r} + \frac{1}{r^2}\frac{\partial^2}{\partial\theta^2}\right)(\phi_1 + \phi_2) - \frac{\partial}{\partial r}\left(\frac{1}{r}\frac{\partial\psi}{\partial\theta}\right)\right], \\
\frac{\sigma_{\theta\theta}}{C_{44}} &= -(1+k_1)\frac{\partial^2\phi_1}{\partial z^2} - (1+k_2)\frac{\partial^2\phi_2}{\partial z^2} - \frac{2}{\vartheta_3}\left[\frac{\partial^2}{\partial r^2}(\phi_1 + \phi_2) + \frac{\partial}{\partial r}\left(\frac{1}{r}\frac{\partial\psi}{\partial\theta}\right)\right], \\
\frac{\sigma_{zz}}{C_{44}} &= \frac{(k_1C_{33} - \vartheta_1C_{13})}{C_{44}}\frac{\partial^2\phi_1}{\partial z^2} + \frac{(k_2C_{33} - \vartheta_2C_{13})}{C_{44}}\frac{\partial^2\phi_2}{\partial z^2}, \\
\frac{\sigma_{r\theta}}{C_{44}} &= \frac{2}{\vartheta_3}\left[\frac{1}{r}\frac{\partial^2}{\partial r\partial\theta} - \frac{1}{r^2}\frac{\partial}{\partial\theta}\right](\phi_1 + \phi_2) + \frac{1}{\vartheta_3}\left[\frac{2}{r}\frac{\partial\psi}{\partial r} + \vartheta_3\frac{\partial^2\psi}{\partial z^2} + \frac{2}{r^2}\frac{\partial^2\psi}{\partial\theta^2}\right], \\
\frac{\sigma_{\theta z}}{C_{44}} &= (1+k_1)\frac{1}{r}\frac{\partial^2\phi_1}{\partial\theta\partial z} + (1+k_2)\frac{1}{r}\frac{\partial^2\phi_2}{\partial\theta\partial z} - \frac{\partial^2\psi}{\partial r\partial z}, \\
\frac{\sigma_{rz}}{C_{44}} &= (1+k_1)\frac{\partial^2\phi_1}{\partial r\partial z} + (1+k_2)\frac{\partial^2\phi_2}{\partial r\partial z} + \frac{1}{r}\frac{\partial^2\psi}{\partial\theta\partial z}.
\end{aligned} \tag{12.20}$$

## 12.5 Simple shear problem for transversely isotropic linearly elastic materials

The simple shear problem shown in Figure 12.2 is considered by assuming that

$$\phi_1 = Ar^2z + Bz^3 + Cz \log r, \quad \phi_2 = Dr^2z + Ez^3 + Fz \log r, \tag{12.21}$$

are the solutions for a transversely isotropic linearly elastic material, where  $A, B, C, D, E$  and  $F$  are constants. Since they satisfy

$$\left(\frac{\partial^2}{\partial r^2} + \frac{1}{r}\frac{\partial}{\partial r} + \frac{1}{r^2}\frac{\partial^2}{\partial\theta^2} + \vartheta_i\frac{\partial^2}{\partial z^2}\right)\phi_i = 0, \quad i = 1, 2,$$

the following conditions are obtained

$$2A + 3\vartheta_1B = 0, \quad 2D + 3\vartheta_2E = 0.$$

In this problem, the oscillation of carbon nanotubes in the axial-direction ( $z$ -direction) is considered and the two boundary conditions for each tube are assumed

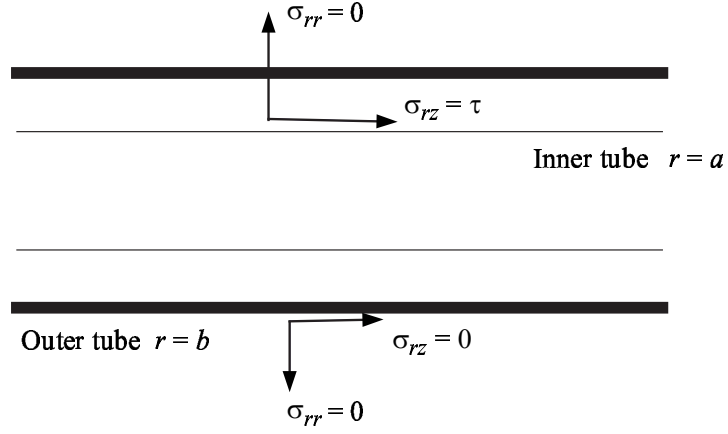


Figure 12.2: Diagram of double-walled carbon nanotubes.

to be

$$\begin{aligned} \sigma_{rr} &= 0, & \sigma_{rz} &= 0, & r &= b, \\ \sigma_{rr} &= 0, & \sigma_{rz} &= \tau, & r &= a, \end{aligned}$$

where  $\tau$  denotes the tangential friction generated by the inner tube which is assumed to be constant. From the stress equations in (12.20)<sub>1</sub> and (12.20)<sub>6</sub>, the boundary conditions and the solutions given by (12.21), they may be deduced

$$-\frac{2}{\vartheta_3} \left( 2A + \frac{C}{b^2} + 2D + \frac{F}{b^2} \right) - 6(1 + k_1)B - 6(1 + k_2)E = 0,$$

$$(1 + k_1) \left( 2Ab + \frac{C}{b} \right) + (1 + k_2) \left( 2Db + \frac{F}{b} \right) = 0,$$

$$-\frac{2}{\vartheta_3} \left( 2A + \frac{C}{a^2} + 2D + \frac{F}{a^2} \right) - 6(1 + k_1)B - 6(1 + k_2)E = 0,$$

$$(1 + k_1) \left( 2Aa + \frac{C}{a} \right) + (1 + k_2) \left( 2Da + \frac{F}{a} \right) = \frac{\tau}{\mu}.$$

On solving these equations, the constants  $A, B, C, D, E$  and  $F$  are obtained

$$\begin{aligned}
 A &= \frac{\tau a \vartheta_1 [\vartheta_2 - \vartheta_3 (1 + k_2)]}{2\mu(b^2 - a^2)[\vartheta_1 \vartheta_2 (k_2 - k_1) + \vartheta_3 (\vartheta_1 - \vartheta_2)(1 + k_1)(1 + k_2)]}, \\
 B &= \frac{-\tau a [\vartheta_2 - \vartheta_3 (1 + k_2)]}{3\mu(b^2 - a^2)[\vartheta_1 \vartheta_2 (k_2 - k_1) + \vartheta_3 (\vartheta_1 - \vartheta_2)(1 + k_1)(1 + k_2)]}, \\
 C &= \frac{-\tau a b^2}{\mu(b^2 - a^2)(k_2 - k_1)}, \\
 D &= \frac{-\tau a \vartheta_2 [\vartheta_1 - \vartheta_3 (1 + k_1)]}{2\mu(b^2 - a^2)[\vartheta_1 \vartheta_2 (k_2 - k_1) + \vartheta_3 (\vartheta_1 - \vartheta_2)(1 + k_1)(1 + k_2)]}, \\
 E &= \frac{\tau a [\vartheta_1 - \vartheta_3 (1 + k_1)]}{3\mu(b^2 - a^2)[\vartheta_1 \vartheta_2 (k_2 - k_1) + \vartheta_3 (\vartheta_1 - \vartheta_2)(1 + k_1)(1 + k_2)]}, \\
 F &= \frac{\tau a b^2}{\mu(b^2 - a^2)(k_2 - k_1)}.
 \end{aligned}$$

Further, the displacements in the  $r$ -direction and  $z$ -direction can be written as follows:

$$\begin{aligned}
 \mu u &= \frac{\tau a \vartheta_3 [\vartheta_2 (1 + k_1) - \vartheta_1 (1 + k_2)]}{(b^2 - a^2)[\vartheta_1 \vartheta_2 (k_2 - k_1) + \vartheta_3 (\vartheta_1 - \vartheta_2)(1 + k_1)(1 + k_2)]} r z, \\
 \mu w &= \frac{\tau a \{k_1 \vartheta_1 [\vartheta_2 - \vartheta_3 (1 + k_2)] - k_2 \vartheta_2 [\vartheta_1 - \vartheta_3 (1 + k_1)]\}}{2(b^2 - a^2)[\vartheta_1 \vartheta_2 (k_2 - k_1) + \vartheta_3 (\vartheta_1 - \vartheta_2)(1 + k_1)(1 + k_2)]} r^2 + \frac{\tau a b^2}{(b^2 - a^2)} \log r \\
 &\quad - \frac{\tau a \{k_1 [\vartheta_2 - \vartheta_3 (1 + k_2)] - k_2 [\vartheta_1 - \vartheta_3 (1 + k_1)]\}}{(b^2 - a^2)[\vartheta_1 \vartheta_2 (k_2 - k_1) + \vartheta_3 (\vartheta_1 - \vartheta_2)(1 + k_1)(1 + k_2)]} z^2. \quad (12.22)
 \end{aligned}$$

If in the quadratic equation (12.9), values of  $C_{ij}$  are substituted for the isotropic linearly elastic material, then  $k_1 = k_2 = 1$  and the values of  $\vartheta_i$  corresponding to  $k_i$  in (12.10) are  $\vartheta_1 = \vartheta_2 = \vartheta_3 = 1$ . Thus, in order to deduce the isotropic solution from the above equations,  $k_1$  and  $k_2$  are assumed to be given by

$$k_1 = 1 + \epsilon, \quad k_2 = 1 - \epsilon,$$

where  $\epsilon \ll 1$ . From (12.10) and (12.14),  $\vartheta_1, \vartheta_2$  and  $\vartheta_3$  are determined to be

$$\vartheta_1 = 1 + \frac{\epsilon}{2(1 - \nu)}, \quad \vartheta_2 = 1 - \frac{\epsilon}{2(1 - \nu)}, \quad \vartheta_3 = 1,$$

and on substituting those values of  $k_i$  and  $\vartheta_i$  into (12.22)<sub>1</sub> and (12.22)<sub>2</sub> and then letting  $\epsilon$  tend to zero, it can be shown that

$$\mu u = \frac{-\tau a \nu}{(b^2 - a^2)(1 + \nu)} r z,$$

$$\mu w = \frac{\tau a}{2(b^2 - a^2)(1 + \nu)} (z^2 - r^2) + \frac{\tau a b^2}{(b^2 - a^2)} \log r.$$

## 12.6 Simple shear problem for isotropic linearly elastic materials

In this section, the solution for the simple shear problem of a isotropic linearly elastic material as given by Lure [143] is formally derived. The displacement equations for isotropic linearly elastic materials of torsion-free axial-symmetric problems are given in [143], and can be written as

$$\begin{aligned} u &= 4(1 - \nu)B_r - \frac{\partial}{\partial r}(rB_r + zB_z + B_0), \\ w &= 4(1 - \nu)B_z - \frac{\partial}{\partial z}(rB_r + zB_z + B_0), \end{aligned}$$

where  $B_r$ ,  $B_z$  and  $B_0$  satisfy Laplace's equation. Suppose  $B_r$  is zero and that

$$B_0 = \frac{A}{2}(2z^3 - 3zr^2) + Bz \log r, \quad B_z = \frac{C}{2}(2z^2 - r^2) + B \log r,$$

are solutions for the isotropic linearly elastic material. From the stress and displacement equations for the isotropic linearly elastic material and the boundary conditions

$$\begin{aligned} \sigma_{rr} &= 0, & \sigma_{rz} &= \tau_0, & \text{for } r &= b, \\ \sigma_{rr} &= 0, & \sigma_{rz} &= -\tau_1, & \text{for } r &= a, \end{aligned}$$

the following four equations are obtained

$$(3A + C) + 8\nu(1 - \nu)C - 6\nu(A + C) + (1 - 2\nu)(B + D)\frac{1}{b^2} = 0,$$

$$(3A + C) + 8\nu(1 - \nu)C - 6\nu(A + C) + (1 - 2\nu)(B + D)\frac{1}{a^2} = 0,$$

$$[(3A + C) - 2(1 - \nu)C]b + [2(1 - \nu)D - (B + D)]\frac{1}{b} = \frac{\tau_0(1 + \nu)}{E},$$

$$[(3A + C) - 2(1 - \nu)C]a + [2(1 - \nu)D - (B + D)]\frac{1}{a} = \frac{-\tau_1(1 + \nu)}{E}.$$

On solving these equations,  $A, B, C$  and  $D$  are given by

$$\begin{aligned} A &= \frac{(4\nu + 1)(\tau_0 b + \tau_1 a)}{6E(b^2 - a^2)}, & B &= \frac{ab(1 + \nu)(\tau_0 a + \tau_1 b)}{2E(1 - \nu)(b^2 - a^2)}, \\ C &= \frac{-(\tau_0 b + \tau_1 a)}{2E(b^2 - a^2)}, & D &= \frac{-ab(1 + \nu)(\tau_0 a + \tau_1 b)}{2E(1 - \nu)(b^2 - a^2)}, \end{aligned}$$

and the displacement equations for torsion-free axial-symmetric deformations for isotropic linearly elastic materials yield

$$\begin{aligned} \mu u &= \frac{\nu(\tau_0 b + \tau_1 a)}{(b^2 - a^2)(1 + \nu)} r z, \\ \mu w &= \frac{(\tau_0 b + \tau_1 a)}{2(b^2 - a^2)(1 + \nu)} (r^2 - z^2) - \frac{ab(\tau_0 a + \tau_1 b)}{(b^2 - a^2)} \log r. \end{aligned} \tag{12.23}$$

Now, for the special case  $\tau_0 = 0$  and  $\tau_1 = -\tau$  the displacements become

$$\begin{aligned} \mu u &= \frac{-\tau a \nu}{(b^2 - a^2)(1 + \nu)} r z, \\ \mu w &= \frac{\tau a}{2(b^2 - a^2)(1 + \nu)} (z^2 - r^2) + \frac{\tau a b^2}{(b^2 - a^2)} \log r, \end{aligned}$$

which are in complete agreement with those obtained in the previous section.

# Chapter 13

## Wave-like deformations for oscillating carbon nanotubes

Double-walled carbon nanotubes are widely studied as possible gigahertz oscillators, where the inner tube oscillates within the outer tube. These oscillators can generate frequencies in the gigahertz range. They are also known to generate wave-like deformations on the outer surface. In this chapter, such induced deformations on the surface of the outer tube are studied, as generated by the moving inner tube. Double-walled carbon nanotubes are modelled as transversely isotropic linearly elastic materials. Using a force distribution for the resultant van der Waals forces arising from the interatomic interactions, a dynamical linearly elastic problem is solved, and it is shown that the resulting solution exhibits wave-like behaviour.

### 13.1 Nomenclature

$\sigma_{ij}$  are element of the Cauchy stress tensor

$\tau$  is the coefficient of tangential friction

$C_{ij}$  are the elastic constants

$J_n$  is the Bessel function of the first kind

$L_1, L_2$  are the half-lengths of the inner and the outer tubes, respectively

$Y_n$  is the Bessel function of the second kind

$W$  is the maximum force value

$a, b$  are the radii of the inner and the outer carbon nanotubes, respectively

$h$  is the thickness of the outer tube

$r, \theta, z$  are a system of cylindrical coordinates

$u, w$  are the displacements in the  $r$ - and  $z$ -directions, respectively

## 13.2 Model formulation and boundary conditions

A double-walled uncapped carbon nanotube is considered where the half-length of the inner and outer tubes are  $L_1$  and  $L_2$ , respectively, the inner tube has radius  $a$ , the outer tube has radius  $b$  and the thickness of the outer tube is assumed to be  $h$ , and for convenience,  $c$  is defined as  $c = b + h$ . The force distribution for double-walled carbon nanotubes is determined using the continuum approach for which the atoms are assumed to be smeared over the surfaces on both the inner and outer tubes as derived in §3.3. The resultant van der Waals force is calculated assuming prescribed surface densities of carbon atoms along the surfaces  $r = a$  for the inner tube and  $r = b$  for the outer tube, and is evaluated by two surface integrals. Further, these surface inter-atomic interactions described by the van der Waals force are assumed to dominate. Transversely isotropic linearly elastic equations are utilised to model the deformations for the outer tube assuming a stress free boundary condition on the outer surface  $r = c$  and a stress  $\sigma_{rz} = \tau$  and  $\sigma_{rr} = 0$  acting on the inner surface  $r = b$ . The stress  $\tau$  is the van der Waals force per unit contact area which is assumed to arise from the motion of the inner tube moving in the  $z$ -direction, as illustrated in Figure 13.1.

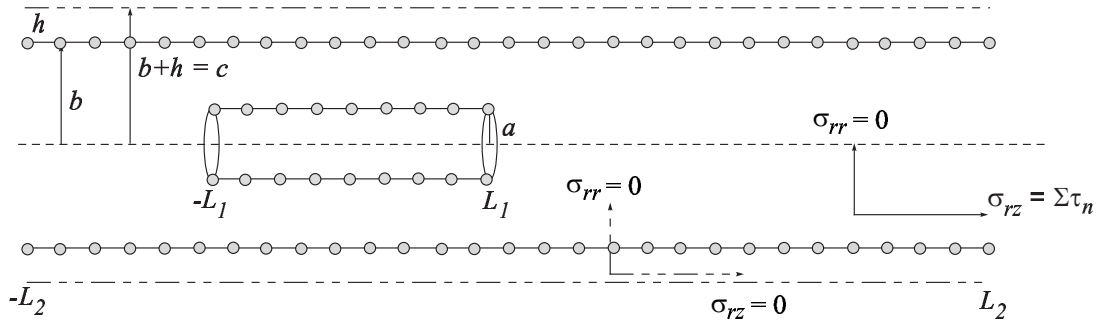


Figure 13.1: Diagram of double-walled carbon nanotube.

The length of the outer tube is assumed to be very long in comparison to the length of the inner tube, so that the contact area is given by  $A = 4\pi a L_1$ . Further,

the force distribution for double-walled carbon nanotubes, derived in §3.3 and shown in Figure 13.2, can be idealised by the dotted line shown, that is, the actual force distribution is approximated in terms of rectangular functions as follows

$$f(z) = W[H(z + L_1 + L_2) - H(z - L_1 + L_2)] - W[H(z + L_1 - L_2) - H(z - L_1 - L_2)], \quad (13.1)$$

where  $W$  denotes the maximum value on the force axis. The Fourier series expansion for an odd function is given by

$$f(z) = \sum_{n=1}^{\infty} b_n \sin nz, \quad b_n = \frac{1}{2L} \int_{-2L}^{2L} f(z) \sin \left( \frac{n\pi z}{2L} \right) dz, \quad (13.2)$$

where  $f(z)$  is a piecewise continuous function in the interval  $[-2L, 2L]$  and has period  $4L$ . Using (13.1) and (13.2), the Fourier series expansion for the van der Waals force with period  $4(L_1 + L_2)$  for arbitrary lengths  $L_1$  and  $L_2$  can be written as

$$f(z) = \frac{2W}{\pi} \sum_{n=1}^{\infty} \frac{1}{n} \left\{ \cos \left( \frac{n\pi}{2} \right) - \cos \left[ \frac{n\pi(L_2 - L_1)}{2(L_1 + L_2)} \right] \right\} \sin \left[ \frac{n\pi z}{2(L_1 + L_2)} \right]. \quad (13.3)$$

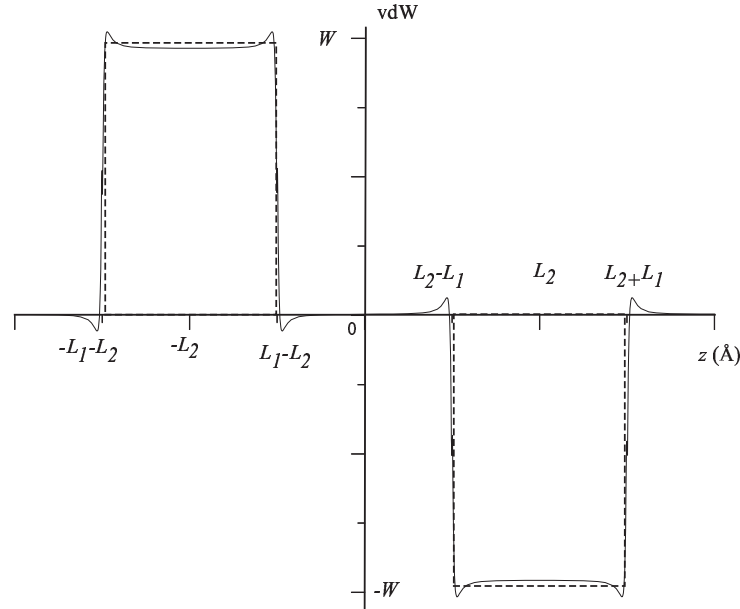


Figure 13.2: Force distribution approximated by rectangular functions.

From the oscillatory behaviour, this force is time dependent with angular fre-



quency  $\omega$  and from (13.3) it may be supposed

$$f(z, t) = \frac{2W}{\pi} \sum_{n=1}^{\infty} \frac{1}{n} \left\{ \cos\left(\frac{n\pi}{2}\right) - \cos\left[\frac{n\pi(L_2 - L_1)}{2(L_1 + L_2)}\right] \right\} \sin\left[\frac{n\pi z}{2(L_1 + L_2)}\right] e^{i\omega t}. \quad (13.4)$$

Further, the angular frequency  $\omega$  is assumed to be obtained from the oscillation frequency  $f$  derived in §3.3 where  $\omega = 2\pi f$  and  $L_1 \neq L_2$ . This oscillation frequency is derived for an inner tube extruded an initial distance  $d$  from the end of the outer tube and simultaneously given an initial velocity  $v_0$  in the negative  $z$ -direction. Finally, the stress boundary conditions at  $r = c$  are  $\sigma_{rz} = \sigma_{rr} = 0$ , while at  $r = b$  they can be written as

$$\begin{aligned} \sigma_{rz} &= \frac{W}{2aL_1\pi^2} \sum_{n=1}^{\infty} \frac{1}{n} \left\{ \cos\left(\frac{n\pi}{2}\right) - \cos\left[\frac{n\pi(L_2 - L_1)}{2(L_1 + L_2)}\right] \right\} \sin\left[\frac{n\pi z}{2(L_1 + L_2)}\right] e^{i\omega t}, \\ \sigma_{rr} &= 0. \end{aligned}$$

In the process of modelling the van der Waals force by equation (13.3), the usual continuum practice of ignoring the small scale effects are employed, which occur at the four points  $Z = \pm(L_1 + L_2)$  and  $Z = \pm(L_1 - L_2)$ .

In adopting this approach, by necessity any information pertaining to the atomic lattice length characteristics is excluded, and the critical length characteristic embodied in (13.3) is the macro-length  $(L_1 + L_2)$ . Having established (13.3) as the van der Waals force, (13.4) is merely the time-dependent form of (13.3) with a prescribed angular velocity  $\omega$ , which is specifically adopted in order that the governing continuum equations admit separable solutions. However, (13.4) is by no means unique and other forms are possible, but these alternatives would not necessarily give rise to tractable equations.

### 13.3 Displacement and shear force solutions

Assuming that the displacements of the outer tube  $(u, v, w)$ , where  $u$ ,  $v$  and  $w$  are the physical components of displacement in the  $r$ ,  $\theta$  and  $z$  directions, are synchronised with respect to the motion of the inner tube and they therefore have the same angular frequency. Moreover, assuming that there is no torsional motion,  $v$  becomes

zero and  $u$  and  $w$  can be written as

$$u(r, z, t) = \sum_{n=1}^{\infty} f_n(r) \cos(k_n z) e^{i\omega t}, \quad w(r, z, t) = \sum_{n=1}^{\infty} g_n(r) \sin(k_n z) e^{i\omega t}.$$

On solving the momentum equations (12.18) neglecting any body force, it may be readily shown that the functions  $f_n(r)$  and  $g_n(r)$  are given by

$$f_n(r) = A_{n1}J_1(p_{n1}r) + A_{n2}Y_1(p_{n1}r) + A_{n3}J_1(p_{n2}r) + A_{n4}Y_1(p_{n2}r),$$

$$g_n(r) = S_{n1}[A_{n1}J_0(p_{n1}r) + A_{n2}Y_0(p_{n1}r)] + S_{n2}[A_{n3}J_0(p_{n2}r) + A_{n4}Y_0(p_{n2}r)],$$

where  $J_0$ ,  $J_1$  and  $Y_0$ ,  $Y_1$  are Bessel functions of the first and second kinds, respectively,  $A_{n1}$ ,  $A_{n2}$ ,  $A_{n3}$  and  $A_{n4}$  denote four arbitrary constants and  $p_{n1}$ ,  $p_{n2}$ ,  $S_{n1}$  and  $S_{n2}$  are constants which involve the elastic constants and are given by

$$\begin{aligned} p_{n1} &= \sqrt{\frac{(C_{13}^2 - C_{11}C_{33} + 2C_{13}C_{44})k_n^2 + (C_{11} + C_{44})\rho\omega^2 + \sqrt{q_n}}{2C_{11}C_{44}}}, \\ p_{n2} &= \sqrt{\frac{(C_{13}^2 - C_{11}C_{33} + 2C_{13}C_{44})k_n^2 + (C_{11} + C_{44})\rho\omega^2 - \sqrt{q_n}}{2C_{11}C_{44}}}, \\ S_{n1} &= \frac{p_{n1}}{2k_n(C_{13} + C_{44})(\rho\omega^2 - C_{33}k_n^2)} \left[ (2C_{13}C_{44} + C_{13}^2 + C_{11}C_{33})k_n^2 \right. \\ &\quad \left. + (C_{44} - C_{11})\rho\omega^2 - \sqrt{q_n} \right], \\ S_{n2} &= \frac{p_{n2}}{2k_n(C_{13} + C_{44})(\rho\omega^2 - C_{33}k_n^2)} \left[ (2C_{13}C_{44} + C_{13}^2 + C_{11}C_{33})k_n^2 \right. \\ &\quad \left. + (C_{44} - C_{11})\rho\omega^2 + \sqrt{q_n} \right], \end{aligned}$$

and

$$\begin{aligned} q_n &= (C_{11}C_{33} - C_{13}^2) \left[ C_{11}C_{33} - 4 \left( C_{44} + \frac{C_{13}}{2} \right)^2 \right] k_n^4 + (C_{11} - C_{44})^2 \rho^2 \omega^4 \\ &\quad - 2\rho\omega^2 k_n^2 \left\{ C_{33}C_{11}^2 - [2C_{44}^2 + (C_{33} + 2C_{13})C_{44} + C_{13}^2]C_{11} - 2C_{13}C_{44}^2 - C_{13}^2C_{44} \right\}. \end{aligned}$$

From the stress-strain relations for  $\sigma_{rr}$  and  $\sigma_{rz}$  in (12.16) and (12.17), they can

be written as

$$\begin{aligned}
 \sigma_{rr} = & \sum_{n=1}^{\infty} \cos(k_n z) e^{i\omega t} \left\{ A_{n1} \left[ \alpha_n J_0(p_{n1} r) - \frac{C_{11}}{r} J_1(p_{n1} r) \right] \right. \\
 & + A_{n2} \left[ \alpha_n Y_0(p_{n1} r) - \frac{C_{11}}{r} Y_1(p_{n1} r) \right] + A_{n3} \left[ \beta_n J_0(p_{n2} r) \right. \\
 & \left. \left. - \frac{C_{11}}{r} J_1(p_{n2} r) \right] + A_{n4} \left[ \beta_n Y_0(p_{n2} r) - \frac{C_{11}}{r} Y_1(p_{n2} r) \right] \right\}, \\
 \sigma_{rz} = & - \sum_{n=1}^{\infty} C_{44} \sin(k_n z) e^{i\omega t} \left[ A_{n1} \gamma_n J_1(p_{n1} r) + A_{n2} \gamma_n Y_1(p_{n1} r) \right. \\
 & \left. + A_{n3} \delta_n J_1(p_{n2} r) + A_{n4} \delta_n Y_1(p_{n2} r) \right],
 \end{aligned} \tag{13.5}$$

where  $\alpha_n, \beta_n, \gamma_n$  and  $\delta_n$  are further constants defined by

$$\begin{aligned}
 \alpha_n &= p_{n1} C_{11} - k_n S_{n1} C_{13}, & \beta_n &= p_{n2} C_{11} - k_n S_{n2} C_{13}, \\
 \gamma_n &= p_{n1} S_{n1} + k_n, & \delta_n &= p_{n2} S_{n2} + k_n.
 \end{aligned}$$

From the boundary conditions at  $r = b$  and (13.5)<sub>2</sub>, it can be deduced

$$k_n = \frac{n\pi}{2(L_1 + L_2)}, \quad \tau_n = \frac{W}{2naL_1\pi^2 C_{44}} \left\{ \cos \left[ \frac{n\pi(L_2 - L_1)}{2(L_1 + L_2)} \right] - \cos \left( \frac{n\pi}{2} \right) \right\},$$

and from the stress boundary conditions, a system of four equations in the four unknowns  $A_{ni}$  ( $i = 1, 2, 3, 4$ ) can be formulated. These may be readily solved using the algebraic computer package MAPLE and the details are summarised in Appendix F.

## 13.4 Tables of elastic constants

Experiments and theoretical studies have shown that carbon nanotubes can be modelled as transversely isotropic linearly elastic materials where the elastic constants and elastic moduli define their elastic properties. In this study, three contributions by Jin and Yuan [15], Lu [20] and Shen and Li [134] are examined, all of whom evaluate the elastic constants and elastic moduli for both single-walled and multi-walled carbon nanotubes.

Jin and Yuan [15] use molecular dynamics simulations as well as the Lennard-Jones potential to study the elastic properties of single-walled carbon nanotubes. They determine the values of elastic moduli, denoted as Poisson's ratio  $\nu_{z\theta}$ ,  $\nu_{\theta z}$ ,

Young's moduli  $E_z$ ,  $E_\theta$  and shear modulus  $G_{\theta z}$ , and elastic constants  $C_{33}$  and  $C_{23}$ , by using energy and force approaches, which give approximately the same numerical values. Here, the values of elastic moduli from the force approach are employed throughout. Terminology utilised here:  $E$ ,  $E'$ ,  $\mu'$  and  $C_{13}$  refer to their  $E_z$ ,  $E_\theta$ ,  $G_{\theta z}$  and  $C_{23}$ , respectively. Poisson's ratio in longitudinal direction  $\nu'$  is given by averaging  $\nu_{\theta z}$  and  $\nu_{z\theta}$  and Poisson's ratio in transverse plane  $\nu$  is obtained by solving  $C_{33}$  in (12.4). Thus, the values of elastic constants for single-walled carbon nanotubes based on Jin and Yuan [15] are shown in Appendix G, Table G.1.

Lu [20] uses an empirical force-constant model and the Lennard-Jones potential function to investigate the elastic properties of carbon nanotubes and nanoropes. For the carbon nanotube structures, he finds that the elastic moduli are insensitive to the radius, the helicity and the number of walls. He also reports values of the elastic constants  $C_{11}$  and  $C_{33}$  and elastic moduli, namely Poisson ratio  $\nu$ , bulk modulus  $B$ , Young's modulus  $Y$  and shear modulus  $M$  for both single-walled and multi-walled carbon nanotubes. Here, Poisson ratio, Young's modulus and shear modulus are defined by  $\nu'$ ,  $E'$  and  $\mu'$ , respectively.  $E$  and  $\nu$  are obtained by solving the equations for  $C_{11}$  and  $C_{33}$  in (12.4). Finally, the elastic constants for single-walled and multi-walled carbon nanotubes based on Lu [20] are shown in Appendix G, Table G.2 and Table G.3, respectively.

Shen and Li [134] also study the elastic properties of single-walled and double-walled carbon nanotubes by assuming that carbon nanotube structures are transversely isotropic linearly elastic materials. They calculate five elastic moduli, denoted as Poisson's ratio  $\nu_{12}$ , Young's modulus  $E_{11}$ , shear moduli  $G_{12}$ ,  $G_{23}$  and bulk modulus  $K_{23}$ , by analysing the deformations under loading conditions. Note that in their work 1 denotes the longitudinal or  $Z$  direction, and  $E_{11}$ ,  $\nu_{12}$ ,  $G_{12}$ ,  $K_{23}$  and  $G_{23}$  refer to  $E'$ ,  $\nu'$ ,  $\mu'$ ,  $K$  and  $G$ , respectively. Therefore, the values of elastic constants are obtained by using the formulae in (12.4), shown in Appendix G, Table G.4 and Table G.5.

The large variation in the numerical values of these elastic constants is primarily due to the uncertainty regarding the actual values of the wall thickness, the different potential functions in the study, the calculation methods, and the size of the time step [148, 149].

## 13.5 Numerical results

In this section, the displacements  $u$  and  $w$  for a double-walled carbon nanotubes modelled as a transversely isotropic linearly elastic material are plotted. Using the algebraic computer package MAPLE, the displacements  $u$  and  $w$  versus an arbitrary point on the  $z$  axis of the outer surface of the outer tube are shown. Following the determination in §3.3, the same values of the van der Waals constants to determine the van der Waals force are used. For the elastic constants  $C_{ij}$ , the values given in Table G.3 for  $n = 2$  are used. Of particular practical interest is the case when the initial velocity is zero and the extrusion distance is  $d = L_1$ , for which the graphs of the displacements  $u$  and  $w$  are given in Figure 13.3 and Figure 13.4 where  $W = 1$ ,  $h = 0.66 \text{ \AA}$ ,  $L_1 = 10 \text{ nm}$  and  $L_2 = 500 \text{ nm}$ .

The wave-like deformations which depend on both space and time on the outer surface of the outer tube are observed. The deformation in the  $r$ -direction is a transverse wave representing the rippling on the surface, whereas the deformation in the  $z$ -direction is a longitudinal wave tending to compress the tube. Further, the deformation amplitude in the  $z$ -direction is much larger than that in the  $r$ -direction, showing that the tube behaves more like a spring. Moreover, the largest deformations are at the ends of the outer tube arising from the large attractive force there. Due to the assumed negligible friction, the deformation has the same pattern every 14.24 ps, which is the period  $T$  of the oscillation. At  $t = 0$  and  $t = T/2$ , the deformations have the same shape in both  $r$  and  $z$  directions but are opposite in phase. Similarly for  $t = T/4$  and  $t = 3T/4$ , the deformations at these times also have the same pattern but are opposite in phase, as shown in Figure 13.3 and Figure 13.4.

## 13.6 Summary

Here oscillating carbon nanotubes have been modelled as transversely isotropic linearly elastic materials where the oscillating inner tube moves in the axial direction while the outer tube remains fixed. Furthermore, the length of the inner tube  $L_1$  is assumed to be very small in comparison to the length of the outer tube  $L_2$ . The van der Waals force distribution evaluated in §3.3 is assumed. On neglecting any

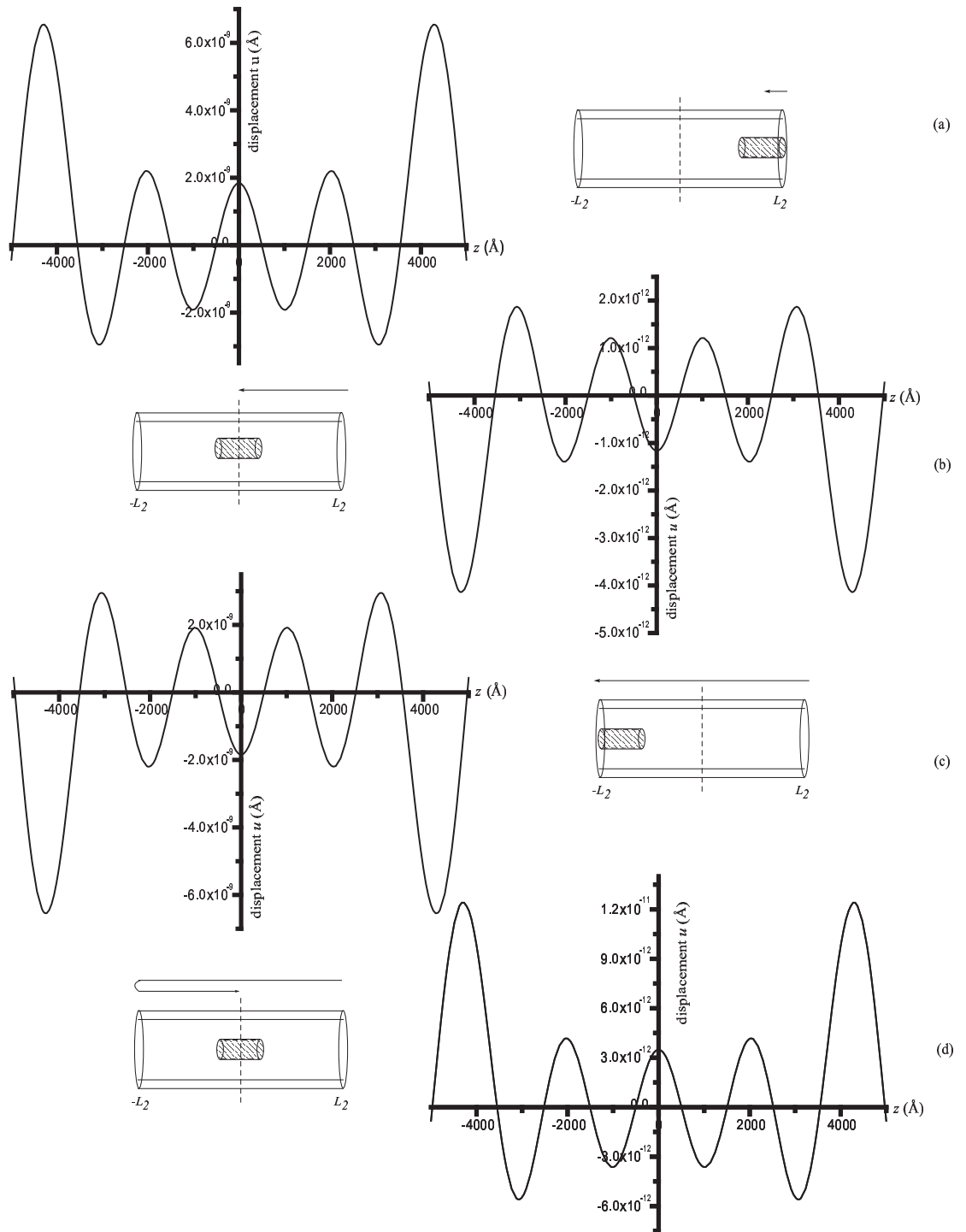


Figure 13.3: The displacement  $u(c, z, t)$  on the outer surface of the outer tube (a) at  $t = 0$ , (b) at  $t = T/4$ , (c) at  $t = T/2$  and (d) at  $t = 3T/4$  where  $T$  is the period of the oscillation.

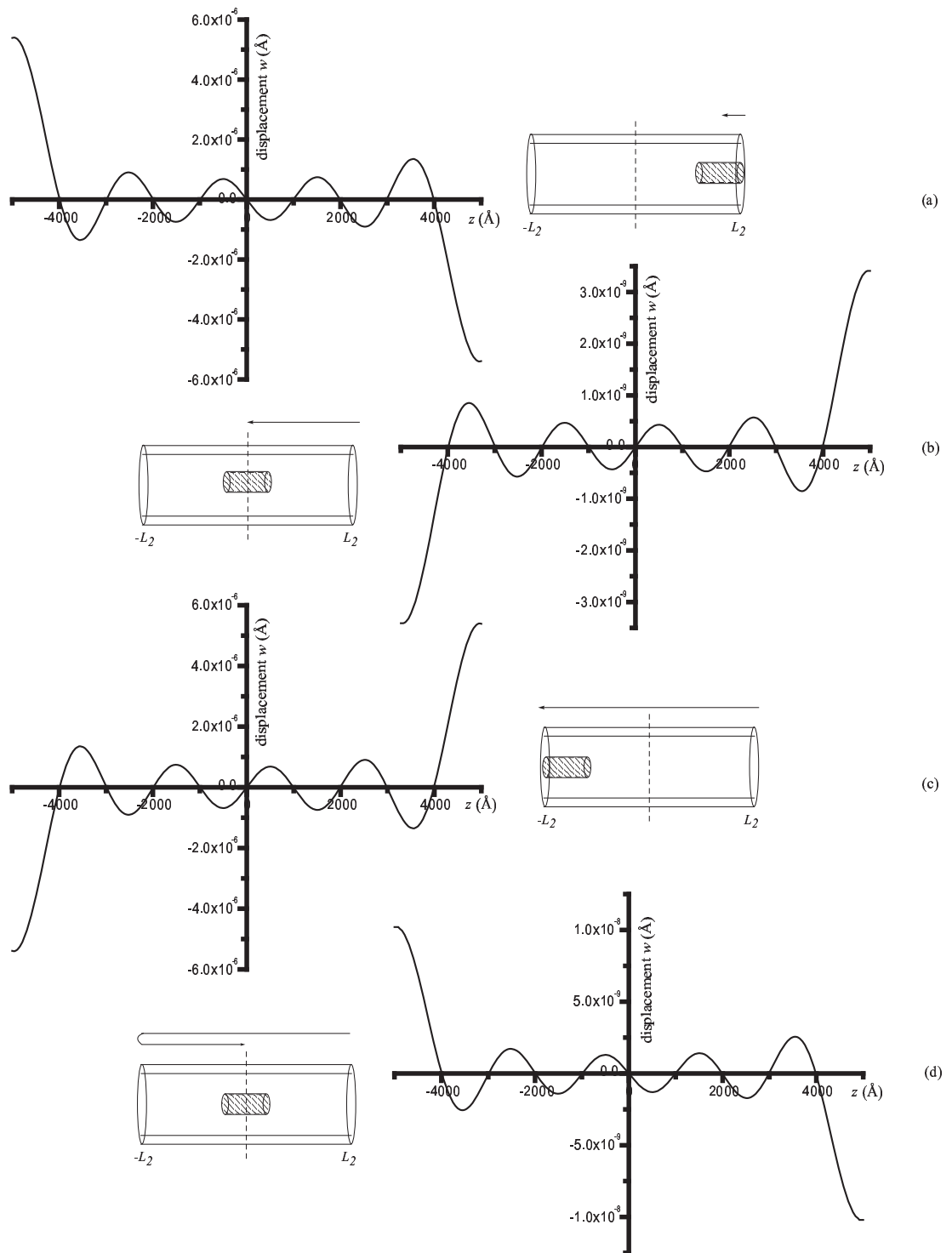


Figure 13.4: The displacement  $w(c, z, t)$  on the outer surface of the outer tube (a) at  $t = 0$ , (b) at  $t = T/4$ , (c) at  $t = T/2$  and (d) at  $t = 3T/4$  where  $T$  is the period of the oscillation.

frictional effects and assuming that the inner surface atoms of the outer tube and those located on the outer surface of the inner tube dominate the van der Waals force, the transversely isotropic linear elastic model is applied to the outer tube and expressions for displacements in the  $r$ - and  $z$ -directions are calculated. Deformations on the outer surface of the double-walled carbon nanotube due to the oscillations of the inner tube occur in both the  $r$ - and  $z$ -directions. A transverse wave occurs in the  $r$ -direction which gives a rippling effect on the surface, while a longitudinal wave occurs in the  $z$ -direction which tends to compress the tube. The amplitude of the deformation in the axial direction is much larger than that in the radial direction, which implies that the nanotube oscillator behaves like a spring.

The analysis presented here represents only a first step, and a more realistic model might result if the two effects of inter-tube friction and fluctuations in the nanotube due to a finite temperature are incorporated. These effects may conceivably be larger than those examined here. We comment that these calculations ignore the small variations in potential arising from the discrete structure or the corrugation of the tubes and there are two points to be noted. The first is that the corrugation energy gives rise to a conservative potential which does not give a frictional force and ultimately these interaction will decrease the amplitudes to zero. Secondly, the corrugation energy per bump is small but there are many bumps per cycle, and these corrugation barriers convert some potential energy to heat and thermal effects.



# Part V

## Summary

# Chapter 14

## Summary

In this thesis, applied mathematical modelling and elementary mechanical techniques have been employed to formulate analytical expressions for certain systems of nanostructures. In addition, the algebraic computer package MAPLE is utilized throughout to calculate numerical solutions of each of the problems. These theoretical investigations have generated new physical formulae applicable at the nanoscale, and which might be seen as a first step to create new derives in the field of nanotechnology. There are three main focuses in this thesis:

1. Continuum modelling of nanostructures,
2. Geometry of joining nanostructures,
3. Carbon nanotubes as transversely isotropic materials,

and a brief summary of each of these three topics is given below.

### 14.1 Continuum modelling for nanostructures

The Lennard-Jones potential function and the continuum approximation employed throughout Part II are introduced in Chapter 2. The van der Waals interaction energies and the resulting oscillatory behaviours for both carbon and boron nitride nanostructures are studied.

In Chapter 3, force distributions arising from the interatomic interactions for two concentric carbon nanotubes are considered and shown to be approximated by the Heaviside step functions. This has the advantage that Newton's second law can be utilized to describe the oscillatory motion of the inner carbon nanotube when it is extruded and given an initial velocity. The oscillation frequency is shown to be in

the order up to 80 gigahertz, and the shorter the inner tube the higher the frequency. In terms of the suction energy, its value depends on the difference of the tube radii, where the closer this value to zero, the less likely the inner tube will be accepted into the outer one. Further, the inner tube is spontaneously sucked into the outer tube and has its maximum suction energy when the difference of their radii is precisely equal to 3.44 Å. The equilibrium offset position for a double-walled carbon nanotube is also determined, assuming that the inner tube is already accepted inside. This equilibrium position of the offset inner tube tends to be closer to the outer tube wall as the radius of the outer tube increases. Particularly, the two notions of acceptance and suction energy are fundamental to the process of encapsulating drugs or genes in nano-carriers for targeted deliveries.

In Chapter 4, a well-known self-assembled hybrid carbon nanostructure comprising the  $C_{60}$  fullerenes and a carbon nanotube, the so-called nanopeapods, is investigated. Firstly, three suction site scenarios for a  $C_{60}$  molecule entering a carbon nanotube are determined. The binding energies for the three mechanisms are compared and it is found that the  $C_{60}$  molecule is most likely to enter through the carbon nanotube by the head-on configuration, and least likely by the molecule entering around the edge of the tubes open end. Once  $C_{60}$  fullerenes are encapsulated into a single-walled carbon nanotube, two nonlinear patterns for a  $C_{60}$  fullerene chain, zigzag and spiral, are examined. The chain is found to be formed linearly along the (10,10) tube axis and discernible zigzag patterns exist for both the (16,16) and (20,20) tubes. Likewise, a linear  $C_{60}$  fullerene chain is observed along the (10,10) tube axis and spiral patterns are detected for the (16,16) and (20,20) tubes. In general, the interaction between the  $C_{60}$  molecules determines the equilibrium position and the angular spacing of the system, whereas the interaction between the  $C_{60}$  fullerene and the carbon nanotube determines the offset position of the chain.

Chapter 5 considers the three related problems for nanocones entering carbon nanotubes, which are (i) the potential energy, (ii) the suction energy and (iii) the frequency of oscillation. Both carbon and boron nitride nanocones are investigated. Due to the lack of specific data, the known Lennard-Jones constants determined for plane sheets of carbon-carbon atoms are employed for carbon cones, and the mixing rule is undertaken for boron nitride cones. The equilibrium position increases

with decreasing cone angle or increasing number of pentagons. Furthermore, the equilibrium location always occurs when one cone is inside the other, so that nested double-cones might be expected to form in practice. The carbon cone which is assumed initially at rest outside the tube is sucked into the tube when the cone base radius and the tube radius differ by 2.49 Å to 2.54 Å, and this is irrespective of the direction of the vertex. The oscillatory behaviour is then examined assuming that the carbon nanocone is located co-axially and that it is sucked into the tube by van der Waals forces alone. Newton's second law, neglecting the frictional force, is employed to determine the frequency, which is shown to be in gigahertz range, 15 to 90 GHz.

In Chapter 6, the interspacing between two adjacent layers of spherical and ellipsoidal carbon onions is considered. The analysis gives rise to the possible dimensions for each shell of the carbon onions. Moreover, the equilibrium spacing is observed to decrease as the shell is further away from the inner core and this is due to the decreasing curvature for the larger spheroids. Finally, an approximate equation for the determination of the equilibrium spacing for any two adjacent layers of a spherical and an ellipsoidal carbon onion is provided.

## 14.2 Geometry of joining nanostructures

A key new concept for determining the joining of nanostructures is presented in Chapter 7. Here, the principle is invoked that two nanostructures join in such a way that the total least squares derivations from some ideal bond length is minimized. Two geometric approaches, the variations in bond length and in bond angle, are employed to determine model structures for physically occurring molecules for nanotori and connecting structures for tubes and sheets of carbon and boron nitride. Furthermore, Euler's theorem is used to check the consistency for each topological configuration for such structures, and the calculations for the bonded potential energy for a small deformation are carried out to verify combined molecules.

The main contribution of Chapter 8 is the application of the a least squares approach to determine the basic elbow unit and toroidal structures formed from three distinct carbon nanotubes. There are two approaches used in the minimization routines, which are the unconstrained and constrained cases for the bend angles. In

terms of the unconstrained procedure, all the physical parameters are allowed to attain their optimum values themselves, however there is no guarantee that the elbow sections can be joined to each other and form a complete toroidal shaped structure with a  $360^\circ$  turn. Therefore, the analysis is repeated with the angles  $\phi_1$  and  $\phi_2$  constrained to the value  $\phi_1 + \phi_2 = 180^\circ/n$  where  $n \in \{2, 3, 4, \dots\}$ . Here, two distinct elbows are considered which are (5,0)-(4,4)-(7,0) and (3,3)-(6,0)-(4,4). Since the principal aim is to construct toroidal molecules by joining elbow sections, these elbow sections are exploited so that the sum of their bend angles is a factor of 360. Following the analysis of two elbow types, toroidal shaped molecules are then investigated. A straightforward procedure is established to determine the mean generating toroidal radius  $c$  and the mean tube radius  $a$ .

In Chapter 9, the use of two distinct least squares approaches are employed to determine the perpendicular joining of three particular carbon nanotubes to a flat graphene sheet. Firstly, all possible structures for connecting the zigzag (8,0) and the armchair (4,4) carbon nanotubes to a flat graphene sheet are determined using the variation in bond length to minimize the bond length between two carbon atoms at each inter-atomic junction. There are sixteen structures for joining the zigzag tube and thirty-two configurations for joining the armchair tube. Euler's theorem is utilized to prescribe the polygons which occur at the junction, and for reasons of stability, the only carbon rings realizable are pentagonal, hexagonal, heptagonal and octagonal, and by imposing these conditions the number of configurations is reduced. Furthermore, octagonal rings are considered less likely to occur in practice, and therefore only one configuration for the zigzag tube and two structures for the armchair tube might be expected to be found in practice. In terms of the variation in bond angle approach, a simple example for joining a flat graphene sheet to a (6,0) carbon nanotube is presented, which is the most symmetrical possibility for the defect. Subsequently for the (8,0) tube and the defect structure, a least squares bond angle approach is undertaken. The structure obtained for the (8,0) and the sheet is shown to be very similar in terms of atom locations to that found using the bond length approach.

Chapter 10 considers two aspects of defect classification and connection for boron nitride structures. Given that rings with an even number of sides are energetically

favourable for boron nitride nanostructures, the number of possible distinct defect configurations is determined utilizing the necklace and bracelet problems from combinatorial theory, where an armchair (zigzag) tube requires all odd (even) number of bonds connecting between two adjacent atoms at the defect site. Once the defects are obtained, two distinct least squares approaches are employed to determine the connected structures for the tube and the sheet of boron nitride. Three examples of perpendicular joining boron nitride nanotubes, which are (3,3), (6,0) and (9,0) tubes and the most symmetrical defects are used to illustrate such approaches. Three dimensional illustrations for all cases of the two variation approaches are depicted, and Euler's theorem is utilized to verify that the connected structures are geometrically acceptable. Furthermore, the bonded potential energy for small deformations is evaluated to determine a measure of the stability of the system. Since the value for the bond stretching constant is significantly larger than that for the bending angle and from the least squares calculations, this are led to conclude that the minimization for the bond angle procedure provides lower energy values than the minimization for the bond length procedure, so that the former most likely provides a better model for physically occurring molecular structures.

### 14.3 Carbon nanotubes as transversely isotropic linearly elastic materials

A brief overview of the elasticity of carbon nanotubes is given in Chapter 11. Assuming that the carbon nanotube can be modelled as transversely isotropic linearly elastic materials, Hooke's law and the equilibrium equations for such materials are presented in Chapter 12. In addition, a simple shear problem for both isotropic and transversely isotropic materials is investigated and it is found that there is a relationship between the two types of isotropic materials.

In Chapter 13, oscillating carbon nanotubes are modelled as transversely isotropic linearly elastic materials, and the oscillating inner tube moves only in the axial direction while the outer tube remains fixed. Furthermore, the length of the inner tube is assumed to be very small in comparison to the length of the outer tube. The van der Waals force distribution is calculated from the continuum approximation. On neglecting any frictional effects and assuming that the inner surface atoms of

the outer tube and those located on the outer surface of the inner tube dominate the van der Waals force, the transversely isotropic linear elastic model is applied to the outer tube and expressions for the displacements in the  $r$ - and  $z$ -directions are obtained. A transverse wave occurs in the  $r$ -direction, which gives rise to a rippling effect on the surface, while a longitudinal wave occurs in the  $z$ -direction which tends to compress the tube. The amplitude of the deformation in the axial direction is much larger than that in the radial direction, implying that the nanotube oscillator behaves like a spring.

In summary, the new elements of this thesis comprise:

- Analytical expressions to determine the equilibrium locations, force distributions and oscillatory behaviour for nested carbon and boron nitride nanostructures including double-walled carbon nanotubes, nanopeapods, nanocones and onions,
- Two simple least squares procedures to connect two nanostructures, and a method to classify the defects for a boron nitride sheet,
- Transversely isotropic linearly elastic model for the deformations of double-walled carbon nanotubes with an oscillating the inner tube.

## Part VI

### Appendices and Bibliography



# Appendix A

## Analytical solution for double-walled carbon nanotubes

Analytically three types of integrals for the Lennard-Jones potential function are evaluated. These three integrals are involved in the solution for the total potential energy of the nanostructure system, mainly for the double-walled carbon nanotubes, and they are determined in following sections.

### A.1 Evaluation of the integral $J_n$

Consider the integral

$$J_n^* = \int_0^{2\pi} \int_0^{2\pi} \frac{d\theta_1 d\theta_2}{\lambda^n}, \quad (\text{A.1})$$

where  $\lambda^2 = a^2 + b^2 - 2ab \cos(\theta_1 - \theta_2)$ . Since the integrand is a symmetric function of  $\theta_1 - \theta_2$ , the intermediate integral  $J_n^{**}$  defined by

$$J_n^{**} = \int_0^{2\pi} \frac{d\theta_1}{\{\alpha + \beta \sin^2[(\theta_1 - \theta_2)/2]\}^{n/2}},$$

where  $\alpha = (a - b)^2$  and  $\beta = 4ab$  can be shown by differentiation with respect to  $\theta_2$  to be independent of  $\theta_2$ , namely

$$\frac{dJ_n^{**}}{d\theta_2} = \int_0^{2\pi} -\frac{\partial}{\partial \theta_1} \left( \frac{1}{\{\alpha + \beta \sin^2[(\theta_1 - \theta_2)/2]\}^{n/2}} \right) d\theta_1 = 0.$$

Thus,  $\theta_2$  is set to zero and one can trivially perform the  $\theta_2$  integration so that (A.1) becomes

$$J_n^* = 8\pi \int_0^{\pi/2} \frac{dx}{\lambda^n},$$

where  $\lambda^2 = (a - b)^2 + 4ab \sin^2 x$  and the integral  $J_n$  may be defined by

$$J_n = \int_0^{\pi/2} \frac{dx}{\lambda^n} = \int_0^{\pi/2} \frac{dx}{(\alpha + \beta \sin^2 x)^{n/2}}.$$

Making the substitution  $t = \cot x$  to obtain

$$J_n = \int_0^\infty \frac{(1+t^2)^{n/2-1}}{(\beta + \alpha + \alpha t^2)^{n/2}} dt = \frac{1}{(\alpha + \beta)^{n/2}} \int_0^\infty \frac{(1+t^2)^{n/2-1}}{(1 + \gamma t^2)^{n/2}} dt,$$

where  $\gamma = \alpha/(\alpha + \beta)$ . Now on writing this integral in the form

$$J_n = \frac{1}{(\alpha + \beta)^{n/2}} \int_0^\infty \frac{1}{[1 - (1 - \gamma)t^2/(1 + t^2)]^{n/2}} \frac{dt}{(1 + t^2)},$$

this leads to make the substitution

$$z = \frac{t}{(1 + t^2)^{1/2}}, \quad t = \frac{z}{(1 - z^2)^{1/2}}, \quad dt = \frac{dz}{(1 - z^2)^{3/2}},$$

and the substitution  $u = z^2$  gives

$$\begin{aligned} J_n &= \frac{1}{(\alpha + \beta)^{n/2}} \int_0^1 \frac{dz}{[1 - (1 - \gamma)z^2]^{n/2} (1 - z^2)^{1/2}} \\ &= \frac{1}{2(\alpha + \beta)^{n/2}} \int_0^1 \frac{u^{-1/2} (1 - u)^{-1/2}}{[1 - (1 - \gamma)u]^{n/2}} du. \end{aligned}$$

From Gradshteyn and Ryzhik [150] (p. 995, eq. 9.111) it may be deduced

$$J_n = \frac{\pi}{2(a + b)^n} F\left(\frac{n}{2}, \frac{1}{2}; 1; \frac{4ab}{(a + b)^2}\right),$$

where  $F(a, b; c; z)$  denotes a hypergeometric function. From Erdélyi [151], since two of the numbers  $\pm(1 - c)$ ,  $\pm(a - b)$ ,  $\pm(a + b - c)$  are equal to each other it can be shown that this result admits a quadratic transformation, which leads to a Legendre function. Using the transformation

$$F(a, b; 2b; 4z/(1 + z)^2) = (1 + z)^{2a} F(a, a + 1/2 - b; b + 1/2; z^2),$$

gives

$$J_n = \frac{\pi(1 + \xi)^n}{2(a + b)^n} F(n/2, n/2; 1; \xi^2),$$

where  $\xi = b/a$ . Using the definitions from Gradshteyn and Pyzhik [150] (pp. 960, 998)

$$P_\nu^\mu(z) = \frac{1}{\Gamma(1-\mu)} \left( \frac{z-1}{z+1} \right)^{-\mu/2} \left( \frac{z+1}{2} \right)^\nu F \left( -\nu, -\nu-\mu; 1-\mu; \frac{z-1}{z+1} \right),$$

and

$$F(a, b; c, z) = (1-z)^{c-a-b} F(c-a, c-b; c; z),$$

where  $P_\nu^\mu(z)$  is a Legendre function of the first kind. In this case  $\mu$  is zero, and the integral in terms of the Legendre function is obtained and given by

$$J_n = \frac{\pi}{2(a^2 - b^2)^{n/2}} P_{n/2-1} \left( \frac{a^2 + b^2}{a^2 - b^2} \right).$$

## A.2 Evaluation of the integral $K_n$

Here the integral  $K_n$  is determined. Since  $\lambda^2$  is an even function of  $\theta_1 - \theta_2$ , as mentioned in §A.1 either intermediate integral is independent of the other variables, and therefore this second variable is assigned to have zero value. In this event one integration may be trivially performed and may be deduced

$$K_n^* = 8\pi \int_0^{\pi/2} \frac{dx}{\lambda^m (\lambda^2 + P_j^2)^n},$$

where  $\lambda^2 = (a-b)^2 + 4ab \sin^2 x$ . Instead of considering the above equation, only the integral  $K_n$  is considered which is given by

$$K_n = \int_0^{\pi/2} \frac{dx}{\lambda^m (\lambda^2 + P_j^2)^n}. \quad (\text{A.2})$$

On letting  $\mu = (a-b)^2$ ,  $\sigma = (a-b)^2 + P_j^2$  and  $\nu = 4ab$ , (A.2) becomes

$$K_n = \int_0^{\pi/2} \frac{dx}{(\mu + \nu \sin^2 x)^{m/2} (\sigma + \nu \sin^2 x)^n}.$$

Making the substitution  $t = \cot x$  to obtain

$$\begin{aligned} K_n &= \int_0^\infty \frac{(1+t^2)^{n+\frac{m}{2}-1}}{(\nu + \mu + \mu t^2)^{m/2} (\nu + \sigma + \sigma t^2)^n} dt \\ &= \frac{1}{(\mu + \nu)^{m/2} (\sigma + \nu)^n} \int_0^\infty \frac{(1+t^2)^{n+\frac{m}{2}-1}}{(1 + \beta t^2)^{m/2} (1 + \gamma t^2)^n} dt, \end{aligned}$$

where  $\beta = \mu/(\mu + \nu)$  and  $\gamma = \sigma/(\sigma + \nu)$ . Now on writing this integral in the form

$$K_n = \frac{1}{(\mu + \nu)^{m/2}(\sigma + \nu)^n} \times \int_0^\infty \frac{1}{[1 - (1 - \beta)t^2/(1 + t^2)]^{m/2}[1 - (1 - \gamma)t^2/(1 + t^2)]^n} \frac{dt}{(1 + t^2)},$$

and makes the substitution

$$z = \frac{t}{(1 + t^2)^{1/2}}, \quad t = \frac{z}{(1 - z^2)^{1/2}}, \quad dt = \frac{dz}{(1 - z^2)^{3/2}},$$

and the substitution  $u = z^2$ , so that

$$K_n = \frac{1}{2(\mu + \nu)^{m/2}(\sigma + \nu)^n} \int_0^1 \frac{u^{-1/2}(1 - u)^{-1/2}}{[1 - (1 - \beta)u]^{m/2}[1 - (1 - \gamma)u]^n} du,$$

noting that  $\mu + \nu = (b + a)^2$ ,  $\sigma + \nu = (b + a)^2 + P_j^2$ ,  $\beta = (b - a)^2/(b + a)^2$  and  $\gamma = [(b - a)^2 + P_j^2]/[(b + a)^2 + P_j^2]$ . According to Bailey [152] (p. 73), the definition of an Appell hypergeometric function of two variables and of the first kind is defined by

$$F_1(\alpha; \beta, \beta'; \gamma; x, y) = \sum_{n=0}^{\infty} \sum_{m=0}^{\infty} \frac{(\alpha)_{m+n}(\beta)_m(\beta')_n}{m!n!(\gamma)_{m+n}} x^m y^n. \quad (\text{A.3})$$

Also from Bailey [152], the expression for the function  $F_1$  in terms of a definite integral and a series involving the ordinary hypergeometric function (pp. 77 and 79), are

$$\frac{\Gamma(\alpha)\Gamma(\gamma - \alpha)}{\Gamma(\gamma)} F_1(\alpha; \beta, \beta'; \gamma; x, y) = \int_0^1 \frac{u^{\alpha-1}(1 - u)^{\gamma-\alpha-1}}{(1 - ux)^\beta(1 - uy)^{\beta'}} du, \quad (\text{A.4})$$

$$F_1(\alpha; \beta, \beta'; \gamma; x, y) = \sum_{i=0}^{\infty} \frac{(\alpha)_i(\beta)_i}{i!(\gamma)_i} F(\alpha + i, \beta'; \gamma + i; y) x^i,$$

so that  $K_n$  becomes

$$K_n = \frac{\pi}{2(a + b)^m[(a + b)^2 + P_j^2]^n} \sum_{i=0}^{\infty} \frac{(1/2)_i(m/2)_i}{(i!)^2} \times F\left(\frac{1}{2} + i, n; 1 + i; \frac{4ab}{(a + b)^2 + P_j^2}\right) \left[\frac{4ab}{(a + b)^2}\right]^i,$$

where  $F(a, b; c; z)$  denotes the usual hypergeometric function.

### A.3 Evaluation of the integral $L_n$

Similar to the previous two sections, the integral  $L_n$  can be written as

$$L_n^* = 8\pi \int_0^{\pi/2} \frac{1}{\lambda^n} \tan^{-1} \left( \frac{P_j}{\lambda} \right) dx,$$

where  $\lambda^2 = (a - b)^2 + 4ab \sin^2 x$ . For convenience,  $L_n$  is defined by

$$L_n = \int_0^{\pi/2} \frac{1}{\lambda^n} \tan^{-1} \left( \frac{P_j}{\lambda} \right) dx.$$

Since  $(P_j/\lambda)^2 < \infty$ , from Gradshteyn and Ryzhik [150] (p. 59, eq. 1.644.1), it is obtained

$$\tan^{-1} \left( \frac{P_j}{\lambda} \right) = \frac{P_j}{\sqrt{\lambda^2 + P_j^2}} \sum_{k=0}^{\infty} \frac{(2k)!}{2^{2k} (k!)^2 (2k+1)} \left( \frac{P_j^2}{\lambda^2 + P_j^2} \right)^k,$$

and thus

$$L_n = \sum_{k=0}^{\infty} \frac{P_j^{2k+1} (2k)!}{2^{2k} (k!)^2 (2k+1)} \int_0^{\pi/2} \frac{1}{\lambda^n (\lambda^2 + P_j^2)^{k+1/2}} dx.$$

From the result for  $K_n$  in Appendix A.2, it may be deduced

$$\begin{aligned} L_n &= \frac{\pi}{2} \sum_{k=0}^{\infty} \frac{P_j^{2k+1} (2k)!}{2^{2k} (k!)^2 (2k+1)} \cdot \frac{1}{(\mu + \nu)^{n/2} (\sigma + \nu)^{k+1/2}} \times \\ &\quad \times F_1 \left( \frac{1}{2}; \frac{n}{2}, k + \frac{1}{2}; 1; 1 - \beta, 1 - \gamma \right), \end{aligned}$$

and using the reduction of Appell's hypergeometric functions (A.4), the formula for  $L_n$  is given by

$$\begin{aligned} L_n &= \frac{\pi}{2} \sum_{k=0}^{\infty} \sum_{i=0}^{\infty} \frac{P_j^{2k+1} (2k)!}{2^{2k} (k!)^2 (2k+1) (a+b)^n [(a+b)^2 + P_j^2]^{k+1/2}} \frac{(1/2)_i (n/2)_i}{(i!)^2} \times \\ &\quad \times F \left( \frac{1}{2} + i, k + \frac{1}{2}; 1 + i; \frac{4ab}{(a+b)^2 + P_j^2} \right) \left[ \frac{4ab}{(a+b)^2} \right]^i. \end{aligned}$$

Commenting that Colavecchia *et al.* [153] examine in some detail the numerical evaluation of the usual hypergeometric and the Appell hypergeometric functions.

## Appendix B

### Analytical solution for an offset position defined in (3.5)

The analytical solution of the total potential energy for an offset inner tube inside an outer tube given by (3.5) is determined. For convenience, the integral  $E_n$  is defined by

$$E_n = \int_0^{\pi/2} \int_0^{\pi/2} \frac{1}{\lambda^n} d\theta_1 d\theta_2, \quad n = 5, 11, \quad (\text{B.1})$$

where

$$\lambda^2 = a^2 + b^2 - 2ab \cos(\theta_1 - \theta_2) - 2\varepsilon(b \cos \theta_2 - a \cos \theta_1) + \varepsilon^2. \quad (\text{B.2})$$

On letting  $x = a \cos \theta_1 - b \cos \theta_2$  and  $y = a \sin \theta_1 - b \sin \theta_2$ , it may be deduced

$$x^2 + y^2 = a^2 + b^2 - 2ab \cos(\theta_1 - \theta_2).$$

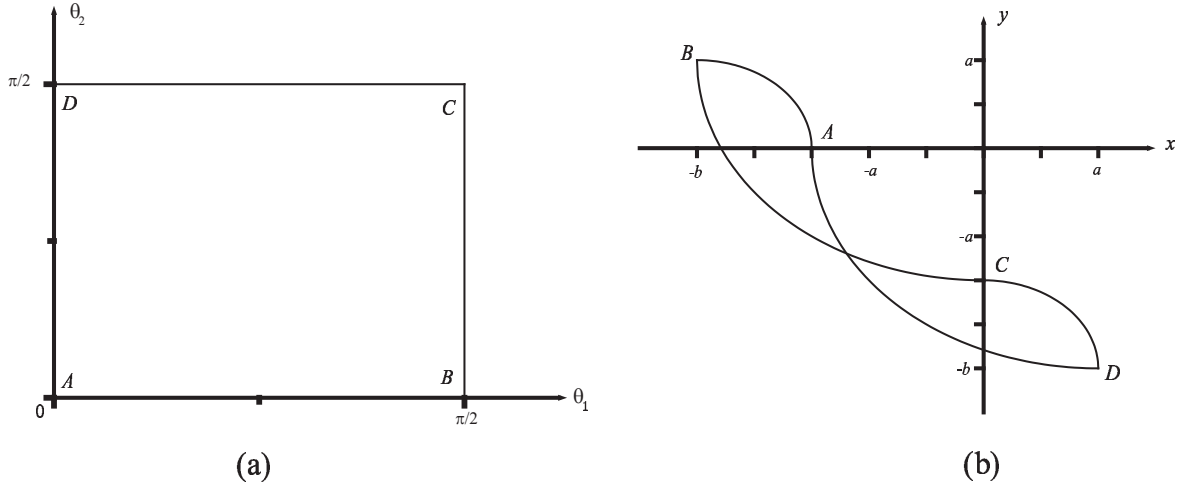
From (B.2),  $\lambda^2 = (x + \varepsilon)^2 + y^2$  is deduced and the Jacobian matrix can be written as

$$dxdy = \sqrt{4a^2b^2 - [a^2 + b^2 - (x^2 + y^2)]^2} d\theta_1 d\theta_2.$$

Then (B.1) becomes

$$E_n = \int \int_R \frac{dxdy}{\sqrt{4a^2b^2 - [a^2 + b^2 - (x^2 + y^2)]^2} [(x + \varepsilon)^2 + y^2]^{n/2}}, \quad (\text{B.3})$$

where  $R$  is a region shown in Figure B.1(b). The equations for each segment can be written as  $\overline{AB}$ :  $x \in [-b, a - b]$  and  $y = \sqrt{a^2 - (x + b)^2}$ ,  $\overline{BC}$ :  $x \in [-b, 0]$  and  $y = a - \sqrt{b^2 - x^2}$ ,  $\overline{CD}$ :  $x \in [0, a]$  and  $y = -b + \sqrt{a^2 - x^2}$  and  $\overline{AD}$ :  $x \in [a - b, a]$  and  $y = -\sqrt{b^2 - (x - a)^2}$ .

Figure B.1: Mapping diagram of (a)  $\theta_1 - \theta_2$  plane to (b)  $x - y$  plane.

Firstly,  $x = r \cos \theta$  and  $y = r \sin \theta$  are substituted into (B.3) to deduce

$$E_n = \iint_S \frac{r dr d\theta}{\sqrt{4a^2b^2 - (a^2 + b^2 - r^2)^2} [r^2 + 2r\varepsilon \cos \theta + \varepsilon^2]^{n/2}},$$

where  $S$  is a region shown in Figure B.2. On letting  $A = r^2 + \varepsilon^2$ ,  $B = 2r\varepsilon$  and  $C = \sqrt{4a^2b^2 - (a^2 + b^2 - r^2)^2}$ , the expression  $E_n$  becomes

$$E_n = \iint_S \frac{r dr d\theta}{C(A + B \cos \theta)^{n/2}}.$$

Using the fact that  $\cos \theta = 1 - 2 \sin^2(\theta/2)$ , it may be deduced

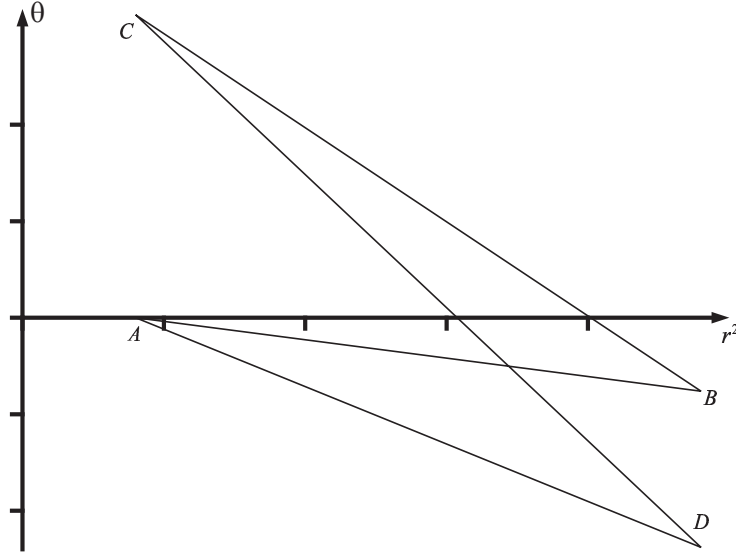
$$E_n = 2 \iint_{S^*} \frac{r dr dt}{C(A + B)^{n/2} (1 - k^2 \sin^2 t)^{n/2}}, \quad (\text{B.4})$$

where  $t = \theta/2$  and  $k^2 = 2B/(A + B) > 0$  and  $S^*$  denotes the region shown in Figure B.2. For convenience, the intermediate integral is defined as

$$F_n = \int_0^t \frac{ds}{(1 - k^2 \sin^2 s)^{n/2}}, \quad n = 5, 11,$$

which is given by

$$\begin{aligned} F_5 = & \frac{1}{3(k^2 - 1)^2} [(k^2 - 1)F(t, k) - 2(k^2 - 2)E(t, k)] \\ & - \frac{k^2 \{5 - k^2[3 + 2(2 - k^2) \sin^2 t]\}}{3(k^2 - 1)^2 (1 - k^2 \sin^2 t)^{3/2}} \sin t \cos t, \end{aligned} \quad (\text{B.5})$$

Figure B.2: Diagram of  $r^2 - \theta$  plane.

and

$$\begin{aligned}
F_{11} = & \frac{1}{315(k^2 - 1)^5} [4(k^2 - 1)(k^2 - 2)(16k^4 - 31k^2 + 31)F(t, k) \\
& - (128k^8 - 616k^6 + 1179k^4 - 1126k^2 + 563)E(t, k)] \\
& + \frac{k^2 \sin t \cos t}{315(k^2 - 1)^5 (1 - k^2 \sin^2 t)^{9/2}} [k^8(128k^8 - 616k^6 + 1179k^4 - 1126k^2 \\
& + 563) \cos^8 t - 4k^6(k^2 - 1)(128k^8 - 632k^6 + 1242k^4 - 1219k^2 + 625) \cos^6 t \\
& + k^4(k^2 - 1)^2(768k^8 - 3888k^6 + 7878k^4 - 8015k^2 + 4265) \cos^4 t \quad (\text{B.6}) \\
& - 2k^2(k^2 - 1)^3(256k^8 - 1328k^6 + 2784k^4 - 2973k^2 + 1681) \cos^2 t \\
& + (k^2 - 1)^4(128k^8 - 680k^6 + 1479k^4 - 1681k^2 + 1069)],
\end{aligned}$$

where  $F$  and  $E$  are the incomplete elliptic integral of the first kind and the second kind, respectively. Substituting (B.5) and (B.6) back into (B.4), the final integral with respect to  $r$  is numerically determined to obtain  $E_n$ .

Alternatively, (B.3) can be evaluated by defining the intermediate integral  $G_n$ ,

$$G_n = \int_R \frac{dy}{\sqrt{4a^2b^2 - [a^2 + b^2 - (x^2 + y^2)]^2}[(x + \varepsilon)^2 + y^2]^{n/2}}, \quad n = 5, 11,$$

and letting  $y^2 = a^2 + b^2 - x^2 - \xi$ ,  $P = a^2 + b^2 + 2x\varepsilon + \varepsilon^2$ ,  $A = 4a^2 + b^2$ ,  $B = a^2 + b^2 - x^2$  and  $C = -4a^2b^2$  to obtain

$$G_n = -\frac{1}{2} \int_{R^*} \frac{d\xi}{(P - \xi)^{(n-1)/2} \sqrt{(P - \xi)(A - \xi)(B - \xi)(\xi - C)}},$$



where  $R^*$  denotes the region shown in Figure B.1 with  $y^2 = a^2 + b^2 - x^2 - \xi$ . This integral structure has been evaluated by Byrd and Friedman [154], and in this case  $(n-1)/2 = 2$  and 5. From the formula by Byrd and Friedman [154] (eq. 253.24) which is given by

$$\int_y^c \frac{dt}{(b-t)^m \sqrt{(a-t)(b-t)(c-t)(t-d)}} = \frac{g}{(b-c)^m} \int_0^{u_1} (1 - \alpha^2 \text{sn}^2 u)^m du, \quad (\text{B.7})$$

where  $\text{sn} u$  is a Jacobian elliptic function,  $k^2 = [(a-b)(c-d)]/[(a-c)(b-d)]$ ,  $\text{sn} u_1 = \sin \phi = \sqrt{[(b-d)(c-y)]/[(c-d)(b-y)]}$ ,  $\alpha^2 = (c-d)/(b-d)$  and  $g = 2/\sqrt{(a-c)(b-d)}$ . It follows from Byrd and Friedman [154] (eq. 331) that

$$\gamma_m = \int (1 - \alpha^2 \text{sn}^2 u)^m du, \quad (\text{B.8})$$

and

$$\begin{aligned} \gamma_0 &= u, \\ \gamma_1 &= \frac{(k^2 - \alpha^2)u + \alpha^2 E(\phi, k)}{k^2}, \\ \gamma_2 &= \frac{1}{3k^4} [(3k^4 - 6\alpha^2 k^2 + 2\alpha^4 + k^2 \alpha^4)u + 2(3\alpha^2 k^2 - \alpha^4 - k^2 \alpha^4)E(\phi, k) \\ &\quad + \alpha^4 k^2 \text{sn} u \text{cnu} \text{dnu}], \\ \gamma_{m+3} &= \frac{1}{(2m+5)k^2} [2(m+2)(3k^2 - \alpha^2 - k^2 \alpha^2)\gamma_{m+2} + (2m+3)(2\alpha^2 k^2 + 2\alpha^2 \\ &\quad - \alpha^4 - 3k^2)\gamma_{m+1} + 2(m+1)(\alpha^2 - 1)(k^2 - \alpha^2)\gamma_m + \alpha^4 (1 - \alpha^2 \text{sn}^2 u)^{m+1} \times \\ &\quad \times \text{sn} u \text{cnu} \text{dnu}], \end{aligned}$$

where  $u = F(\phi, k)$ ,  $k'^2 = 1 - k^2$ ,  $F$  and  $E$  are the incomplete elliptic integral of the first kind and the second kind, respectively, and  $\text{cnu}$  and  $\text{dnu}$  are the Jacobian elliptic functions. By using (B.7) and (B.8) together with the recurrence formulae for  $\gamma_m$ , it is possible to determine  $E_n^*$  analytically. However, for the final solution for  $E_n$ , equation (B.3) needs to be integrated with respect to  $x$  which is determined numerically.

## Appendix C

### Derivation of interaction energy for C<sub>60</sub> fullerenes

The derivation of the potential energy between two C<sub>60</sub> molecules is summarised here. To start, the calculation of the interaction energy between a carbon atom and a C<sub>60</sub> fullerene is reviewed, utilising the Lennard-Jones potential function and the continuum approximation. Subsequently, the potential energy between the two C<sub>60</sub> fullerenes is obtained by performing another surface integral over a spherical fullerene.

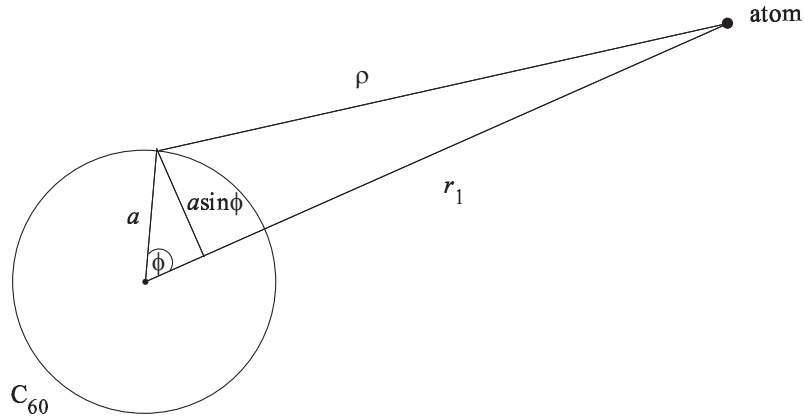


Figure C.1: Diagram of atom interacting with C<sub>60</sub> fullerene

The derivation of the potential energy between a carbon atom and a C<sub>60</sub> fullerene was first given by Ruoff and Hickman [43] and Mahanty and Ninham [155] and then later adopted by Cox *et al.* [57]. As shown in Figure C.1, with the carbon atom located outside the spherical fullerene, the distance between the atom and a typical atom on the C<sub>60</sub> fullerene  $\rho$  is given by  $\rho^2 = a^2 + r_1^2 - 2ar_1 \cos \phi$ , where  $a$  is a radius of a C<sub>60</sub> fullerene. The potential energy for a carbon atom interacting with the

spherical fullerene is obtained by  $E^* = -Q_6 + Q_{12}$  where  $Q_n$  ( $n = 6, 12$ ) are defined by

$$Q_n = C_n \eta_f \int_{\Sigma} \frac{1}{\rho^n} d\Sigma,$$

where  $\rho$  denotes the distance from a carbon atom to a typical surface element of the spherical molecule  $d\Sigma$ . The constants  $C_6$  and  $C_{12}$  are the Lennard-Jones potential constants  $A$  and  $B$ , respectively, and  $\eta_f$  represents the atomic surface density of a  $C_{60}$  fullerene. Therefore, the interaction energy between the carbon atom and the  $C_{60}$  fullerene is given by

$$E^*(r_1) = \frac{\pi a \eta_f}{r_1} \left[ \frac{A}{2} \left( \frac{1}{(r_1 + a)^4} - \frac{1}{(r_1 - a)^4} \right) - \frac{B}{5} \left( \frac{1}{(r_1 + a)^{10}} - \frac{1}{(r_1 - a)^{10}} \right) \right]. \quad (C.1)$$

Following the work of Cox *et al.* [57], the fractions over common denominators are expanded and reduced to fractions in terms of powers of  $(r_1^2 - a^2)$ , hence

$$\frac{A}{2r_1} \left( \frac{1}{(r_1 + a)^4} - \frac{1}{(r_1 - a)^4} \right) = -4aA \left( \frac{1}{(r_1^2 - a^2)^3} + \frac{2a^2}{(r_1^2 - a^2)^4} \right), \quad (C.2)$$

and

$$\begin{aligned} \frac{B}{5r_1} \left( \frac{1}{(r_1 + a)^{10}} - \frac{1}{(r_1 - a)^{10}} \right) &= -\frac{4aB}{5} \left( \frac{5}{(r_1^2 - a^2)^6} + \frac{80a^2}{(r_1^2 - a^2)^7} \right. \\ &\quad \left. + \frac{336a^4}{(r_1^2 - a^2)^8} + \frac{512a^6}{(r_1^2 - a^2)^9} + \frac{256a^8}{(r_1^2 - a^2)^{10}} \right). \end{aligned} \quad (C.3)$$

The full details of the derivation of (C.1) can be found in Cox *et al.* [57].

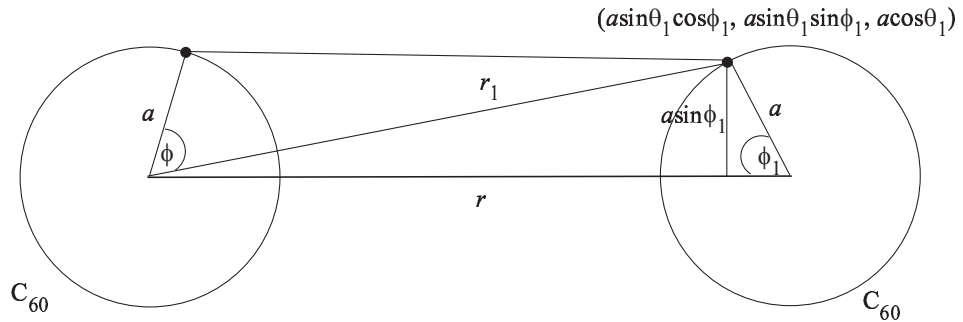


Figure C.2: Diagram of two interacting  $C_{60}$  fullerenes

To determine the interaction between two spherical fullerenes, with their centres at a distance  $r$  apart, a surface integral of (C.1) over another spherical fullerene needs to be performed, which has the parametric equation  $(x_1, y_1, z_1) = (a \sin \theta_1 \cos \phi_1,$

$a \sin \theta_1 \sin \phi_1, a \cos \theta_1$ ). Here, the distance  $r_1$ , as illustrated in Figure C.2, is given by  $r_1^2 = a^2 + r^2 - 2ar \cos \phi_1$ . Thus, the potential energy between two spherical fullerenes is obtained from  $E^{**} = -P_6 + P_{12}$ , where  $P_n$  ( $n = 6, 12$ ) are defined by

$$P_n = \eta_f \int_0^{2\pi} \int_0^\pi Q_n a^2 \sin \phi_1 d\phi_1 d\theta_1.$$

By using appropriate substitutions and integrations,  $P_n$  becomes

$$P_n = \frac{4\pi^2 a^2 C_n \eta_f^2}{r(2-n)(3-n)} \left( \frac{1}{(2a+r)^{n-3}} - \frac{1}{r^{n-3}} - \frac{1}{(2a-r)^{n-3}} + \frac{1}{(-r)^{n-3}} \right), \quad (\text{C.4})$$

and for  $n$  even this simplifies to yield

$$P_n = \frac{4\pi^2 a^2 C_n \eta_f^2}{r(2-n)(3-n)} \left( \frac{1}{(2a+r)^{n-3}} - \frac{1}{(2a-r)^{n-3}} - \frac{2}{r^{n-3}} \right),$$

a formula which is also given in Girifalco [42]. Using the constant values given in Table 3.1, the equilibrium distance for two  $\text{C}_{60}$  fullerenes is obtained and given by  $r_0 = 10.0550 \text{ \AA}$ .

# Appendix D

## Analytical solution for nanopeapods

The analytical calculations for the potential energy of nanopeapods in Chapter 4 are presented.

### D.1 Evaluation of the integral $G_n$

Firstly, the integral  $G_n$  is defined, which can be written as

$$G_n = \int_0^\infty \frac{dz}{[b^2 - a^2 + (z - Z)^2]^n}.$$

On letting  $\lambda^2 = b^2 - a^2$  and making the substitution  $x = z - Z$ , it can be deduced

$$G_n = \int_{-Z}^\infty \frac{dx}{(\lambda^2 + x^2)^n},$$

where  $n$  is a certain positive integer. Then the substitution  $x = \lambda \tan \psi$  yields

$$\begin{aligned} G_n &= \int_{-\tan^{-1}(Z/\lambda)}^{\pi/2} \frac{\lambda \sec^2 \psi}{\lambda^{2n} \sec^{2n} \psi} d\psi \\ &= \frac{1}{\lambda^{2n-1}} \int_{-\tan^{-1}(Z/\lambda)}^{\pi/2} \cos^{2(n-1)} \psi d\psi. \end{aligned} \quad (\text{D.1})$$

The evaluation for (D.1) can be found in Gradshteyn and Ryzhik [150] (page 149, No. 2.513 3) from which it can be deduced

$$\int \cos^{2(n-1)} \psi d\psi = \frac{1}{2^{2(n-1)}} \left[ \binom{2(n-1)}{(n-1)} \psi + \sum_{k=0}^{n-2} \binom{2(n-1)}{k} \frac{\sin[(2n-2k-2)\psi]}{(n-k-1)} \right], \quad (\text{D.2})$$

where  $\binom{n}{m}$  is the binomial coefficient. By evaluating (D.2) at  $\psi = \pi/2$  and  $\psi = -\tan^{-1}(Z/\lambda)$  an analytical expression for  $G_n$  may be obtained.

## D.2 Evaluation of the integral $H_n$

The integral  $H_n$  is defined in the form of

$$H_n = \int_{-\pi}^{\pi} \int_0^{\infty} \frac{1}{(\rho^2 - a^2)^n} dz d\theta,$$

where  $n$  is a certain positive integer and  $\rho^2 = (b-x)^2 + 4bx \sin(\theta/2) + (z-Z)^2$ . On letting  $\lambda^2 = (b-x)^2 + 4bx \sin^2(\theta/2) - a^2$ , it can be deduced

$$H_n = \int_{-\pi}^{\pi} \int_0^{\infty} \frac{1}{[\lambda^2 + (z-Z)^2]^n} dz d\theta.$$

On making the substitution  $u = z - Z$ ,  $H_n$  becomes

$$\begin{aligned} H_n &= \int_{-\pi}^{\pi} \int_{-Z}^{\infty} \frac{1}{(\lambda^2 + u^2)^n} du d\theta \\ &= \int_{-\pi}^{\pi} \int_{-\tan^{-1}(Z/\lambda)}^{\pi/2} \frac{\lambda \sec^2 \psi}{\lambda^{2n} \sec^{2n} \psi} d\psi d\theta, \end{aligned}$$

where the final line is obtained by substituting  $x = \lambda \tan \psi$ . Finally,  $H_n$  simplifies to become

$$H_n = \frac{1}{\lambda^{2n-1}} \int_{-\pi}^{\pi} \int_{-\tan^{-1}(Z/\lambda)}^{\pi/2} \cos^{2(n-1)} \psi d\psi d\theta.$$

By using the formula given by (D.2) and evaluating the above equation at  $\psi = \pi/2$  and  $\psi = -\tan^{-1}(Z/\lambda)$ , there are three forms for the integral for  $\theta \in (0, \pi/2)$  which need to be determined, and are given by

$$J_s = \int_0^{\pi/2} \frac{dv}{\lambda^s}, \quad K_{s,t} = \int_0^{\pi/2} \frac{dv}{\lambda^t (\lambda^2 + Z^2)^s}, \quad L_s = \int_0^{\pi/2} \frac{1}{\lambda^s} \tan^{-1} \left( \frac{Z}{\lambda} \right) dv, \quad (\text{D.3})$$

where  $\lambda$  is defined by  $\lambda^2 = (b-x)^2 + 4bx \sin^2(v/2) - a^2$ . The detailed integrations of (D.3) can be found in Appendix A.

## D.3 Evaluation of the integral $I_n$

The integral  $I_n$  is given by

$$I_n = \int_{-\infty}^{\infty} \int_{-\pi}^{\pi} \frac{1}{(\rho_m^2 - a^2)^n} dz d\theta,$$

where  $m = i$  and  $j$ . On letting  $\lambda_i^2 = (b + \varepsilon)^2 - 4b\varepsilon \sin^2(\theta/2) - a^2$  and  $\lambda_j^2 = (b - \varepsilon)^2 + 4b\varepsilon \sin^2(\theta/2) - a^2$ ,  $I_n$  becomes

$$I_n = \int_{\pi}^{-\pi} \int_{-L}^L \frac{1}{[\lambda_m^2 + (z + Z_m)^2]^n} dz d\theta,$$

where  $Z_i = Z(2i - 1)$  ( $i = 1, 2, \dots, k$ ) and  $Z_j = 2Z(j - 1)$  ( $j = 1, 2, \dots, k + 1$ ). Upon making the substitution  $x_m = z + Z_m$ , it can be deduced

$$I_n = \int_{\pi}^{-\pi} \int_{Z_m-L}^{Z_m+L} \frac{1}{(\lambda_m^2 + x_m^2)^n} dx_m d\theta = \int_{-\pi}^{\pi} \int_{-\pi/2}^{\pi/2} \frac{\lambda_m \sec^2 \psi}{\lambda_m^{2n} \sec^{2n} \psi} d\psi d\theta,$$

where the final line is obtained by substituting  $x_m = \lambda_m \tan \psi$  and letting  $L$  tend to infinity. Finally,  $I_n$  simplifies to become

$$I_n = \frac{1}{\lambda_m^{2p+1}} \int_{-\pi}^{\pi} \int_{-\pi/2}^{\pi/2} \cos^{2p} \psi d\psi d\theta, \quad (\text{D.4})$$

where  $p = n - 1$ . The solution for (D.4) can be found in Gradshteyn and Ryzhik [150] (page 149, No. 2.513 3) and is given by (D.2). By evaluating (D.2) at  $\psi = \pi/2$  and  $\psi = -\pi/2$  and using the fact that  $\sin 2x = 2 \sin x \cos x$ , it may be deduced

$$I_n = \frac{\pi}{2^{2p}} \binom{2p}{p} \int_{-\pi}^{\pi} \frac{1}{\lambda_m^{2p+1}} d\theta = \frac{4\pi}{2^{2p}} \binom{2p}{p} \int_0^{\pi/2} \frac{1}{\lambda_m^{2p+1}} dx,$$

where  $x = \theta/2$  and  $\lambda_i^2 = (b + \varepsilon)^2 - 4b\varepsilon \sin^2 x - a^2$  and  $\lambda_j^2 = (b - \varepsilon)^2 + 4b\varepsilon \sin^2 x - a^2$ .

The analytical expression for this equation can be found in Appendix A.1.

# Appendix E

## Degenerate hypergeometric functions

The details of the degenerate hypergeometric function of (5.3) are presented in this appendix. The degenerate hypergeometric function is the hypergeometric function which can be written as the finite summation of a polynomial. For convenience,  $J_m$  is defined as

$$J_m = F(m, 1/2; 1; z), \quad (\text{E.1})$$

where  $m$  is a positive integer. Following Erdélyi [151], (E.1) admits the degenerate hypergeometric function in the case number 16 (p.72) with a degenerated solution

$$F(a, b; c; z) = (1 - z)^{c-a-b} F(c - a, c - b; c; z).$$

Then it can be deduced

$$J_m = (1 - z)^{1/2-m} F(1 - m, 1/2; 1; z). \quad (\text{E.2})$$

In terms of a series, the hypergeometric function is given by

$$F(a, b; c; z) = \sum_{n=0}^{\infty} \frac{(a)_n (b)_n}{n! (c)_n} z^n,$$

where

$$(a)_n = \Gamma(a + n)/\Gamma(a) = a(a + 1)(a + 2) \dots (a + n - 1) \quad \text{and} \quad (a)_0 = 1.$$



Here,  $J_3$  and  $J_6$  need to be evaluated, and from (E.2) they can be written as

$$\begin{aligned}
 J_3 &= \frac{1}{(1-z)^{5/2}} \sum_{n=0}^2 \frac{(-2)_n (1/2)_n}{n! (1)_n} z^n = \frac{1}{(1-z)^{5/2}} \left( 1 - z + \frac{3}{8} z^2 \right), \\
 J_6 &= \frac{1}{(1-z)^{11/2}} \sum_{n=0}^5 \frac{(-5)_n (1/2)_n}{n! (1)_n} z^n \\
 &= \frac{1}{(1-z)^{11/2}} \left( 1 - \frac{5}{2} z + \frac{15}{4} z^2 - \frac{25}{8} z^3 + \frac{175}{128} z^4 - \frac{63}{256} z^5 \right).
 \end{aligned}$$

## Appendix F

### Mathematical solution for $A_{ni}$ ( $i = 1, 2, 3, 4$ ) defined in §13.3

In this appendix, the main details for solving the stress boundary conditions, as a system of four equations in four unknowns, is shown. The system of four equations and four unknowns can be written in matrix form which is given by

$$\mathbf{MA} = \begin{pmatrix} M_{11} & M_{12} & M_{13} & M_{14} \\ M_{21} & M_{22} & M_{23} & M_{24} \\ M_{31} & M_{32} & M_{33} & M_{34} \\ M_{41} & M_{42} & M_{43} & M_{44} \end{pmatrix} \begin{pmatrix} A_{n1} \\ A_{n2} \\ A_{n3} \\ A_{n4} \end{pmatrix} = \begin{pmatrix} 0 \\ 0 \\ 0 \\ \tau_n \end{pmatrix}, \quad (\text{F.1})$$

where the components of the matrix  $\mathbf{M}$  depend on  $n$  and are defined by

$$\begin{aligned} M_{11} &= \alpha_n J_0(p_{n1}c) - \frac{C_{11}}{c} J_1(p_{n1}c), & M_{12} &= \alpha_n Y_0(p_{n1}c) - \frac{C_{11}}{c} Y_1(p_{n1}c), \\ M_{13} &= \beta_n J_0(p_{n2}c) - \frac{C_{11}}{c} J_1(p_{n2}c), & M_{14} &= \beta_n Y_0(p_{n2}c) - \frac{C_{11}}{c} Y_1(p_{n2}c), \\ M_{21} &= \gamma_n J_1(p_{n1}c), & M_{22} &= \gamma_n Y_1(p_{n1}c), \\ M_{23} &= \delta_n J_1(p_{n2}c), & M_{24} &= \delta_n Y_1(p_{n2}c), \\ M_{31} &= \alpha_n J_0(p_{n1}b) - \frac{C_{11}}{b} J_1(p_{n1}b), & M_{32} &= \alpha_n Y_0(p_{n1}b) - \frac{C_{11}}{b} Y_1(p_{n1}b), \\ M_{33} &= \beta_n J_0(p_{n2}b) - \frac{C_{11}}{b} J_1(p_{n2}b), & M_{34} &= \beta_n Y_0(p_{n2}b) - \frac{C_{11}}{b} Y_1(p_{n2}b), \\ M_{41} &= \gamma_n J_1(p_{n1}b), & M_{42} &= \gamma_n Y_1(p_{n1}b), \\ M_{43} &= \delta_n J_1(p_{n2}b), & M_{44} &= \delta_n Y_1(p_{n2}b), \end{aligned}$$

and  $\tau_n$  is defined by

$$\tau_n = \frac{W}{2naL_1\pi^2C_{44}} \left\{ \cos \left[ \frac{n\pi(L_2 - L_1)}{2(L_1 + L_2)} \right] - \cos \left( \frac{n\pi}{2} \right) \right\}.$$

On using Cramer's rule to solve (F.1), it can be obtained

$$\begin{aligned} A_{n1} &= \frac{1}{\Delta} \begin{vmatrix} 0 & M_{12} & M_{13} & M_{14} \\ 0 & M_{22} & M_{23} & M_{24} \\ 0 & M_{32} & M_{33} & M_{34} \\ \tau_n & M_{42} & M_{43} & M_{44} \end{vmatrix} = \frac{-\tau_n}{\Delta} \begin{vmatrix} M_{12} & M_{13} & M_{14} \\ M_{22} & M_{23} & M_{24} \\ M_{32} & M_{33} & M_{34} \end{vmatrix}, \\ A_{n2} &= \frac{1}{\Delta} \begin{vmatrix} M_{11} & 0 & M_{13} & M_{14} \\ M_{21} & 0 & M_{23} & M_{24} \\ M_{31} & 0 & M_{33} & M_{34} \\ M_{41} & \tau_n & M_{43} & M_{44} \end{vmatrix} = \frac{\tau_n}{\Delta} \begin{vmatrix} M_{11} & M_{13} & M_{14} \\ M_{21} & M_{23} & M_{24} \\ M_{31} & M_{33} & M_{34} \end{vmatrix}, \\ A_{n3} &= \frac{1}{\Delta} \begin{vmatrix} M_{11} & M_{12} & 0 & M_{14} \\ M_{21} & M_{22} & 0 & M_{24} \\ M_{31} & M_{32} & 0 & M_{34} \\ M_{41} & M_{42} & \tau_n & M_{44} \end{vmatrix} = \frac{-\tau_n}{\Delta} \begin{vmatrix} M_{11} & M_{12} & M_{14} \\ M_{21} & M_{22} & M_{24} \\ M_{31} & M_{32} & M_{34} \end{vmatrix}, \\ A_{n4} &= \frac{1}{\Delta} \begin{vmatrix} M_{11} & M_{12} & M_{13} & 0 \\ M_{21} & M_{22} & M_{23} & 0 \\ M_{31} & M_{32} & M_{33} & 0 \\ M_{41} & M_{42} & M_{43} & \tau_n \end{vmatrix} = \frac{\tau_n}{\Delta} \begin{vmatrix} M_{11} & M_{12} & M_{13} \\ M_{21} & M_{22} & M_{23} \\ M_{31} & M_{32} & M_{33} \end{vmatrix}, \end{aligned}$$

where  $\Delta = \det(\mathbf{M})$ .

# Appendix G

## Relationship of moduli for transversely isotropic linearly elastic materials

With the notation

$E \equiv$  Young's modulus,  $\nu \equiv$  Poisson's ratio

$K \equiv$  bulk modulus,  $\mu$  and  $\lambda$  are Lamé constants,

the relationships between these constants are given by:

$$\lambda = \frac{2\mu\nu}{1-2\nu} = \frac{\mu(E-2\mu)}{3\mu-E} = K - \frac{2}{3}\mu = \frac{E\nu}{(1+\nu)(1-2\nu)} = \frac{3K\nu}{1+\nu} = \frac{3K(3K-E)}{9K-E},$$

$$\mu = \frac{\lambda(1-2\nu)}{2\nu} = \frac{3}{2}(K-\lambda) = \frac{E}{2(1+\nu)} = \frac{3K(1-2\nu)}{2(1+\nu)} = \frac{3KE}{9K-E},$$

$$\nu = \frac{\lambda}{2(\lambda+\mu)} = \frac{\lambda}{3K-\lambda} = \frac{E}{2\mu} - 1 = \frac{3K-2\mu}{2(3K+\mu)} = \frac{3K-E}{6K},$$

$$E = \frac{\mu(3\lambda+2\mu)}{\lambda+\mu} = \frac{\lambda(1+\nu)(1-2\nu)}{\nu} = \frac{9K(K-\lambda)}{3K-\lambda} = 2\mu(1+\nu)$$

$$= \frac{9K\mu}{3K+\mu} = 3K(1-2\nu),$$

$$K = \lambda + \frac{2}{3}\mu = \frac{\lambda(1+\nu)}{3\nu} = \frac{2\mu(1+\nu)}{3(1-2\nu)} = \frac{\mu E}{3(3\mu-E)} = \frac{E}{3(1-2\nu)}.$$

Moreover, the following expressions are frequently used,

$$\frac{\mu}{\lambda+\mu} = 1-2\nu, \quad \frac{\lambda}{\lambda+2\mu} = \frac{\nu}{1-\nu}.$$

The formulae (12.4) are utilised to convert the elastic moduli to the elastic constants  $C_{ij}$  and to compare the values of the elastic constants based on the work of Jin and Yuan [15], Lu [20] and Shen and Li [134].

The values of the elastic constants based on the three sets of data given by Jin and Yuan [15], Lu [20] and Shen and Li [134] are shown in Tables G.2 - G.5. The values of the elastic moduli and elastic constants for single-walled carbon nanotubes (10, 10) are compared as shown in Table G.6. The major problem in this study is that every author describes the various elastic moduli by a different nomenclature. However, the values of the elastic moduli in the longitudinal direction of each author compare very well, but there are quite significant differences in the transverse plane. In terms of the elastic constants, the results from Jin and Yuan [15] and Lu [20] are only slightly different, but there are significant differences with the results of Shen and Li [134]. The value of the in-plane shear modulus ( $G_{23}$ ) from [134] is reported in GPa, whereas the other elastic moduli are expressed in TPa.

Table G.1: Elastic constants of single-walled carbon nanotubes ( $n, n$ ) based on Jin and Yuan [15].

$n$	$C_{11}$	$C_{12}$	$C_{13}$	$C_{33}$	$C_{44}$	$C_{11} - C_{12}$
6	1.368	0.198	0.254	1.432	0.483	1.169
7	1.348	0.145	0.251	1.432	0.487	1.203
8	1.388	0.075	0.249	1.432	0.489	1.263
9	1.388	0.054	0.247	1.432	0.492	1.284
10	1.342	0.125	0.246	1.431	0.493	1.217
11	1.346	0.139	0.245	1.431	0.494	1.210
12	1.336	0.073	0.244	1.430	0.493	1.263
13	1.341	0.098	0.243	1.430	0.494	1.243
14	1.335	0.065	0.243	1.429	0.494	1.269
15	1.339	0.092	0.242	1.427	0.495	1.247
16	1.335	0.064	0.242	1.428	0.495	1.271
17	1.332	0.030	0.242	1.428	0.495	1.302
18	1.335	0.064	0.241	1.428	0.492	1.271
19	1.338	0.087	0.241	1.427	0.495	1.251
20	1.337	-0.022	0.241	1.427	0.495	1.359

Table G.2: Values of elastic constants for single-walled carbon nanotubes  $(n_1, n_2)$  based on Lu [20].

$(n_1, n_2)$	$C_{11}$	$C_{12}$	$C_{13}$	$C_{33}$	$C_{44}$	$C_{11} - C_{12}$
(5,5)	0.397	0.132	0.148	1.054	0.436	0.265
(6,4)	0.397	0.126	0.146	1.054	0.437	0.271
(7,3)	0.397	0.126	0.146	1.055	0.454	0.271
(8,2)	0.397	0.132	0.148	1.057	0.452	0.265
(9,1)	0.396	0.140	0.150	1.058	0.465	0.256
(10,0)	0.396	0.133	0.148	1.058	0.451	0.263
(10,10)	0.398	0.133	0.147	1.054	0.457	0.265
(50,50)	0.399	0.135	0.148	1.054	0.458	0.264
(100,100)	0.399	0.135	0.148	1.054	0.462	0.264
(200,200)	0.399	0.135	0.148	1.054	0.478	0.264

Table G.3: Values of elastic constants for the series of multi-walled carbon nanotubes  $(5n, 5n)$  where  $n = 1, 2, 3, \dots$  and  $N$  is a number of walls based on Lu [20].

$N$	$C_{11}$	$C_{12}$	$C_{13}$	$C_{33}$	$C_{44}$	$C_{11} - C_{12}$
1	0.397	0.113	0.143	1.050	0.436	0.283
2	0.412	0.137	0.148	1.130	0.455	0.275
3	0.413	0.071	0.130	1.150	0.464	0.342
4	0.412	0.141	0.149	1.170	0.472	0.271
5	0.411	0.142	0.149	1.180	0.481	0.269
6	0.411	0.142	0.149	1.180	0.491	0.269
7	0.410	0.074	0.130	1.180	0.502	0.336
8	0.410	0.143	0.149	1.190	0.514	0.267
9	0.410	0.143	0.149	1.190	0.527	0.267
10	0.410	0.143	0.149	1.190	0.541	0.267

Table G.4: Values of elastic constants of single-walled carbon nanotubes  $(n, n)$  based on Shen and Li [134].

n	$C_{11}$	$C_{12}$	$C_{13}$	$C_{33}$	$C_{44}$	$C_{11} - C_{12}$
10	0.00664	0.00330	0.00161	1.06052	0.44200	0.00334
15	0.00198	0.00099	0.00048	0.70715	0.30100	0.00099
20	0.00083	0.00042	0.00020	0.53106	0.22700	0.00042
25	0.00043	0.00021	0.00010	0.42503	0.18200	0.00021
30	0.00025	0.00012	0.00006	0.35402	0.15200	0.00012
35	0.00016	0.00008	0.00004	0.30401	0.13100	0.00008
40	0.00010	0.00005	0.00002	0.26601	0.11400	0.00005
45	0.00007	0.00004	0.00002	0.23601	0.10200	0.00004
50	0.00005	0.00003	0.00001	0.21300	0.09200	0.00003

Table G.5: Values of elastic constants of double-walled carbon nanotubes which the inner tube (5, 5) and the outer tube ( $n, n$ ) based on Shen and Li [134].

n	$C_{11}$	$C_{12}$	$C_{13}$	$C_{33}$	$C_{44}$	$C_{11} - C_{12}$
10	0.04090	0.01972	0.00946	1.58295	0.49300	0.02118
15	0.03492	0.01675	0.00775	1.41233	0.39800	0.01818
20	0.03129	0.01496	0.00680	1.32200	0.35300	0.01633
25	0.02882	0.01376	0.00618	1.27179	0.32700	0.01506
30	0.02703	0.01290	0.00571	1.24163	0.31000	0.01413
35	0.02565	0.01224	0.00538	1.21153	0.29800	0.01341
40	0.02454	0.01171	0.00511	1.19144	0.28900	0.01284
45	0.02365	0.01128	0.00489	1.18137	0.28200	0.01236
50	0.02288	0.01092	0.00470	1.17131	0.27700	0.01196

Table G.6: The values of elastic moduli and elastic constants for single-walled carbon nanotube (10, 10) of three studies [15, 20, 134].

Elastic moduli, constants	[15]	[20]	[134]
$E'$	1.235	0.972	1.060
$\nu'$	0.259	0.278	0.162
$\mu'$	0.493	0.457	0.442
$E$	1.241	0.344	0.005
$\nu$	0.019	0.296	0.497
$C_{11}$	1.342	0.398	0.00664
$C_{12}$	0.125	0.133	0.00330
$C_{13}$	0.246	0.147	0.00161
$C_{33}$	1.431	1.054	1.06052
$C_{44}$	0.493	0.457	0.44200

# Bibliography

- [1] J. Cumings and A. Zettl, 2000 “Low-friction nanoscale linear bearing realized from multiwall carbon nanotubes”, *Science*, **289**, 602–604.
- [2] S. B. Legoas, V. R. Coluci, S. F. Braga, P. Z. Coura, S. O. Dantas and D. S. Galvão, 2003 “Molecular-dynamics simulations of carbon nanotubes as gigahertz oscillators”, *Phys. Rev. Lett.*, **90**, 055504.
- [3] D. Qian, W. K. Liu and R. S. Ruoff, 2001 “Mechanics of C<sub>60</sub> in nanotubes”, *J. Phys. Chem. B*, **105**, 10753–10758.
- [4] Q. Zheng and Q. Jiang, 2002 “Multiwalled carbon nanotubes as gigahertz oscillators”, *Phys. Rev. Lett.*, **88**, 045503.
- [5] Q. Zheng, J. Z. Liu and Q. Jiang, 2002 “Excess van der Waals interaction energy of a multiwalled carbon nanotube with and extruded core and the induced core oscillation”, *Phys. Rev. B*, **65**, 245409.
- [6] J. L. Rivera, C. McCabe and P. T. Cummings, 2003 “Oscillatory behavior of double-walled nanotubes under extension: A simple nanoscale damped spring”, *Nano Lett.*, **3**, 1001–1005.
- [7] J. L. Rivera, C. McCabe and P. T. Cummings, 2005 “The oscillatory damped behavior of incommensurate double-walled carbon nanotubes”, *Nanotech.*, **16**, 186–198.
- [8] M. Otani, S. Okada and A. Oshiyama, 2003 “Energetics and electronic structures of one-dimensional fullerene chains encapsulated in zigzag nanotubes”, *Phys. Rev. B*, **68**, 125424.
- [9] K. Sattler, 1995 “Scanning tunneling microscopy of carbon nanotubes and nanocones”, *Carbon*, **33**, 915–920.



- [10] J.-C. Charlier and G.-M. Rignanese, 2001 “Electronic structure of carbon nanocones”, *Phys. Rev. Lett.*, **86**, 5970–5973.
- [11] B. J. Cox and J. M. Hill, 2007 “New carbon molecules in the form of elbow-connected nanotori”, *J. Phys. Chem. C*, **111**, 10855–10860.
- [12] R. Ramani, K. K. Mani and R. P. Singh, 1978 “Long optical vibrations and elastic constants of hexagonal boron nitride”, *Phys. Stat. Sol. (b): basic solid state physics*, **86**, 759 – 763.
- [13] W. D. Cornell, P. Cieplak, C. I. Bayly, I. R. Gould, K. M. Merz Jr., D. M. Ferguson, D. C. Spellmeyer, T. Fox, J. W. Caldwell and P. A. Kollman, 1995 “A second generation force field for the simulation of proteins, nucleic acids, and organic molecules”, *J. Am. Chem. Soc.*, **117**, 5179–5197.
- [14] C. Li and T.-W. Chou, 2003 “A structural mechanics approach for the analysis of carbon nanotubes”, *Int. J. Solids Struct.*, **40**, 2487–2499.
- [15] Y. Jin and F. G. Yuan, 2003 “Simulation of elastic properties of single-walled carbon nanotubes”, *Comp. Sci. Technol.*, **63**, 1507–1515.
- [16] T. Natsuki, K. Tantrakarn and M. Endo, 2004 “Effects of carbon nanotube structures on mechanical properties”, *Appl. Phys. A*, **79**, 117–124.
- [17] D. Qian, G. J. Wagner and W. K. Liu, 2002 “Mechanics of carbon nanotubes”, *Appl. Mech. Rev.*, **55**, 495–533.
- [18] M. F. Yu, B. I. Yakobson and R. S. Ruoff, 2000 “Controlled sliding and pullout of nested shells in individual multiwalled carbon nanotubes”, *J. Phys. Chem. B Lett.*, **104**, 8764–8767.
- [19] Q. Zhao, M. B. Nardelli and J. Bernholc, 2002 “Ultimate strength of carbon nanotubes: A theoretical study”, *Phys. Rev. B*, **65**, 144105.
- [20] J. P. Lu, 1997 “Elastic properties of carbon nanotubes and nanoropes”, *Phys. Rev. Lett.*, **79**, 1297–1300.
- [21] L. Shen and J. Li, 2004 “Transversely isotropic elastic properties of single-walled carbon nanotubes”, *Phys. Rev. B*, **69**, 045414.

- [22] H. A. Elliott, 1948 “Three-dimensional stress distributions in hexagonal aeolotropic crystals”, *Proc. Camb. Phil.*, **44**, 522–533.
- [23] R. T. Shield, 1951 “Notes on problems in hexagonal aeolotropic materials”, *Proc. Camb. Phil.*, **47**, 401–409.
- [24] L. E. Payne and A. E. Green, 1954 “On axially symmetric crack and punch problems for a medium with transverse isotropy”, *Proc. Camb. Phil.*, **50**, 466–473.
- [25] A. P. S. Selvadurai, 1980 “Asymmetric displacements of a rigid disc inclusion embedded in a transversely isotropic elastic medium of infinite extent”, *Int. J. Engng Sci.*, **18**, 979–986.
- [26] A. P. S. Selvadurai, 1980 “Elastic contact between a flexible circular plate and a transversely isotropic elastic halfspace”, *Int. J. Solids Struct.*, **16**, 167–176.
- [27] M. S. Dresselhaus, G. Dresselhaus and P. C. Eklund, 1995 *Science of Fullerenes and Carbon Nanotubes*, Academic Press, California, 1<sup>st</sup> edition.
- [28] H. Terrones and M. Terrones, 2003 “Curved nanostructured materials”, *New J. Phys.*, **5**, 126.1–126.37.
- [29] S. Weber “Crystallography picture book”,  
<http://www.jcrystal.com/steffenweber/pb/>.
- [30] H. B. Peng, C. W. Chang, S. Aloni, T. D. Yuzvinsky and A. Zettl, 2006 “Ultrahigh frequency nanotube resonators”, *Phys. Rev. Lett.*, **97**, 087203.
- [31] V. Buntar, F. M. Sauerzopf and H. W. Weber, 1997 “Solid state and magnetic properties of pure, intercalated and superconducting fullerenes”, *Aust. J. Phys.*, **50**, 329–361.
- [32] S. Iijima, 1991 “Helical microtubules of graphitic carbon”, *Nature*, **354**, 56–58.
- [33] R. S. Pease, 1952 “An X-ray study of boron nitride”, *Acta Cryst.*, **5**, 356–361.
- [34] A. Rubio, J. L. Corkill and M. L. Cohen, 1994 “Theory of graphitic boron nitride nanotubes”, *Phys. Rev. B*, **49**, 5081–5084.

- [35] L. Liu, Y. P. Feng and Z. X. Shen, 2003 “Structural and electronic properties of  $h$ -BN”, *Phys. Rev. B*, **68**, 104102.
- [36] L. A. Girifalco, M. Hodak and R. S. Lee, 2000 “Carbon nanotubes, buckyballs, ropes, and a universal graphitic potential”, *Phys. Rev. B*, **62**, 13104–13110.
- [37] M. Hodak and L. A. Girifalco, 2001 “Fullerenes inside carbon nanotubes and multi-walled carbon nanotubes: Optimum and maximum sizes”, *Chem. Phys. Lett.*, **350**, 405–411.
- [38] T. Belytschko, S. P. Xiao, G. C. Schatz and R. S. Ruoff, 2002 “Atomistic simulations of nanotube fracture”, *Phys. Rev. B*, **65**, 235430.
- [39] K. M. Liew, B. J. Chen and Z. M. Xiao, 2005 “Analysis of fracture nucleation in carbon nanotubes through atomistic-based continuum theory”, *Phys. Rev. B*, **71**, 235424.
- [40] J. H. Walther, R. Jaffe, T. Halicioglu and P. Koumutsakos, 2001 “Carbon nanotubes in water: Structural characteristics and energetics”, *J. Phys. Chem. B*, **105**, 9980–9987.
- [41] M. Rieth, 2003 *Nano-Engineering in Science and Technology: An Introduction to the World of Nano-Design*, World Scientific Publishing, Singapore.
- [42] L. A. Girifalco, 1992 “Molecular properties of  $C_{60}$  in the gas and solid phases”, *J. Phys. chem.*, **96**, 858–861.
- [43] R. S. Ruoff and A. P. Hickman, 1993 “van der Waals binding of fullerenes to a graphite plane”, *J. Phys. Chem.*, **97**, 2494–2496.
- [44] L. Henrard, E. Hernández, P. Bernier and A. Rubio, 1999 “van der Waals interaction in nanotube bundles: Consequences on vibrational modes”, *Phys. Rev. B*, **60**, R8521–R8524.
- [45] S. Iglesias-Groth, J. Breton and C. Girardet, 1997 “An analytical approach for interlayer interaction in spherical buckyonions”, *Chem. Phys. Lett.*, **264**, 351–358.

- [46] H. Guérin, 1997 “Interacion energy between shells of spherical carbon onions”, *J. Phys. B: At. Mol. Opt. Phys.*, **30**, L481–L485.
- [47] J. P. Lu and W. Yang, 1994 “The shape of large single- and multi-shell fullerenes”, *Phys. Rev. B*, **49**, 11421–11424.
- [48] B. Verberck and K. H. Michel, 2006 “Nanotube field of C<sub>60</sub> molecules in carbon nanotubes: Atomistic versus continuous approach”, *Phys. Rev. B*, **74**, 045421.
- [49] T. A. Hilder and J. M. Hill, 2007 “Continuous versus discrete for interacting carbon nanostructures”, *J. Phys. A: Math. Theor.*, **40**, 38513868.
- [50] M. Bockrath, D. H. Cobden, P. L. McEuen, N. G. Chopra, A. Zettl, A. Thess and R. E. Smalley, 1997 “Single-electron transport in ropes of carbon nanotubes”, *Science*, **275**, 1922–1925.
- [51] B. N. J. Persson, U. Tartaglino, E. Tosatti and H. Ueba, 2004 “Electronic friction and liquid-flow-induced voltage in nanotubes”, *Phys. Rev. B*, **69**, 235410.
- [52] S. Sapmaz, Y. M. Blanter, L. Gurevich and H. S. J. van der Zant, 2003 “Carbon nanotubes as nanoelectromechanical systems”, *Phys. Rev. B*, **67**, 235414.
- [53] Z.-C. Tu and Z.-C. Ou-Yang, 2002 “Single-walled and multiwalled carbon nanotubes viewed as elastic tubes with the effective Young’s moduli dependent on layer number”, *Phys. Rev. B*, **65**, 233407.
- [54] B. J. Cox, N. Thamwattana and J. M. Hill, 2007 “Mechanics of atoms and fullerenes in single-walled carbon nanotubes. II. Oscillatory behaviour”, *Proc. R. Soc. A*, **463**, 477–494.
- [55] T. A. Hilder and J. M. Hill, 2007 “Orbiting atoms and C<sub>60</sub> fullerenes inside carbon nanotori”, *J. Appl. Phys.*, **101**, 064319.
- [56] C.-C. Ma, Y. Zhao, C.-Y. Yam, G. Chen and Q. Jiang, 2005 “A tribological study of double-walled and triple-walled carbon nanotube oscillators”, *Nanotech.*, **16**, 1253–1264.

- [57] B. J. Cox, N. Thamwattana and J. M. Hill, 2007 “Mechanics of atoms and fullerenes in single-walled carbon nanotubes. I. Acceptance and suction energies”, *Proc. R. Soc. A*, **463**, 461–476.
- [58] B. J. Cox, N. Thamwattan and J. M. Hill, 2008 “Mechanics of nanotubes oscillating in carbon nanotube bundles”, *Proc. R. Soc. A*, **464**, 691710.
- [59] P. Liu, Y. W. Zhang and C. Lu, 2005 “Oscillatory behavior of C<sub>60</sub>-nanotube oscillators: A molecular-dynamics study”, *J. Appl. Phys.*, **97**, 094313.
- [60] P. J. F. Harris, 2003 *Carbon Nanotubes and Related Structures*, Cambridge University Press, UK, 1<sup>st</sup> edition.
- [61] B. W. Smith, M. Monthieux and D. E. Luzzi, 1998 “Encapsulated C<sub>60</sub> in carbon nanotubes”, *Nature*, **396**, 323–324.
- [62] B. W. Smith and D. E. Luzzi, 2000 “Formation mechanism of fullerene peapods and coaxial tube: A path to large scale synthesis”, *Chem. Phys. Letts.*, **321**, 169–174.
- [63] F. Simon, H. Peterlik, R. Pfeiffer, J. Bernardi and H. Kuzmany, 2007 “Fullerene release from the inside of carbon nanotubes: a possible route toward drug delivery”, *Chem. Phys. Lett.*, **445**, 288–292.
- [64] T. A. Hilder and J. M. Hill, 2007 “Modelling the encapsulation of the anti-cancer drug cisplatin into carbon nanotubes”, *Nanotech.*, **18**, 275704.
- [65] S. Okada, S. Saito and A. Oshiyama, 2001 “Energetics and electronic structures of encapsulated C<sub>60</sub> in a carbon nanotube”, *Phys. Rev. Lett.*, **86**, 3835–3838.
- [66] M. Hodak and L. A. Girifalco, 2003 “Systems of C<sub>60</sub> molecules inside (10,10) and (15,15) nanotube: A Monte Carlo study”, *Phys. Rev. B*, **68**, 085405.
- [67] A. Rochefort, 2003 “Electronic and transport properties of carbon nanotube peapods”, *Phys. Rev. B*, **67**, 115401.
- [68] E. G. Noya, 2004 “Thermal conductivity of carbon nanotube peapods”, *Phys. Rev. B*, **70**, 115416.

- [69] M. Yoon, S. Berber and D. Tomanek, 2005 “Energetics and packing of fullerenes in nanotube peapods”, *Phys. Rev. B*, **71**, 155406.
- [70] K. H. Michel, B. Verberck and A. V. Nikolaev, 2005 “Anisotropic packing and one-dimensional fluctuations of  $C_{60}$  molecules in carbon nanotubes”, *Phys. Rev. Lett.*, **95**, 185506.
- [71] H. Ulbricht and T. Hertel, 2003 “Dynamics of  $C_{60}$  encapsulation into single-wall carbon nanotubes”, *J. Phys. Chem. B*, **107**, 14185–14190.
- [72] S. Berber, Y.-K. Kwon and D. Tomanek, 2002 “Microscopic formation mechanism of nanotube peapods”, *Phys. Rev. Lett.*, **88**, 185502.
- [73] H. Ulbricht, G. Moos and T. Hertel, 2003 “Interaction of  $C_{60}$  with carbon nanotubes and graphite”, *Phys. Rev. Lett.*, **90**, 095501.
- [74] M. Hodak and L. A. Girifalco, 2003 “Ordered phases of fullerene molecules formed inside carbon nanotubes”, *Phys. Rev. B*, **67**, 075419.
- [75] A. N. Khlobystov, D. A. Britz, A. Ardavan and G. A. D. Briggs, 2004 “Observation of ordered phases of fullerenes in carbon nanotubes”, *Phys. Rev. Lett.*, **92**, 245507.
- [76] O. Dubay and G. Kresse, 2004 “Density functional calculations for  $C_{60}$  peapods”, *Phys. Rev. B*, **70**, 165424.
- [77] M. Hodak, 2002 *Statistical mechanics and structural properties of  $C_{60}$  molecules inside carbon nanotubes*, Ph.D. thesis, Materials Science and Engineering University of Pennsylvania.
- [78] D. Qian, W. K. Liu, S. Subramoney and R. S. Ruoff, 2003 “Effect of interlayer potential on mechanical deformation of multiwalled carbon nanotubes”, *J. Nanosci. Nanotech.*, **3**, 185–191.
- [79] R. Pincak and V. A. Osipov, 2003 “Localized electron states near pentagons in variously shaped carbon nanoparticles”, *Phys. Lett. A*, **314**, 315–321.

- [80] A. Krishnan, E. Dujardin, M. M. J. Treacy, J. Hugdahl, S. Lynam and T. W. Ebbesen, 1997 “Graphitic cones and the nucleation of curved carbon surfaces”, *Nature*, **388**, 451–545.
- [81] Y. A. Kim, T. Hayashi, K. Osawa, M. Endo and M. S. Dresselhaus, 2003 “Cone-type multi-shell in the hollow core of multi-wall carbon nanotube”, *Chem. Phys. Lett.*, **367**, 537–540.
- [82] S. P. Jordan and V. H. Crespi, 2004 “Theory of carbon nanocones: Mechanical chiral inversion of a micron-scale three-dimensional object”, *Phys. Rev. Lett.*, **93**, 255504.
- [83] M. Ge and K. Sattler, 1994 “Observation of fullerene cones”, *Chem. Phys. Lett.*, **220**, 192–196.
- [84] H. Anton, 1992 *Calculus with Analytic Geometry*, John Wiley & Sons, Inc., USA, 4<sup>th</sup> edition.
- [85] L. Bourgeois, Y. Bando, S. Shinozaki, K. Kurashima and T. Sato, 1999 “Boron nitride cones: Structure determination by transmission electron microscopy”, *Acta Cryst.*, **A55**, 168–177.
- [86] L. Bourgeois, Y. Bando, W. Q. Han and T. Sato, 2000 “Structure of boron nitride nanoscale cones: Ordered stacking of 240° and 300° disclinations”, *Phys. Rev. B*, **61**, 7686–7691.
- [87] W. Q. Han, L. Bourgeois, Y. Bando, K. Kurashima and T. Sato, 2000 “Formation and structure of boron nitride conical nanotubes”, *Appl. Phys. A*, **71**, 83–85.
- [88] F. F. Xu, Y. Bando and D. Golberg, 2003 “The tubular conical helix of graphitic boron nitride”, *New J. Phys.*, **5**, 118.1–16.
- [89] J. H. Lee, 2006 “A study on a boron-nitride nanotube as a gigahertz oscillator”, *J. Korean Phys. Soc.*, **49**, 172–176.
- [90] J. O. Hirschfelder, C. F. Curtiss and R. B. Bird, 1954 *Molecular theory of gases and liquids*, John Wiley & Sons, Inc.

- [91] Z. Slanina, P. Pulay and S. Nagase, 2006 “H<sub>2</sub>, Ne, and N<sub>2</sub> energies of encapsulation in C<sub>60</sub> evaluated with the MPWB1K functional”, *J. Chem. Theory Comput.*, **2**, 782–785.
- [92] O. E. Glukhova, A. I. Zhbanov and A. G. Rezkov, 2005 “Rotation of the inner shell in a C<sub>20</sub>@C<sub>80</sub> nanoparticle”, *Phys. Solid and State*, **47**, 376–382.
- [93] M. Yoshida and E. Osawa, 1993 “Molecular mechanics calculations of giant- and hyperfullerenes with icosahedral symmetry”, *Fullerene Sci. & Technol.*, **1**, 55–74.
- [94] H. Kitahara, T. Oku and K. Suganuma, 2001 “Atomic structure and stability of elliptical carbon onion”, *Eur. Phys. J. D*, **16**, 361–363.
- [95] I. Narita, T. Oku, K. Suganuma, K. Hiraga and E. Aoyagi, 2001 “Formation and atomic structure of a tetrahedral carbon onion”, *J. Mater. Chem.*, **11**, 1761–1762.
- [96] H. W. Kroto and K. McKay, 1988 “The formation of quasi-icosahedral spiral shell carbon particles”, *Nature*, **331**, 328–331.
- [97] S. Itoh, P. Ordejón, D. A. Drabold and R. M. Martin, 1996 “Structure and energetics of giant fullerenes: An order-*n* molecular-dynamics study”, *Phys. Rev. B*, **53**, 2132–2140.
- [98] B. Dunlap and R. Zope *Efficient quantum-chemical geometry optimization and the structure of large icosahedral fullerenes*, <http://arxiv.org/abs/cond-mat/0603225>.
- [99] M. Terrones, G. Terrones and H. Terrones, 2002 “Structure, chirality, and formation of giant icosahedral fullerenes and spherical graphitic onions”, *Struct. Chem.*, **13**, 373–384.
- [100] F. Banhart and P. M. Ajayan, 1996 “Carbon onions as nanoscopic pressure cells for diamond formation”, *Nature*, **382**, 433–435.
- [101] H. W. Kroto, 1987 “The stability of the fullerenes C<sub>*n*</sub>, with *n* = 24, 28, 32, 36, 50 and 70”, *Nature*, **329**, 529–531.



- [102] H. Terrones and A. L. Mackay, 1992 “The geometry of hypothetical curved graphite structures”, *Carbon*, **30**, 1251–1260.
- [103] T. W. Ebbesen and T. Takada, 1995 “Topological and  $sp^3$  defect structures in nanotubes”, *Carbon*, **33**, 973–978.
- [104] B. I. Dunlap, 1994 “Relating carbon tubules”, *Phys. Rev. B*, **49**, 5643–5650.
- [105] R. Saito, G. Dresselhaus and M. S. Dresselhaus, 1996 “Tunneling conductance of connected carbon nanotubes”, *Phys. Rev. B*, **53**, 2044–2050.
- [106] J. C. Charlier, T. W. Ebbesen and P. Lambin, 1996 “Structural and electronic properties of pentagon-heptagon pair defects in carbon nanotubes”, *Phys. Rev. B*, **53**, 11108–11113.
- [107] L. Chico, V. H. Crespi, L. X. Benedict, S. G. Louie and M. L. Cohen, 1996 “Pure carbon nanoscale devices: Nanotube heterojunctions”, *Phys. Rev. Lett.*, **76**, 971–974.
- [108] M. Menon and D. Srivastava, 1997 “Carbon nanotube “T junctions”: Nanoscale metal-semiconductor-metal contact devices”, *Phys. Rev. Lett.*, **79**, 4453–4456.
- [109] B. J. Cox and J. M. Hill, 2007 “Exact and approximate geometric parameters for carbon nanotubes incorporating curvature”, *Carbon*, **45**, 1453–1462.
- [110] P. R. Cromwell, 1997 *Polyhedra*, Cambridge University Press.
- [111] B. I. Dunlap, 1992 “Connecting carbon tubules”, *Phys. Rev. B*, **46**, 1933–1936.
- [112] B. I. Dunlap, 1994 “Constraints on small graphitic helices”, *Phys. Rev. B*, **50**, 8134–8137.
- [113] S. Itoh, S. Ihara and J. Kitakami, 1993 “Toroidal form of carbon  $C_{60}$ ”, *Phys. Rev. B*, **47**, 1703–1704.
- [114] S. Ihara, S. Itoh and J. Kitakami, 1993 “Toroidal forms of graphitic carbon”, *Phys. Rev. B*, **47**, 12908–12911.

- [115] S. Itoh and S. Ihara, 1993 “Toroidal forms of graphitic carbon. II. Elongated tori”, *Phys. Rev. B*, **48**, 8323–8328.
- [116] S. Ihara and S. Itoh, 1995 “Helically coiled and toroidal cage forms of graphitic carbon”, *Carbon*, **33**, 931–939.
- [117] X. F. Zhang and Z. Zhang, 1995 “Polygonal spiral of coil-shaped carbon nanotubules”, *Phys. Rev. B*, **52**, 5313–5317.
- [118] A. Fonseca, K. Hernadi, J. B. Nagy, P. Lambin and A. A. Lucas, 1995 “Model structure of perfectly graphitizable coiled carbon nanotubes”, *Carbon*, **33**, 1759–1775.
- [119] J. Gavillet, A. Loiseau, C. Journet, F. Willaime, F. Ducastelle and J. C. Charlier, 2001 “Root-growth mechanism for single-wall carbon nanotubes”, *Phys. Rev. Lett.*, **87**, 275504.
- [120] R. S. Lee, J. Gavillet, M. L. de la Chapelle, A. Loiseau, J. L. Cochon, D. Pigache, J. Thibault and F. Willaime, 2001 “Catalyst-free synthesis of boron nitride single-wall nanotubes with a preferred zig-zag configuration”, *Phys. Rev. B*, **64**, 121405.
- [121] J. Gavillet, J. Thibault, O. Stephan, H. Amara, A. Loiseau, C. Bichara, J. P. Gaspard and F. Ducastelle, 2004 “Nucleation and growth of single-walled nanotubes: The role of metallic catalysts”, *J. Nanosci. Nanotech.*, **4**, 346–359.
- [122] A. Maiti, C. J. Brabec and J. Bernholc, 1997 “Kinetics of metal-catalyzed growth of single-walled carbon nanotubes”, *Phys. Rev. B*, **55**, R6097–R6100.
- [123] R. Geick, C. H. Perry and G. Rupprecht, 1966 “Normal modes in hexagonal boron nitride”, *Phys. Rev.*, **146**, 543–547.
- [124] M. Terrones, W. K. Hsu, H. Terrones, J. P. Zhang, S. Ramos, J. P. Hare, R. Castillo, K. Prassides, A. K. Cheetham, H. W. Kroto and D. R. M. Walton, 1996 “Metal particle catalysed production of nanoscale BN structures”, *Chem. Phys. Lett.*, **259**, 568–573.

- [125] A. Loiseau, F. Willaime, N. Demoncy, G. Hug and H. Pascard, 1996 “Boron nitride nanotubes with reduced numbers of layers synthesized by arc discharge”, *Phys. Rev. Lett.*, **76**, 4737–4740.
- [126] X. Blase, A. D. Vita, J. C. Charlier and R. Car, 1998 “Frustration effects and microscopic growth mechanisms for BN nanotubes”, *Phys. Rev. Lett.*, **80**, 1666–1669.
- [127] D. Golberg, Y. Bando, M. Eremets, K. Takemura, K. Kurashima, K. Tamiya and H. Yusa, 1997 “Boron nitride nanotube growth defects and their annealing-out under electron irradiation”, *Chem. Phys. Lett.*, **279**, 191–196.
- [128] J. C. Charlier, X. Blase, A. D. Vita and R. Car, 1999 “Microscopic growth mechanisms for carbon and boron-nitride nanotubes”, *Appl. Phys. A*, **68**, 267–273.
- [129] M. Menon and D. Srivastava, 1999 “Structure of boron nitride nanotubes: tube closing versus chirality”, *Chem. Phys. Lett.*, **307**, 407–412.
- [130] L. Vaccarini, C. Goze, L. Henrard, E. Hernandez, P. Bernier and A. Rubio, 2000 “Mechanical and electronic properties of carbon and boron-nitride nanotubes”, *Carbon*, **38**, 1681–1690.
- [131] D. E. Knuth, 1974 “Computer science and its relation to mathematics”, *Amer. Math. Monthly*, **81**, 323–343.
- [132] F. Ruskey and J. Sawada, 1999 “An efficient algorithm for generating necklaces with fixed density”, *SIAM J. Comput.*, **29**, 671–684.
- [133] AT&T Lab Research *The On-Line Encyclopedia of Integer Sequence*, <http://www.research.att.com/~njas/sequences/>.
- [134] L. Shen and J. Li, 2005 “Transversely isotropic elastic properties of multiwalled carbon nanotubes”, *Phys. Rev. B*, **71**, 035412.
- [135] J. Tersoff and R. S. Ruoff, 1994 “Structural properties of a carbon-nanotube crystal”, *Phys. Rev. Lett.*, **73**, 676–679.

- [136] V. N. Popov, V. E. V. Doren and M. Balkanski, 2000 “Elastic properties of crystals of single-walled carbon nanotubes”, *Solid State Commun.*, **114**, 395–399.
- [137] E. T. Thostenson and T.-W. Chou, 2003 “On the elastic properties of carbon nanotube-based composites: Modelling and characterization”, *J. Phys. D*, **36**, 573–582.
- [138] H. A. Elliott, 1949 “Axial symmetric stress distributions in aeolotropic hexagonal crystals. the problem of the plane and related problems”, *Proc. Camb. Phil.*, **45**, 621–630.
- [139] Y. C. Fung, 1965 *Foundations of Solid Mechanics*, Prentice-Hall International Series in Dynamics, Prentice-Hall, Englewood Cliffs, New Jersey.
- [140] I. S. Sokolnikoff, 1956 *Mathematical Theory of Elasticity*, McGraw-Hill Book Company, New York, 2<sup>nd</sup> edition.
- [141] L. D. Landau and E. M. Lifshitz, 1970 *Theory of Elasticity*, Pergamon Press, Oxford-New York-Toronto-Sydney-Paris-Frankfurt, 2<sup>nd</sup> edition.
- [142] H. Ding, W. Chen and L. Zhang, 2006 *Elasticity of Transversely Isotropic Materials*, Springer, 1<sup>st</sup> edition.
- [143] A. I. Lure, D. B. McVean and J. R. M. Radok, 1964 *Three-Dimensional Problems of the Theory of Elasticity*, Interscience Publishersk, New York-London-Sydney.
- [144] T. Tran-Cong, 1979 *A Study on the Papkovitch-Neuber Solution in Elasticity and its Applications*, Ph.D. thesis, University of Sydney, Australia.
- [145] A. E. Green and W. Zerna, 1968 *Theoretical Elasticity*, Oxford university press, Oxford, 2<sup>nd</sup> edition.
- [146] A. E. H. Love, 1927 *A Treatise on the Mathematical Theory of Elasticity*, Dover Publications, New York, 4<sup>th</sup> edition.
- [147] V. G. Rekach, 1979 *Manual of the Theory of Elasticity*, MIR Publishers, Moscow, 1<sup>st</sup> edition.

- [148] K. Mylvaganam and L. C. Zhang, 2004 “Important issues in a molecular dynamics simulation for characterising the mechanical properties of carbon nanotubes”, *Carbon*, **42**, 2025–2032.
- [149] T. Vodenitcharova and L. C. Zhang, 2003 “Effective wall thickness of a single-walled carbon nanotube”, *Phys. Rev. B*, **68**, 165401.
- [150] I. S. Gradshteyn and I. M. Ryzhik, 2000 *Table of Integrals, Series, and Products*, Academic Press, 6<sup>th</sup> edition.
- [151] A. Erdélyi, 1953 *Higher Transcendental Functions*, McGraw-Hill, New York.
- [152] W. N. Bailey, 1972 *Generalized Hypergeometric Series*, Hafner publishing company, New York, 1<sup>st</sup> edition.
- [153] F. D. Colavecchia, G. Gasaneo and J. E. Miraglia, 2001 “Numerical evaluation of appell’s  $F_1$  hypergeometric function”, *Comput. Phys. Comm.*, **138**, 29–43.
- [154] P. F. Byrd and M. D. Friedman, 1971 *Handbook of Elliptic Integrals for Engineers and Scientists*, Springer-Verlag Berlin, 2<sup>nd</sup> edition.
- [155] J. Mahanty and B. W. Ninham, 1976 *Dispersion forces*, Academic Press, New York.

# List of the author's publications

## Journal articles

- D. Baowan, B. J. Cox and J. M. Hill, 2008 “Junctions between a boron nitride nanotube and a boron nitride sheet”, *Nanotechnology*, **19**, 075704.
- D. Baowan and J. M. Hill, 2008 “Equilibrium locations for nested carbon nanocones”, *Journal of Mathematical Chemistry*, **43**, 1489-1504.
- D. Baowan and J. M. Hill, 2008 “Suction energy and oscillatory behaviour for carbon nanocones”, *Journal of Computational and Theoretical Nanoscience*, **5**, 302-310.
- B. J. Cox, T. A. Hilder, D. Baowan, N. Thamwattana and J. M. Hill, 2008 “Continuum modelling of gigahertz nano-oscillators”, *International Journal of Nanotechnology*, **5**, 195-217.
- D. Baowan, N. Thamwattana and J. M. Hill, 2008 “Suction energy and off-set configuration for double-walled carbon nanotubes”, *Communications in Nonlinear Science and Numerical Simulation*, **13**, 1431-1447.
- D. Baowan, B. J. Cox and J. M. Hill, 2007 “Two least squares analyses of bond lengths and bond angles for the joining of carbon nanotubes to graphenes”, *Carbon*, **45**, 2972-2980.
- D. Baowan and J. M. Hill, 2007 “Wave-like deformations for oscillating carbon nanotubes”, *International Journal of Solids and Structures*, **44**, 8297-8312.
- D. Baowan, N. Thamwattana and J. M. Hill, 2007 “Encapsulation of C<sub>60</sub> fullerene into single-walled carbon nanotubes: Fundamental mechanical principles and conventional applied mathematical modeling”, *Physical Review B*, **76**, 155411.

- D. Baowan and J. M. Hill, 2007 “Nested boron nitride and carbon-boron nitride nanocones”, *Micro & Nano Letters*, **2**, 46-49.
- D. Baowan and J. M. Hill, 2007 “Force distribution for double-walled carbon nanotubes and gigahertz oscillators”, *Zeitschrift für angewandte Mathematik und Physik (ZAMP)*, **58**, 857-875.
- D. Baowan, N. Thamwattana and J. M. Hill, 2007 “Continuum modelling of spherical and spheroidal carbon onions”, *The European Physical Journal D*, **44**, 117-123.
- D. Baowan, N. Thamwattana and J. M. Hill, 2007 “Zigzag and spiral C<sub>60</sub> chain configurations for fullerenes in carbon nanotubes”, *Journal of Physics A: Mathematical and Theoretical*, **40**, 7543-7556.
- D. Baowan, B. J. Cox and J. M. Hill, 2007 “Toroidal molecules formed from three distinct carbon nanotubes”, *Journal of Mathematical Chemistry*, doi:10.1007/s10910-007-9325-8.

## Conference papers

- D. Baowan, N. Thamwattana and J. M. Hill, 2007 “Mathematical modeling double-walled carbon nanotube oscillators: Gigahertz oscillatory behavior”, *Proceedings of The Asian Simulation and Modeling Conference 2007*, Chiang Mai, Thailand, 9-11 January, 169-175.
- D. Baowan and J. M. Hill, 2006 “Force distribution for double-walled carbon nanotubes”, *Proceedings of the 2006 International Conference on Nanoscience and Nanotechnology*, Brisbane, 3-7 July 2006, 681-684.